UNIVERSITY OF NAPLES FEDERICO II
SCHOOL OF MEDICINE
DEPARTMENT OF PHARMACY

PhD programme in Pharmaceutical Sciences

Synthesis and structural characterization of molecules with specific biological activity

PhD student
Avazbek Abduvakhidov

Tutor
Prof. Michela Varra

Co-Tutor
Prof. Carmela Dell'Aversano

Coordinator
Prof. Rosaria Meli

XXXVIII CYCLE (2023-2025)

Table of Contents

PART III. STUDIES ON PHOTORESPONSIVE AZOBENZENE DERIVATIVES AND PROTEIN - PROTEIN INTERACTION MODULATORS WITH POTENTIAL BIOLOGICAL ACTIVITY

CHAPTER VII: Investigation of The Photochemical and Structural Effects of Ortho-Substitution in 7-Azobenzothiazole Derivatives

CHAPTER VIII: Tetrasubstituted Pyrrole Derivative Mimetics of Protein–Protein Interaction Hot-Spot Residues: A Promising Class of Anticancer Agents Targeting Melanoma Cells

Summary

The doctoral research presented in this thesis lies at the intersection of materials science, analytical chemistry, and organic synthesis, moving across different scientific contexts but united by a common objective: the design, preparation, and characterisation of functional materials and molecules tailored for specific purposes, ranging from biomedical applications to analytical detection.

The first part of this research was carried out in collaboration with several research groups at the University of Naples Federico II, under the coordination of Professor Carlo Altucci (Department of Medical Physics). The work forms part of a broader interdisciplinary project aimed at the development and functionalisation of nanosheet materials with tailored organic molecules to enhance their performance in biomedical applications.

Particular attention was devoted to the use of environmentally sustainable approaches for nanosheet production. MoS_2 and WS_2 were exfoliated in liquid phase using Cyrene, a bio-derived, low-toxicity solvent fully consistent with the principles of green chemistry. This strategy allowed the preparation of stable dispersions of mono- and few-layer nanosheets without resorting to harmful solvents such as NMP or DMF. In parallel, I worked on the synthesis and characterisation of antimonene nanosheets non-covalently functionalised with cyclodextrins, designed to improve their colloidal stability and biodegradability, thereby evaluating their potential suitability for biomedical applications.

During these studies, I became familiar with key structural characterisation techniques, including Scanning Electron Microscopy (SEM), Transmission Electron Microscopy (TEM), and X-ray Photoelectron Spectroscopy (XPS). The extensive analysis and interpretation of experimental data strengthened my ability to address critical aspects related to the structural investigation of complex materials, from sample preparation to the correlation of experimental findings with literature data.

These activities are presented in **Part I** of the thesis, which is composed of three chapters. **Chapter 1** provides a general introduction to nanomaterials, with particular emphasis on transition metal dichalcogenides (TMDs) and on antimony-based nanomaterials, outlining the main production and functionalisation methodologies. **Chapter 2** describes the results obtained from the green exfoliation and characterisation of MoS_2 and WS_2 nanosheets, while **Chapter 3** reports the outcomes related to the preparation, functionalisation with cyclodextrins, and biodegradation behaviour of antimonene nanosheets.

My expertise in the design and preparation of functional systems expanded through participation in the European project Blueshellfish (*Solutions to prevent and mitigate the impacts of HABs in Aquaculture and Fisheries, in the context of global warming*). The project focuses on developing strategies to prevent and mitigate the impact of harmful algal blooms (HABs) in aquaculture and fisheries. Under the supervision of Dr. Mònica Campàs, I joined the research line dedicated to the design of biosensing systems for marine toxins, focusing on the

use of nucleic acid–based recognition elements (aptamers) as alternatives or complements to antibodies in analytical assays.

Within this context, my research activities were devoted to the development of aptamer-based biosensors for the detection of saxitoxin (STX), a potent marine neurotoxin of high regulatory and ecological relevance. The work was performed in the framework of a secondment agreement between the University of Naples Federico II and IRTA. After synthesizing biotinylated DNA aptamers for STX by means of an automated oligonucleotide synthesizer and the phosphoramidite method, I applied these aptamers in various analytical formats, including microplate, electrochemical, and magnetic bead-based systems, exploring their potential as recognition elements in colorimetric and hybrid antibody–aptamer assays. The assays did not yet achieve complete functional detection of STX, and further studies will be fundamental in identifying the critical parameters affecting aptamer performance, such as the surface chemistry of the different applied supports and the preservation of aptamer folding upon immobilisation.

In parallel, I contributed to an interlaboratory validation study (Ring Test) developed by the Interfibio Research Group (University Rovira i Virgili, Spain), in collaboration with IRTA and the Hellenic Centre for Marine Research (HCMR, Greece). The study assessed the reproducibility of a hybrid aptamer-antibody lateral flow assay (LFA) for tetrodotoxin (TTX) detection. These activities are presented in **Part II** of the thesis, composed of three chapters. **Chapter 4** introduces the aptamers and their use in biosensing, with an overview of optical and electrochemical systems currently employed for saxitoxin detection.

Chapter 5 describes the experimental approaches adopted during my research period at IRTA, focusing on saxitoxin detection using aptamer-based biosensing assays. **Chapter 6** presents the interlaboratory study on the aptamer-antibody lateral flow assay for TTX.

Part III of the thesis focused on the synthesis and structural characterization of small molecules having specific properties. In this context, my work involved the synthesis, optimisation, and characterisation of new azobenzene derivatives, designed to achieve efficient visible-light responsiveness and enhanced stability of the cis isomer in aqueous environments. These studies provided important insight into the relationship between molecular structure and photo-chemical behaviour. The overall results are discussed in **Chapeter 7**. In parallel, I actively participated in a multidisciplinary study aimed at the discovery and development of bioactive small molecules capable of modulating protein–protein interactions (PPIs), which play a central role in cellular signalling and disease progression. The results are presented **Chapter 8.**

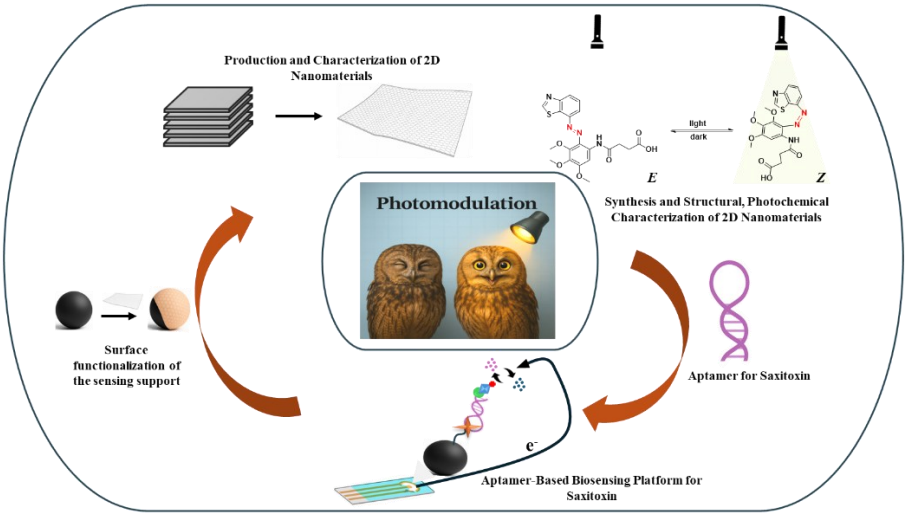

Schematic overview of the interdisciplinary scope of this doctoral research, highlighting the three main thematic areas explored throughout the thesis: (i) the green synthesis and functionalisation of 2D nanomaterials for biomedical applications; (ii) the design and analytical implementation of nucleic acid–based biosensing strategies for marine toxin detection; and (iii) the synthesis and photochemical modulation of functional small molecules. The figure summarises the conceptual framework connecting these research lines, ranging from material preparation and molecular design to analytical detection and light-controlled modulation.

PART I

TWO-DIMENSIONAL NANOMATERIALS: FUNDAMENTALS, SUSTAINABLE PROCESSING AND BIOCOMPATIBILITY

CHAPTER I

GENERAL INTRODUCTION TO NANOMATERIALS

1.1 Definition and Classification of Nanomaterials

In the past few decades, nanomaterials have moved from being a niche research curiosity to one of the most dynamic and influential fields in modern materials science. Materials are defined as nanomaterials if their size or one of their dimensions is in the range of 1 to 100 nm [1]. At these dimensions, surface effects dominate, electronic structures are reshaped, and phenomena linked to quantum confinement emerge. As a result, nanomaterials can exhibit optical, mechanical, and electronic properties that simply do not exist at larger scales, opening opportunities in areas as diverse as energy storage, catalysis, electronics, environmental remediation, and medicine [2]. In recent decades, the exponential growth of nanoscience has been driven by advances in synthetic methodologies, characterization techniques, and a better understanding of how atomic and molecular arrangements determine macroscopic properties.

A widely used framework for classifying nanomaterials is based on dimensionality, which reflects the number of spatial dimensions that lie within the nanoscale range:

- Zero-dimensional (0D) nanomaterials, have all three spatial dimensions below 100 nm. Examples include nanoparticles, quantum dots, and fullerenes. Their properties are strongly size-dependent, often displaying discrete energy levels because of quantum confinement [3].
- One-dimensional (1D) nanomaterials, have two dimensions within the nanoscale and one dimension extended at the microscale or beyond. Nanowires, nanotubes, and nanorods fall into this category. Their high aspect ratios often yield

anisotropic electrical, optical, or thermal transport properties [4].

- Two-dimensional (2D) nanomaterials, possess one dimension in the nanoscale range (thickness) while extending laterally over much larger distances. This category includes graphene, transition metal dichalcogenides (TMDs), hexagonal boron nitride, and black phosphorus. They are characterised by strong in-plane bonding and weak van der Waals interactions between layers, which allows them to be exfoliated into atomically thin sheets [5].
- Three-dimensional (3D) nanomaterials are bulk materials that contain nanoscale features throughout their structure, such as nanoporous frameworks, nanocomposites, or polycrystalline solids with nanosized grains. These materials combine bulk mechanical stability with enhanced properties arising from their nanoscale morphology [3]

It is important to note that dimensionality is not merely a descriptive attribute; it directly affect the electronic density of states, the phonon dispersion, the surface reactivity, and the interaction with external fields. Consequently, the classification of nanomaterials according to dimensionality offers a useful conceptual framework for predicting and rationalising their properties, as well as for guiding their synthesis and application.

1.2 Two dimensional materials (2DMs): structure, types, and general properties

2DMs form a fascinating and relatively young branch of nanoscience. What makes them distinct is their extreme anisotropy: one dimension the thickness is reduced to the scale of atoms, while the other two dimensions can extend over micrometres or even millimetres. In this flattened world, the typical properties of bulk materials dramatically change, and in many cases, entirely new behaviours emerge [6].

The concept of studying matter in atomically thin form may seem self-evident today, but prior to 2004 isolating a single-layer crystal was deemed nearly impossible. That perception changed when graphene, was successfully obtained by mechanical exfoliation [7]. Its exceptional conductivity, strength, and transparency sparked global interest in two-dimensional (2D) materials. Since then, a wide range of 2D systems has been discovered: insulating and inert hexagonal boron nitride (h-BN) [8]; transition metal dichalcogenides (TMDs), which become direct band gap semiconductors at the monolayer level; and elemental 2D materials, or Xenes, such as silicene, phosphorene, and antimonene, whose electronic properties can be tuned through chemical or physical stimuli [9].

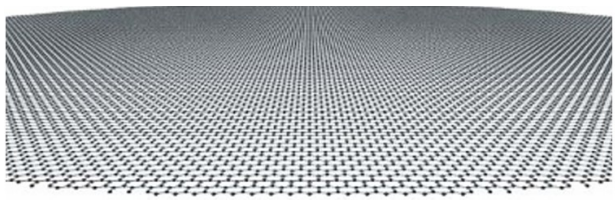

Figure 1. *Flat graphene crystal in real space (perspective view)[8].*

The main features of 2D materials arise from their high surface-to-volume ratio: a large fraction of their atoms are directly exposed to the surrounding environment, enabling strong interaction with other materials, molecules, or biological systems. Their basal planes are typically flat and defect-free, contributing to chemical stability in many conditions, while edges and defects often display enhanced reactivity. This combination makes 2D materials versatile platforms for applications in sensing, catalysis, energy conversion, and biomedicine. Despite their potential, 2D materials pose significant challenges in synthesis and processing. Controlling layer number, defect density, and lateral dimensions remains critical, especially for applications demanding uniformity and reproducibility. Consequently, scalable, environmentally sustainable methods for producing high-quality materials are a key focus of ongoing research. The following sections provide a concise overview of the principal physicochemical properties, methods for preparation and application areas of nanosheets derived from two chalcogenides, MoS_2 and WS_2, as well as antimony, which has been the focus of my research.

1.3 Transition Metal Dichalcogenides

TMDs are a broad class of layered materials with the general formula MX_2, where M is a transition metal from group IV–VI and X is a chalcogen (S, Se, or Te) [9]. Their crystal structure consists of a plane of transition metal atoms sandwiched between two planes of chalcogen atoms, forming an X–M–X configuration. Strong in-plane M–X bonds hold the layers together in-plane, while weak van der Waals forces between layers allow for exfoliation into atomically thin sheets [10].

One of the defining features of many semiconducting TMDs is the thickness-dependent electronic transition. Bulk crystals generally exhibit an indirect band gap, but upon thinning to a single layer, several TMDs undergo a transformation to a direct band gap.

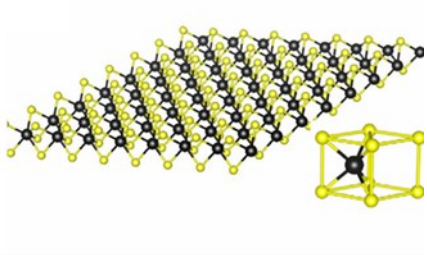

Figure 2. *Monolayer transition metal dichalcogenide crystal structure. The transition metal atoms appear in black, the chalcogen atoms in yellow. [11].*

From a mechanical standpoint, TMD monolayers are both strong and flexible, with reported Young's moduli in the 200–300 GPa range and fracture strains of up to ~10%. Chemically, basal planes are often inert under ambient conditions, whereas edges and defects show enhanced reactivity, particularly relevant for catalysis, sensing, and functionalisation strategies [12].

These combined structural, electronic and optical features make TMDs extremely attractive in a broad spectrum of technological domains. In nanoelectronics, semiconducting monolayers can operate as active channels in field-effect transistors, offering high on/off ratios and scalability down to nanometre dimensions [13]. Their direct band gap in the monolayer regime also makes them ideal candidates for optoelectronic applications, where efficient light absorption, emission, and modulation are essential. In the field of energy storage, the intrinsic

layered architecture facilitates ion intercalation, enabling their integration into next-generation batteries and supercapacitors. Finally, when appropriately functionalised to ensure biocompatibility, TMDs can serve valuable roles in biomedical applications, where their strong optical absorption and high surface area can be exploited for imaging, photothermal therapy, and biosensing.

1.4 Molybdenum disulfide

Molybdenum disulfide (MoS_2) is widely regarded as the prototypical semiconducting TMD and serves as a reference point for understanding the physics, chemistry, and applications of two-dimensional semiconductors. While bulk MoS_2 has long been known for its lubricating properties stemming from its lamellar structure and low interlayer shear strength, its isolation in monolayer form following the breakthrough of graphene research revealed a markedly different set of behaviours, most notably the transition from an indirect to a direct band gap [14]. Bulk MoS_2 is an indirect band gap semiconductor with a gap of approximately 1.29 eV. Upon thinning to a monolayer, it becomes a direct band gap semiconductor with a gap of around 1.8–1.9 eV. This transition, mainly due to quantum confinement and the loss of interlayer coupling, results in a strong interaction with light and an intense photoluminescence signal absent in bulk MoS_2 [15]. The optical response is dominated by excitons, with two prominent peaks (A and B excitons) separated by about 0.15–0.2 eV owing to spin–orbit coupling in the valence band.

1.4.1 Biomedical Applications of MoS_2

More recently, biomedical applications of MoS_2 have emerged as a rapidly expanding field. Functionalized MoS_2 nanosheets have demonstrated significant potential in different area spanning from photothermal therapy to theranostic. Indeed, due to strong NIR absorption MoS_2 efficiently converts near-infrared (NIR) light into heat, potentially enabling targeted tumor ablation [16]. As an example 1T-MoS_2 NSs decorated with AuNRs (MoS2@AuNRs) by electrostatic adsorption were used as antibacterial agent in a phototherapy application [17]whereas exploiting the tunable surface chemistry of the material, MoS_2 nanosheets can be engineered to co-deliver chemotherapeutic agents [18] and genetic material (e.g., siRNA), showing very promising potentialities in therapy for multidrug-resistant cancers [19].

1.5 Tungsten Disulfide

Tungsten disulfide (WS_2) belongs to the family of TMDs and crystallises in a layered hexagonal structure, where each monolayer consists of a tungsten atom plane sandwiched between two sulfur atom planes in trigonal prismatic coordination. These S–W–S layers are stacked along the c-axis and held together by weak van der Waals forces, which facilitate their mechanical or chemical exfoliation into single- or few-layer nanosheets [22]. Bulk WS_2 is an indirect band gap semiconductor with a gap of approximately 1.3–1.35 eV, but when thinned to a single layer it undergoes an indirect-to-direct band gap transition, with a monolayer gap of ~2.0 eV [23]. This change leads to a significant enhancement in photoluminescence efficiency, making

monolayer WS_2 attractive for optoelectronic applications. Its optical response is dominated by strong excitonic features, including A and B excitons separated by spin–orbit splitting of about 0.4 eV, as observed in photoluminescence and absorption spectroscopy. Raman spectroscopy of WS_2 reveals two prominent modes: the in-plane E^2g mode and the out-of-plane A_1g mode. Their frequency separation is sensitive to the number of layers, enabling rapid thickness determination.

The photoluminescence stability at elevated temperatures and the strong light–matter interaction in the visible spectrum make WS_2 highly promising for photodetectors, light-emitting diodes, and valleytronic devices where thermal robustness is critical [24]. In electrocatalysis, particularly for the hydrogen evolution reaction (HER, relevant for H2 production), metallic 1T-WS_2 and defect-rich 2H-WS_2 nanosheets demonstrate enhanced activity due to their higher electrical conductivity and the abundance of active edge sites.

1.6 Antimonene

1.6.1 Structure and properties

As a member of the group 15 elements, antimonene, the two-dimensional allotrope of antimony, presents a valuable alternative to the most commonly studied 2D material, that is graphene, thanks to its intrinsic band gap, high carrier mobility, and promising potential in biomedical applications [20].

The crystalline landscape of antimonene is defined by several allotropes. The β-phase, with its hexagonal symmetry, is generally the

most stable form under ambient conditions and for isolated monolayers. The α-phase, orthorhombic in nature, is also accessible, particularly under epitaxial growth on selected substrates or through the application of uniaxial strain [21].

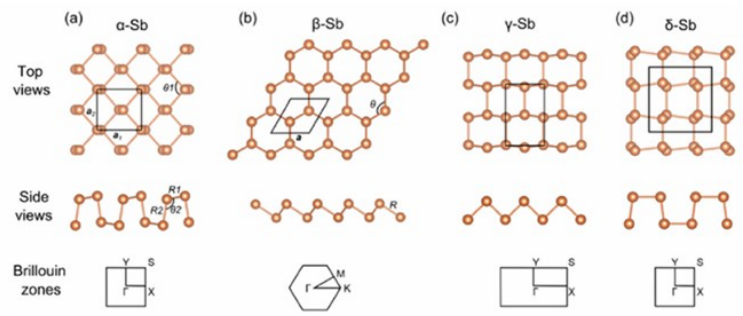

***Figure 4**. Structural configurations of antimonene allotropes: (a) a-Sb, (b) b-Sb, (c) g-Sb, and (d) d-Sb [21].*

The layered bulk crystal of antimony consists of Sb sheets stacked through van der Waals forces, allowing exfoliation into monolayers or few-layer flakes [20]. Bulk antimony is a semimetal, but in its monolayer form a finite band gap opens, typically in the range of 1.2–2.4 eV depending on thickness, allotrope, and environmental factors such as strain or the choice of supporting substrate [22]. This intrinsic gap is a key differentiator from graphene and allows antimonene to operate as a genuine semiconductor in electronic devices, enabling efficient on/off switching in field-effect transistors.

1.6.2 Chemical stability and Oxidation behaviour

Compared to other two-dimensional materials from elements of group 15, antimonene particularly in its β-phase exhibits remarkable

chemical stability under ambient conditions. However, it is not entirely resistant to oxidation. Recent studies have shown that the oxidation process occurs progressively, beginning with the formation of surface oxidized species such as Sb_2O_3, which can further evolve into Sb_2O_5 under more aggressive or prolonged conditions. This transformation is highly dependent on the surrounding environment: oxidation proceeds slowly in dry air but is significantly accelerated in the presence of humidity or light exposure [23].

Oxidation typically initiates at structurally reactive sites such as edges and defects, where the local energy landscape favours chemical interaction with oxygen. The degree of oxidation is also influenced by the material's thickness, with antimonene monolayer being more susceptible than multilayer structures. Nonetheless, even single layers can retain a substantial part of their structural and functional integrity over extended periods. Experimental investigations have confirmed the presence of non-oxidized and oxidized antimonene through X-ray photoelectron spectroscopy (XPS), which revealed characteristic Sb^{3+} and Sb^{5+} states, consistent with Sb_2O_3 and Sb_2O_5 formation (**Figure 5**) [24]. Complementary Raman spectroscopy and microscopy analyses further showed vibrational and morphological changes associated with surface oxidation [24]. Interestingly, the controlled formation of surface oxides has been found to enhance certain properties, such as near-infrared absorption, which can be advantageous in biomedical applications [25].

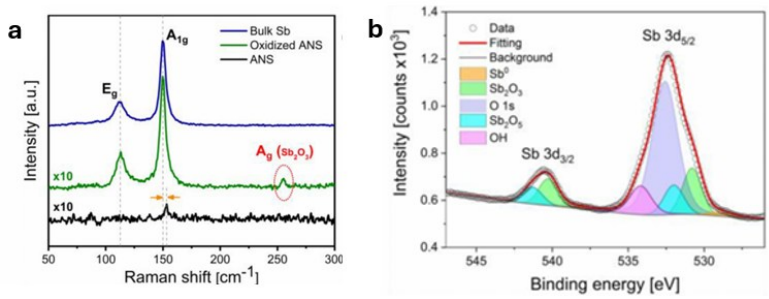

***Figure 5**. Spectroscopic characterization of antimonene oxidation. (a) Raman spectra of bulk antimony, exfoliated antimonene nanosheets (Sb-NS), and oxidized Sb-NS, highlighting the Sb_2O_3 Raman fingerprint at 254.6 cm^{-1}. (b) XPS spectra of the Sb $3d_{5/2}$ and $3d_{3/2}$ core levels for as-exfoliated ANS (after 40 min sonication), showing the coexistence of metallic Sb and oxidized Sb components [24].*

Several strategies have been proposed to mitigate or control the oxidation of antimonene. Among them, surface passivation using polyethylene glycol (PEG) and encapsulation with inert protective layers have proven effective in preserving both the electronic and structural properties of the material, particularly in humid or biologically active environments [26].

1.6.3 Biomedical Application

The biomedical interest in antimonene originates from a convergence of properties that are rarely found together in a single material. Its high specific surface area facilitates drug loading through physical adsorption or chemical attachment, while the tunable band gap and strong near-infrared (NIR) absorption enable efficient photothermal conversion an asset for minimally invasive cancer therapies. Photothermal therapy (PTT) is one of the most explored biomedical applications of antimonene, largely due to its strong absorption in the

near-infrared (NIR) region, particularly around 808 nm, which enables efficient conversion of light into heat. This property allows localised hyperthermia to be induced in tumour tissues, leading to cell damage and necrosis. In a landmark study, Tao et al. demonstrated that few-layer antimonene nanosheets could serve as a multifunctional platform for cancer theranostics, combining both therapeutic and diagnostic capabilities [26]. Upon NIR laser irradiation, the nanosheets exhibited high photothermal conversion efficiency, sufficient to achieve complete ablation of tumours in vivo, while simultaneously enabling real-time photoacoustic and infrared thermal imaging to monitor treatment progression. Beyond thermal ablation, the layered structure and tunable surface chemistry of antimonene also enable high drug-loading capacities and controlled release profiles. Surface functionalisation with biocompatible polymers improves dispersibility and prolongs blood circulation, while conjugation with targeting ligands or biomolecules enhances selective accumulation in tumour via the enhanced permeability and retention (EPR) effect. As illustrated in **Figure 6**, Tao et al. further schematized the preparation of PEGylated antimonene nanosheets loaded with doxorubicin (AM-PEG/DOX NSs) and their systemic administration as photonic nanomedicines. In combined photothermal–chemotherapy strategies, NIR-induced heating not only accelerates drug release but also increases cell membrane permeability, thereby amplifying cytotoxic effects. This synergistic action reduces the required dosage of chemotherapeutic agents while improving therapeutic efficacy, underscoring the potential of antimonene as an integrated theranostic system for multimodal-imaging-guided cancer treatment.

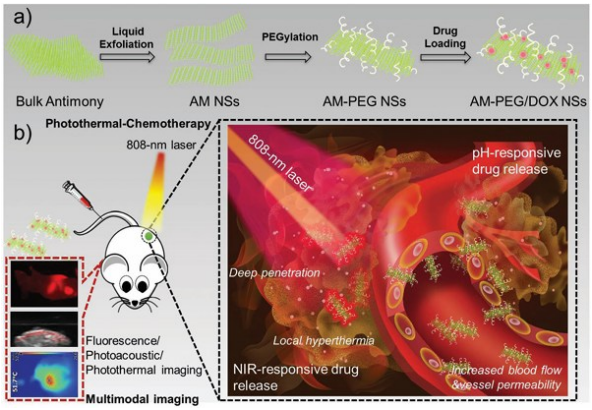

Figure 6. *Schematic illustrations of: a) the preparation of 2D AM-PEG/DOX NSs; and b) the systemic administration of AM-PEG/DOX NSs as pho tonic nanomedicines for multimodal-imaging-guided cancer theranostiocs [26].*

In addition to therapeutic and imaging applications, antimonene has attracted attention in biosensing. Its high conductivity, chemical reactivity, and ability to be functionalised with recognition elements such as aptamers or antibodies make it an excellent transducer for electrochemical detection. Zhang et al. developed an aptamer-functionalised Sb nanosheets-based electrochemical sensor for the detection of alpha-fetoprotein (AFP), an important biomarker for hepatocellular carcinoma. The device operated via electrochemical impedance spectroscopy (EIS), where the binding of AFP to the immobilised aptamer induced measurable changes in charge transfer resistance [27].

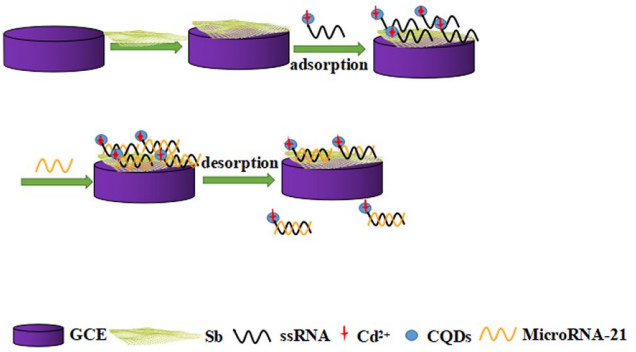

Figure 7. *Micro RNA biosensor schematic diagram and detection principle [27].*

1.7 Fabrication methods of 2d nanomaterials

The synthesis of 2D materials has been the subject of intense research since the discovery of graphene, as the properties of these materials are highly dependent on their structural quality, layer number, lateral size, and defect density. Achieving precise control over these parameters is essential for tailoring 2D materials for specific applications in electronics, energy storage, catalysis, and biomedicine. The preparation strategies can be divided mainly in two approaches named top-down and bottom-up, each with its own advantages and limitations. Top-down methods start from bulk layered crystals, which are broken down into atomically thin sheets by overcoming the weak van der Waals forces between layers. This category includes techniques such as mechanical exfoliation, liquid-phase exfoliation (LPE), and electrochemical exfoliation. These methods are particularly effective for producing high-quality nanosheets while preserving the intrinsic structure of the crystal. However, achieving uniformity in thickness and lateral size, as well as scaling up production, can be challenging.

Bottom-up methods, in contrast, build the 2D material directly from atoms or molecular precursors, assembling the layers during the growth process. Chemical vapor deposition (CVD), atomic layer deposition (ALD), and solvothermal synthesis are the most commonly used bottom-up approaches which allow greater control over thickness, crystallinity, and large-area uniformity, making them attractive for device fabrication. Nevertheless, they often require sophisticated equipment and stringent reaction conditions.

1.7.1 Chemical vapor deposition

Chemical Vapor Deposition (CVD) is a bottom-up synthesis approach that has gained considerable attention for the fabrication of high-quality, single- and few-layer transition metal dichalcogenides (TMDs), particularly for applications in advanced electronics and optoelectronics. In this technique, volatile precursors containing the transition metal and chalcogen are reacted under carefully controlled conditions, enabling the direct growth of crystalline 2D layers on selected substrates [28]. To obtain an uniform single-layer growth a precise control over reaction kinetics and nucleation mechanisms rather than only the fundamental stoichiometry should be adopted. However, the intrinsic anisotropy of layered TMDs is advantageous for 2D growth. The process typically necessitates of elevated growth temperatures, long reaction times, and considerable energy input [29]. Several CVD configurations can be used to produce monolayer TMDs:

1. Vaporization of metal and chalcogen precursors in the reaction zone, followed by simultaneous deposition on the substrate.

2. Co-deposition of metal and chalcogen sources from the vapor phase.
3. Metal thin film deposition on a heated substrate, followed by chalcogenization.
4. Sulfurization of pre-deposited metal oxides, a common route for MoS_2 and WS_2 synthesis.

The morphology, crystallinity, and thickness of the resulting films are strongly influenced by parameters such as precursor placement, temperature gradients, substrate type, and the use of molecular seeding promoters. Moreover, as illustrated in **Figure 8**, surface plasma treatment has been employed to achieve layer-controlled CVD growth of large-area MoS_2 films, further highlighting how substrate modification strategies can be used to tune nucleation and film thickness.

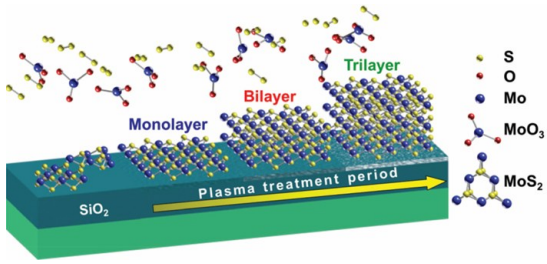

***Figure 8**. Schematic diagram of the layer-controlled CVD growth of large-area MoS_2 films after the surface plasma treatment [28].*

Although CVD can produce large-area, high-quality 2D layers, it presents limitations that hinder its scalability for certain applications. The need for elevated temperatures, controlled atmospheres, and specific substrates complicates transfer to industrial-scale manufacturing. Moreover, the high *thermal budget* and the need to

avoid damage to delicate 2D layers pose additional challenges. For this reason, while CVD remains a method of choice for high-performance electronic and optoelectronic devices, it is generally less suited for biomedical applications, where milder, more biocompatible synthesis conditions are preferred.

1.7.2 Top-Down methods

1.7.2.1 Mechanical Exfoliation

Scotch tape method

Mechanical exfoliation using adhesive tape, famously known as the *Scotch tape method*, was the technique that first led to the isolation of monolayer graphene in 2004 [7]. In this method, adhesive tape is repeatedly pressed against the surface of a bulk crystal and peeled away, progressively thinning the crystal down to few- or single-layer flakes. The exfoliated flakes are then transferred to a substrate, typically SiO_2/Si, for characterization or device fabrication. An illustrative procedure of this method is shown in **Figure 9**, where the Scotch tape–based micromechanical cleavage of highly oriented pyrolytic graphite (HOPG) is presented as a model system for producing ultrathin flakes [30]. The main advantage of this technique is the exceptional crystalline quality and low defect density of the obtained layers, which makes them ideal for fundamental studies of optical and electronic properties. However, the yield is extremely low, the lateral size is limited, and there is no reliable control over the number of layers, making it unsuitable for large-scale production.

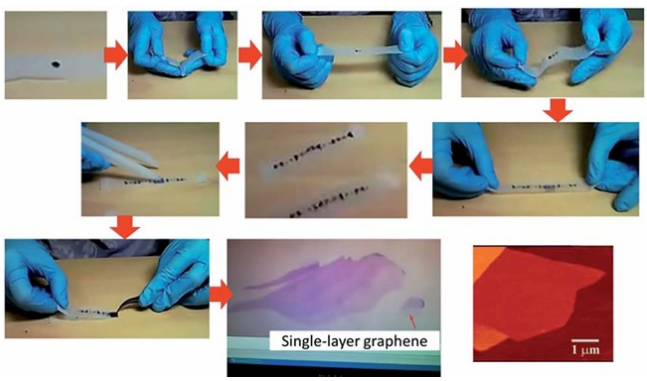

Figure 9. *An illustrative procedure of the Scotch-tape based micro mechanical cleavage of HOPG [30].*

Ball milling

Ball milling represents another purely mechanical route, where bulk material is subjected to repeated high-energy impacts from milling balls inside a rotating jar. The resulting shear and compressive forces can break the interlayer bonds, producing nanosheets. Ball milling can be performed in dry conditions or in the presence of a liquid medium. This method, widely used in industrial powder production, has proven to be a promising candidate for generating 2D nanosheets from layered crystals. Two operational approaches can be distinguished. In the first, shear forces dominate, promoting layer delamination while largely preserving the lateral dimensions of the flakes, thus yielding nanosheets with relatively larger sizes. In the second, fragmentation occurs mainly through vertical collisions or impacts between the balls and the material during rotation, resulting in smaller nanosheets with reduced lateral dimensions. The choice between these regimes depends on milling parameters such as ball size, rotation speed, and the use of process control agents. An illustrative schematic of the ball milling

process is shown in **Figure 10**, highlighting how repeated shear and impact forces can delaminate layered crystals into nanosheets [30].

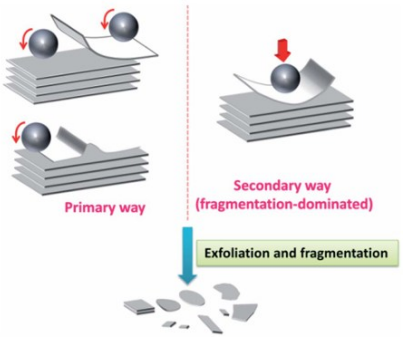

***Figure 10**. Illustration of the mechanical mechanism for exfoliation via ball milling [30].*

1.7.2.2 Intercalation-assisted exfoliation

The intercalation method, as the name suggests, involves the insertion of guest species between the layers of a layered material. In the case of transition metal dichalcogenides (TMDs), such insertion increases the interlayer spacing and weakens the van der Waals forces that normally hold the layers together. When followed by an additional mechanical stimulus such as ultrasonication, this approach enables the production of high-yield, high-concentration dispersions of single- or few-layered nanosheets, often surpassing other exfoliation methods in efficiency and scalability [31]. The choice of intercalating species is dictated by their ability to react and generate a gas as a by-product. The generated gas expands within the interlayer galleries, acting as a delamination force that promotes the separation of layers into individual nanosheets. Direct gaseous intercalants, acid treatments, and, most prominently, alkali metals such as lithium have been reported as effective strategies to achieve complete exfoliation of TMDs. Among these, lithium

intercalation has received the greatest attention, enabling the isolation of ultrathin, single-layer MoS_2 and related compounds with remarkable structural and electronic properties [32]. This process is schematically illustrated in **Figure 11**, where the intercalation of lithium ions into layered MoS_2 followed by exfoliation yields ultrathin nanosheets [33].

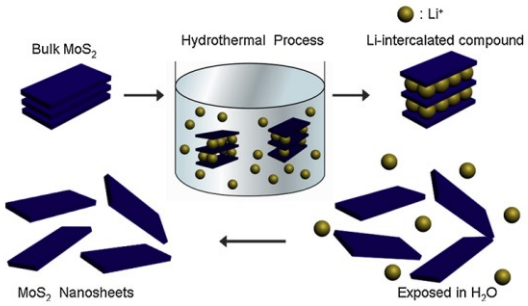

***Figure 11**. Schematic representation of the formation of MoS_2 nanosheets [33].*

1.7.2.3 Ultrasonication-assisted exfoliation

Among the various top-down approaches for producing 2D materials, ultrasonication-assisted exfoliation has gained significant attention as a versatile and scalable method that is well-suited for applications requiring mild processing conditions, including those in the biomedical field [31]. Unlike intercalation or ion-exchange strategies, which often involve harsh chemicals, toxic solvents, or specialized setups, sonication-based techniques can be performed in relatively benign environments, making them adaptable to a wide range of layered materials such as graphite, MoS_2, WS_2, and other emerging members of the 2D family.

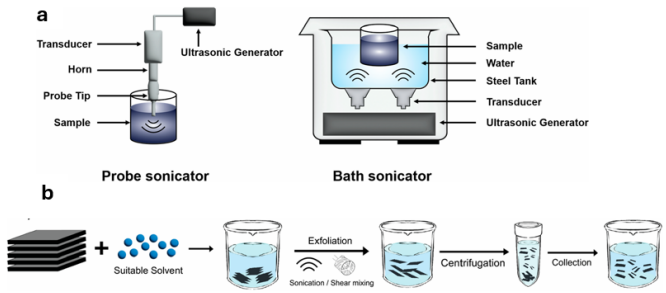

Figure 12. *Schematic representation of (a) probe and bath sonicators, and (b) the sonication/shear-assisted exfoliation process leading to the delamination of layered crystals into nanosheets [34].*

The underlying mechanism relies on the ability of ultrasonic energy to generate intense hydrodynamic forces in a liquid medium. When a bulk layered crystal is dispersed in a suitable solvent and subjected to high-frequency acoustic waves, the periodic pressure variations produce two main physical effects: vibration and cavitation. Cavitation refers to the formation, growth, and collapse of microscopic bubbles in the solvent. The implosive collapse of these bubbles' releases localized bursts of energy, generating shock waves and microjets that can overcome the van der Waals forces holding the layers together. The combined effect of vibration and cavitation progressively peels apart the stacked layers, producing suspensions of single- and few-layer nanosheets.

Optimizing the process parameters is crucial for achieving high yields and controlling the morphology of the resulting nanosheets. Key variables include sonication power, duration, solvent choice, and temperature control. High-power sonication can enhance exfoliation efficiency, but excessive exposure causes introducing structural defects or reducing lateral size. The solvent plays a dual role: it must stabilize the exfoliated sheets through non-covalent interactions and

match the surface energy of the target material to minimize restacking. This distinction gives rise to “good solvents”, which provide high exfoliation efficiency, and “bad solvents”, where energy mismatch leads to aggregation and poor yields. Commonly used solvents for this purpose include N-methyl-2-pyrrolidone (NMP), dimethylformamide (DMF), though for biomedical applications low-toxicity and biocompatible solvents are preferred.

Figure 13. *Sonication-assisted exfoliation of layered crystals in solvents: good solvents stabilize nanosheets, while bad solvents lead to reaggregation and sedimentation [31].*

A typical workflow involves dispersing the bulk material in the selected solvent, subjecting it to ultrasonic treatment under controlled conditions, and then applying post-exfoliation steps such as centrifugation to remove unexfoliated particles and select specific size fractions (**Figure 12b**).

1.8 Functionalisation strategies of 2D materials

In pristine form many 2D nanosheets suffer from limited stability in aqueous media, uncontrolled aggregation, and sometimes undesired toxicity, posing important concerns in biomedical applications. To overcome these drawbacks and expand their practical utility, functionalisation strategies have been developed to modulate surface chemistry, enhance dispersibility, and introduce additional

functionalities. Broadly, these approaches can be categorised into covalent and non-covalent functionalisation, each with its advantages and limitations.

1.8.1 Covalent functionalisation

Covalent functionalisation involves the direct formation of chemical bonds between the nanosheet and external moieties. In transition metal dichalcogenides (TMDs), such modifications typically occur at defect sites, sulfur vacancies, or edges, where reactive sites are more accessible [35]. Among the various strategies, thiol-based chemistry has been particularly effective: amphiphilic ligands bearing thiol groups can anchor at sulfur sites, simultaneously promoting exfoliation and providing functional handles for further derivatisation. This principle is illustrated in **Figure 14**, which depicts the ligand structure and possible binding modes on MoS_2 [36].

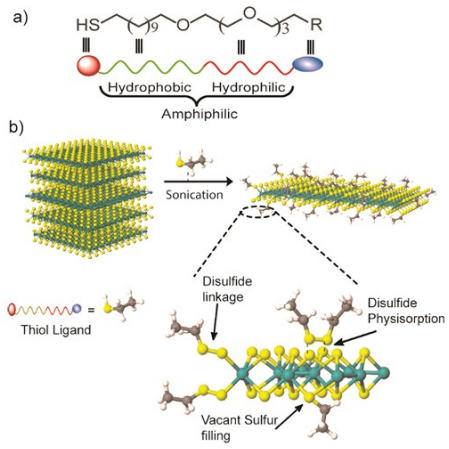

***Figure 14**. Exfoliation of 2H-MoS_2 with amphiphilic ligands showing structure and possible surface functionalisation modes [36].*

Although non-covalent functionalization strategies are the most widely employed to stabilize antimonene in aqueous or biological environments, covalent modification has also proven feasible. One example is diazonium-based chemistry, where aryl radicals react with surface atoms of antimonene to form stable covalent bonds, thereby enhancing stability and enabling the grafting of functional aromatic moieties (**Figure 15**) [37].

Figure 15*. Graphical illustration of covalent functionalization of antimonene/bismuthene with p-nitrobenzenediazonium tetrafluoroborate (p-NBD) under ambient white ligh [37].*

More recently, silane-based functionalization has been demonstrated as an alternative approach, in which organosilane molecules covalently anchor to the surface of antimonene nanosheets. This modification not only protects the nanosheets from oxidation but also provides a versatile platform for integrating antimonene into hybrid materials such as copolymerized gel glasses (**Figure 16**), thereby broadening its potential applications from biomedicine to catalysis, electronics, and optoelectronics [38]

Covalent attachment ensures long-term stability and strong integration of the functional groups; however, it may also disrupt the lattice and alter the electronic band structure, which can be detrimental for optoelectronic applications.

***Figure 16**. Schematic Diagram for the Preparation of Silane-Functionalized Antimonene Nanosheets and Their Copolymerized Gel Glasses [38].*

1.8.2 Noncovalent functionalisation

Noncovalent functionalization strategies are widely employed to tailor the surface properties of 2D materials while preserving their intrinsic crystal structure and electronic characteristics. Unlike covalent modifications, which rely on the creation of chemical bonds, non-covalent approaches exploit weak interactions such as electrostatic forces, π–π stacking, van der Waals interactions, and host–guest chemistry. This renders them particularly advantageous for applications where the preservation of the intrinsic electronic conductivity and photophysical characteristics of the nanosheets is critical [39].

For TMDs, non-covalent functionalisation has proven to be an effective strategy to achieve stable aqueous dispersions. A representative example is the use of DNA and RNA nucleotides, which adsorb on MoS_2 surfaces through a combination of π–π stacking, hydrophobic interactions, and Lewis's acid–base interactions between surface atoms of MoS_2 and nucleotide functional groups. Such

interactions result in markedly enhanced dispersibility compared to graphene, as schematically depicted in **Figure 17**. This non-covalent approach not only prevents aggregation but also preserves the intrinsic band structure of MoS_2, providing a versatile platform for developing hybrid bio-functional systems relevant to biosensing and optoelectronic applications [40].

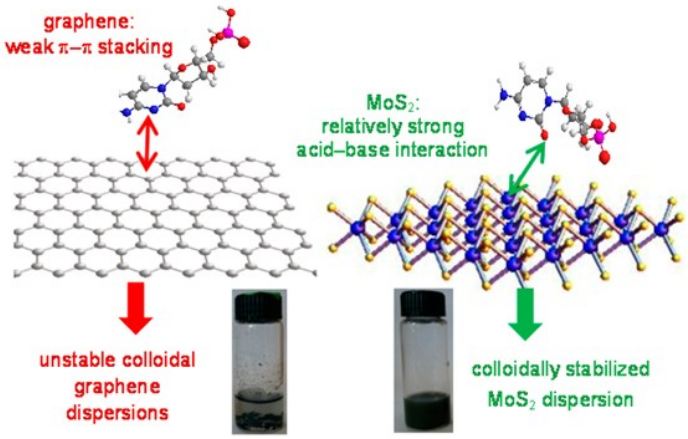

***Figure 17**. Schematic illustrating the different mechanisms of stabilization of colloidal dispersions of graphene and MoS2 flakes with DNA/RNA nucleotides [40].*

Another versatile route involves host–guest supramolecular chemistry. Cyclodextrins, cucurbiturils, and calixarenes can form inclusion complexes with nanosheets or with functional molecules anchored on their surfaces, enhancing hydrophilicity, colloidal stability, and bioavailability [41].

CHAPTER II

Green Exfoliation and Characterisation of MoS_2 and WS_2 Nanosheets

This chapter is published in:

Adam, J., Singh, M., **Abduvakhidov, A**., Del Sorbo, M. R., Feoli, C., Hussain, F., Kaur, J., Mirabella, A., Rossi, M., Sasso, A., Valadan, M., Varra, M., Rusciano, G., & Altucci, C. (**2023**). The Effectiveness of Cyrene as a Solvent in Exfoliating 2D TMDs Nanosheets. *International Journal of Molecular Sciences*, *24*(13), 10450. https://doi.org/10.3390/ijms241310450

2.1 Sustainability Challenges in the Production of 2D Nanomaterials

The scalability and sustainability of the production of 2D-nanomaterials remain key challenges that must be addressed before these materials can translate from laboratory synthesis to widespread industrial application [42]. According to the methodologies described in the Chapter 1 at present, one of the most widely employed strategies for obtaining high-quality dispersions of layered materials is liquid-phase exfoliation [43]. Traditionally, solvents such as N-methyl-2-pyrrolidone, dimethylformamide, and dimethyl sulfoxide, have been the standard media for exfoliation due to their surface energy compatibility with 2D crystals, enabling the formation of stable dispersions [44]. Despite their efficiency, these solvents are associated with severe limitations. NMP and DMF, for instance, are recognized as toxic and potentially carcinogenic, with restrictions placed on their use in both Europe and the United States [42]. Their high boiling points (>150 °C) not only complicate solvent removal and recycling but also increase the energy demand of the process, thereby reducing overall sustainability. Moreover, residual solvent molecules often remain adsorbed on nanosheet surfaces, which may alter the intrinsic properties of the material and limit their use in sensitive applications such as biomedicine or optoelectronics.

From an industrial perspective, these factors pose barriers to scalability, as processes that are energy-intensive, environmentally hazardous, or reliant on regulated chemicals cannot be easily adopted for large-scale manufacturing. Consequently, the field of 2D

nanomaterials synthesis faces an urgent need to transition towards greener and safer alternatives, in line with the principles of Green Chemistry [43]. Addressing this challenge is not only essential for reducing the environmental footprint of production but also critical for enabling the safe integration of 2D materials into biomedical and energy-related applications.

2.2 Green Chemistry and Alternative Solvents for Liquid-Phase Exfoliation

In recent years, the production of two-dimensional materials has increasingly incorporated the conceptual framework of Green Chemistry, which encourages the reduction of hazardous substances, the use of safer solvents, and greater energy efficiency in synthetic processes. These principles are particularly relevant for LPE, where the choice of solvent plays a central role [42]. In particular, a solvent suitable for LPE must balance several physicochemical properties, efficiently stabilizing exfoliated nanosheets, exhibiting surface energy compatibility with the layered crystal, and at the same time it must satisfy sustainability criteria such as low toxicity and biodegradability. Conventional solvents like NMP and DMF meet the requirements for dispersion, but they are toxic, difficult to recycle, and environmentally persistent, making them incompatible with the principles of safe and sustainable materials processing. To address this issue, solvent selection is progressively moving from empirical screening toward more rational, theory-driven approaches. A key tool in this regard is the use of Hansen solubility parameters (HSPs), which offer a predictive framework based on intermolecular interactions. By

matching the dispersive, polar, and hydrogen bonding contributions of the solvent with those of the exfoliated material, it becomes possible to identify greener alternatives with similar exfoliation performance [45]. This approach has enabled the successful application of a variety of bio-based and low-toxicity solvents, some of which have even surpassed traditional media in performance. For example, solvents such as dimethyl 2-methylglutarate (Iris) and Polarclean have been shown to yield stable dispersions of MoS_2 and graphene with narrow flake size distributions and high exfoliation yields, while offering a better environmental profile and simplified post-processing [46].

	Surface Tension σ_s [mNm^{-1}]	Hansen Solubility Parameters		
		δ_d [MPa$^{1/2}$]	δ_p [MPa$^{1/2}$]	δ_H [MPa$^{1/2}$]
NMP	40.1	18.0	12.3	7.2
DMF	37.1	17.4	13.7	11.3
IPA	21.7	15.8	6.1	16.4
Acetone	58.1	15.5	10.4	7.0
Ethanol	46.1	15.8	8.8	19.4
Urea 30% in H_2O	74.0	17.0	16.7	38.0
TEA	45.9	17.3	7.6	21.0
Cyrene	72.5	18.7	10.5	6.9
Polarclean	38.0	15.8	10.7	9.2
Iris	33.0	16.6	8.7	5.0

***Table 1**. Surface tension and the Hansen solubility parameters for NMP, DMF, IPA, Cyrene, Polarclean, and Iris [47].*

In parallel, studies have also demonstrated the potential of binary solvent systems, where mixtures of water and short-chain alcohols or esters can be tuned to optimize polarity and surface tension, enhancing exfoliation while maintaining biocompatibility. Such strategies also allow operation under milder conditions, reducing energy input and further aligning with green chemistry goals [45].

Thus, the integration of Green Chemistry into the exfoliation of 2D materials represents not just an environmental imperative, but a

strategic pathway to scalable, safe, and application-ready nanomaterials. This has driven the exploration of new solvent systems that combine efficiency with sustainability among which Cyrene has emerged as one of the most promising candidates, as discussed in the following section.

2.3 Cyrene as a Promising Green Solvent

In the search for safer and more sustainable alternatives to conventional solvents used in the liquid-phase exfoliation of 2D materials, Cyrene™ (dihydrolevoglucosenone) has emerged as a particularly promising candidate. Derived from cellulose via a two-step catalytic process, Cyrene is a bio-based, biodegradable, and non-toxic dipolar aprotic solvent, presenting physicochemical characteristics comparable to toxic solvents such as NMP and DMF but without the associated environmental and health concerns [48].

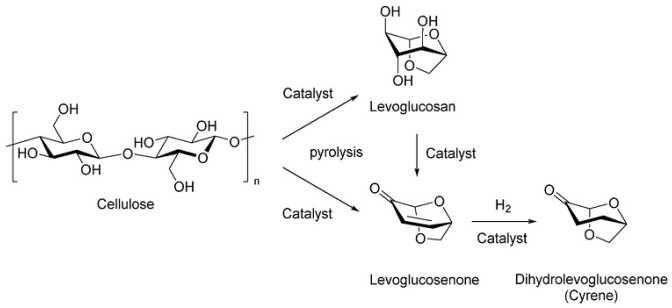

***Figure 18**. Schematic representation of the process for synthesizing Cyrene from cellulose [49].*

Beyond exfoliation performance, green credentials of Cyrene are firmly established: it is readily biodegradable (99% in 14 days), has a low potential for bioaccumulation, and is classified as practically non-

toxic according to the Globally Harmonized System (GHS) [50]. Furthermore, its low vapor pressure and high boiling point make it safer to handle in large-scale processes, reducing risks associated with solvent volatilization or flammability.

Recent studies have shown Cyrene to be remarkably versatile, enabling the exfoliation of a wide range of 2D materials. For example, it has been used to prepare graphene inks with high concentration and excellent electrical conductivity, suitable for screen-printable electronics and wireless devices [48]. It has also proven successful in the exfoliation of black phosphorus into phosphorene nanosheets, where it outperformed NMP in terms of exfoliation efficiency and biocompatibility. Based on these encouraging results, we explored the use of Cyrene in exfoliation of MoS_2 and WS_2.

2.4 The Effectiveness of Cyrene as a Solvent in Exfoliating 2D TMDs Nanosheets

2.4.1 Abstract

The work focuses on the exfoliation of MoS_2 and WS_2 nanosheets in Cyrene using a modified liquid-phase exfoliation protocol. A key objective was to investigate the morphological and optical characteristics of the nanosheets produced in this green solvent, assessing the effectiveness of the exfoliation route and the resulting dispersion stability under ambient conditions.

The exfoliation process was designed to minimize structural degradation while achieving efficient delamination of the TMDs in a viscous, biocompatible medium. To this end, a combination of bath and

probe sonication steps was employed, followed by low-speed centrifugation to remove unexfoliated aggregates. The resulting colloidal dispersions were then characterized by a suite of techniques including atomic force microscopy (AFM), UV–Vis spectroscopy, Z-potential measurements, scanning electron microscopy (SEM), and Raman spectroscopy.

Particular attention was given to the influence of Cyrene's viscosity and polarity on the morphology of the exfoliated flakes, as well as to the stability of the dispersions over time. The spectroscopic and microscopic analyses provided complementary insights into nanosheet thickness, lateral dimensions, and the preservation of the semiconducting phase. The outcomes of this work offer valuable indications for the implementation of Cyrene-based protocols in the sustainable production of TMD nanomaterials.

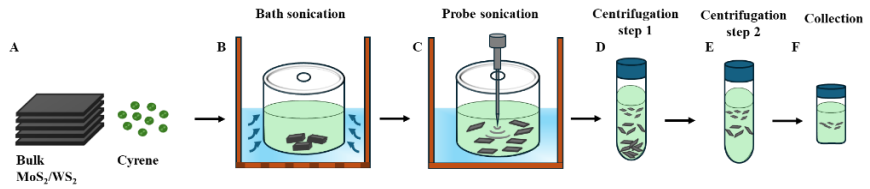

***Figure 19**. Liquid phase exfoliation of MoS_2 and WS_2 in Cyrene.*

2.4.2 Results and Discussion

Exfoliation of MoS_2 and WS_2

To date, Cyrene has primarily been applied for the exfoliation of graphene in bio-inkjet printing and IoT-related applications, where tailored processing parameters enabled the production of high-quality graphene nanosheet dispersions [48].

Based on our previous results, we adopted a modified LPE approach to prepare MoS_2 and WS_2 nanosheets in cyrene [51]. The process was carried out under controlled temperature during sonication, which allowed the formation of highly stable and concentrated dispersions of 2D TMDs. Details concerning the exfoliation procedure have been reported in the paragraph 2.4.4 page 69 (exfoliation and size selection of MoS_2 and WS_2)

Optical Characterization of TMDs nanosheets: UV–Vis Spectra

Liquid-phase exfoliation typically yields dispersions of polydisperse nanosheets, which vary in both lateral size and thickness. This intrinsic heterogeneity implies that within a single dispersion, nanosheets can present markedly different optical behaviors depending on their morphology. In this context, UV–Vis spectroscopy provides a rapid and non-destructive method for estimating the average number of layers ⟨N⟩, lateral dimensions ⟨L⟩, and concentration ⟨C⟩ of exfoliated 2D materials [52]. These estimations are derived from spectral changes that reflect both absorbance and scattering contributions to the total extinction, often influenced by basal plane and edge effects.

In this study, the analysis of MoS_2 exfoliated in Cyrene was initially complicated by the strong UV absorption of the solvent, especially in the 200–400 nm range, as shown in **figure 20**. To mitigate this background interference, we diluted the dispersions with either water or methanol. However, dilution with water (1:1 v:v) yielded spectra with very low-intensity extinction bands, and further dilution (1:20 v:v) rendered the spectral features almost entirely unrecognizable (data not shown). On the other hand, methanol dilution (1:1 v:v) preserved

the key spectral features of MoS_2, allowing for clearer detection of the characteristic excitonic peaks.

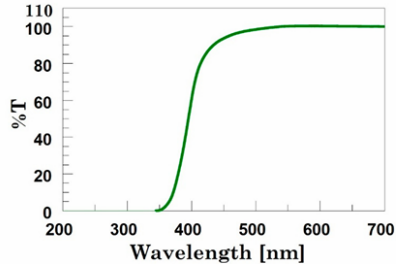

***Figure 20**. UV spectra of pure Cyrene (y axis is reported %Transmittance). A total extinction of the UV radiation from 200 to 360 occurs.*

In the UV-vis spectra of methanol-diluted samples two distinct absorption bands were evident at 669 nm and 610 nm, corresponding to the A and B excitons of MoS_2, respectively (**Figure 21 A,B**). From these features, the average number of layers was calculated to be ⟨N⟩ = 5.6, consistent with a dispersion dominated by few-layer flakes [53]. In addition to layer estimation, lateral flake size was also extracted from UV data. Typically, MoS_2 dispersions display a spectral minimum around 345 nm, where the extinction is governed primarily by in-plane absorption rather than edge scattering [44]. However, in our methanol-diluted MoS_2/Cyrene samples, this minimum appeared blue-shifted to 334 nm (**Figure 4 C**), likely due to residual background absorption from Cyrene. Based on the extinction values at 334 nm and for exciton B, the average lateral size was calculated using the equation [54]:

$$L(\mu m) = \frac{3.5 Ext_B/Ext_{334} - 0.14}{11.5 - Ext_B/Ext_{334}}$$

The resulting ⟨L⟩ was approximately 121 ± 3 nm, a value that fits within the expected range (70–350 nm) for nanosheets produced by LPE.

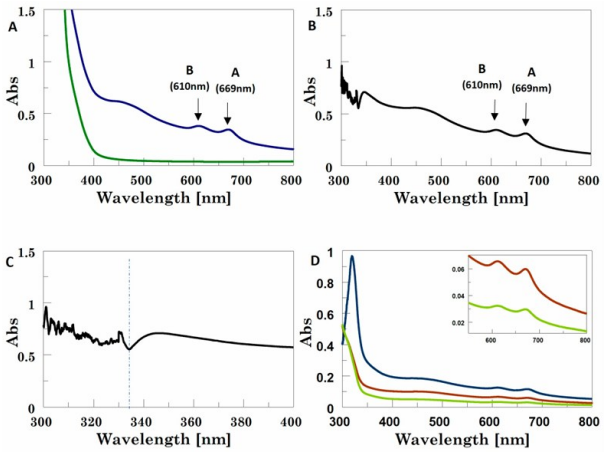

***Figure 21**. (**A**) UV spectra for cyrene (green line) and MoS_2/cyrene dispersion (blue line), both diluted with methanol (1:1; v:v). (**B**) Differential spectrum between MoS_2/Cyrene:methanol (1:1) and Cyrene:methanol (1:1). (**C**) Enlargement of the difference spectrum highlighting the position of the minimum at 334 nm. (**D**) Differential spectra at different methanol dilution ratios (1:5 blue, 1:9 red, 1:17 green). The inset highlights the excitonic peaks of MoS_2 (600–800 nm). Each spectrum was acquired as the mean of n=3 measurements. Cuvette o.l. 1.0 cm; V= 3 mL.*

To further reduce the background interference and improve peak resolution, UV spectra were acquired at increasing methanol dilution ratios (5:1, 9:1, 17:1 methanol:MoS_2/Cyrene). While greater dilution improved transmittance, it also weakened the band intensities, making the absorption minimum less distinguishable. To address this, spectral deconvolution using a Gaussian FWHM approach was employed (**figure 22**)[55]. The analysis revealed the minimum at ~336 nm across different dilution levels, with minimal spectral shifting, suggesting that

Cyrene did not significantly interfere with UV absorption under these conditions. Using this method, lateral sizes in the range of 165–179 nm were obtained.

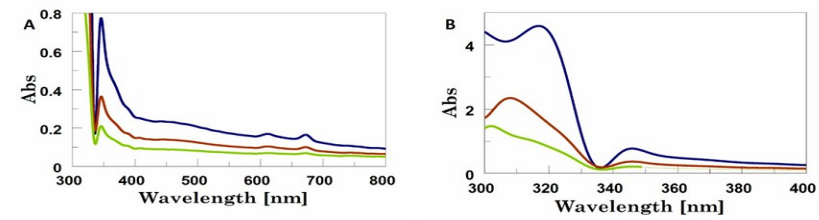

Figure 22. *(**A**) Deconvoluted UV-vis spectra of MoS_2/Cyrene: MeOH at dilution level 1:5 (blue line), 1:9 (red line) and 1:17 (green line). (**B**). Enlargement of the deconvoluted UV-vis spectra reported in A in the range 300-400 nm.*

In contrast, UV spectra for WS_2 dispersions regardless of dilution with water or methanol did not exhibit identifiable absorption bands, even at a final 2:1 WS_2–Cyrene to solvent ratio. This behaviour suggests a different exfoliation outcome, potentially the formation of WS_2 quantum dots, as inferred from previous studies [56]. These smaller structures undergo quantum confinement and associated bandgap changes, likely explaining the absence of the excitonic peak at ~243 nm. Additionally, the WS_2–Cyrene mixtures appeared visually transparent, resembling true solutions rather than colloidal suspensions, further supporting this interpretation.

Microscopic Characterization: AFM

Atomic force microscopy (AFM) was employed to evaluate the morphology and thickness of WS_2 and MoS_2 nanosheets obtained through exfoliation in Cyrene, following the protocol detailed in the

Materials and Methods section. Representative AFM images for WS_2 and MoS_2 nanoflakes are shown in **figure 23A** and **C**, respectively, alongside selected height profiles extracted from individual flakes. In both cases, the presence of few-layer nanosheets is clear from the topographical profiles. A statistical analysis of multiple AFM scans allowed for the construction of thickness distribution histograms for each material (**figure 23B** for WS_2 and **23D** for MoS_2). The resulting distributions were well-described by lognormal functions an outcome frequently associated with exfoliated nanosheet populations [57]. For WS_2, the peak of the fitted curve was centered around 3 nm, with over half of the measured flakes exhibiting thicknesses below 4 nm, highlighting the efficiency of the exfoliation protocol in generating predominantly few-layer structures. In contrast, MoS_2 nanosheets showed a broader thickness distribution. While the peak of the distribution was located near 4 nm, a significant proportion of flakes (~35%) displayed thicknesses in the 4–8 nm range. This broader profile may reflect a slightly reduced exfoliation efficiency under the applied sonication conditions. Nonetheless, approximately 25% of the flakes had thicknesses below 4 nm, and around 60% were under the 8 nm threshold dimensions compatible with many bio-related applications where nanoscale thickness is a key parameter.

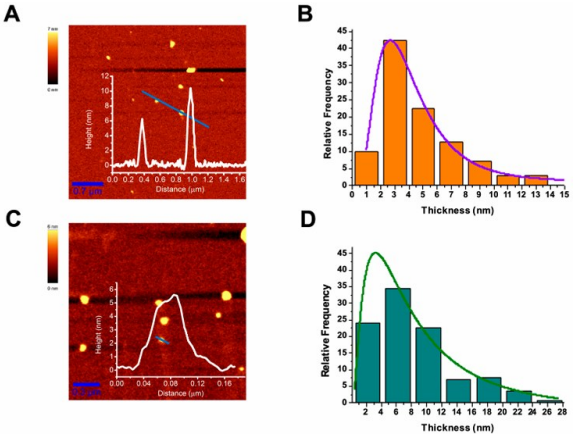

Figure 23. *Typical AFM images of WS_2 (**A**) and MoS_2 (**C**) nanoflakes acquired in intermittent-contact mode. The two insets correspond to the height profiles across the blue lines shown in the respective topographies. (**B, D**) Analysis of flake thickness for WS_2 and MoS_2 nanoflakes, respectively. In both cases, the fitting curves of the data with a lognormal distribution are also shown. Measurements were performed using a 100× infinite-corrected objective, which provided in-plane and axial resolutions (PSF-HWHM) of ~0.3 and 1 μm, respectively. Relative frequencies were calculated over numerous scans (at least 30).*

Spectroscopic Characterization: Raman Spectra

Raman spectroscopy was employed to further investigate the structural features of the exfoliated MoS_2 and WS_2 nanoflakes, providing valuable insight into their vibrational modes and layer-dependent behavior. This technique is widely recognized as a powerful, non-destructive tool for the characterization of two-dimensional materials, owing to its sensitivity to structural order, number of layers, and interlayer interactions. In layered TMDs, the evolution of the in-plane E^1_{2g} and out-of-plane A_{1g} modes serves as a reliable fingerprint to estimate nanosheet thickness, as these peaks exhibit characteristic frequency shifts when transitioning from bulk to monolayer structures

[58]. In the present study, the lateral dimensions of the exfoliated nanosheets were smaller than the lateral resolution of the Raman system (point spread function ~0.3 μm in-plane), preventing the acquisition of spectra from isolated flakes. Consequently, the recorded Raman signals represent averaged information from multiple flakes within the confocal detection volume. **Figure 24** displays the averaged Raman spectra collected from ten distinct locations for both WS_2 (**figure 24A**) and MoS_2 (**figure 24B**) samples, along with their corresponding multipeak Gaussian fitting.

For MoS_2, the spectrum was fitted using two primary Gaussian components corresponding to the E^1_{2g} and A_{1g} vibrational modes. The frequency difference between these modes ($\Delta\nu = \nu_{A1g} - \nu_{E^1_{2g}}$) is commonly employed to estimate the number of layers in exfoliated TMDs. In this case, the deconvolution yielded a $\Delta\nu_{MoS_2}$ of approximately 24.6 cm^{-1}, indicative of a three- to four- layers nanosheet thickness. This result aligns well with the structural information obtained from UV–Vis spectroscopy and AFM, confirming the effective exfoliation in Cyrene.

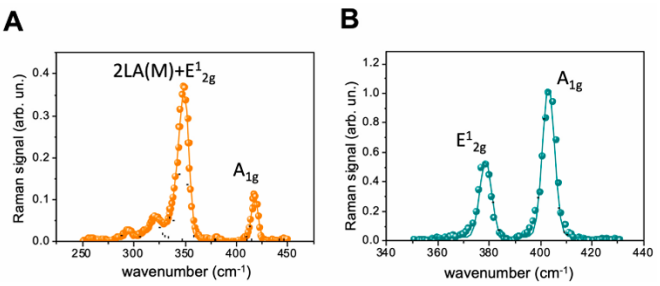

Figure 24. *Raman spectra of WS_2 (**A**) and MoS_2 (**B**) nanoflakes using 532 nm laser excitation. For both spectra, colored dots correspond to experimental data points (obtained by averaging 10 spectra acquired from different points of the samples), while solid lines correspond to curves fitted with a multipeak Gaussian function. Finally, the single Gaussian peaks are indicated by black dotted lines.*

Conversely, the Raman profile of WS_2 presented a more intricate spectral pattern, primarily due to the resonance enhancement at the 532 nm excitation wavelength, which led to overlapping of the 2LA(M) and E^1_{2g} modes [59]. Based on literature guidance [60], the spectrum was fitted with five Gaussian components to account for the various overlapping features. While the overall fit quality was satisfactory, the convolution of bands in the 325–360 cm^{-1} region introduced a degree of uncertainty (~3 cm^{-1}), complicating the direct assignment of layer number based on the conventional mode separation. Nonetheless, some structural inference was still possible from the position of the A_{1g} peak alone. Previous studies [59], [60] have reported A_{1g} values around 416.7 cm^{-1} for few-layer WS_2 under similar resonance conditions, which closely matches the observed peak near 417.0 cm^{-1} in our spectrum. This observation supports the AFM-derived conclusion that the exfoliated WS_2 flakes possess a few-layer character, confirming the consistency between spectroscopic and microscopic data.

Morphological Characterization: SEM

To gain further insight into the structural features of the exfoliated 2D nanosheets in Cyrene, scanning electron microscopy (SEM) was employed. This analysis was particularly valuable, as it allowed visualization of the nanoflakes within the Cyrene matrix itself, highlighting both their lateral dimensions and spatial distribution following deposition. Notably, the nanoflakes were embedded in a thin Cyrene film which, depending on the substrate and local morphology, presented diverse textures within the same sample. These variations were explored across different magnifications, ranging from macroscopic regions (100 μm scale) to smaller domains (100–200 nm), enabling a detailed examination of localized flake populations. The SEM analyses were performed on MoS_2 and WS_2 nanosheets deposited onto both regular (**figure 25A–F**) and irregular (**figure 26A–D**) glass substrates. These investigations provided not only dimensions of the exfoliated flakes but also a broader view of their dispersion behaviour within the Cyrene film. Understanding how the nanoflakes are incorporated into and distributed throughout the solvent matrix is especially relevant for potential applications in biomedicine.

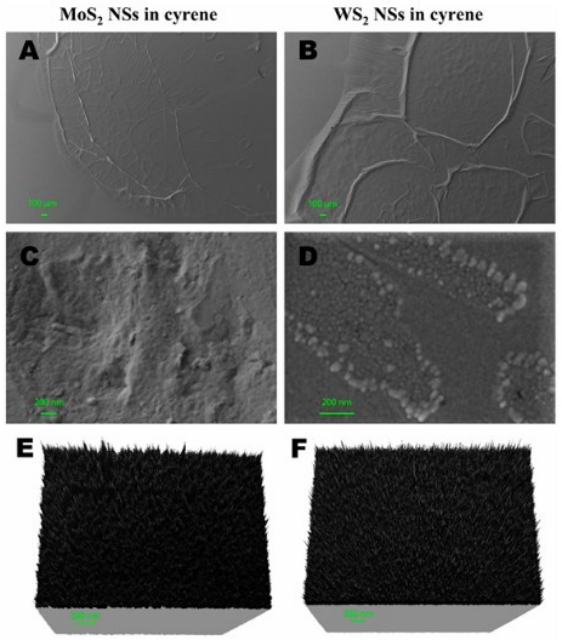

Figure 25. *(**A**) MoS_2 NSs deposited over the silicon substrate absorbed by Cyrene at the rim and center of the solid solution. Some coffee ring structures are also visible. (**B**) WS_2 NSs deposited over the silicon substrate absorbed by Cyrene on the rim (green arrows) with the largest coffee ring. (**C**) MoS_2 NSs chaotically absorbed under the Cyrene film at the rim of the solid solution. (**D**) A detailed SEM image of the area with imperfections in the Cyrene film. The image shows the presences of WS_2 NSs arranged in a line and mostly presenting a specific oval-shaped pattern at the periphery. (**E,F**) Three-dimensional (3D) maps on a regular surface film (far from the rim) of the MoS_2 and WS_2 NSs in Cyrene, respectively. Statistical sampling of 30 detected single nanoflakes resulted in an average of 26±7 and 13 ± 5 nm, for MoS_2 and WS_2, respectively.*

In the case of MoS_2 nanosheets deposited on regular glass (**figure 25**), the Cyrene film showed distinct morphological patterns between the rim and the core of the drop-casted area. At the rim (**figure 25A**), the film appeared thicker, often wrinkled or folded, with the presence of well-defined coffee-ring structures. Here, nanoflakes exhibited a wide distribution in size, averaging around 122 ± 44 nm based on 30 single measurements (**figure 25C**). The dispersion was chaotic, with the flakes absorbed in the film in a non-uniform fashion. At the core (**figure 25E**), the film became thinner and more homogeneous, with a notable reduction in wrinkles and coffee rings[61]. In this region, MoS_2 flakes appeared smaller and more evenly distributed, showing an average lateral size of 26 ± 7 nm, with several domains containing flakes below 20 nm, suggesting the presence of quantum dot-like structures. While the overall distribution remained heterogeneous, especially near fracture zones, the nanosheets at the core were less aggregated and exhibited better spatial order than at the rim. The intensity of the 2D-MoS_2 NS signal was quite low in comparison to that obtained from deposition in other dipolar aprotic solvents (**details** in **Table 2**), as the high viscosity of Cyrene hindered the visualization of morphology, even after diluting the dispersion.

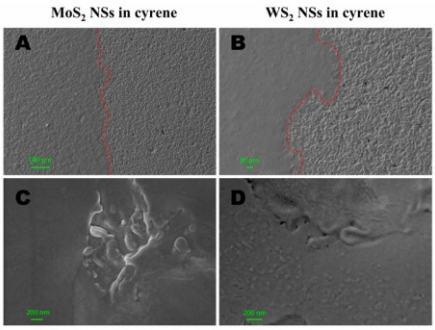

***Figure 26**. (**A**) Morphological features of MoS_2 NS film dispersed in Cyrene (left) on an irregular glass substrate (right). (**B**) Morphological features of WS_2 NSs exfoliated in Cyrene film (left) on an irregular glass substrate (right). (**C**) Two-dimensional (2D) MoS_2 NSs deposited and partially absorbed on the irregular surface of the Cyrene film. (**D**) Two-dimensional (2D) WS_2 NSs in the proximity of the irregular surface of the Cyrene film.*

For WS_2 nanosheets in Cyrene (**Figure 25B,D,F**), the morphology was comparatively more regular. The Cyrene film displayed a more continuous and uniform texture, with fewer wrinkles and a more homogenous flake distribution. Coffee rings were broader than those seen for MoS_2, but their formation did not appear to compromise the internal uniformity of the film. Flakes observed in defective regions (**figure 25D**) formed aggregates with an average lateral size of 43 ± 16 nm, ranging from 29 to 69 nm. Notably, in the central region of the drop (**figure 25F**), WS_2 flakes were well distributed and absorbed into the thin film, with minimal aggregation. Here, the average size of individual flake dropped to 13 ± 5 nm, indicative of extensive exfoliation and the formation of structures approaching the quantum dot regime.

The impact of substrate morphology was further explored by depositing the same dispersions onto irregular glass wafers (**figure**

26A–D). These images revealed clear differences in how the Cyrene film adapted to the underlying surface. In the case of WS_2 (**Figure 26B**), the film formed a continuous layer that conformed well to the substrate micro-cavities. For MoS_2 (**figure 26A**), the adaptation was less complete, with irregularities and partial coverage observed. At higher magnification (**figure 26C,D**), nanosheets were visible primarily near depressions in the substrate, highlighting how topography may influence local flake organization and distribution. From a comparative standpoint, both AFM (thickness) and SEM (lateral size) analyses consistently indicated that MoS_2 flakes tended to be larger and thicker than their WS_2 counterparts. This trend was attributed in part to differences in the pristine materials' bulk particle size (6 μm for MoS_2 vs. 2 μm for WS_2) as well as their intrinsic crystallographic properties. The energy applied during sonication is known to promote flake scission, which in turn reduces both lateral dimensions and thickness [62] [63]. The observation that MoS_2 produced larger flakes under identical exfoliation conditions aligns with this concept: larger bulk particles and potentially different mechanical responses to sonication result in less fragmentation.

Crystallographic factors may also play a role. The interlayer spacing of MoS_2 (0.615 nm) and WS_2 (0.618 nm) is comparable, but small differences in their binding energies (−0.216 eV vs. −0.226 eV, respectively) could influence their response to exfoliation processes [64]. A further parameter, the L/N ratio (lateral size/thickness), has been proposed as an indicator of exfoliation efficiency [65] [66]. In Cyrene, our results yielded L/N ratios of 6.5 for MoS_2 and 4.3 for WS_2, suggesting that while MoS_2 remains easier to exfoliate, WS_2 undergoes

more extensive fragmentation, potentially reaching the quantum dot domain more readily.

Solvents	Surface Tension (mNm^{-1})	Stability (Days)		Lateral Size (nm)		Thickness (nm)		Surface Charge (mV)		Ref.
		MoS_2	WS_2	MoS_2	WS_2	MoS_2	WS_2	MoS_2	WS_2	
NMP	40.1	21	14	340	390-500	1–4.5	2–5	-32.1	- 41.1	[67]
DMF	37.1	-	21	220–340	1–2	3–7	~10	–	–	[68] [69]
Ethanol-H_2O	32.98	21	30	130–150	~100	1–3	~3–4	-22.	-32	[70]; [71]
H_2O	72	30	7	150–250	700–800	1–3.5	4.56	-27	–	[72]; [73]
Porcelain	38	7	7	~2.5	~1–2	4–5	<5	–	–	[74]
Cyrene	33.6	>30	>60	19–38	11–21	0.9–1.5	0.5–0.9	-50.4	-86.5	Present Work

Table 2. *Exfoliation of 2DTMDs in organic solvents in comparison with Cyrene: main characteristics of the obtained nanoflakes in terms of the principal parameters of the production.*

Altogether, SEM analyses confirmed the effective exfoliation of both MoS_2 and WS_2 in Cyrene, while also revealing clear differences in their morphological behavior. MoS_2 nanosheets were more heterogeneous in distribution and morphology, whereas WS_2 flakes exhibited greater uniformity across substrates.

Comparative Analysis of TMD Exfoliation in Cyrene and Conventional Solvents: Key Nanoflake Parameters

As summarized in **Table 2**, the key parameters obtained in this work such as thickness, lateral size, and dispersion stability place Cyrene on par with, if not above, other commonly used organic solvents. Notably, the nanosheet dispersions achieved here showed extended stability over time, which is particularly advantageous for biomedical applications where prolonged dispersion stability is often required.

In terms of structure, the nanosheets exfoliated in Cyrene exhibited some of the lowest thickness values reported ranging from approximately 0.7 to 1.5 nm corresponding to mono- and few-layer flakes. This characteristic is especially relevant for maximizing surface to volume ratio, a key factor for enhancing reactivity and performance in nanotechnology-based systems.

Moreover, among the solvents compared, Cyrene facilitated the formation of nanosheets with the highest negative surface charge. This feature is indicative of stronger edge-dangling bond interactions and could prove beneficial for subsequent functionalization steps or for promoting selective binding with chemical groups of interest. Altogether, these observations position Cyrene as a compelling green alternative for the sustainable exfoliation of 2D TMDs suitable for a broad range of applications.

Surface Charge Analysis: ς-Potential

The colloidal stability of 2D nanomaterials is largely governed by electrostatic repulsion between the dispersed flakes [75]. In this context, the surface charge commonly evaluated through ς-potential measurements represents a key parameter to assess dispersion stability in different solvent environments. Although pristine MoS_2 and WS_2 are intrinsically neutral, they can acquire surface charge through the adsorption of specific solvents or ionic species [76] [77]. This behavior depends on the dielectric properties and ionic strength of the surrounding medium and can be described using theoretical frameworks such as the Poisson–Boltzmann equation and the Debye–Hückel model.

In this work, we measured the ς -potential values of MoS_2 and WS_2 nanosheets exfoliated in Cyrene. The measurements were repeated three times per scan across 100 runs. Notably, the exfoliated 2D TMDs exhibited high negative surface charge densities, indicative of stable colloidal dispersions. Specifically, the ς -potential for MoS_2 was measured at -50 ± 3 mV, while WS_2 displayed an even more negative value of -86.5 ± 1.5 mV. These values are significantly higher (in absolute terms) than those typically observed for the same nanomaterials in water, which range between −26 −32 mV [72][73]. Such pronounced surface charging can be attributed to several factors. First, during sonication-assisted exfoliation, chemical interactions occur between Cyrene and the exposed edges of the nanosheets. The cavitation process not only facilitates the delamination of bulk material but also introduces reactive edge sites and dangling bonds due to Mo–S or W–S bond cleavage. These edge sites can further interact with functional groups from Cyrene or promote the formation of ionizable moieties such as –SH and $–HSO_3$, which contribute to the overall negative surface charge via proton dissociation. In addition, the lateral dimensions

of the nanosheets significantly influence ς-potential. As demonstrated in our comparative analysis (**Table 3**), smaller nanosheets due to a higher proportion of edge atoms show enhanced charge densities and greater electrophoretic mobility. WS_2, which yielded smaller flakes in our experiments, exhibited a stronger ς -potential than MoS_2, consistent with this edge-dominated effect. Moreover, solvent viscosity plays a non-negligible role in the process. Cyrene, due to its high viscosity, improves the mechanical energy transfer during sonication, thereby enhancing exfoliation efficiency and promoting the formation of smaller, highly charged flakes. This property, combined with Cyrene's polarity and ability to interact with the flake surfaces, supports both efficient exfoliation and long-term colloidal stability. It is also worth noting that the initial bulk particle size and post-exfoliation centrifugation steps contribute to the final size distribution and surface characteristics of the nanosheets [78].

Modeling the Interaction between 2D NSs and Cyrene: DLVO Theory

To gain further insight into the behavior of MoS_2 and WS_2 nanosheets in Cyrene during exfoliation and dispersion, we applied the modified Derjaguin–Landau–Verwey–Overbeek (DLVO) theory to estimate the total interaction energy (V_tot) between individual flakes. The model considers the sum of the van der Waals attractive forces (V_vw) and the electrostatic interaction energies (V_EL), expressed as:

$$V^{tot} = V^{EL} + V^{vw}$$

The van der Waals interaction energy was calculated using the equation:

$$V^{vw} = -Aa/12d$$

where A is the effective Hamaker constant (defined as $A = (\sqrt{A_{nano}} - \sqrt{A_{cyrene}})^2$), a is the effective nanosheet radius, and d is the separation distance between sheets. For our calculations, values of A_{nano} were taken

as 29.6 x 10^{-20} J for MoS_2 and 32 x 10^{-20} J for WS_2, while A_{cyrene} was 2.84 × 10^{-20} , based on literature data [79].

The electrostatic repulsive energy (V^{EL}) was modeled as a function of inter-flake distance d, zeta potential ς, and dielectric permittivity ε of Cyrene, following this expression:

$$V^{EL} = \pi\epsilon a\left(\zeta^2\right) \times \left\{\ln\left[\frac{1+\exp(-kd)}{1-\exp(-kd)}\right] + \ln[1-\exp(-2kd)]\right\},$$

Here, *k* is the inverse Debye–Hückel length, which for Cyrene at room temperature is approximately 1/0.4 μm. The required experimental parameters such as ς and *a* were obtained from our ς -potential and dimensional measurements (**Table 3**).

2D TMDS	**a (nm)** ±SD	**ς (mV)** ±SD
MoS_2	26± 7	-50.4 ± 3.0
WS_2	13± 5	-86.5 ± 1.5

Table 3*. Measured values of a, ς for the calculation of the total interaction energy between 2D NSs and cyrene. a values were obtained averaging 30 sampling in SEM experiments and the results expressed as the mean ±SD. ζ-potential were measured as the mean of 5 scans and the results are expressed as the mean ± SD.*

Plotting V_{tot} against d revealed a consistent trend for both materials: repulsive interactions dominate at larger distances, whereas attraction becomes significant at closer proximities. Notably, the crossover points where the net interaction changes sign were identified at approximately *d = 13.5 nm* for WS_2 and *d = 35.8 nm* for MoS_2. These distances match remarkably well with the average lateral dimensions obtained from our characterization techniques, particularly for WS_2 (13.5 nm vs. 13 nm measured) and with reasonable agreement for MoS_2 (35.8 nm vs. 26 nm). This correspondence suggests that the theoretical zero-force points derived

from DLVO modeling may serve as indicative thresholds for the minimum lateral size of exfoliated nanosheets in Cyrene under the given conditions. Furthermore, the energy barrier for transition from repulsion to attraction was found to be broader and higher for WS_2, supporting the observed greater colloidal stability and lower aggregation tendency compared to MoS_2 findings that align with AFM and SEM observations.

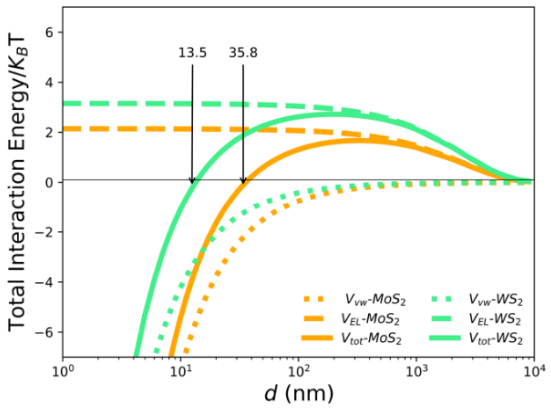

Figure 27. *The total interaction energy between nanosheets in cyrene normalized to the thermal energy KBT resulting from the sum of the van der Waals (dotted) and electrostatic (dashed) interaction energies (green for WS_2 and orange for MoS_2).*

2.4.3 Conclusions

This work presents, to the best of our knowledge, the first comprehensive experimental investigation of the exfoliation of MoS_2 and WS_2 nanosheets in Cyrene, a dipolar, aprotic, and environmentally friendly solvent. Liquid-phase exfoliation, one of the most scalable and widely adopted fabrication methods for 2D materials, was here optimized through the introduction of a preliminary bath sonication step. This pre-treatment, carried out prior to the conventional probe sonication, contributed to the production of nanosheets with reduced lateral dimensions and predominantly mono- or few-layered structures.

The resulting dispersions exhibited notable colloidal stability, remaining homogeneous for over a month, a promising feature for potential applications requiring extended storage and consistent material performance, particularly in biomedical contexts. UV–Vis spectroscopy provided average structural parameters in good agreement with those obtained via Raman analysis and AFM measurements, further validating the successful exfoliation of both MoS_2 and WS_2.

SEM characterization revealed distinct morphological differences between the two materials, likely influenced by the high viscosity of Cyrene. MoS_2 nanosheets formed wrinkled and fractured films, with significant variations in lateral size depending on the region of observation. In contrast, WS_2 nanosheets displayed a more homogeneous and regular film morphology, with smaller flake dimensions and minimal surface defects. Across both systems, nanosheet lateral size was shown to correlate with film texture, larger and more irregular structures forming at the rim of the drop-casted samples, and smaller, more uniform flakes present at the core.

AFM confirmed that the thicknesses of the exfoliated nanostructures aligned with spectral estimations, further supporting the presence of predominantly mono- and few-layered nanosheets. Additionally, ς-potential measurements indicated that both MoS_2 and WS_2 acquired negative surface charges in Cyrene, with values more pronounced than those typically observed in aqueous dispersions. This result reflects strong electrostatic stabilization and suggests favourable conditions for long-term dispersion and possible functionalization.

Despite certain challenges related to Cyrene's physical properties, such as viscosity and boiling point, that complicate some post-processing and characterization steps, the quality of the resulting nanoflakes was high. In

several respects, including minimal layer number and electrostatic stability, Cyrene-performed exfoliation showed results comparable or superior to those obtained with traditional organic solvents. Given its green chemistry profile and the results obtained in this study, Cyrene emerges as a viable and sustainable alternative for the exfoliation of 2D TMD nanosheets, adding a further step toward more environmentally responsible and biocompatible approaches in nanomaterial synthesis.

2.4.4 Materials and Methods

Exfoliation and Size Selection

The initial, commercialized bulk molybdenum disulphide (MoS2) powder (Sigma- Aldrich, Darmstadt, Germany, 69860, particle size: 6 µm, 99%, density: 5.06 g/mL at 25 ◦C) and tungsten disulfide (WS2) powder (Sigma-Aldrich, Darmstadt, Germany, 243639, particle size: 2 µm, 99%, density: 7.5 g/mL at 25 ◦C) were exfoliated in cyrene as a solvent (Sigma-Aldrich, 807796, molecular weight: 128.13 g/mol, flash point: 108 ◦C, density: 1.25 g/mL). The materials were dispersed in cyrene at an initial concentration of 5 mg/mL. The solution was pretreated with bath sonication for 15 min. Then, LPE was executed using tip sonication with a Bandelin Ultrasound SONOPLUS HD3200, Berlin, Germany (operating frequency of 20 kHz and maximum power of 200 W) tip sonicator equipped with a probe (KE-76). The pretreated solution was exfoliated for a further 2 h at 60% amplitude using pulse mode (10 s on, 10 s off) in a quartz bottle. To avoid the production of high heat and temperature due to the collision of cavitation bubbles, sonication was performed using an ice bath and the operating temperature of the device was set at 15 ◦C. Simultaneously, the output power was calculated, and it was consistent throughout the sonication period, resulting in a homogeneous dispersion of the given

material. After sonication, the dispersion was centrifuged (Megafuge™ 16 Centrifuge, Thermo Scientific™, Waltham, MA, USA, equipped with a rotating angle rotor) at room temperature at 300 rpm for 60 min and the sediment containing the un-exfoliated part of the material was discarded. The supernatant was moved to 5000 rpm, after which the sediment was discarded in the last step. The supernatant was stored at 4 ◦C for further use.

Characterization: UV–Vis

To characterize the resulting 2DMs, we used a range of techniques, including ultraviolet– visible (UV–Vis) spectroscopy, Raman spectroscopy, ζ-potential, scanning electron microscopy (SEM) and atomic force microscopy (AFM). These techniques allowed us to assess the thickness, shape and concentration of the resulting materials, as well as their optical properties. The UV–Vis spectroscopy measurements were performed using a Jasco-700 UV–Vis spectrophotometer, Italy with a 1 cm thick quartz cuvette and a spectral range of 200–800 nm to determine the exfoliated MoS_2/WS_2 absorption spectra.

Characterization: Raman and AFM

Measurements of Raman spectra were conducted using the commercial WiTec Alpha 300 confocal micro-Raman system. This system is composed of an inverted confocal Raman microscope and an atomic force microscope (AFM) placed on top of the inverted confocal microscope. This latter is equipped with a 532 nm probe generated with a frequency-doubled Nd-YAG laser and a 1800 grove/mm grating, assuring a spectral resolution of ~1.5 cm^{-1}. Raman spectroscopy was used to assess the quality of the exfoliated materials by investigating the structural properties

of the exfoliated flakes. AFM was used to measure the flake thickness and to investigate the NSs' surface topography. For this purpose, flake suspensions were first diluted in methanol (1:4 v/v) and then 50 μL portions of these suspensions were spun on a clean SiO_2/Si substrate at 3000 rpm for 60 s. Finally, the substrates were washed with acetone and dried with a gentle N_2 flux. This last step was performed to reduce the embedding of flakes in the cyrene films, which clearly would have prevented the observation of the thinner flakes and the correct evaluation of flake thickness. AFM analysis was performed in intermittent contact mode to avoid the perturbation of flakes' adhesion to the substrate. For the AFM characterization, nanoflake suspensions were drop-cast on glass coverslips and stored for 48 h at room temperature to allow complete cyrene evaporation. Measurements were performed using a 100×−infinite-corrected objective, which provided in-plane and axial resolutions (PSF-HWHM) of ~0.3 and 1 μm, respectively.

Surface Charge and Average Lateral Size Measurement: ς-Potential

Electrostatic stabilization is an important parameter to analyze the stability of liquid- exfoliated dispersions. The surface charges generated during the exfoliation can be at- tributed to electrophoretic mobility (μ). The ζ-potential measurements were performed using a Malvern Zetasizer Nano system, United Kingdom (UK) with a He-Ne laser as the excitation source. The ζ-potential measurements were performed to determine the charge on the surface of the exfoliated NMs. All the measurements were carried out at 25 ◦C.

Morphological Measurements: SEM

A Zeiss Merlin VP Compact SEM apparatus (DiSTAR laboratory, Università degli Studi di Napoli Federico II) was used for morphological analyses of the samples. The Zeiss Merlin VP Compact field-emission electron microscope was equipped with a Gemini II camera and FeSEM: SmartSem software controller. The SEM was composed of three secondary electron detectors (SE2 (classic detector), VPSE (variable pressure) and InlensDuo (low voltage)) and two backscattered electron detectors (AsB and InlensDuo). The SEM was equipped with a charge compensation system and with Oxford Instruments Microanalysis (both EDS X-max 50 and WDS Wave). Data processing was undertaken using INCA version 4.081 (Oxford Instruments (2006): INCA—The microanalysis suite issue 17a C SP1—Version 4.08. Oxford Instr. Anal. Ltd., Oxfordshire, UK); (EDS and WDS) and Aztec (EDS). The Software for data imaging of FeSEM is SmartSem. The samples were placed on a glass support with both smooth and irregular surfaces with an appropriate droplet drop-casting method; then, they were metalized with gold using a sputter coater.

CHAPTER III

FROM SYNTHESIS TO BIODEGRADATION: DESIGNING ANTIMONENE FOR BIOMEDICAL IMPLEMENTATION

This chapter is published in:

Kaur, J., Swetha, K., Singh, M., **Abduvakhidov, A**., Varra, M., Lakavathu, M., Adam, J., Prajapati, A., Bonam, S. R., Altucci, C., & Kurapati, R. (**2025**). Functionalization dependent biodegradability of two-dimensional antimonene by peroxidases: impact on immune modulation. *Nanoscale, 17(18), 11293–11304.* https://doi.org/10.1039/d4nr04786a

3.1 Introduction

In biochemical applications, without appropriate chemical modification, many 2D materials suffer from aggregation, poor dispersibility, and uncontrolled interactions with proteins and cells, leading to unpredictable biological responses. In contrast, functionalization offers a chemical "control point" through which the performance and fate of nanosheets can be rationally tuned (see Chapter 1).

Given the growing interest in antimonene for biomedical applications, such as near-infrared (NIR) phototherapy, targeted drug delivery, and other advanced therapeutic strategies, it becomes essential not only to optimize its functional properties but also to understand its biological fate once introduced into living systems. Within this framework, in the present work we successfully produced antimonene nanosheets functionalised with β-cyclodextrin (f-Sb), a strategy aimed at improving aqueous stability and controlling the material's surface chemistry. This functionalisation approach was designed to preserve the integrity of the nanosheets in biological media while enabling interaction with relevant enzymatic systems. The structure of resulting 2D nanomaterials of both pristine and β-cyclodextrin-functionalised antimonene nanosheets was investigated by means of different spectroscopic techniques (UV, FTIR, Raman, SEM, TEM). Then, the enzymatic biodegradation of both type of nanomaterials was evaluated in the presence of human myeloperoxidase (hMPO) and horseradish peroxidase (HRP), two peroxidases involved in oxidative immune responses. In parallel, the effects of functionalisation on degradation kinetics, structural evolution, and cytotoxicity were also evaluated. To this end, a range of complementary techniques, including UV–vis and Raman spectroscopy, electron microscopy, and in vitro

cellular assays, was employed to gain insights into the degradation process and its biological implications.

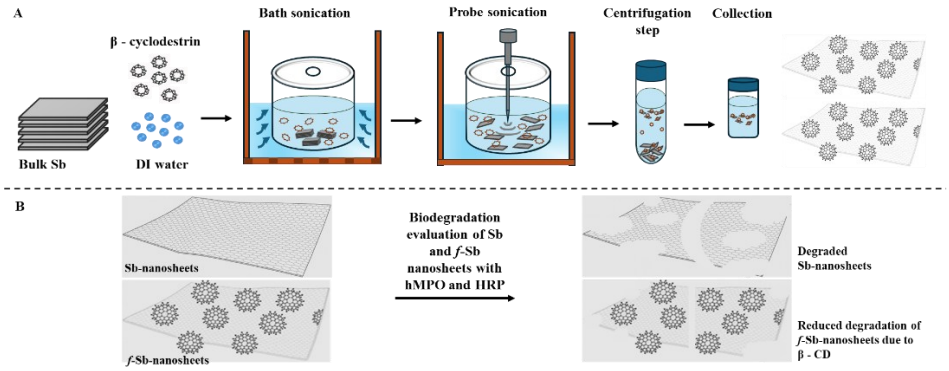

Figure 28. (**A**) Functionalization of Sb nanosheets using 2-hydroxypropyl-β-cyclodextrin (β-CD) to obtain f-Sb nanosheets and (**B**) biodegradation of Sb and f-Sb nanosheets using the human enzyme hMPO and the plant enzyme HRP in low concentrations of hydrogen peroxide, respectively.

3.2 Results and Discussion

3.2.1 Synthesis and characterization of Sb and f-Sb nanosheets

The production of pristine and β-cyclodextrin-functionalised antimonene (f-Sb) was achieved through a sonication-assisted exfoliation strategy, adapted from previously established protocols for other 2D materials such as MoS_2 and ReS_2 [80] and discussed in details in chapter II (pages 53-54). In this context, special attention was devoted to controlling thermal effects during sonication, in order to minimise degradation or unwanted oxidation during the exfoliation phase. The combined use of probe and bath sonication, although frequently employed in the context of liquid-phase exfoliation, was here optimised to preserve the nanosheets' structural integrity and achieve a homogeneous dispersion.

The UV–vis absorption spectrum of the exfoliated pristine Sb nanosheets (**figure 29**) displayed a broad peak in the range of 250–260 nm, a feature typically associated with the successful formation of few-layered

antimonene [81]. This observation confirms the effective exfoliation of the material in aqueous dispersion. In the case of f-Sb, a slight shift of the peak was detected. This spectral change can be attributed to the interaction between the antimonene surface and the β-cyclodextrin molecules, similar to β-CD functionalized 2D MoS_2 [80]. Given the minimal absorbance of β-CD in the 200–400 nm range, the shift is most likely due to its adsorption or coating onto the Sb surface, resulting in a modified local environment around the nanosheets.

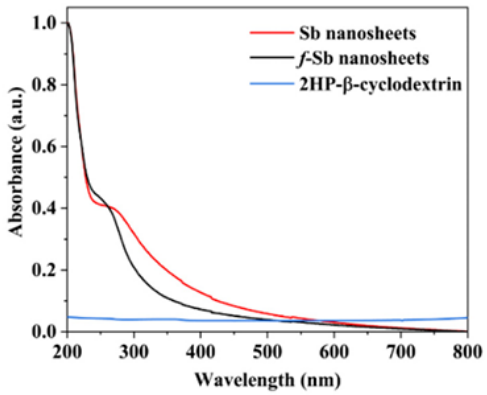

***Figure 29**. UV-vis absorption spectra of pristine Sb (red line), f-Sb nanosheets (black line), and 2HP β-cyclodextrin (blue line) in water, respectively. The analysis was performed using a 1 mL quartz cuvette with o.l. of 10 mm.*

In support of this functionalization, surface potential measurements further revealed a clear difference between pristine and modified samples. The pristine Sb nanosheets exhibited a negative surface potential of −25.6 ± 5.03 mV. Upon functionalization with β-cyclodextrin, this value shifted to −18.8 ± 3.67 mV, indicating the functionalization of Sb sheets, thereby reducing its aqueous oxidation [82].

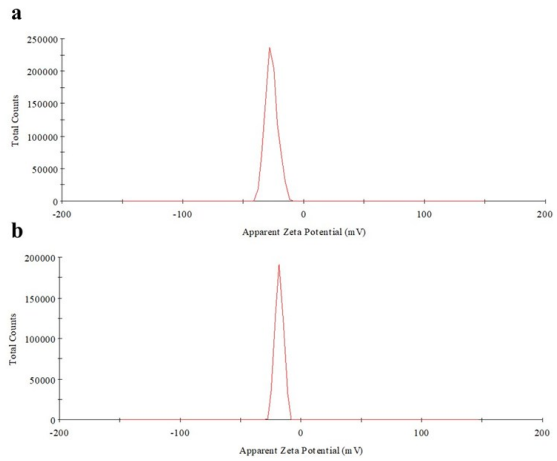

***Figure 30**. Zeta potential graph of **a)** Sb nanosheets. **b)** f-Sb nanosheets. Each measurement was repeated 3 times.*

Dynamic light scattering (DLS) was employed to assess the size distribution of the dispersed nanosheets. The measurements indicated that the Sb flakes predominantly ranged from approximately 200 to 500 nm in lateral dimension, consistent with the formation of well-dispersed nanoscale structures in aqueous solution (**figure 31**).

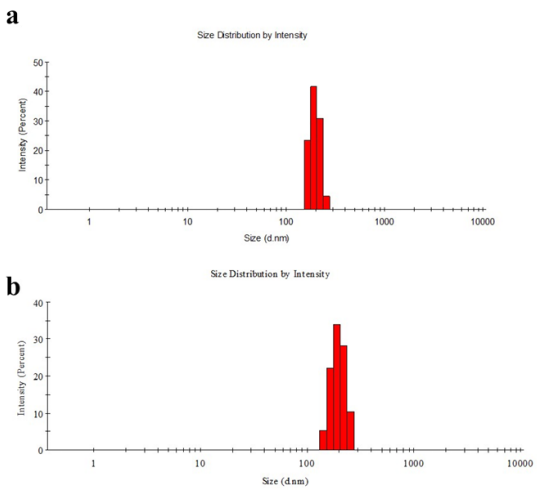

***Figure 31.** Size measurement graph of **a)** Sb nanosheets and **b)** f-Sb nanosheets, respectively.*

Further structural insights were obtained through Raman spectroscopy (**figure 32**). In the pristine sample, the spectrum displayed two well-defined bands at 118 cm^{-1} and 149 cm^{-1}, corresponding to the Eg (in-plane) and A1g (out-of-plane) vibrational modes of layered antimonene, respectively [83]. These features are indicative of few-layer structures. Additional peaks observed at 185, 250, 373, and 435 cm^{-1} were attributed to antimony oxide species, reflecting partial surface oxidation in aqueous media [84]. The Raman profile of the β-cyclodextrin-functionalized material exhibited the same characteristic features, yet with a systematic redshift and increased peak intensities, which could be due to the surface adsorption of β-CDs on the Sb sheets [85].

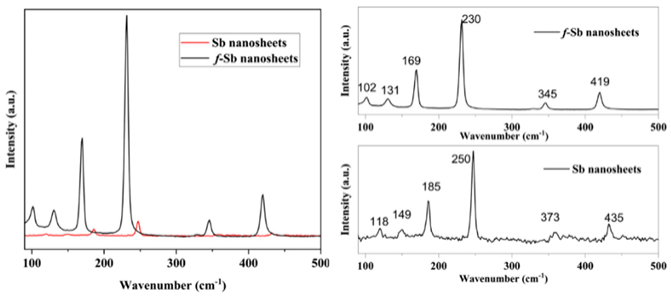

***Figure 32**. **(left)** Raman spectra of Sb nanosheets (red line) and f-Sb nanosheets (black line) exfoliated in water, respectively. **(right)** Raman spectra of Sb nanosheets (bottom) and f-Sb nanosheets (top) show distinctive peaks for each type of nanosheet vibration mode, respectively.*

To gain further insights into the interaction between the β-cyclodextrin molecules and the antimonene nanosheets, Fourier-transform infrared (FTIR) spectroscopy was employed (**figure 33**). The spectrum of the pristine Sb sample revealed distinct peaks around 722 and 830 cm^{-1}, which are attributable to Sb–O–Sb linkages and vibrational modes of Sb_2O_3

species, respectively. Additionally, the broad overlapping bands between 3600 and 2600 cm^{-1}, along with peaks near 1580 and 1346 cm^{-1}, were consistent with the presence of strongly adsorbed water molecules on the surface [86].

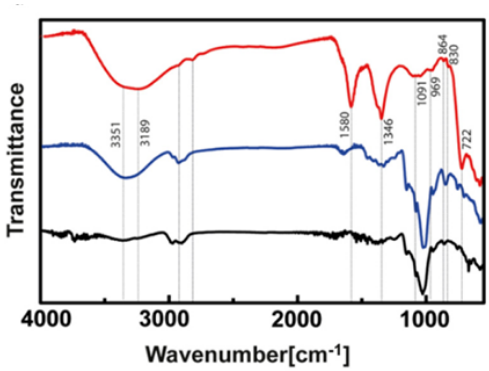

***Figure 33**. FTIR spectra of 2-HP-β-cyclodextrin (blue line), Sb nanosheets (red line) and f-Sb nanosheets (black line). Spectra were acquired in triplicate on three different samples of 2-hydroxypropyl-β-cyclodextrin and f-Sb nanosheets and shown as the average of the obtained results.*

These findings confirm that aqueous exfoliation leads to partial oxidation of the Sb surface[23] [87]. In contrast, the FTIR spectrum of pure β-CDs exhibited prominent features typical of hydroxyl-rich structures, such as a broad O–H stretching band around 3300 cm^{-1} and weaker C–H stretching bands near 2900 cm^{-1} [88]. When examining the spectrum of the functionalized Sb material, notable changes were observed in the relative intensities and positions of these bands, indicating that β-CDs engage in direct interactions with the nanosheet surfaces. The attenuation of water-associated signals, together with specific variations in the 600–1500 cm^{-1} region (**figure 34**), suggest that the oxygen-containing groups of β-CDs likely displace surface-bound water and form hydrogen bonds with oxidized Sb sites.

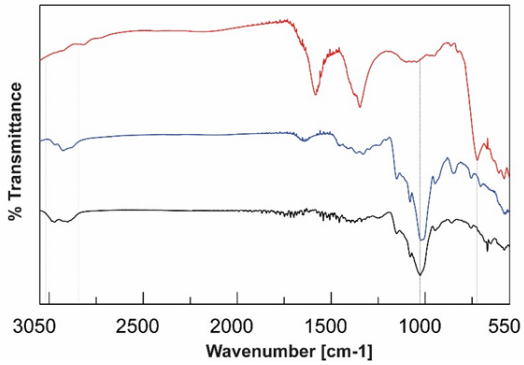

Figure 34. *Enlarged FTIR spectra of Sb sheets (red line) β-cyclodextrin (blue line) and f-Sb nanosheets (black line).*

High-resolution transmission electron microscopy (HR-TEM) was used to investigate the morphology and lateral dimensions of both pristine and β-cyclodextrin-functionalized antimonene nanosheets (**figure 35**).

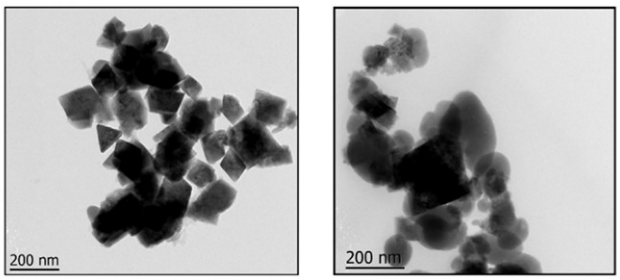

Figure 35*. HR-TEM images of (left) Sb nanosheets and (right) f-Sb nanosheets, respectively. Nearly 10 µL of sample was deposited on a carbon-coated copper TEM grid and left to dry for 20 minutes under an IR lamp.*

The images revealed a polydisperse distribution of nanosheets, with dimensions ranging between 200 and 500 nm, in agreement with the results obtained via dynamic light scattering analysis. No significant variation in sheet size was observed following functionalization, indicating that the cyclodextrin coating does not affect the nanoscale

morphology of the material. To further elucidate the chemical composition and surface states of the exfoliated nanosheets, X-ray photoelectron spectroscopy (XPS) was performed (**figure 36, 37 and Table 4**). The spectra of pristine samples displayed well-resolved Sb $3d_{3/2}$ and Sb $3d_{5/2}$ peaks at 534 and 537 eV, which corresponds to the Sb_2O_3 oxidation states of antimonene. The peak at 532.2 eV corresponds to the O1s, confirmed the incorporation of oxygen species on the nanosheet surface, a likely consequence of aqueous exfoliation. Notably, prolonged sonication appeared to intensify these oxygen-related signals, suggesting an enhancement of surface oxidation with increased energy input [89].

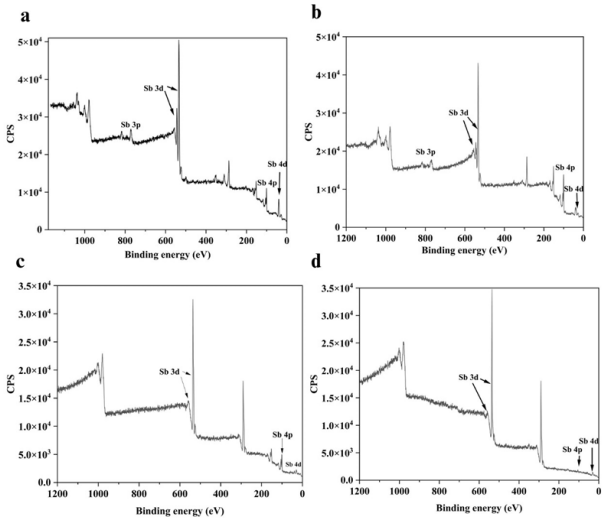

Figure 36. *XPS Survey spectra of Sb nanosheets* ***a)*** *at 0 day, and* ***b)*** *after 7 days in buffer. f-Sb nanosheets* ***c)*** *at 0 day, and* ***d)*** *after 7 days in buffer.*

In the case of β-CD-functionalized nanosheets, the O 1s peak was still present but exhibited reduced intensity relative to the pristine sample (**figure 37b**). This suggests that the surface was oxidized, although not to the same extent as the bare ones, as the β-CD molecules covered the surface of nanosheets through adsorption. These findings further

underscore the stabilizing role of β-CD functionalization in limiting surface oxidation.

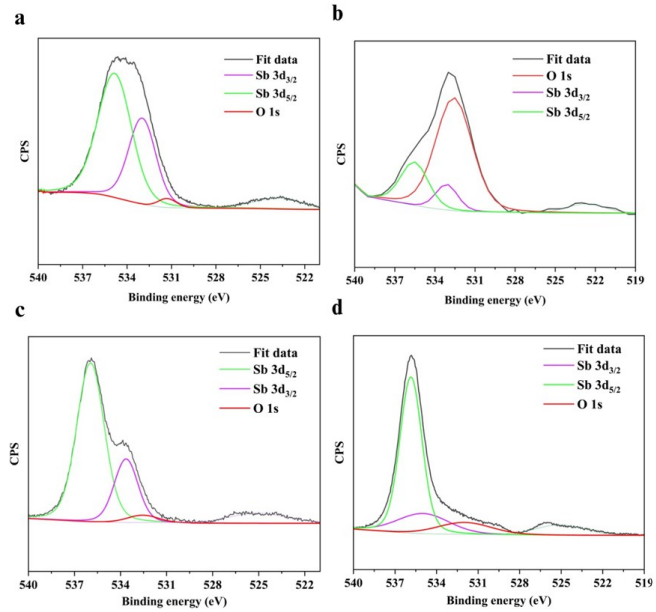

***Figure 37**. XPS spectra of Sb nanosheets **a**) at 0 day, and **b**) after 7 days in buffer. f-Sb nanosheets **c**) at 0 day, and **d**) after 7 days in buffer.*

	Spectral range(eV)	area		%area	
Sb nanosheets					
		Before	After	Before	After
O1s	520~540	28552.29	78722.13	16.25	56.40
Sb $3d_{5/2}$		116895.39	14608.85	66.51	10.47
Sb $3d_{3/2}$		20991.10	38278.74	11.94	27.41
Sb MNN		9288	7967.83	5.29	5.72
f-Sb nanosheets					
		Before	After	Before	After
O1s	520~540	566.93	4481.03	1.69	12.54
Sb $3d_{5/2}$		9119.44	5768.2	27.17	16.14
Sb $3d_{3/2}$		21099.14	22373.47	62.83	62.58
Sb MNN		2788.64	3120.54	8.32	8.72

***Table 4**. Main features retrieved by Figure 14.*

3.2.2 Chemical stability studies

Assessing the stability of antimonene nanosheets in aqueous media is essential for evaluating their environmental persistence and potential

reactivity under physiological conditions. In this context, UV–vis spectroscopy was employed as a non-invasive tool to monitor temporal changes in the dispersions, providing qualitative insights into degradation phenomena. For pristine Sb nanosheets, a marked decrease in absorbance intensity was observed within the first two days, which is most likely attributable to reaggregation or sedimentation rather than immediate chemical degradation [90]. Nonetheless, such behaviour reflects limited colloidal stability in water, consistent with previous observations for Sb systems dispersed in organic solvents [91]. Importantly, the exfoliation process itself, conducted in aqueous media and under sonication, appears to promote oxidation. The generation of cavitation bubbles and sonic jets during sonication facilitates the penetration of atmospheric oxygen, promoting the formation of oxide species such as Sb_2O_3 and Sb_2O_5 at the nanosheet surface. With prolonged incubation, the progressive increase in surface oxidation alters the physicochemical properties of the material, including a decline in thermal conductivity and a corresponding reduction in UV–vis absorbance intensity.

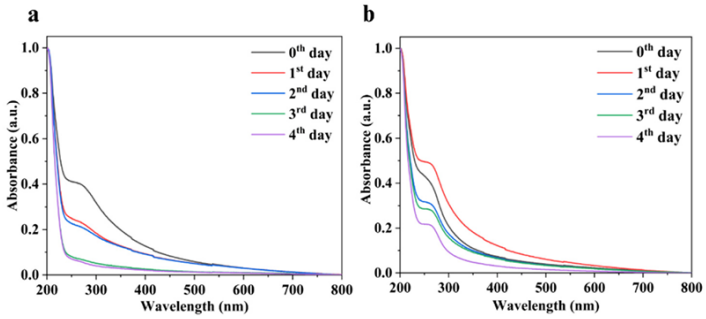

***Figure 38**. UV-visible spectra of (**a**) Sb nanosheets and (**b**) f-Sb nanosheets acquired over five days.*

These findings align with the XPS and FTIR data, which point to significant surface oxidation in pristine samples. In contrast, the β-CD-

functionalized Sb nanosheets exhibited a more gradual decrease in absorbance over time, indicative of enhanced colloidal and chemical stability [92]. The attenuated oxidation process in these samples suggests that cyclodextrin molecules form a partial protective barrier on the surface, limiting access of water and oxygen to reactive sites.

3.2.3 Degradation of Sb and f-Sb nanosheets using hMPO

The biodegradability of pristine and β-cyclodextrin-functionalized antimonene nanosheets was evaluated by incubating the samples with hMPO, a peroxidase enzyme secreted by neutrophils and macrophages, in the presence of hydrogen peroxide (H_2O_2). This enzymatic system was selected to mimic physiologically relevant oxidative environments, providing insight into the potential fate of antimonene in vivo. Samples were incubated for 10 hours, and morphological and structural changes were assessed through transmission electron microscopy (TEM) (**figure 39**) and Raman spectroscopy (**figure 40**).

Initial TEM images confirmed the sheet-like morphology of both Sb and f-Sb nanosheets before treatment. After 10 hours in phosphate-buffered saline (PBS) alone, no major morphological changes were observed in either sample. However, in the presence of hMPO and H_2O_2, both Sb and f-Sb underwent evident structural alterations. Pristine Sb nanosheets exhibited pronounced fragmentation and loss of sheet integrity, resulting in nanoscale debris and irregular structures. In contrast, f-Sb nanosheets retained partial structural integrity, with fewer signs of morphological disruption, suggesting a protective role of the β-cyclodextrin coating.

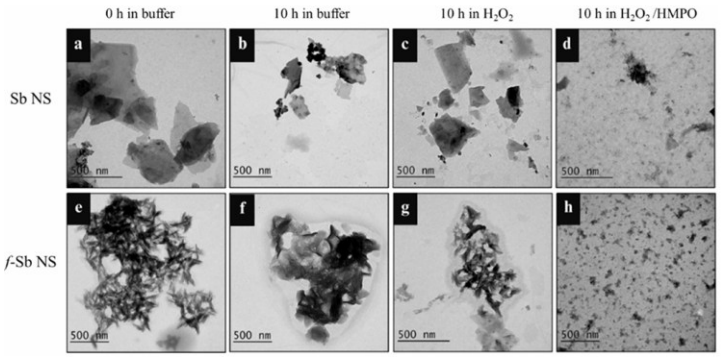

Figure 39. *TEM images of hMPO-catalysed degradation of* ***(a)*** *Sb NSs and* ***(e)*** *f-Sb NSs dispersed in buffer at 0 h, respectively.* ***(b)*** *Sb NSs and* ***(f)*** *f-Sb NSs after 10 h of incubation in the buffer.* ***(c)*** *Sb NSs and* ***(g)*** *f-Sb NSs in the buffer along with H_2O_2 after 10 h of incubation.* ***(d)*** *10 h treated Sb NSs and (h) f-Sb NSs with PBS/H_2O_2/hMPO.*

These observations were corroborated by Raman spectroscopy. At time zero (0 h), all characteristic peaks of 2D Sb were present. After 10 hours in PBS alone, these peaks decreased in intensity, and additional broad features emerged at 375 cm^{-1} and 453 cm^{-1}, consistent with oxidized forms of antimony [84] [93].

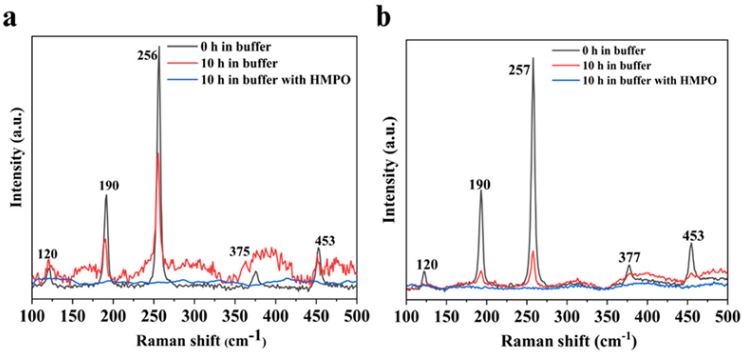

Figure 40*. Raman spectra of* ***(a)*** *Sb NSs dispersed in buffer at 0 h (black line), after 10 h of incubation in the buffer (red line) and Sb NSs treated with PBS/H_2O_2/hMPO (blue line).* ***(b)*** *f-Sb nanosheets in buffer at 0 h (black line) and after 10 h of incubation in the buffer (red line), and f-Sb nanosheets treated with PBS/H_2O_2 /hMPO for 10 h (blue line).*

This indicates that surface oxidation progressed even in the absence of enzymatic catalysis. More strikingly, after incubation with hMPO/H_2O_2, the Raman spectrum of pristine Sb displayed no detectable Sb-specific peaks, confirming extensive enzymatic degradation. For f-Sb nanosheets, Raman analysis after 10 hours in PBS revealed a reduction in peak intensity, but the characteristic features remained visible, indicating only mild oxidation. In the hMPO/H_2O_2-treated f-Sb samples, most characteristic Sb peaks disappeared, yet a broad residual peak at 456 cm^{-1}, associated with oxidized antimony, remained detectable [84]. This finding suggests that while enzymatic degradation occurred, the β-cyclodextrin functionalization mitigated the extent of structural breakdown. Collectively, these results highlight that enzymatic degradation of Sb nanosheets is driven by oxidative stress catalyzed by peroxidase activity, and that surface functionalization with β-cyclodextrin confers a measurable degree of protection [80]. This behavior parallels findings in other 2D materials such as MoS_2, where functionalization has similarly been shown to delay or reduce degradation under oxidative enzymatic conditions [94].

3.2.4 Degradation of Sb and f-Sb nanosheets using HRP

To further explore the oxidative degradation of antimonene nanosheets, an additional enzymatic study was conducted using HRP, a widely adopted plant peroxidase model. Both pristine Sb and f-Sb nanosheets were incubated in the presence of HRP and H_2O_2 for ten days, with daily renewal of the enzyme. The structural evolution of the nanosheets was monitored via TEM (**figure 41**) and Raman spectroscopy (**figure 42**) to assess their morphological and chemical transformations. TEM analyses at day 0 revealed well-defined sheet-like structures for both Sb and f-Sb

samples, confirming their initial stability in PBS. After 10 days of incubation in PBS alone, pristine Sb nanosheets displayed partial degradation, evidenced by the appearance of small pores and slight morphological disruption.

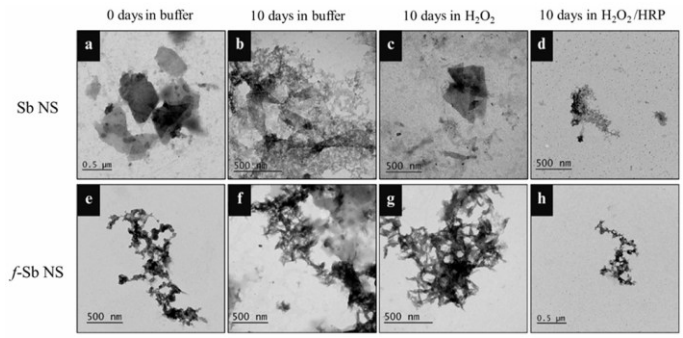

***Figure 41**. TEM images of HRP-catalysed degradation of (**a**) Sb NSs and (e) f-Sb NSs dispersed in buffer on day 0. (**b**) Sb NSs and (**f**) f-Sb NSs after 10 days of incubation in the buffer. (**c**) Sb NSs and (**g**) f-Sb NSs in the buffer, along with H_2O_2, after 10 days of incubation. (**d**) 10 day treated Sb NSs and (**h**) f-Sb NSs with PBS/H_2O_2/HRP.*

When incubated in H_2O_2 alone, Sb nanosheets exhibited only minimal changes, indicating that H_2O_2 in the absence of enzymatic catalysis does not significantly drive degradation. In contrast, exposure to HRP in combination with H_2O_2 resulted in substantial structural degradation of pristine Sb nanosheets. The typical sheet morphology was no longer discernible, replaced by a heterogeneous distribution of debris and porous fragments. These findings closely mirror those observed in the hMPO-mediated degradation, supporting the conclusion that HRP is similarly capable of catalyzing oxidative breakdown of Sb nanosheets. The f-Sb nanosheets demonstrated greater morphological stability across all conditions. After 10 days in PBS or in H_2O_2 alone, no significant alterations in morphology were observed. When treated with HRP/H_2O_2,

however, moderate degradation was detected, evidenced by the appearance of minor debris and surface irregularities, yet the characteristic sheet-like structure remained partially preserved. This comparative resilience underscores the stabilizing effect of β-cyclodextrin functionalization, which appears to reduce susceptibility to enzymatic oxidation. Raman spectroscopic data corroborated the morphological observations. At day 0, both Sb and f-Sb samples exhibited the characteristic Raman features of antimonene. After 10 days in PBS, both samples displayed broadened peaks with decreased intensity, which can be attributed to partial oxidation and nanosheet aggregation. The degradation became more pronounced upon treatment with HRP/H_2O_2. In the case of pristine Sb, the Raman peaks were entirely absent, confirming extensive structural degradation and loss of crystallinity. For f-Sb, the spectra showed significant peak broadening but retained residual features, indicating that degradation was incomplete. These results highlight the critical role of surface functionalization in modulating the enzymatic degradability of antimonene. While both hMPO and HRP catalyze oxidative breakdown of the material, the protective β-cyclodextrin coating delays degradation, likely by impeding direct enzymatic access to the nanosheet surface. This finding is consistent with trends observed in other functionalized 2D materials and reinforces the importance of surface chemistry in determining biological fate.

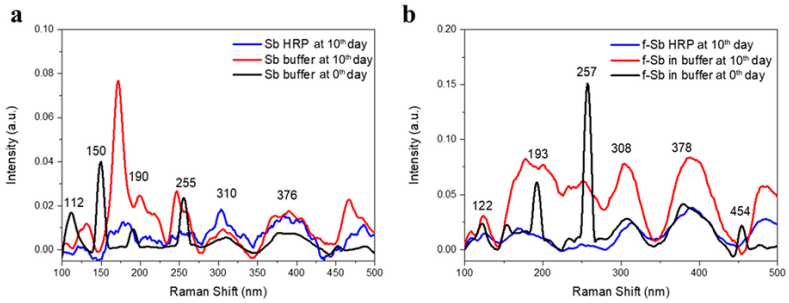

***Figure 42**. Raman spectra of **(a)** Sb NSs dispersed in buffer on day 0 (black line) and after 10 days of incubation in the buffer (red line) and Sb NSs treated with PBS/H_2O_2 /HRP (blue line). **(b)** f-Sb nanosheets in the buffer on day 0 (black line) and after 10 days of incubation in the buffer (red line), and f-Sb nanosheets after 10 days of treatment with PBS/H_2O_2 /HRP (blue line).*

3.2.5 Cytotoxicity of Sb and f-Sb nanosheets in THP-1 human monocytes

To evaluate the potential biological impact of antimonene before and after degradation, cytotoxicity assays were conducted on human monocytic THP-1 cells. The comparison focused on both pristine and functionalized nanosheets, assessing their effects at increasing concentrations and after partial enzymatic degradation. As reported in **Figure 43**, exposure to pristine Sb nanosheets at concentrations of 10 and 20 μg mL^{-1} resulted in a clear reduction in cell viability compared to the cell control. In contrast, f-Sb nanosheets displayed lower cytotoxic effects under the same conditions, suggesting that surface functionalization may play a protective role. Interestingly, upon partial degradation, pristine Sb nanosheets showed slightly increased cytotoxicity at higher doses compared to their non-degraded counterparts. This response may be linked to changes in surface chemistry and the release of oxidized species, which can influence cellular interactions. On the other hand, partially degraded f-Sb nanosheets did not show a cytotoxic effect; instead, they appeared to promote cell

proliferation relative to the undegraded f-Sb samples. This unexpected response may point to degradation-associated maturation phenomena.

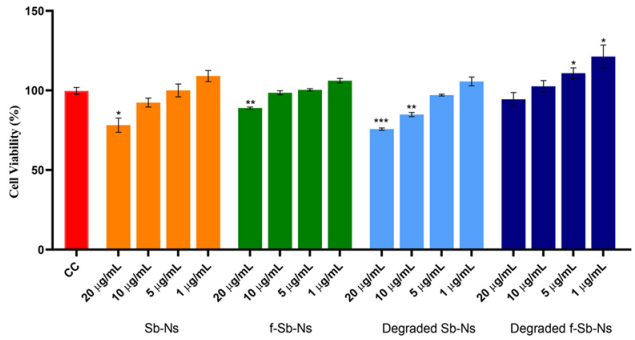

Figure 43. *Cytotoxicity analysis of Sb nanosheets and f-Sb nanosheets done before and after degradation using THP-1 cells. The experiment was performed in triplicate (n = 3); no. of cells: 10000; incubated with compounds for 24 hours; Sb-nanosheet concentration: 20, 10, 5, and 1 µgmL^{-1}; cell control (CC) containing THP-1 cells only. Statistical comparison is made between the cell control and nanosheets, Student's t-test, unpaired, para metric; *p value ≤0.05; **p value ≤0.01; and ***p value ≤0.001.*

3.2.6 Immunomodulatory activity of Sb nanosheets– TNF-α production analysis

Tumor necrosis factor-alpha (TNF-α) is a key pro-inflammatory cytokine involved in orchestrating immune responses, functioning as a critical signaling molecule within the immune system. Although the immunomodulatory effects of several metal-based nanomaterials have been investigated, studies focused specifically on antimonene nanosheets remain limited. To evaluate the potential impact of pristine and functionalized Sb nanosheets on immune activity, both before and after partial degradation, their effect on TNF-α production was assessed in THP-1 monocytes.

As illustrated in **Figure 44**, untreated THP-1 cells did not exhibit detectable TNF-α production. Treatment with Sb nanosheets induced a modest increase in TNF-α levels, indicating a slight immunostimulatory

effect. However, in comparison with lipopolysaccharide (LPS), a well-established immunostimulant, the response induced by Sb nanosheets was significantly lower, both in their intact and partially degraded forms. Moreover, no notable differences were observed between pristine and functionalized nanosheets, nor between degraded and non-degraded conditions. These observations suggest that, at the tested concentration, Sb nanosheets do not elicit a robust immune activation. The minimal immunostimulatory response may be attributable to structural features resembling damage-associated molecular patterns.

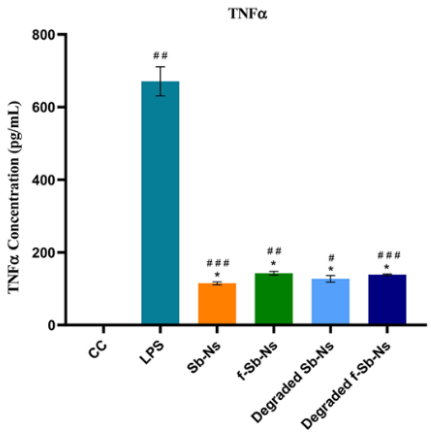

Figure 44. *Immunomodulatory activity of Sb nanosheets assessed through TNF-α production analysis. The experiment was performed with two independent sets in triplicate (n = 6); no. of cells: 20000; incubated with compounds for 24 hours; Sb-nanosheet concentration taken was 5 μgmL^{-1} and LPS was used as a positive control with a concentration of 100 ng mL−1; cell control (CC) containing THP-1 cells only. Statistical comparison was made between LPS and nanosheets, Student's t-test, unpaired, non-parametric, Mann–Whitney test; *p value ≤0.05; **p value ≤0.01; and ***p value ≤0.001. Moreover, a statistical comparison was carried out between the cell control and nanosheets as well, Student's t-test, parametric, paired t-test; $^{\#}$p value ≤0.05; $^{\#\#}$p value ≤0.01; and $^{\#\#\#}$p value ≤0.001*

3.3 Conclusions

Cyclodextrins (CDs) are cyclic oligosaccharides with a hydrophobic inner cavity and hydrophilic rims that form inclusion complexes and serve as versatile non-covalent surface functionalizers, enhancing solubility, stability, and biocompatibility in diverse nanomaterial systems. The present work reports the fabrication and characterization of both pristine and β-cyclodextrin-functionalized antimonene nanosheets (Sb and f-Sb), with a focus on their enzymatic degradation mediated by hMPO and HRP. Structural analyses indicated that, upon sonication-assisted exfoliation in aqueous media, a significant degree of surface oxidation occurred, with only a limited fraction of metallic Sb likely retained. However, the notably higher absolute intensity of Raman signals observed in the presence of β-cyclodextrin suggests a greater preservation of partially unoxidized material. Thus, CD functionalization produces a protective coating that modulates ζ-potential, improves colloidal stability, and reduces peroxidase-mediated biodegradation, thereby limiting enzymatic access to reactive sites. A key physical driver of this interfacial assembly is the high polarizability of the antimonene surface, which supports attractive London-dispersion (van der Waals) interactions with the glucopyranose framework of the CD torus, facilitating robust non-covalent adsorption. Concomitantly, the outer hydrophilic hydroxyls present on CDs can promote close packing and adsorption onto relatively hydrophobic or weakly oxidized Sb basal planes, favoring the formation of a coherent coating at the bio–nano interface. Such physisorption confers steric stabilization in dispersion and partially masks reactive sites from further oxidations. In addition to dispersion and hydrophobic contacts, hydroxyl groups on the CD can form hydrogen bonds with surface oxygen species (e.g., Sb–O, hydroxides) introduced during exfoliation or aging, as well as

with adsorbed water layers; this anchors CDs preferentially at edges/defects, yielding heterogeneous coverage and further stabilization against oxidation. Accordingly, higher degradation of Sb nanosheets was observed upon treatment with hMPO compared to HRP, likely due to the higher redox potential of hMPO enzyme intermediates (Compounds I and II at 1.16 and 1.34 V, respectively), as well as the generation of the strong oxidant HOCl (1.48 V). In contrast, HRP intermediates exhibit lower oxidation potentials (~0.9 V), resulting in less pronounced degradation of Sb nanosheets. Cell viability results were in line with the degradation data: f-Sb nanosheets showed lower cytotoxicity compared to pristine Sb, likely due to the formation of oxidized species such as Sb_2O_3. Overall, the results demonstrate that Sb nanosheets are susceptible to functionalization-dependent enzymatic degradation when treated with human myeloperoxidase, a key enzyme secreted by neutrophils. Additionally, the degradation products did not adversely affect human cells, offering important insight into the potential in vivo use of Sb nanosheets and their suitability for biomedical applications such as cancer theranostics.

3.4 Materials and Methods

Sb bulk powder and 2-hydroxypropyl-beta-cyclodextrin were purchased from Sigma-Aldrich. The enzyme human myeloperoxidase (hMPO, isolated from human polymorphonuclear leukocytes) and horseradish peroxidase (HRP) were commercially obtained from Sigma-Aldrich, India. The chemicals $Na_2HPO_4 \cdot 2H_2O$, $NaH_2PO_4 \cdot 2H_2O$, NaCl, KCl, KH_2PO_4, hydrogen peroxide (30% aqueous solution) and diethylenetriamine pentaacetic acid (DTPA) were obtained from Sigma-

Aldrich and used directly without any further purification. Deionized water (DI) was acquired using a Milli-Q® Millipore filter system.

Synthesis of Sb nanosheets

First, 100 mg of bulk Sb powder (initial concentration of 5 mg mL^{-1}) was dispersed in 20 mL of DI water. The dispersion was then exfoliated by combining probe and bath sonication pro cesses [23]. During the probe sonication process, an ice bath was employed to prevent heat generation due to cavitation bubbles. After sonication, the dispersion was centrifuged at room temperature at 3000 rpm for 20 minutes to remove the unexfoliated Sb from the solution. Finally, the sediment part was discarded, and the supernatant was collected and stored at 4 °C for further use.

Functionalization of Sb sheets with 2-hydroxypropyl β-cyclodextrin

According to a previous report, Sb sheets were functionalized with 2-hydroxypropyl-beta-cyclodextrin (CD) [80]. Briefly, 180 mg of CD (initial concentration, 9 mg mL^{-1}) and 100 mg of Sb bulk powder (initial concentration, 5 mg mL^{-1}) were dispersed in 20 mL of DI water. The resulting dispersion was exfoliated using probe and bath sonication, respectively. After sonication, the dispersion was centrifuged at 3000 rpm for 20 minutes, and the sediment was discarded. Finally, the supernatant was collected and stored at 4 °C for further characterisation.

Characterization of Sb and f-Sb nanosheets

Ultraviolet–visible spectroscopy. The ultraviolet visible (UV) absorption spectra of Sb and f-Sb nanosheets were obtained using a spectrophotometer (Shimadzu UV-3600 Vis NIR spectrophotometer). The analysis was then performed using a 1 mL quartz cuvette with a light path length of 10 mm. All the measurements were taken at room temperature and baseline correction was performed using water as a blank.

Zeta potential measurements. The size and surface charges of Sb and f-Sb nanosheets were measured using a Zetasizer Nano-ZS instrument (Malvern Instruments, Malvern, UK). The samples underwent 1 minute of sonication before the measurements. All the measurements were taken at room temperature using a disposable zeta sizer cuvette. Each measurement was repeated 3 times, and the results are presented as the mean and standard deviation.

Raman spectroscopy. Raman spectroscopy was employed to characterize the pristine Sb and f-Sb nanosheets using a LabRAM HR Raman spectrophotometer with a 633 nm laser at 3% power and using a microscope. Both samples were sonicated for 5 minutes. Then, 6 µL of each sample was drop casted onto two separate clean glass slides and dried under IR radiation. Raman spectra were recorded using a 100× objective lens. The graphs were plotted using Origin software, where the baseline correction was done by subtracting the origin values, with 8 points selected in the graph. The Raman characterization of exfoliated (thin) sheets is very difficult because of very low non-resonant Raman intensities and therefore, we could not get more Raman spectra for each sample, unlike graphene materials. The Raman plots present only one spectrum.

Fourier transform infrared spectroscopy. Fourier transform infrared (FTIR) spectra of samples were collected using a Jasco FT/IR 4100

spectrometer (Easton, MD) in a single-reflection ATR with an ATR PRO ONE X (Jasco) equipped with a ZnSe prism (ATR/sample contact area of 2.5 mm diameter, no. of reflections = 1 and an angle of incidence of 45°) at a resolution of 2 cm^{-1} and a total of 100 scans (scan range 4000–550 cm^{-1}). Spectra were acquired in triplicate on three different samples of 2-hydroxypropyl-β-cyclodextrin and f-Sb nanosheets.

Transmission electron microscopy (TEM). The morphology and lateral dimension of the nanosheets were meticulously examined using transmission electron microscopy (TEM) (FEI TECHNAI G2 F30 S-Twin, operating at 120 kV). The sample was subjected to 5 minutes of sonication using an ANM Industries ultrasonic cleaner (USC-300 50 Hz). Nearly 10 μL of each sample was deposited on a carbon-coated copper TEMgrid and left to dry for 20 minutes under an IR lamp.

X-ray photoelectron spectroscopy. Sb and f-Sb nanosheets underwent examination utilizing X-ray photo electron spectroscopy (XPS) (Omicron Nanotechnology XPS) and the data acquisition was performed using VISION software, while data interpretation was performed using CASAXPS software (Casa Software Ltd, UK). The analysis was carried out with a monochromatic AL K X-ray source (1486.7 eV) operating at 15 kV (90 W).

Colloidal and chemical stability of Sb nanosheets with and without functionalization

In order to study the chemical stability of both types of nanosheets, 2 mL of each prepared nanosheet was taken in separate vials. The UV spectra of each vial were recorded daily over 4 days. The data were also recorded on the same day and the nanosheets were synthesized. All the measurements

were recorded at room temperature and baseline correction was per formed using water as a blank control.

Degradation of Sb and f-Sb nanosheets with the HRP enzyme

For the degradation with HRP, 78.33 µL of Sb nanosheets (final concentration of −0.3 mg mL^{-1}) was added to 921.67 µL of PBS buffer. For f-Sb nanosheets, 67 µL of nanosheets (final concentration of 0.6 mg mL^{-1}) was added to 933 µL. To both suspensions, 0.175 mg of HRP was added. 4 µL of 10 mM H_2O_2 were added daily for ten days. All suspensions were maintained under dark conditions and were subjected to continuous stirring throughout the experimental period. The portions of 20 µL were collected at 0, 5, and 10 days and stored at −20 °C for further characterization. Similarly, sample degradation was conducted using the same amount in the absence of HRP. 4 µL of H_2O_2 was added once daily for 10 days.

Degradation of Sb and f-Sb nanosheets with the hMPO enzyme

Next, 42 µL of Sb nanosheet solution was added to 70.5 µL of 50 mM PBS buffer (final concentration is 0.3 mg mL^{-1}). To this suspension, 12.5 µL of hMPO (1 mg mL^{-1}), pre-dissolved in PBS buffer, was added. Every hour, 2 µL of 10 mM H_2O_2 was added for 10 hours. The hMPO enzyme was refreshed every 5 hours. The reaction mixture was kept at 37 °C in an incuba tor. The fractions of 10 µL were collected at 0 h, 5 h, and 10 h and stored at −20 °C until they were characterized using various techniques. To investigate the degradation process without hMPO, 42 µL of Sb nanosheets was combined with 70.5 µL of PBS buffer. Subsequently, 2 µL of H_2O_2 was added every hour for 10 hours. Likewise, the degradation of f-Sb nanosheets was conducted by adding 12.5 µL of f-Sb nanosheets

(final concentration: 0.9 mg mL−1) to 98 µL of PBS buffer. 12.5 µL of hMPO was introduced. Next, 2 µL of H_2O_2 was introduced every hour for 10 hours. In the same way, the degradation only in the presence of H2O2 was carried out by adding 12.5 µL of f-Sb nanosheets to 99 µL of PBS buffer. The reaction was carried out at 37 °C.

Characterization of degraded Sb and f-Sb nanosheets

Raman analyses. Raman analyses were performed on the degraded samples (buffer and buffer/H_2O_2/enzyme) for both types of nanosheets (Sb and f-Sb) using a LabRAM HR Raman spectrophotometer equipped with a 633 nm laser at 3% power and a microscope. All the samples were sonicated for 5 minutes before deposition on clean glass slides. Next, 6 µL of each sample was drop-cast and dried under IR radiation. Raman spectra were recorded using a 100× objective lens.

Transmission electron microscopy analyses. TEM analyses were conducted using an FEI TECNAI G2 Spirit Bio Twin microscope with an accelerating voltage of 120 kV. Next, 6 µL of each degraded sample (buffer, buffer/H_2O_2, and buffer/ H_2O_2/enzyme) for both types of nanosheets (Sb and f-Sb) was drop-cast onto separate carbon-coated copper TEM grids. The grids were dried under an IR lamp for 20 minutes and then washed with Milli-Q water for approximately 8–10 minutes to remove salts from the buffer. Finally, the grids were again dried under an IR lamp for another 20 minutes.

Cell viability of Sb and f-Sb nanosheets before and after degradation

Cytotoxicity was assessed using a colorimetric assay based on the reduction of 3-[4,5-dimethylthiazol-2-yl]-2,5-diphenyl-tetrazolium

bromide (MTT) by mitochondrial dehydrogenases in viable cells, resulting in the formation of a blue formazan precipitate.

THP-1 human monocyte cells. The cytotoxicity of the pristine Sb and f-Sb nanosheets before and after partial degradation was assessed on THP-1 cells. Partial degradation was performed by incubating pristine Sb and f-Sb nanosheets in PBS buffer for 3–4 days. THP-1 cells were maintained in complete RPMI-1640 medium (Sigma-R6504) supplemented with 10% fetal bovine serum (FBS) (Gibco-16170078) and 1% penicillin–streptomycin (Gibco-15140-122) solution under standard conditions of 37 °C and 5% CO_2 for 24 hours. THP-1 cells were added to a 96-well plate at a density of 10000 cells per well. Then, the cells were treated with decreasing concentrations of Sb and f-Sb nanosheets and partially degraded Sb and f-Sb nanosheets (1 μg mL^{-1}–20 μg mL^{-1}) and incubated for 24 hours at 37 °C and 5% CO_2. Before treatment, non-degraded, pristine and functionalised nanosheets were freshly reconstituted as per the concentrations. The experiment was conducted in triplicate for each concentration of each nanosheet. Control wells contained only the cells without any treatment. After 24 hours of incubation, 50 μL of MTT (Sigma, M5655) solution (5 mg mL^{-1} concentration in PBS) was added into each well and incubated for 4 hours at 37 °C and 5% CO_2 for 24 hours. Later, ∼100 μL of media was aspirated and discarded, and formazan crystals were dissolved in 50 μL of dimethyl sulfoxide (DMSO) and incubated for 15 minutes. Absorbance (O.D.) was then measured at 570 nm using a MEGALLAN (Tecan Life Sciences) microplate reader. Percentage cell viability was then calculated based on the nanosheet treatment's absorbance relative to the cell control's absorbance.

Cytokine TNF-α production analysis: ELISA

Secreted cytokines were measured by sandwich enzyme-linked immunosorbent assay (ELISA). For this, human THP-1 monocytic cells (1 × 106 cells) were cultured in a 48-well tissue culture plate in a complete medium (RPMI-10% FBS). The cells were then treated with pristine Sb and f-Sb nanosheets before and after partial degradation with a concentration of 5 μg mL^{-1} and incubated at 37 °C with 5% CO_2 for 24 hours. Culture supernatants were then collected and centrifuged at 1500 rpm for 5 minutes to remove any cell debris. TNF-α in supernatants was measured using ELISA kits (Human TNF-α DuoSet ELISA kit, DY210-05) following the manufacturer's protocol.

Statistical analysis

Data were analysed using GraphPad Prism 8. A comparison of two groups was performed either using Student's unpaired and paired t-tests or with Mann–Whitney rank sum nonparametric and parametric tests depending on the results.

3.5 References

[1] L. H. Madkour, "Chemistry and Physics for Nanostructures Semiconductivity," in *Advanced Structured Materials*, vol. 116, Springer Verlag, 2019, pp. 457–478. doi: 10.1007/978-3-030-21621-4_13.

[2] M. C. Roco, C. A. Mirkin, and M. C. Hersam, "Nanotechnology research directions for societal needs in 2020: Summary of international study," Mar. 2011. doi: 10.1007/s11051-011-0275-5.

[3] N. Joudeh and D. Linke, "Nanoparticle classification, physicochemical properties, characterization, and applications: a

comprehensive review for biologists," Dec. 01, 2022, *BioMed Central Ltd*. doi: 10.1186/s12951-022-01477-8.

[4] G. Cho, Y. Park, Y. K. Hong, and D. H. Ha, "Ion exchange: an advanced synthetic method for complex nanoparticles," Dec. 01, 2019, *Korea Nano Technology Research Society*. doi: 10.1186/s40580-019-0187-0.

[5] F. Findik, "Nanomaterials and their applications," vol. 9, no. 3, pp. 62–75, 2021.

[6] D. Chimene, D. L. Alge, and A. K. Gaharwar, "Two-Dimensional Nanomaterials for Biomedical Applications: Emerging Trends and Future Prospects," *Advanced Materials*, vol. 27, no. 45, pp. 7261–7284, Dec. 2015, doi: 10.1002/adma.201502422.

[7] K. S. Novoselov *et al.*, "Electric field in atomically thin carbon films," *Science (1979)*, vol. 306, no. 5696, pp. 666–669, Oct. 2004, doi: 10.1126/science.1102896.

[8] J. C. Meyer, A. K. Geim, M. I. Katsnelson, K. S. Novoselov, T. J. Booth, and S. Roth, "The structure of suspended graphene sheets," *Nature*, vol. 446, no. 7131, pp. 60–63, Mar. 2007, doi: 10.1038/nature05545.

[9] M. Chhowalla, H. S. Shin, G. Eda, L. J. Li, K. P. Loh, and H. Zhang, "The chemistry of two-dimensional layered transition metal dichalcogenide nanosheets," Apr. 2013. doi: 10.1038/nchem.1589.

[10] Q. H. Wang, K. Kalantar-Zadeh, A. Kis, J. N. Coleman, and M. S. Strano, "Electronics and optoelectronics of two-dimensional transition metal dichalcogenides," 2012, *Nature Publishing Group*. doi: 10.1038/nnano.2012.193.

[11] A. Ramasubramaniam, “Large excitonic effects in monolayers of molybdenum and tungsten dichalcogenides,” *Phys Rev B Condens Matter Mater Phys*, vol. 86, no. 11, Sep. 2012, doi: 10.1103/PhysRevB.86.115409.

[12] S. Bertolazzi, J. Brivio, and A. Kis, “Stretching and breaking of ultrathin MoS 2,” *ACS Nano*, vol. 5, no. 12, pp. 9703–9709, Dec. 2011, doi: 10.1021/nn203879f.

[13] B. Radisavljevic, A. Radenovic, J. Brivio, V. Giacometti, and A. Kis, “Single-layer MoS2 transistors,” *Nat Nanotechnol*, vol. 6, no. 3, pp. 147–150, 2011, doi: 10.1038/nnano.2010.279.

[14] K. F. Mak, C. Lee, J. Hone, J. Shan, and T. F. Heinz, “Atomically thin MoS2: A new direct-gap semiconductor,” *Phys Rev Lett*, vol. 105, no. 13, Sep. 2010, doi: 10.1103/PhysRevLett.105.136805.

[15] A. Kormányos *et al.*, “Erratum: K.p theory for two-dimensional transition metal dichalcogenide semiconductors (2D Materials (2015) 2 (022001)),” Dec. 16, 2015, *IOP Publishing Ltd*. doi: 10.1088/2053-1583/2/4/049501.

[16] N. Salehi and A. Abareshi, “Study of structural, optical, and thermal properties in MoS2-based nanocomposites: iron and gold,” *Eur Phys J Plus*, vol. 137, no. 11, Nov. 2022, doi: 10.1140/epjp/s13360-022-03502-z.

[17] S. Yougbaré *et al.*, “Gold nanorod-decorated metallic mos2 nanosheets for synergistic photothermal and photodynamic antibacterial therapy,” *Nanomaterials*, vol. 11, no. 11, Nov. 2021, doi: 10.3390/nano11113064.

[18] M. H. Karami and O. M. Jazani, “The Progress of Molybdenum Disulfide 2D Nanosheets as Bionanocarriers for Drug Delivery Systems: A Groundbreaking Approach with Multiple Therapeutic Applications,” 2025, *Springer*. doi: 10.1007/s10904-025-03735-2.

[19] L. Zhu *et al.*, “A Biodegradable 2D Metallic MoS2 Genesheet for Synergistic NIR-II Photothermal Immunotherapy,” *Small*, vol. 21, no. 30, Jul. 2025, doi: 10.1002/smll.202502577.

[20] T. Zhong *et al.*, “Research Progress and Applications of 2D Antimonene,” Jan. 01, 2023, *MDPI*. doi: 10.3390/app13010035.

[21] G. Wang, R. Pandey, and S. P. Karna, “Atomically thin group v elemental films: Theoretical investigations of antimonene allotropes,” *ACS Appl Mater Interfaces*, vol. 7, no. 21, pp. 11490–11496, Jun. 2015, doi: 10.1021/acsami.5b02441.

[22] J. A. Carrasco, P. Congost-Escoin, M. Assebban, and G. Abellán, “Antimonene: a tuneable post-graphene material for advanced applications in optoelectronics, catalysis, energy and biomedicine,” Feb. 06, 2023, *Royal Society of Chemistry*. doi: 10.1039/d2cs00570k.

[23] C. Gibaja *et al.*, “Liquid phase exfoliation of antimonene: Systematic optimization, characterization and electrocatalytic properties,” *J Mater Chem A Mater*, vol. 7, no. 39, pp. 22475–22486, 2019, doi: 10.1039/c9ta06072c.

[24] M. Assebban *et al.*, “Unveiling the oxidation behavior of liquid-phase exfoliated antimony nanosheets,” *2d Mater*, vol. 7, no. 2, Apr. 2020, doi: 10.1088/2053-1583/ab755e.

[25] A. A. Kistanov, Y. Cai, D. R. Kripalani, K. Zhou, S. V. Dmitriev, and Y. W. Zhang, "A first-principles study on the adsorption of small molecules on antimonene: Oxidation tendency and stability," *J Mater Chem C Mater*, vol. 6, no. 15, pp. 4308–4317, 2018, doi: 10.1039/c8tc00338f.

[26] W. Tao *et al.*, "Two-Dimensional Antimonene-Based Photonic Nanomedicine for Cancer Theranostics," *Advanced Materials*, vol. 30, no. 38, Sep. 2018, doi: 10.1002/adma.201802061.

[27] Y. Zhang *et al.*, "Ultrasensitive detection of microRNA-21 by using specific interaction of antimonene with RNA as electrochemical biosensor," *Bioelectrochemistry*, vol. 142, Dec. 2021, doi: 10.1016/j.bioelechem.2021.107890.

[28] J. Jeon *et al.*, "Layer-controlled CVD growth of large-area two-dimensional MoS2 films," *Nanoscale*, vol. 7, no. 5, pp. 1688–1695, Feb. 2015, doi: 10.1039/c4nr04532g.

[29] J. R. Brent, N. Savjani, and P. O'Brien, "Synthetic approaches to two-dimensional transition metal dichalcogenide nanosheets," Aug. 01, 2017, *Elsevier Ltd*. doi: 10.1016/j.pmatsci.2017.06.002.

[30] M. Yi and Z. Shen, "A review on mechanical exfoliation for the scalable production of graphene," Jun. 14, 2015, *Royal Society of Chemistry*. doi: 10.1039/c5ta00252d.

[31] J. N. Coleman *et al.*, "Two-dimensional nanosheets produced by liquid exfoliation of layered materials," *Science (1979)*, vol. 331, no. 6017, pp. 568–571, Feb. 2011, doi: 10.1126/science.1194975.

[32] J. J. Cha *et al.*, “Two-dimensional chalcogenide nanoplates as tunable metamaterials via chemical intercalation,” *Nano Lett*, vol. 13, no. 12, pp. 5913–5918, Dec. 2013, doi: 10.1021/nl402937g.

[33] Y. D. Liu *et al.*, “Preparation, characterization and photoelectrochemical property of ultrathin MoS2 nanosheets via hydrothermal intercalation and exfoliation route,” *J Alloys Compd*, vol. 571, pp. 37–42, Sep. 2013, doi: 10.1016/j.jallcom.2013.03.031.

[34] P. Chavalekvirat, W. Hirunpinyopas, K. Deshsorn, K. Jitapunkul, and P. Iamprasertkun, “Liquid Phase Exfoliation of 2D Materials and Its Electrochemical Applications in the Data-Driven Future,” Jul. 22, 2024, *American Chemical Society*. doi: 10.1021/prechem.3c00119.

[35] S. Presolski and M. Pumera, “Covalent functionalization of MoS2,” Apr. 01, 2016, *Elsevier B.V.* doi: 10.1016/j.mattod.2015.08.019.

[36] S. Karunakaran, S. Pandit, B. Basu, and M. De, “Simultaneous Exfoliation and Functionalization of 2H-MoS2 by Thiolated Surfactants: Applications in Enhanced Antibacterial Activity,” *J Am Chem Soc*, vol. 140, no. 39, pp. 12634–12644, Oct. 2018, doi: 10.1021/jacs.8b08994.

[37] M. M. Ayyub, M. Barua, S. Acharya, and C. N. R. Rao, “Covalent Functionalization of Antimonene and Bismuthene Nanosheets,” *Small*, vol. 18, no. 38, Sep. 2022, doi: 10.1002/smll.202203554.

[38] F. Xing *et al.*, “Covalently Silane-Functionalized Antimonene Nanosheets and Their Copolymerized Gel Glasses for Broadband Vis-NIR Optical Limiting,” *ACS Appl Mater Interfaces*, vol. 13, no. 1, pp. 897–903, Jan. 2021, doi: 10.1021/acsami.0c18738.

[39] B. Kost, M. Brzezinski, M. Socka, M. Basko, and T. Biela, “Biocompatible polymers combined with cyclodextrins: Fascinating materials for drug delivery applications,” Aug. 01, 2020, *MDPI AG*. doi: 10.3390/molecules25153404.

[40] M. Ayán-Varela *et al.*, “Aqueous exfoliation of transition metal dichalcogenides assisted by DNA/RNA nucleotides: Catalytically active and biocompatible nanosheets stabilized by acid-base interactions,” *ACS Appl Mater Interfaces*, vol. 9, no. 3, pp. 2835–2845, Jan. 2017, doi: 10.1021/acsami.6b13619.

[41] G. Zhu, X. Zhang, P. Gai, and J. Chen, “Enhanced electrochemical sensing for persistent organic pollutants by nanohybrids of graphene nanosheets that are noncovalently functionalized with cyclodextrin,” *Chempluschem*, vol. 77, no. 9, pp. 844–849, Sep. 2012, doi: 10.1002/cplu.201200144.

[42] J. A. Morton *et al.*, “An eco-friendly solution for liquid phase exfoliation of graphite under optimised ultrasonication conditions,” *Carbon N Y*, vol. 204, pp. 434–446, Feb. 2023, doi: 10.1016/j.carbon.2022.12.070.

[43] J. Fernandes, S. S. Nemala, G. De Bellis, and A. Capasso, “Green Solvents for the Liquid Phase Exfoliation Production of Graphene: The Promising Case of Cyrene,” Apr. 11, 2022, *Frontiers Media S.A.* doi: 10.3389/fchem.2022.878799.

[44] E. Varrla *et al.*, “Large-scale production of size-controlled MoS2 nanosheets by shear exfoliation,” *Chemistry of Materials*, vol. 27, no. 3, pp. 1129–1139, Feb. 2015, doi: 10.1021/cm5044864.

[45] M. S. Gilliam *et al.*, “Evaluating the Exfoliation Efficiency of Quasi-2D Metal Diboride Nanosheets Using Hansen Solubility Parameters,” *Langmuir*, vol. 37, no. 3, pp. 1194–1205, Jan. 2021, doi: 10.1021/acs.langmuir.0c03138.

[46] G. D’Olimpio, J. Occhiuzzi, L. Lozzi, L. Ottaviano, and A. Politano, “Dimethyl 2-Methylglutarate (Iris): A Green Platform for Efficient Liquid-Phase Exfoliation of 2D Materials,” *Adv Sustain Syst*, vol. 6, no. 11, Nov. 2022, doi: 10.1002/adsu.202200277.

[47] J. Occhiuzzi, G. G. Politano, G. D’Olimpio, and A. Politano, “The Quest for Green Solvents for the Sustainable Production of Nanosheets of Two-Dimensional (2D) Materials, a Key Issue in the Roadmap for the Ecology Transition in the Flatland,” *Molecules*, vol. 28, no. 3, Feb. 2023, doi: 10.3390/molecules28031484.

[48] K. Pan *et al.*, “Sustainable production of highly conductive multilayer graphene ink for wireless connectivity and IoT applications,” *Nat Commun*, vol. 9, no. 1, Dec. 2018, doi: 10.1038/s41467-018-07632-w.

[49] D. Kong and A. V. Dolzhenko, “Cyrene: A bio-based sustainable solvent for organic synthesis,” Apr. 01, 2022, *Elsevier B.V.* doi: 10.1016/j.scp.2021.100591.

[50] C. Caponio *et al.*, “Cyrene- and water-based exfoliation of black phosphorus for potential nanolayer-mediated disaggregation of insulin fibrils,” *FlatChem*, vol. 45, May 2024, doi: 10.1016/j.flatc.2024.100665.

[51] M. Singh *et al.*, “Combating Actions of Green 2D-Materials on Gram Positive and Negative Bacteria and Enveloped Viruses,”

Front Bioeng Biotechnol, vol. 8, Sep. 2020, doi: 10.3389/fbioe.2020.569967.

[52] J. Kaur *et al.*, "Biological interactions of biocompatible and water-dispersed MoS2 nanosheets with bacteria and human cells," *Sci Rep*, vol. 8, no. 1, Dec. 2018, doi: 10.1038/s41598-018-34679-y.

[53] C. Backes *et al.*, "Preparation of liquid-exfoliated transition metal dichalcogenide nanosheets with controlled size and thickness: A state of the art protocol," *Journal of Visualized Experiments*, vol. 2016, no. 118, Dec. 2016, doi: 10.3791/54806.

[54] C. Backes *et al.*, "Edge and confinement effects allow in situ measurement of size and thickness of liquid-exfoliated nanosheets," *Nat Commun*, vol. 5, Aug. 2014, doi: 10.1038/ncomms5576.

[55] L. Antonov and D. Nedeltcheva, "Resolution of overlapping UV-Vis absorption bands and quantitative analysis," *Chem Soc Rev*, vol. 29, no. 3, pp. 217–227, 2000, doi: 10.1039/a900007k.

[56] S. Sharma, S. Bhagat, J. Singh, R. C. Singh, and S. Sharma, "Excitation-dependent photoluminescence from WS2 nanostructures synthesized via top-down approach," *J Mater Sci*, vol. 52, no. 19, pp. 11326–11336, Oct. 2017, doi: 10.1007/s10853-017-1303-3.

[57] K. Kouroupis-Agalou *et al.*, "Fragmentation and exfoliation of 2-dimensional materials: A statistical approach," *Nanoscale*, vol. 6, no. 11, pp. 5926–5933, Jun. 2014, doi: 10.1039/c3nr06919b.

[58] H. Li *et al.*, "From bulk to monolayer MoS 2: Evolution of Raman scattering," *Adv Funct Mater*, vol. 22, no. 7, pp. 1385–1390, Apr. 2012, doi: 10.1002/adfm.201102111.

[59] M. A. Bissett, S. D. Worrall, I. A. Kinloch, and R. A. W. Dryfe, “Comparison of Two-Dimensional Transition Metal Dichalcogenides for Electrochemical Supercapacitors,” *Electrochim Acta*, vol. 201, pp. 30–37, May 2016, doi: 10.1016/j.electacta.2016.03.190.

[60] Y. Chen, “Growth of a large, single-crystalline ws2 monolayer for high-performance photodetectors by chemical vapor deposition,” *Micromachines (Basel)*, vol. 12, no. 2, pp. 1–7, 2021, doi: 10.3390/mi12020137.

[61] “NATURE VOL 389 23 OCTOBER 1997”.

[62] C. Backes *et al.*, “Equipartition of Energy Defines the Size−Thickness Relationship in Liquid-Exfoliated Nanosheets,” *ACS Nano*, vol. 13, no. 6, pp. 7050–7061, 2019, doi: 10.1021/acsnano.9b02234.

[63] H. Ma, Z. Shen, and S. Ben, “Understanding the exfoliation and dispersion of MoS2 nanosheets in pure water,” *J Colloid Interface Sci*, vol. 517, pp. 204–212, May 2018, doi: 10.1016/j.jcis.2017.11.013.

[64] A. Elbanna *et al.*, “Perovskite-transition metal dichalcogenides heterostructures: recent advances and future perspectives,” 2022, *Editorial Office of Opto-Electronic Journals, Institute of Optics and Electronics, Chinese Academy of Sciences*. doi: 10.29026/oes.2022.220006.

[65] S. Ott, N. Wolff, F. Rashvand, V. J. Rao, J. Zaumseil, and C. Backes, “Impact of the mos2 starting material on the dispersion quality and quantity after liquid phase exfoliation,” *Chemistry of Materials*, vol.

31, no. 20, pp. 8424–8431, Oct. 2019, doi: 10.1021/acs.chemmater.9b02336.

[66] S. Ott, M. Lakmann, and C. Backes, “Impact of pretreatment of the bulk starting material on the efficiency of liquid phase exfoliation of WS2,” *Nanomaterials*, vol. 11, no. 5, May 2021, doi: 10.3390/nano11051072.

[67] W. Qiao *et al.*, “Effects of ultrasonic cavitation intensity on the efficient liquid-exfoliation of MoS2 nanosheets,” *RSC Adv*, vol. 4, no. 92, pp. 50981–50987, 2014, doi: 10.1039/c4ra09001b.

[68] G. Q. Han *et al.*, “WS2 nanosheets based on liquid exfoliation as effective electrocatalysts for hydrogen evolution reaction,” *Mater Chem Phys*, vol. 167, pp. 271–277, Nov. 2015, doi: 10.1016/j.matchemphys.2015.10.043.

[69] F. Ghasemi and S. Mohajerzadeh, “Sequential Solvent Exchange Method for Controlled Exfoliation of MoS2 Suitable for Phototransistor Fabrication,” *ACS Appl Mater Interfaces*, vol. 8, no. 45, pp. 31179–31191, Nov. 2016, doi: 10.1021/acsami.6b07211.

[70] J. Shi *et al.*, “Temperature-Mediated Selective Growth of MoS2/WS2and WS2/MoS2Vertical Stacks on Au Foils for Direct Photocatalytic Applications,” *Advanced Materials*, vol. 28, no. 48, pp. 10664–10672, Dec. 2016, doi: 10.1002/adma.201603174.

[71] J. Kaur, A. M. Gravagnuolo, P. Maddalena, C. Altucci, P. Giardina, and F. Gesuele, “Green synthesis of luminescent and defect-free bio-nanosheets of MoS2: Interfacing twodimensional crystals with hydrophobins,” *RSC Adv*, vol. 7, no. 36, pp. 22400–22408, 2017, doi: 10.1039/c7ra01680h.

[72] G. Rusciano *et al.*, “Single-Cell Photothermal Analysis Induced by MoS2 Nanoparticles by Raman Spectroscopy,” *Front Bioeng Biotechnol*, vol. 10, Mar. 2022, doi: 10.3389/fbioe.2022.844011.

[73] L. Pan, Y. T. Liu, X. M. Xie, and X. Y. Ye, “Facile and Green Production of Impurity-Free Aqueous Solutions of WS2 Nanosheets by Direct Exfoliation in Water,” *Small*, vol. 12, no. 48, pp. 6703–6713, Dec. 2016, doi: 10.1002/smll.201601804.

[74] V. Paolucci *et al.*, “Sustainable Liquid-Phase Exfoliation of Layered Materials with Nontoxic Polarclean Solvent,” *ACS Sustain Chem Eng*, vol. 8, no. 51, pp. 18830–18840, Dec. 2020, doi: 10.1021/acssuschemeng.0c04191.

[75] H. Ohshima, “Theory of electrostatics and electrokinetics of soft particles,” *Sci Technol Adv Mater*, vol. 10, no. 6, 2009, doi: 10.1088/1468-6996/10/6/063001.

[76] A. Gupta and S. Vasudevan, “Understanding Surfactant Stabilization of MoS2 Nanosheets in Aqueous Dispersions from Zeta Potential Measurements and Molecular Dynamics Simulations,” *Journal of Physical Chemistry C*, vol. 122, no. 33, pp. 19243–19250, Aug. 2018, doi: 10.1021/acs.jpcc.8b05922.

[77] B. Chakraborty, A. Das, A. Kumar, A. Barui, M. Kumar, and C. Roy Chaudhuri, “Real time estimation of stem cell zeta potential and dimension during proliferation using MoS2 nanosheets field effect transistor,” *Sens Actuators B Chem*, vol. 380, Apr. 2023, doi: 10.1016/j.snb.2023.133351.

[78] M. A. DIasio and D. L. Green, “The Effect of Solvent Viscosity on Production of Few-layer Graphene from Liquid-phase Exfoliation

of Graphite," in *MRS Advances*, Materials Research Society, 2019, pp. 241–247. doi: 10.1557/adv.2019.13.

[79] T. M. Mohona *et al.*, "Aggregation Behavior of Inorganic 2D Nanomaterials beyond Graphene: Insights from Molecular Modeling and Modified DLVO Theory," *Environ Sci Technol*, vol. 53, no. 8, pp. 4161–4172, Apr. 2019, doi: 10.1021/acs.est.8b05180.

[80] W. Zhao, X. Tan, J. Jiang, F. Liu, and T. Mu, "Highly Efficient, Green, and Scalable β-Cyclodextrin-Assisted Aqueous Exfoliation of Transition-Metal Dichalcogenides: MoS2 and ReS2 Nanoflakes," *Chem Asian J*, vol. 12, no. 10, pp. 1052–1056, May 2017, doi: 10.1002/asia.201700355.

[81] F. Zhang *et al.*, "Semimetal–Semiconductor Transitions for Monolayer Antimonene Nanosheets and Their Application in Perovskite Solar Cells," *Advanced Materials*, vol. 30, no. 38, Sep. 2018, doi: 10.1002/adma.201803244.

[82] H. Kouchakzadeh, S. A. Shojaosadati, A. Maghsoudi, and E. Vasheghani Farahani, "Optimization of PEGylation conditions for BSA nanoparticles using response surface methodology," *AAPS PharmSciTech*, vol. 11, no. 3, pp. 1206–1211, Sep. 2010, doi: 10.1208/s12249-010-9487-8.

[83] M. Mohamed Ismail *et al.*, "Antimonene nanosheets with enhanced electrochemical performance for energy storage applications," *Dalton Transactions*, vol. 49, no. 39, pp. 13717–13725, Oct. 2020, doi: 10.1039/d0dt01753a.

[84] S. Wolff, R. Gillen, M. Assebban, G. Abellán, and J. Maultzsch, “Two-Dimensional Antimony Oxide,” *Phys Rev Lett*, vol. 124, no. 12, Mar. 2020, doi: 10.1103/PhysRevLett.124.126101.

[85] X. Jin, C. Xu, J. Hu, S. Yao, Z. Hu, and B. Wang, “A biodegradable multifunctional nanoplatform based on antimonene nanosheets for synergistic cancer phototherapy and dual imaging,” *J Mater Chem B*, vol. 9, no. 45, pp. 9333–9346, Dec. 2021, doi: 10.1039/d1tb01275d.

[86] M. J. Nine *et al.*, “Laminated antimonene as an alternative and efficient shielding strategy against X-ray radiation,” *Appl Mater Today*, vol. 29, Dec. 2022, doi: 10.1016/j.apmt.2022.101566.

[87] Q. Xiao *et al.*, “Antimonene-based flexible photodetector,” *Nanoscale Horiz*, vol. 5, no. 1, pp. 124–130, Jan. 2020, doi: 10.1039/c9nh00445a.

[88] M. Agotegaray *et al.*, “β-cyclodextrin coating: improving biocompatibility of magnetic nanocomposites for biomedical applications,” *J Mater Sci Mater Med*, vol. 31, no. 2, Feb. 2020, doi: 10.1007/s10856-020-6361-4.

[89] M. Assebban *et al.*, “Unveiling the oxidation behavior of liquid-phase exfoliated antimony nanosheets,” *2d Mater*, vol. 7, no. 2, Apr. 2020, doi: 10.1088/2053-1583/ab755e.

[90] C. Gibaja *et al.*, “Few-Layer Antimonene by Liquid-Phase Exfoliation,” *Angewandte Chemie - International Edition*, vol. 55, no. 46, pp. 14345–14349, Nov. 2016, doi: 10.1002/anie.201605298.

[91] P. Sahoo, R. C. Sahoo, and H. S. S. R. Matte, “Determination of Hansen Solubility Parameter and In Situ Visualization of Dispersion

Stability of Solution-Processed Antimonene," *ACS Appl Nano Mater*, vol. 6, no. 23, pp. 21957–21966, Dec. 2023, doi: 10.1021/acsanm.3c04189.

[92] P. Congost-Escoin *et al.*, "Interplay between the oxidation process and cytotoxic effects of antimonene nanomaterials," *Nanoscale*, vol. 16, no. 20, pp. 9754–9769, Mar. 2024, doi: 10.1039/d4nr00532e.

[93] D. W. Zeng, C. S. Xie, B. L. Zhu, and W. L. Song, "Characteristics of Sb2O3 nanoparticles synthesized from antimony by vapor condensation method," *Mater Lett*, vol. 58, no. 3–4, pp. 312–315, Jan. 2004, doi: 10.1016/S0167-577X(03)00476-2.

[94] B. Ma, C. Martín, R. Kurapati, and A. Bianco, "Degradation-by-design: How chemical functionalization enhances the biodegradability and safety of 2D materials," Sep. 07, 2020, *Royal Society of Chemistry*. doi: 10.1039/c9cs00822e.

PART II

APTAMER-BASED SYSTEMS FOR DETECTION OF MARINE TOXINS

CHAPTER IV

GENERAL INTRODUCTION TO APTAMERS AND BIOSENSING

4.1 Aptamers: Definition, Origin and Selection Strategies

Aptamers are short single-stranded DNA or RNA oligonucleotides that adopt unique three-dimensional conformations, enabling them to bind molecular targets with high affinity and specificity. The term derives from the Latin *aptus* ("to fit") and the Greek *meros* ("part"), underscoring their ability to adapt their structure to complement a wide variety of targets, ranging from small molecules and peptides to proteins, whole cells, and even viruses. Unlike canonical Watson–Crick base pairing, aptamer recognition relies on complex tertiary structures such as hairpins, loops, G-quadruplexes, and pseudoknots. These conformations create diverse binding pockets that enable highly versatile molecular recognition [95]. The concept of aptamers emerged in 1990, when two seminal studies demonstrated the in vitro selection of nucleic acids with specific binding capabilities. Tuerk and Gold [96] described the selection of RNA ligands against bacteriophage T4 DNA polymerase, introducing the term Systematic Evolution of Ligands by Exponential enrichment (SELEX), while Ellington and Szostak independently reported RNA sequences capable of binding organic dyes [97].

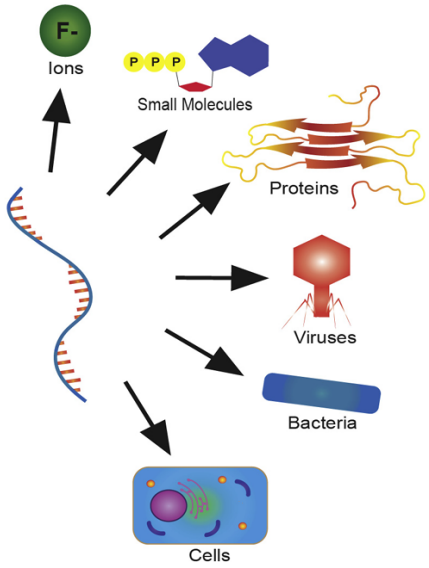

***Figure 45**. Versatility of aptamers. Variety of target molecules that aptamers have been selected for that demonstrate high specificity and affinity [97].*

The SELEX is an *in vitro* selection strategy that mimics the principles of Darwinian evolution. The procedure starts from a highly diverse oligonucleotide library, typically comprising ~10^{13}–10^{15} unique sequences flanked by constant primer regions required for amplification [98]. The library is incubated with the target of interest, and sequences that display binding affinity are separated from non-binders. Bound oligonucleotides are then amplified, by PCR in the case of DNA libraries or by transcription in the case of RNA libraries and reintroduced into subsequent selection cycles. With each round, the stringency of selection is progressively increased, for example by lowering the target concentration or introducing counter-selection steps, in order to enrich for high-affinity and high-specificity binders. After multiple iterative cycles, usually between 8 and 15, the population converges toward a limited set of aptamers with strong binding properties. These candidate sequences are subsequently cloned and sequenced, traditionally by Sanger methods, but increasingly through

next-generation sequencing approaches that allow a deeper characterization of the enriched pools.

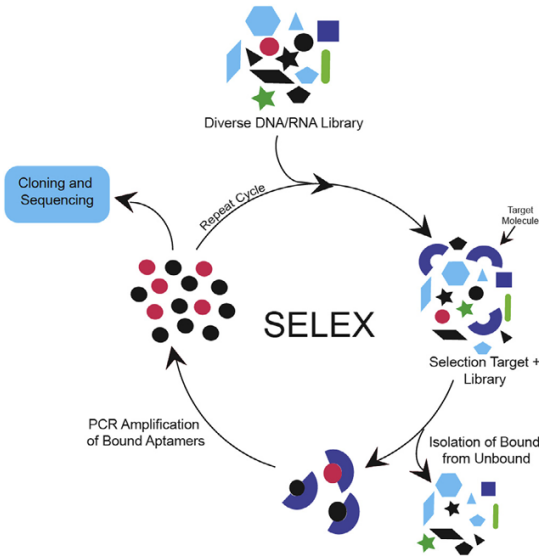

Figure 46. *Schematic representation of in vitro selection (SELEX). A diverse DNA/RNA library undergoes iterative binding, partitioning, and amplification cycles until enrichment of high-affinity sequences [97].*

Over the past three decades, SELEX has evolved into a family of methodologies designed to expand aptamer applicability. Examples include *Cell-SELEX,* which allows the selection of aptamers directly against live cells without prior knowledge of their molecular markers; *Toggle-SELEX*, alternating between related targets to isolate cross-reactive binders; *Negative-SELEX*, where counter-selection removes sequences binding undesired molecules [98]; and more recent innovations such as *Capture-SELEX*, that immobilises nucleic acid libraries to facilitate the selection of aptamers against small molecules [99]. Despite its success, SELEX is not without challenges. Issues such as PCR bias, target immobilisation artifacts, and low success rates for certain targets

highlight the importance of careful experimental design and quality control. Nevertheless, continual advances, including automation, high-throughput sequencing, and the use of chemically modified nucleotides, have significantly improved its efficiency and expanded the functional diversity of aptamers [97].

4.2 Molecular Engineering of Aptamers: Chemical Modifications and Functionalisation

Because aptamers share the chemical basis of natural nucleic acids, they are inherently biocompatible but also prone to enzymatic degradation and rapid clearance *in vivo*. To overcome these barriers, a broad repertoire of chemical modifications and conjugation strategies has been developed, targeting different structural elements of the oligonucleotide scaffold. These modifications can be introduced either during the SELEX process, by incorporating non-natural nucleotides, or post-selection, by chemically editing selected sequences [100]. Sugar and backbone modifications primarily enhance chemical and biological stability, whereas nucleobase modifications broaden or diversify functional properties (**figure 47**).

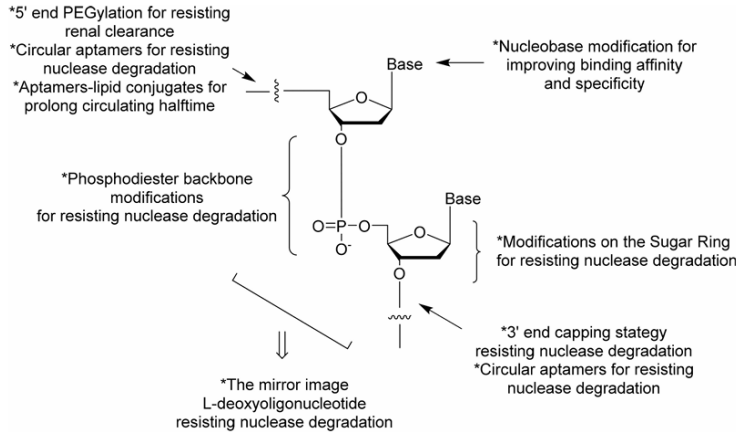

***Figure 47**. Common chemical modification strategies of nucleic acid aptamers to improve stability, affinity, and pharmacokinetics [100].*

Sugar modifications represent one of the most effective ways to improve nuclease resistance (**figure 48 a**). Substitution at the ribose 2′ position with fluorine, amino, or methyl groups stabilises the sugar ring and slows enzymatic cleavage [101]. More advanced chemistries include 2′-fluoro-arabinonucleic acid (FANA), which differs from 2′-F-RNA by its stereoelectronic conformation; locked nucleic acids (LNA), where a methylene bridge locks the ribose into the 3′-endo form; and unlocked nucleic acids (UNA), where the ribose is rendered more flexible by removing the C2′–C3′ bond [102]. These modifications extend circulation time and can also increase the structural rigidity of binding domains, enhancing affinity in certain contexts. *Backbone modifications* provide an additional route to stabilisation. The conventional phosphate linkage can be replaced with phosphorothioates (**figure 48 b**), in which a non-bridging oxygen is substituted by sulfur, conferring resistance against nucleases. More radical approaches include peptide nucleic acids (PNA), in which the sugar–phosphate skeleton is replaced by a synthetic polyamide chain, endowing the ligand with complete nuclease resistance and unique physicochemical behaviour [103]. Other strategies, such as inversion of polarity sites (IPS), can improve aptamer folding and affinity by introducing non-canonical orientations into the backbone. *Base modifications* expand the chemical diversity and functional activity of aptamers. The most accessible positions are the C5 of pyrimidines and the N7 of purines. A key example is represented by SOMAmers (slow off-rate modified aptamers), developed by SomaLogic [104]. In these, the natural thymidine bases are replaced by uridines functionalised with aromatic

groups such as benzyl, naphthyl or indole (**figure 48 c**). The presence of these bulky substituents during the selection process greatly enlarges the chemical space accessible to aptamers, allowing the recovery of ligands with affinities and functions that could not be reached with canonical bases.

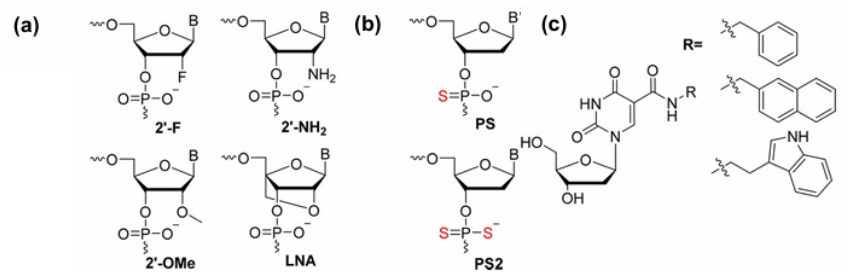

***Figure 48**. Modified nucleotide bases, sugar rings or phosphates. **(a)** Modifications (including F, NH2, OMe, LNA) on sugar rings. **(b)** Phosphorothioate linkages. **(c)** Modifications (R) employed for the selection of SOMAmers [100].*

Stereochemical inversion offers a conceptually different solution to nuclease degradation. *Spiegelmers* (from German mirror, Spiegel, combined with aptamers) are mirror-image aptamers composed of L-ribose nucleotides, as opposed to the natural D-configuration. Because natural nucleases only recognise D-nucleotides, Spiegelmers display exceptional stability in serum and in vivo. Their discovery marked a turning point, proving that aptamer chemistry could generate ligands with pharmacokinetics comparable to synthetic drugs rather than biopolymers [102]. *Conjugation with bulky moieties* is another critical strategy to overcome renal filtration. Increasing the hydrodynamic radius of aptamers by attaching polyethylene glycol (PEG), cholesterol, lipids, or nanomaterials prevents rapid clearance and prolongs circulation. Among

these, PEGylation has been most widely applied, with branched PEG chains extending half-life and improving biodistribution [105].

4.3 Aptamers in Analytical and Biosensing Applications: Advantages, Challenges, and Prospects

Over the past three decades, aptamers have been increasingly recognized as powerful alternatives to antibodies in biosensing and analytical chemistry. While antibodies have long dominated as biorecognition elements, their limitations, linked to biological production, structural rigidity, and high costs, have motivated the search for synthetic surrogates. Aptamers meet this demand by combining the selectivity of antibodies with the flexibility of nucleic acid chemistry, offering unique features that are reshaping the landscape of analytical applications.

Their secondary and tertiary folding can be rationally engineered to tune affinity or introduce switchable conformations. For example, aptamers have been designed to act as molecular beacons or conformational switches, producing a detectable signal only upon binding their target [106]. In addition, aptamers can be site-specifically functionalised with fluorophores, redox mediators, biotin, thiols, or nanomaterials [107]. Such tailored modifications broaden their compatibility with electrochemical, optical, and piezoelectric transduction methods, paving the way for increasingly miniaturized and multiplexed sensors. A key advantage of aptamers lies in their broad target spectrum. Unlike antibodies, whose generation relies on immunogenicity, aptamers can be selected against virtually any compound. Aptamer-based devices, or “aptasensors,” have already been applied to detect contaminants such as pesticides, marine biotoxins, mycotoxins, and heavy metals [108]. Their synthetic origin

ensures reproducible, low-cost production without the batch variability of biological systems, while their stability under ambient conditions reduces reliance on cold chains, an important factor for global diagnostics and field-deployable assays [109]. At the same time, it is important to emphasise that the application of aptamers in real matrices is not without challenges. Their affinity and specificity can be influenced by ionic strength, pH, and nonspecific interactions within complex samples such as seawater or food extracts [95]. Moreover, while SELEX allows the selection of aptamers against virtually any compound, not all targets yield high-affinity sequences, and in certain cases antibodies or engineered proteins still provide superior performance. For this reason, aptamers should be seen not as universal replacements, but as complementary tools whose impact is strongest where conventional methods are limited. Indeed, several biosensing strategies now combine aptamers and antibodies in hybrid "sandwich" assays, where one ligand captures the target and the other one provides signal amplification. Such formats highlight how the two recognition elements can act synergistically, rather than competitively, to improve sensitivity and specificity in complex matrices [110].

4.4 Saxitoxin: Structure, Toxicology and Relevance

Saxitoxin (STX) is widely recognised as one of the most potent naturally occurring neurotoxins and the principal agent of paralytic shellfish poisoning (PSP). Its chemical identity is defined by a unique tricyclic framework containing two guanidinium groups, which confer strong cationic character and high-water solubility [111]. This polarity facilitates dispersion in aquatic environments and efficient uptake by filter-feeding organisms, particularly bivalves, which constitute the primary vectors of

human intoxication. More than fifty naturally occurring analogues of STX have been described, including gonyautoxins, decarbamoyl derivatives, and N-sulfocarbamoyl congeners, each differing in substituents and, consequently, in toxic potency [112]. Carbamoyl derivatives are generally the most toxic, whereas sulfocarbamoyl congeners display reduced activity [113].The coexistence of multiple analogues in contaminated seafood complicates toxicological assessment and analytical detection, as both toxicity equivalence factors and quantitative distribution can vary significantly depending on the producing organism and environmental conditions [114]. The mechanism of action of STX has been extensively characterised: it binds with high affinity to the extracellular pore region of voltage-gated sodium channels (NaV), physically blocking sodium ion influx and thereby inhibiting the initiation and propagation of action potentials [111]. The result is a rapid disruption of neuromuscular transmission, clinically manifesting as tingling, numbness, muscular weakness, and, in severe cases, respiratory arrest [113]

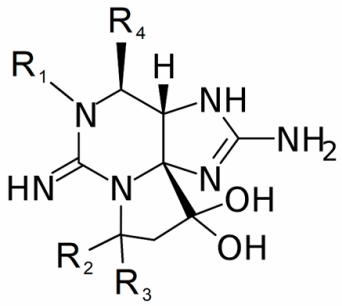

toxin	R1	R2	R3	R4
Non-sulfated				
STX	H	H	H	$OCONH_2$
neoSTX	OH	H	H	$OCONH_2$
Mono-sulfated				
GTX 1	OH	H	OSO_3^-	$OCONH_2$
GTX 2	H	H	OSO_3^-	$OCONH_2$
GTX 3	H	OSO_3^-	H	$OCONH_2$
GTX 4	OH	OSO_3^-	H	$OCONH_2$
Di-sulfated				
C1	H	H	OSO_3^-	$OCONHSO_3^-$
C2	H	OSO_3^-	H	$OCONHSO_3^-$
C3	OH	H	OSO_3^-	$OCONHSO_3^-$
C4	OH	OSO_3^-	H	$OCONHSO_3^-$
Decarbamoylated				
dcSTX	H	H	H	OH
dcneoSTX	OH	H	H	OH
dcGTX 1	OH	H	OSO_3^-	OH
dcGTX 2	H	H	OSO_3^-	OH
dcGTX 3	H	OSO_3^-	H	OH
dcGTX 4	OH	OSO_3^-	H	OH

***Figure 49**. Classes of STX congeners. PSP toxin backbone with various R groups that make toxic and non-toxic congeners of STX [115] .*

Thus, STX is of great relevance to food safety and public health. Because it is odourless, tasteless, and relatively stable under normal cooking

conditions, its accumulation in shellfish and other seafood cannot be detected by consumers through sensory. As a result, contamination events often become unnoticed until cases of human intoxication occur. In summary, saxitoxin illustrates the dual challenge posed by marine biotoxins: its chemical properties make it an exceptionally potent neurotoxin, while its ecological persistence and silent accumulation in seafood represent ongoing risks for human health and for the seafood industry worldwide. These features make essential the development of robust, rapid, and reliable detection strategies.

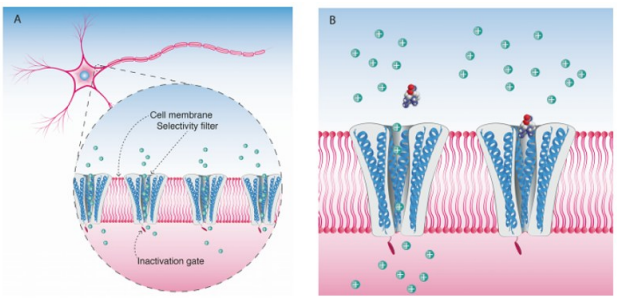

Figure 50. *Schematic figurative representation of the NaV channels in a neuronal cell membrane.* ***(a)*** *Normal Na^+ ion flux through the pores;* ***(b)*** *NaV channels blocked by STX molecules [113].*

4.5 Analytical Challenges in Saxitoxin Detection

More than 40 STX-analogues have been described, each with different toxicities, making it difficult to establish methods that can provide both qualitative identification and reliable quantification across the full spectrum [116]. Regulatory limits are particularly stringent, typically set at 80 µg STX equivalents per 100 g shellfish, leaving little margin for

analytical error [117]. Thus, monitoring STXs remain a significant analytical challenge due to the structural diversity of each compound, low regulatory thresholds, and the complexity of natural samples in which it accumulates.

Historically, the mouse bioassay (MBA) was the official reference method for paralytic shellfish toxins. While it provided a simple screening tool able to capture the cumulative toxicity of all congeners, it suffered from poor sensitivity, low reproducibility, and raised major ethical concerns. These limitations, coupled with the lack of congener-specific information, have led to its gradual replacement [119][118] .

Among chemical methods, high-performance liquid chromatography with fluorescence detection (HPLC-FLD) became one of the first accepted alternatives. Pre- or post-column oxidation strategies allow indirect quantification of STX congeners based on their oxidized fluorescent derivatives. While reliable and standardized (AOAC official methods), this approach requires labour-intensive derivatization and suffers from limited specificity when new or unusual analogues are encountered [116].

The advent of liquid chromatography coupled with tandem mass spectrometry (LC-MS/MS) has transformed the field, enabling highly specific identification of individual congeners with superior sensitivity [118]. Nonetheless, these methods are costly, demand advanced instrumentation, and rely heavily on the availability of certified standards that are often difficult or impossible to obtain. As a result, inter-laboratory comparability and routine application in resource-limited settings remain problematic [117].

In parallel, immunological methods such as ELISA have emerged as attractive tools for rapid screening. New monoclonal and recombinant antibodies have increased assay sensitivity and specificity, enabling the

detection of toxic congeners with minimal cross-reactivity [119]. More recently, lateral flow immunoassays and portable biosensors have been proposed as field-deployable solutions, although their robustness in complex food matrices is still under evaluation.

Another promising area is the development of cell-based bioassays, such as the neuroblastoma (Neuro-2a) assay, which can detect sodium channel blocking activity of STX and its congeners [117]. These in vitro systems offer an ethical alternative to animal models and provide functional readouts that complement chemical and immunological methods. However, many factors, i.e. variability due to culture conditions, sensitivity to many other matrix components, and lack of full standardization, limit their widespread adoption.

Taken together, these approaches reveal a trade-off between sensitivity, specificity, cost, and practicality. While mass spectrometry offers unmatched analytical precision, immunoassays and cell-based methods provide scalability and speed for monitoring programs. The coexistence of these platforms reflects the multifaceted challenge of STX detection, where no single method can yet satisfy all regulatory, economic, and field-deployment requirements.

4.6 Aptamer-Based Strategies for Saxitoxin Detection

Aptamers selected against STX have been integrated into a wide range of biosensing formats. In these systems the aptamer works as the recognition unit, while the signal is generated through an appropriate transduction method. Depending on how the binding event is converted into a measurable response, STX aptasensors can be primarily grouped into optical and electrochemical platforms. In electrochemical sensing, signal

transduction arises from the biochemical interaction between aptamer and its target analyte, leading to the generation or consumption of ions or electrons. The electrodes are commonly fabricated from gold or carbon-based materials. The optical systems determine the concentration of the toxin by measuring the absorption, fluorescence, luminescence, internal reflection, SPR and light-scattering spectroscopy. They can be categorized into label-free and label-based platforms. In label-free systems, the detection signal is directly generated by the transducer, with toxin binding inducing changes in the optical properties. In contrast, label-based aptasensors employ various optical probes and labels to produce luminescent, fluorescent, or colorimetric signals, typically manifested as shifts in analytical wavelengths [120].

4.6.1 Optical systems

A central aspect in the literature, as mentioned above, is the distinction between label-free and label-based optical systems. In label-free systems, the analytical signal is generated directly by the change in optical properties induced by toxin binding. A typical example is the Surface Plasmon Resonance (SPR) sensor. In this case, the STX aptamer is immobilized on a gold surface, and when the toxin binds, the local refractive index changes, producing a measurable shift in the plasmon resonance spectrum. This direct optical response makes the system simple, label-free and quantitative, with applicability also to real seafood samples [121]. In parallel, Surface-Enhanced Raman Scattering (SERS) sensors have shown the ability to reach extremely low detection limits by exploiting the amplification of vibrational signals generated by metallic nanostructures. Different strategies can be adopted to transduce the binding event. For example, Cheng et al. [122] reported a system in which the STX aptamer is immobilized on gold nanoparticles and stabilized in a

G-quadruplex structure able to bind the Raman reporter crystal violet (**figure 51**). In the absence of the toxin, the reporter remains close to the nanoparticle surface, yielding a strong Raman signal. Upon binding of STX, the aptamer conformation is destabilized, crystal violet is released, and the Raman intensity decreases in a concentration-dependent manner. This variation in the spectral response allows sensitive and selective identification of the toxin, even in complex matrices such as shellfish extracts.

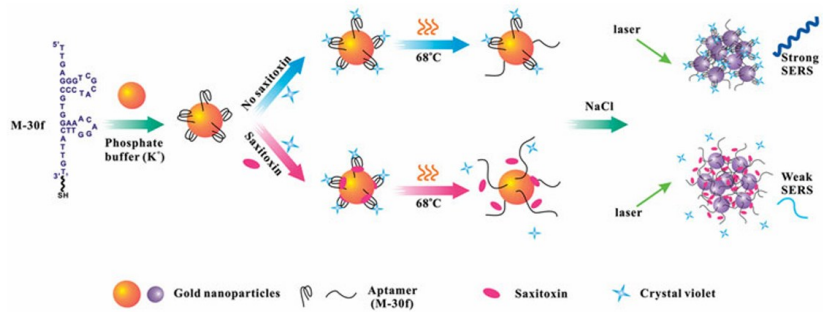

***Figure 51**. Principles of the SERS aptasensor for saxitoxin detection [122].*

In label-based systems, the aptamer is conjugated with optical probes such as fluorophores, nanoparticles, or quantum dots, which act as reporter elements. When STX binds, changes in fluorescence intensity, colorimetric shifts, or luminescence quenching can be observed. Examples include Fluorescence Resonance Energy Transfer (FRET) systems, in which the aptamer can be properly labelled at 3'- and 5'-ends so that its folding upon STX binding causes the changes in the distances between labellers causing an increase of fluorescence. Colorimetric assays based on gold nanoparticles represent another strategy. Dispersed nanoparticles exhibit a red colour, while aggregation induces a visible shift to blue. Gold colloids are intrinsically unstable and tend to aggregate in the presence of

salt (sodium chloride), but when the aptamers are adsorbed on their surface they act as stabilizers, keeping the suspension dispersed and red. When STX is present, its binding to the aptamer reduces the interaction with the nanoparticle surface. Therefore, the aptamers detach, the colloids aggregate, and the colour of the solution shifts from red to blue, producing an eye-visible response [123]. While the assay's simplicity supports field deployment, its susceptibility to ionic strength and protein interference requires sample pre-treatments to preserve its colloidal stability.

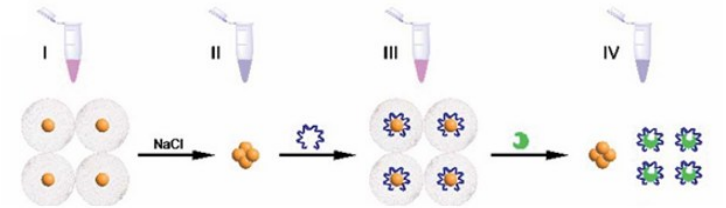

***Figure 52**. The detection scheme of colorimetric STX sensor based on Au NPs. (I) Dispersed Au NPs in the initial reaction system; (II) Au NPs aggregated with NaCl input; (III) Au NPs back to dispersion status after binding with aptamer; (IV) Au NPs aggregated after STX loading [123].*

4.6.2 Electrochemical systems

Electrochemical systems represent another consolidated and highly promising class of aptasensors for STX detection. Their basic principle is to translate the aptamer–toxin interaction into a measurable variation of current, potential, or impedance. The choice of conductive materials and the immobilization strategy of aptamers are crucial for sensitivity and stability.

Amperometric sensors measure the current that flows during redox reactions at the electrode surface. In these systems, the aptamer is immobilized on an electrode, often modified with nanomaterials to

increase surface area and conductivity. A redox probe, such as methylene blue (MB) or ferricyanide, is frequently employed. When STX binds to the aptamer, the aptamer undergoes a conformational change. This structural rearrangement influences how easily electrons can transfer between the redox probe and the electrode. As a result, the measured current decreases or increases in proportion to toxin concentration. A representative example is the work by Hou et al. [124] who developed an STX aptasensor on a gold electrode coated with carbon nanotubes and methylene blue (**figure 53**). Upon STX binding, the aptamer undergoes a conformational change that hinders electron transfer between MB and the electrode surface, resulting in a concentration-dependent decrease in electrochemical signal.

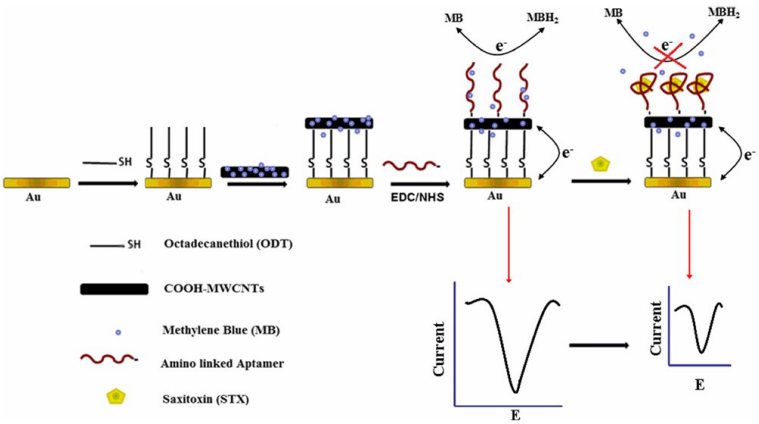

***Figure 53**. The schematic diagram of amperometric aptasensor for STX using a gold electrode modified with carbon nanotubes on a self-assembled monolayer, and MB as an electrochemical indicator probe [124].*

Impedimetric sensors measure changes in the interfacial properties of the electrode surface, focusing on charge transfer resistance (Rct). This is a label-free approach, since it does not require fluorescent tags or enzymatic

amplification. The basic principle is that aptamers are immobilized on the electrode surface, typically gold. When STX binds to the aptamer, the resulting aptamer–toxin complex acts as a physical barrier, reducing the access of redox species in solution to the electrode surface and this appears as an increase in the Rct in the impedance spectrum. One of the first applications to STX was reported by Serrano et al. [125] who immobilized thiolated aptamers on a gold electrode. The sensor showed clear increases in Rct upon STX binding and reached a detection limit of 1 nM. This system was selective and reproducible in aqueous samples, though further testing in complex food matrices is still required.

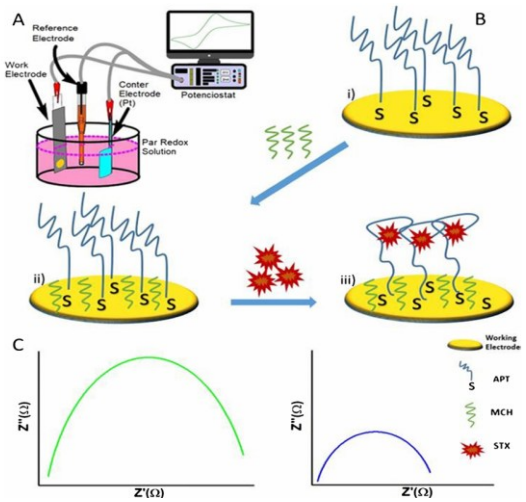

***Figure 54**. (**A**) Electrochemical system. (**B**) Principle of aptasensor operation. Device modification steps based on an APT for STX detection and (**C**) impedance curves of the biosensor steps [125].*

CHAPTER V

FROM IMMUNOASSAYS TO APTAMER-BASED ASSAYS: CHALLENGES AND PERSPECTIVES IN SAXITOXIN DETECTION

5.1 Introduction

The research line led by Dr. Monica Campàs at Institute of Agrifood Research and Technology (IRTA, in La Ràpita, Tarragona, Spain) has played a decisive role by systematically exploring a spectrum of assay architectures. The first advances were made with microplate assays inspired by ELISA [126]. In a conventional competitive immunoassay, the TTX is immobilized on the plate wells, and sample toxin (TTX free, in solution) competes with the immobilized one for antibody binding and the output signal decreases as TTX free concentration increases (**figure 55 A**). The strategy relied on coupling a dithiol–carboxyl self-assembled monolayer (SAM) to the maleimide groups on the plate surface. This bifunctional layer provided carboxyl termini that were then activated for covalent attachment of the TTX, avoiding the need for protein conjugates such as bovine serum albumin (BSA), which often introduce steric hindrance and nonspecific interactions. The result was a microplate-based mELISA capable of presenting the TTX in a controlled orientation, thereby enhancing antibody access and reducing background noise. The readout was colorimetric and relied on the HRP–TMB system. In this format, the enzyme horseradish peroxidase (HRP), linked to the antibody, catalyzes the oxidation of the chromogenic substrate tetramethylbenzidine (TMB) in the presence of hydrogen peroxide. This reaction generates a blue-colored product, which can be quantified spectrophotometrically and is proportional to the amount of antibody bound in the assay.

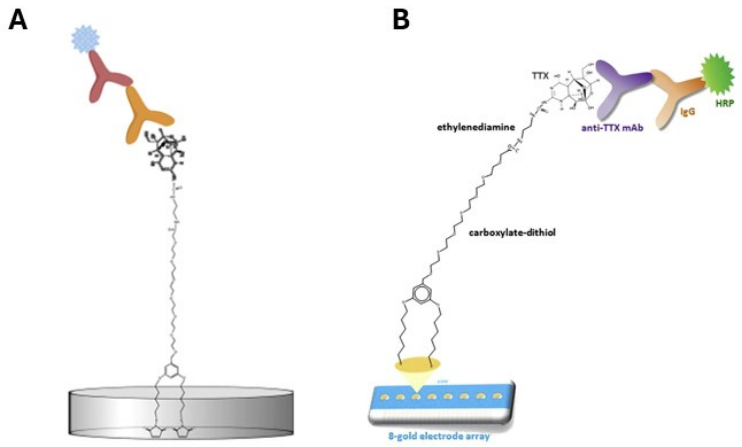

Figure 55. *Scheme of the mELISA configuration [126] (**A**) and electrochemical immunosensor array platform (**B**) for the detection of TTXs [127].*

The same chemistry was later transferred to gold electrodes (**figure 55 B**) [127]. Here, the competitive binding principle was unchanged: free TTX in the sample competed with immobilized TTX on SPGEs (screen-printed gold electrodes) for antibody binding. What changed was the way of detection. Instead of measuring color development, the recognition event was translated into an electrochemical signal recorded by chronoamperometry. When antibodies bound to the immobilized TTX, they carried enzyme labels (HRP) that catalyzes a redox reaction, generating a current whose intensity is proportional to number of binding events. This adaptation retained the advantages of oriented immobilization while enabling miniaturization, rapid response, and portable devices.

A further innovation was the use of magnetic beads (MBs) [128]. Instead of a static planar surface, the maleimide-activated beads provided for a suspension format with a much higher surface-to-volume ratio. MBs functionalization proceeded via cysteamine, whose thiol group reacts with the maleimide, leaving a primary amine free to couple with the TTX (often through formaldehyde-mediated reactions). Once functionalized, these

TTX–MB conjugates acted as mobile capture surfaces, offering rapid binding kinetics and the possibility of easy magnetic separation. Importantly, after the competitive binding step, the beads carrying the immunocomplex could be magnetically deposited onto carbon electrodes (Screen-printed carbon electrode) (**figure 56 A**), where the HRP-mediated signal was recorded. This hybrid approach combined the kinetic advantages of MBs-generated suspension assays with the sensitivity of electrochemical detection, while also improving matrix clean-up. The same chemistry was later reconfigured into a purely colorimetric format carried out entirely in solution (**figure 56 B**) [129]. Here, the MBs served simultaneously as immobilization supports and as separation tools. After competition between MBs-TTX and free TTX in the sample for antibody binding, the beads were simply magnetically isolated, washed, and incubated with HRP–TMB to generate the signal. This procedure eliminated the need for electrode integration and reduced assay time to less than two hours. Most importantly, bead-based suspension assays could cope effectively with complex shellfish matrices, achieving detection limits aligned with regulatory thresholds.

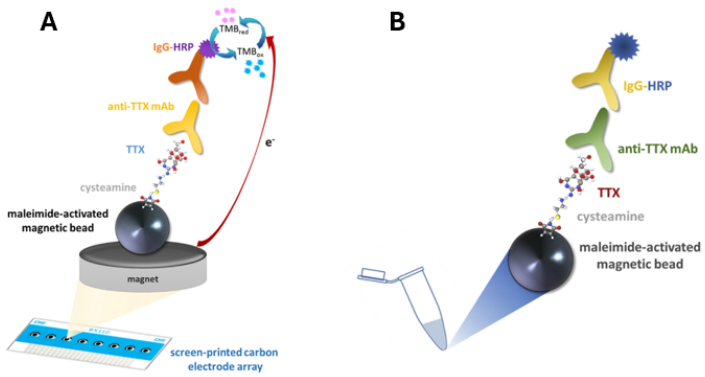

***Figure 56**. MB-based immunosensor (**A**) and colorimetric MB-based immunoassay (**B**) for the detection of TTXs [128] [129].*

Another conceptual step was the introduction of hybrid antibody–aptamer sandwich formats for the detection of TTX [130]. Small molecules like TTX are traditionally unsuitable for sandwich assays due to their limited size, but the combination of monoclonal antibodies with aptamers selected by capture-SELEX made it possible to create dual recognition. In this hybrid format, the monoclonal antibody immobilized on the plate captures the TTX, while the aptamer binds to a different region of toxin, thus forming an antibody–TTX–aptamer complex that enables the sandwich configuration. The readout was colorimetric (HRP–TMB), and the format was benchmarked against the previously established competitive assays, showing comparable sensitivity but with the added advantage of specificity through dual recognition. This innovation underlined the idea that different recognition elements can complement one another, overcoming classical limitations of single-element assays.

Finally, the same maleimide–thiol bead chemistry was adapted for the detection of STX (**figure 57**) [131]. The immobilization followed the cysteamine-mediated linkage onto maleimide MBs, but this time the target was a paralytic shellfish toxin of direct regulatory interest. The assay was validated in shellfish extracts, demonstrating detection limits well below safety thresholds and low susceptibility to matrix interference. Moreover, the STX–MB conjugates could be reused for several assay cycles, highlighting the robustness and practical potential of the approach. This application confirmed that the methodologies refined across different supports and recognition strategies could be directly transposed to STX, providing a screening tool consistent with monitoring needs.

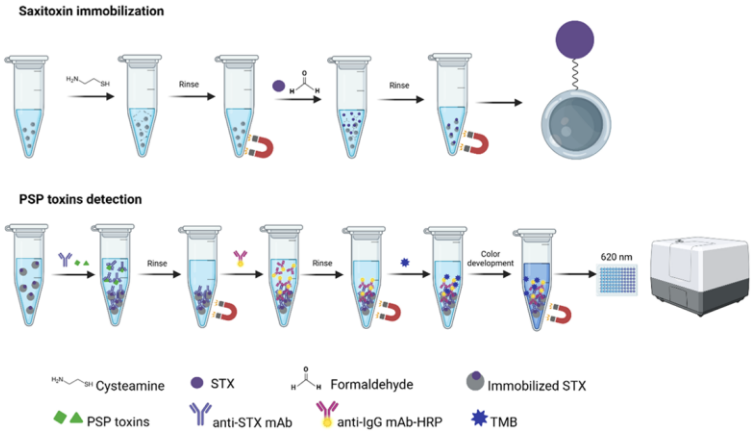

Figure 57*. Protocol for the STX immobilization on MB (top) and the PSP toxins detection with the colorimetric MB-based competitive immunoassay (bottom)[131].*

During my PhD visiting period at the Institute of Agrifood Research and Technology (IRTA), I had the opportunity to contribute to one of the research lines led by Dr. Mònica Campàs, dedicated to the development of detection assays for tetrodotoxin (TTX) in different analytical formats. In these assays, the biological recognition element had always been the antibody, with the only exception of the hybrid antibody–aptamer sandwich format, in which an aptamer specific for TTX was combined with the antibody to achieve dual recognition.

Building on this experience, I set out to investigate whether these assay architectures could be adapted for the detection of STX, employing aptamers specific for STX as the recognition element. This represented the first attempt to apply the same detection formats using aptamers, either alone or in combination with the antibody in a hybrid sandwich configuration. Such an approach required assessing their behaviour within the established immobilization chemistries and detection schemes. Although the study remained largely exploratory, it provided valuable insights into the practical challenges of implementing aptamer-based

strategies for this toxin and laid the groundwork for future developments aimed at fully exploiting their potential in marine toxin biosensing.

5.2 Results and discussion

In the present work, the assay formats described in the previous section were adapted by substituting the antibody with three different aptamer sequences specific for STX (STX1 [132], STX2 and STX3[133]: the sequences are reported in the Materials and Methods section). This modification required specific adaptations in both the immobilization and blocking strategies. The functionalization of maleimide-activated MBs was performed according to the same procedure previously established for TTX, replacing TTX with STX while keeping all other conditions unchanged [128], with specific modification to adapt the system for STX detection. Briefly, MBs were incubated with cysteamine, whose free thiol reacts with maleimide groups, leaving a terminal amine group available for coupling. The STX was subsequently conjugated, resulting in MB functionalized with STX (MB-STX). In parallel, a control was prepared by conjugating TTX, generating MB-TTX. The latter represented a particularly stringent control: unlike unmodified beads, MB–TTX present a surface with the same chemistry and steric environment but displaying a different toxin, thereby offering a more realistic benchmark for nonspecific binding of the aptamer. The chemical structures of both toxins are shown in **figure 58**.

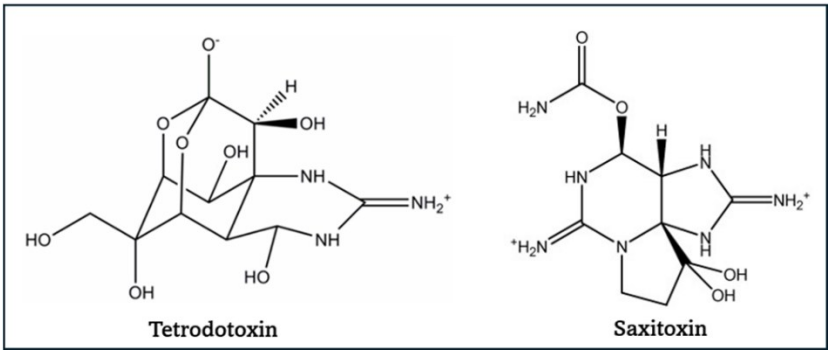

***Figure 58**. Schematic representation of the TTX and STX chemical structures.*

In previously reported immunoassays, nonspecific sites were blocked with bovine serum albumin (BSA).

First set of experiments: use of MBs functionalized with STX and ethanolamine as blocking agent

Since aptamers are much smaller recognition elements compared to antibodies, the use of a large protein such as BSA could hinder access to the immobilized toxin. For this reason, in this first step, ethanolamine was employed as a blocking reagent, to ensure sufficient coverage of reactive sites on MB surface while minimizing steric hindrance associated with the use of BSA. Once the immobilization and blocking were completed, assays were conducted in a competitive format: MB-STX was incubated with the STX-specific aptamers carrying a biotin unit at 5‘-end, in the absence or presence of free STX, followed by HRP–streptavidin affinity interaction, and colorimetric readout with TMB (**figure 59**).

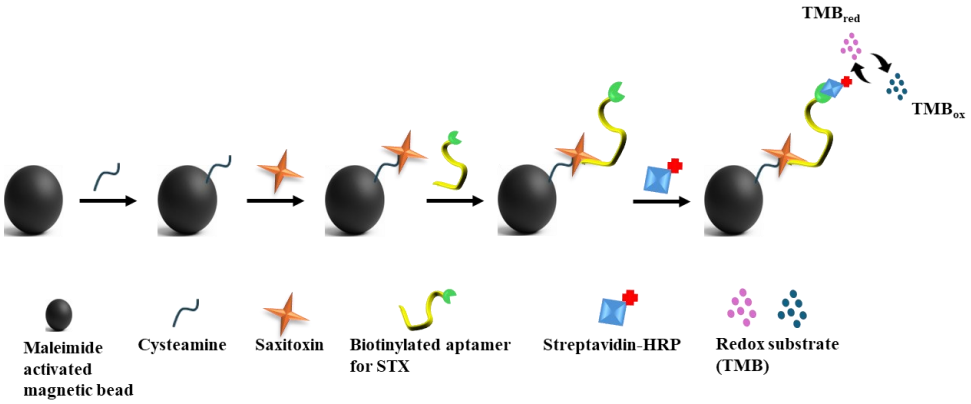

***Figure 59**. Schematic illustration of the colorimetric assay for STX detection using maleimide-activated magnetic beads.*

In this assay, the colorimetric signal originates from the species that remain bound to the MBs after the washing steps, as any unbound species are removed. When free STX is present in solution, it binds part of the aptamer molecules, reducing the fraction of free aptamer available to interact with the STX immobilized on the beads. As a result, fewer biotinylated aptamers are retained, leading to less HRP-streptavidin binding and consequently to a lower colorimetric signal. In contrast, in the absence of free STX, a larger number of aptamers bind to the immobilized STX, producing a stronger color response. Therefore, the measured signal is inversely proportional to the amount of free STX in solution.

Compared to the earlier MB-based assay developed for TTX, the present approach introduced several key modifications. In addition to the use of STX instead of TTX for bead functionalization, the blocking step with BSA was replaced by ethanolamine, which reacts with remaining maleimide groups on the bead surface to minimize nonspecific adsorption. Moreover, the antibody–antigen recognition system of the original immunoassay was substituted with a biotinylated aptamer-streptavidin-HRP detection cascade. In this configuration, the aptamer, through its

biotin moiety, binds to the streptavidin conjugated to HRP, which catalyzes a redox reaction of the chromogenic substrate TMB, producing a blue-colored compound measurable spectrophotometrically. However, the assay produced high background signals, even in controls lacking aptamers or in MB–TTX. These results suggested that the blocking strategy was insufficient and that nonspecific adsorption dominated the signal.

Second set of experiments: reintroduction of BSA as blocking agent

To better understand whether blocking was the critical factor, the same assay configuration was tested with the TTX aptamer D3, which had previously shown reliable performance in a sandwich format [130]. The blocking step was modified by replacing ethanolamine with BSA, following the procedure originally developed for the immunoassay with antibodies. After blocking, the competitive assay was carried out as previously described, incubating MB–TTX with the biotinylated D3 aptamer in the absence or presence of free TTX. In parallel, non-functionalized MBs (without TTX) were also prepared and tested under the same conditions. In these controls, the signal was expected to be close to zero, since the toxin immobilized on the bead surface represents the specific anchoring site required for aptamer binding and for the subsequent recruitment of the HRP-streptavidin complex responsible for color development. The results showed that the signal intensity was proportional to the concentration of aptamer used. However, this trend of signal dependence on aptamer concentration was observed for all MBs prepared (MBs without TTX, MB–TTX, and MB–TTX in the presence of free TTX) (**figure 60**). These findings suggest that the TTX-aptamer interacted non-specifically with bead surfaces rather than with the immobilized toxin.

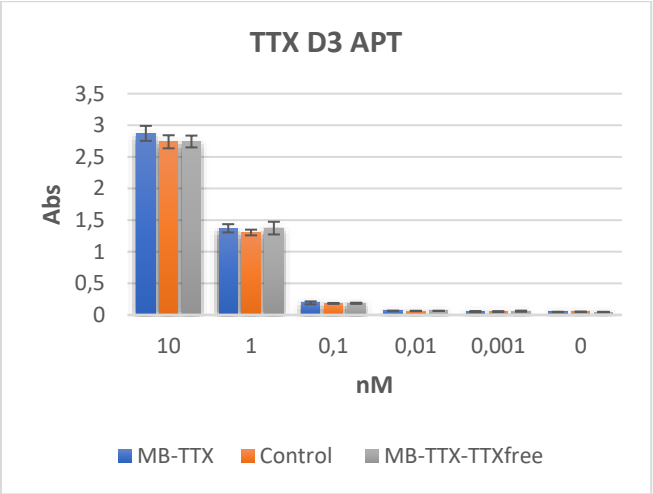

Figure 60. *Signal dependence on TTX-aptamer concentration. Blue bars correspond to MB–TTX (magnetic beads functionalized with TTX); orange bars represent the non-functionalized MBs (control); and green bars correspond to MB–TTX incubated with free TTX (competitive assay). A similar strong decrease in signal intensity with decreasing aptamer concentration was observed in all cases, indicating that the response was independent of both the presence of immobilized and free toxin, and suggesting a nonspecific interaction between the aptamer and the bead surface.*

Given the effective suppression of background noise achieved with BSA, the same blocking strategy was applied to MBs functionalized with STX in order to evaluate the binding specificity of the STX aptamers. The STX-specific aptamers APT1, APT2 and APT3 were incubated with both MB–STX and MB–TTX (used as control). The aim was to determine whether a positive signal would be obtained only with MB–STX, as expected if the aptamers specifically recognized the immobilized STX. However, the results showed that the signal intensity was similar for both MB–STX and MB–TTX and decreased proportionally with decreasing aptamer concentration (**figure 61**). This indicates that the response was not

governed by specific recognition of STX, but rather by a nonspecific interaction between the aptamers and the MB surface.

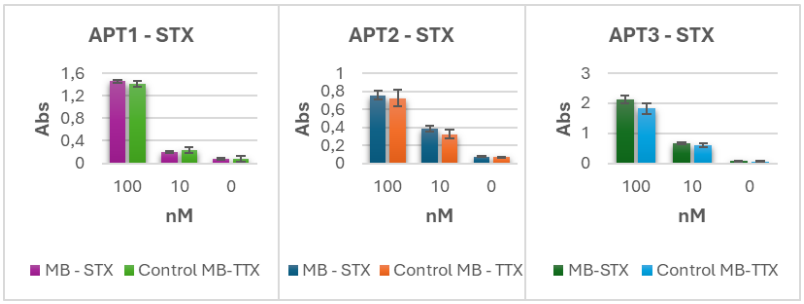

Figure 61. *Decrease in signal with reduced STX - aptamers concentration, also observed in MB functionalized with TTX (control).*

Third set of experiments: transfer of the assay on MaxiSorp plate.

To explore whether the issue was intrinsic to the beads themselves, the assay was transferred to MaxiSorp plate (**figure 62**). Immobilization chemistry followed the same cysteamine-based strategy, with STX linked to the plate surface. Here, however, no detectable signal was obtained in the presence of aptamers, regardless of whether free toxin was added for competition. The absence of any measurable response suggested that immobilization onto a static planar surface may have restricted the folding or accessibility of the aptamers, again preventing specific binding.

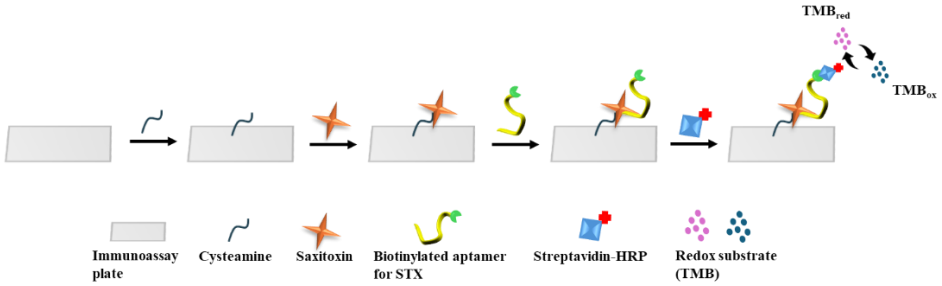

Figure 62*. Schematic illustration of the colorimetric assay for STX detection using maleimide-activated immunoassay plate.*

Fourth set of experiments: construction of a sandwich-type assay

Among the different strategies tested, particular attention was given to the possibility of constructing a sandwich-type assay. For small molecules like STX, such an approach is not straightforward, as the limited molecular size typically precludes simultaneous binding by two recognition elements. Nonetheless, earlier work on tetrodotoxin had demonstrated that combining monoclonal antibodies with aptamers could overcome this constraint, provided that the recognition elements were directed to distinct and accessible binding sites [130]. This gave a strong rationale for testing whether a similar dual-recognition strategy could be extended to STX.

The first configuration immobilized a monoclonal anti-STX antibody on microplate wells, creating a capture layer designed to selectively bind the toxin (**figure 63A**). This step was followed by a blocking treatment with BSA to minimize nonspecific interactions, after which STX was added to allow binding to the immobilized antibody. A biotinylated aptamer was then introduced as the secondary recognition element, with the expectation that it would engage the captured toxin and provide an accessible handle for HRP–streptavidin conjugated complex to generate the colorimetric readout. In principle, this arrangement mirrors classical sandwich immunoassays, with the critical difference that the detection element is a synthetic oligonucleotide rather than a second antibody.

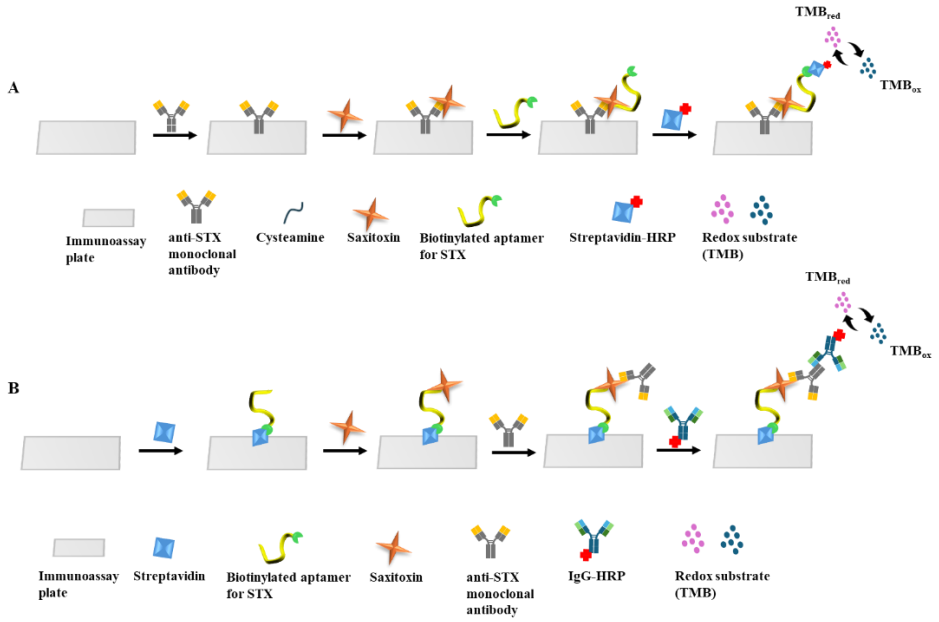

***Figure 63**. Hybrid antibody – aptamer assay for Detection of STX: (**A**) sandwich assay developed by Shkembi et al. adapted for saxitoxin, and (**B**) reverse method using plates functionalized with STX aptamer.*

Despite extensive optimization, varying aptamer concentration, testing both thermodynamically and kinetically annealed aptamers, and adjusting incubation conditions, this format did not produce a significant signal above background. The most plausible explanation is that once bound to the antibody, STX may not present the epitope in a conformation compatible with aptamer recognition, or that steric hindrance prevented the aptamer from effectively engaging the captured toxin. To explore whether inverting the recognition order could overcome this limitation, a second configuration was tested in which the aptamer acted as the capture element (**figure 63 B**). In this case, biotinylated aptamers were immobilized on avidin-coated plates, followed by the addition of STX. Detection was then carried out with a monoclonal anti-STX antibody, and subsequently an HRP-conjugated secondary antibody directed against the

primary antibody. In this design, the aptamer–toxin complex was expected to leave accessible binding sites for the antibody, while the secondary antibody provided the enzymatic amplification step needed for colorimetric readout. Once again, however, no appreciable signal was observed. Even at high aptamer concentrations and under carefully controlled conditions, the HRP–TMB reaction remained at the level of the negative controls. These results indicate that, unlike antibodies, aptamers may lose their recognition capacity when immobilized in particular orientations or when exposed to the steric constraints of surface-bound assays.

Critical Review on Aptamer-Based Biosensing Systems for Saxitoxin and Tetrodotoxin

In parallel with the experimental activities, I conducted a comprehensive critical review entitled *"Aptamer-Based Biosensing Platforms for Saxitoxin and Tetrodotoxin: Advances, Challenges, and Future Perspectives in Food Safety and Environmental Monitoring."*

This review was developed following the experimental work carried out at IRTA, with the aim of contextualizing the obtained results within the broader field of aptamer-based biosensing. The review provides an updated overview of recent progress in the detection of STX and TTX using aptamer-based recognition elements, discussing both the analytical advances achieved and the technological challenges that still hinder their application in real-world conditions. Emphasis was given to matrix effects, assay robustness, and the gap between proof-of-concept studies and field-deployable systems. The manuscript, co-authored with Dr. Mònica Campàs (IRTA), was accepted on *Talanta (Manuscript Number: TAL-D-*

*25-05736.*Dicember 2025) and reflects the critical perspective developed through this PhD research.

5.3 Conclusions

The research conducted at IRTA explored the development of aptamer-based assays for the detection of marine toxins, with a particular focus on STX. Through a combination of experimental work and critical analysis, the results have highlighted the limitations of using aptamers as alternative recognition elements to antibodies in practical biosensing formats.

Different assay configurations were examined, including colorimetric systems employing functionalized magnetic beads, competitive binding formats, and hybrid antibody–aptamer sandwich assays. Each of these approaches provided complementary information on how aptamers behave under varying immobilization and detection conditions. A recurring finding was that aptamer performance is highly sensitive to the physicochemical properties of the solid surface. Nonspecific adsorption to magnetic beads frequently interfered with specific saxitoxin recognition, emphasizing the importance of controlling surface chemistry and buffer composition to preserve aptamer functionality. Furthermore, another contributing factor to the observed results may be the immobilization of the toxin on a solid support, which could have influenced the spatial orientation and accessibility of the molecular regions targeted by the aptamers.

These observations underline a broader and well-recognized challenge in the field: the discrepancy between the conditions used during SELEX and those found in real analytical samples. Most reported saxitoxin aptamers have been evolved in simplified buffer systems that favour stable

secondary structures and efficient amplification, yet these conditions differ markedly from those of natural seawater or shellfish extracts. In such complex matrices, high ionic strength, organic matter, and competing ions can destabilize aptamer conformations and reduce binding affinity. Approaches such as Real-Sample-Assisted SELEX, where selection is performed directly in representative environmental or food matrices, therefore represent a promising direction to obtain aptamers with enhanced robustness and matrix tolerance.

Efforts to translate the hybrid antibody–aptamer sandwich format, previously demonstrated successfully for tetrodotoxin, were not successful in the case of saxitoxin. This outcome reflects the intrinsic difficulty of achieving dual recognition for small-molecule toxins, whose limited molecular size and few available binding sites restrict simultaneous interactions with two receptors. Nevertheless, the concept remains appealing, as combining the stability of antibodies with the versatility of aptamers could offer a path toward more specific and adaptable detection systems, provided that conformational integrity and spatial geometry are carefully optimized.

Although the assays developed in this work have not yet reached the selectivity and reproducibility required for reliable application, the research has clarified the main bottlenecks and provided a clear roadmap for improvement. Future work will be carried out to systematically investigate the influence of buffer composition, ionic strength, and annealing protocols on aptamer folding and stability. Special attention will be given to the role of specific ions, as monovalent and divalent cations can profoundly affect the folding pathway and stabilize distinct secondary and tertiary structures, such as G-quadruplexes or hairpin loops, which are critical for target recognition. Moreover, the aptamers employed in this

study originate from truncation processes previously reported in the literature to reduce sequence length; therefore, it is essential to evaluate how truncation impacts structural integrity and recognition ability. Indeed, the recognition capacity of truncated aptamers may not be evident in certain applications and could even prove detrimental in others, particularly where full structural complexity is required for high-affinity binding. Advanced structural and biophysical characterization techniques, such as circular dichroism spectroscopy, nuclear magnetic resonance, and high resolution mass spectrometry will be essential to elucidate conformational dynamics and interaction mechanisms, both for full-length and truncated aptamers, in relation to immobilization surfaces and the target toxin. These efforts will provide key insights for optimizing assay conditions and improving the reliability and sensitivity of aptamer-based detection platforms.

5.4 Materials and Methods

Reagents and solutions

Certified reference material of saxitoxin was obtained from Cifga (Lugo, Spain). TTX (purity ≥98% by HPLC) was purchased from Tocris Bioscience (Bristol, UK) and a standard solution was prepared at 1 mg/mL in 1% (v/v) acetic acid. The anti-STX monoclonal antibody (mAb) SAA0563 was purchased from Protegenix (Newark, USA). The anti-TTX monoclonal antibody TX-7F (mAb) was produced as described in Kawatsu et al. (1997). The saxitoxin-binding aptamer APT1 [132] (seq: 5'-TTG AGG GTC GCA TCC CGT GGA AAC AGG TTC ATT G-3'), APT2 [133](seq: 5'-CTC GGG GGC GCG GTT GAT CGG AGA GG-3'

Zhou et al. Toxins 2022, 14, 228) and APT 3 [133] (5'-TAG GTG CGT TTC ATA TGA ACT TTC GTG-3') were synthesized on an RNA/DNA Synthesizer (H-16, K&A Labs GmbH). The D3 TTX-binding aptamer (Shkembi et al., 2021) with a 5 ′-biotin was synthesized by Biomers.net (Germany). PureCube maleimide-activated MagBeads (MB) were obtained from Cube Biotech (Monheim, Germany). Cysteamine hydrochloride, formaldehyde solution, potassium phosphate dibasic, potassium phos phate monobasic, Tween® 20, ethylenediaminetetraacetic acid (EDTA), bovine serum albumin (BSA), anti-mouse IgG (whole molecule)-horseradish peroxidase antibody (IgG-HRP) (produced in rabbit) and 3,3 ′ ,5,5 ′-tetramethylbenzidine (TMB) liquid substrate were supplied by Sigma-Aldrich (Tres Cantos, Spain). Ultrapure Milli-Q water (18.2 MΩ/cm) was used to prepare the solutions (Millipore Ib´erica Ltd. Madrid, Spain). Glacial acetic acid, sodium chloride and hydrogen peroxide 30 % v/v reagent grade were obtained from Fluka (Zedelgem, Belgium). The aptamers were annealed prior to experiments. For thermodynamic annealing, APT1, APT2, and APT3 were heated at 90 °C for 5 min and then cooled slowly to room temperature overnight. APT1 was annealed in PBS buffer (10 mM phosphate buffer, 2.7 mM KCl, 137 mM NaCl, pH 7.4), while APT2 and APT3 were annealed in 20 mM Tris-HCl, 100 mM NaCl, 2 mM $MgCl_2$, 5 mM KCl, pH 7.5. As an alternative strategy, APT2 and APT3 were pretreated by heating at 95 °C for 10 min, cooling on ice for 5 min, and equilibrating at room temperature for 5 min.

Equipment

Magnetic separation was performed on a MagneSphere Technology Magnetic Separation Stand (for twelve 0.5-mL tubes) and a PolyATract System 1000 Magnetic Separation Stand (for one 15-mL or 50-mL tube)

from Promega Corporation (Madison, WI, USA). Colorimetric mea surements were performed with a Microplate Reader KC4 from BIO-TEK Instruments, Inc. (Winooski, VT, USA).

MB-based colorimetric assay

STX was covalently immobilized on maleimide-activated MB using a strategy similar to that used for the immobilization of tetrodotoxin Food and Chemical Toxicology 140 (2020) 1113) mediated by the reaction between the amino groups of cysteamine and STX, using formaldehyde. Briefly: (1) 10 μ L of maleimide-activated MB was transferred to a 1-mL tube and rinsed three times with 1 mL of washing buffer (0.1 M phosphate-buffered saline (PBS), 0.05 % v/v Tween® 20, pH 7.2) under vigorous mixing; for the washing steps, the tube was placed on a magnetic separation stand, and the washing solution was removed; (2) 1 mL of 1 mM cysteamine in binding buffer (0.1 M PBS, 10 mM EDTA, pH 7.2) was added and incubated for 2 h at room temperature; (3) after three washing steps, 1 mL of 2 μ g mL^{-1} STX solution in binding buffer containing 10 % v/v formaldehyde was added and incubated overnight at 4 ◦ C; (4) three washing steps were performed followed by blocking with 1 ml of ethanolamine 1 M or 1 ml of 1% w/v BSA in PBST for 30 min. The STX-coated MB were resuspended in 1 mL of binding buffer. When the amounts of MB varied, the volumes were adjusted proportionally.

The competitive assay was performed as follows: (5) 200 μL of the MB-STX conjugate was transferred into a 0.5 mL microtube and, once the supernatant was removed, 100 μL, 50 ng/ml of STX solution was added along with 100 μL, 100 nM of STX-aptamer in binding buffer (APT1in PBS buffer with 10 mM phosphate buffer, 2.7 mM KCl, 137 mM NaCl, pH 7.4; APT2, APT3 in 20 mM Tris- HCl, 100 mM NaCl, 2 mM MgCl2,

5 mM KCl, pH 7.5); the resulting mixture was incubated at room temperature for 1 h; (6) after three washing steps, 200 uL of a 1/2500 streptavidin-HRP dilution in 1 % w/v binding buffer-BSA was incubated for 30 min at room temperature; (7) three washing steps were performed and the complex was resuspended in 200 µL of binding buffer; (8) 50 µL of immunocomplex was transferred to a new 0.5-mL tube and after supernatant removal, 125 µL of TMB liquid substrate was added and incubated for 10 min; (9) the tube was placed on the magnetic separation stand and 100 µL of TMB liquid substrate was collected for colorimetric measurement at 620 nm in a microtiter plate. All incubation steps were performed under agitation. Measurements were performed in triplicate.

Colorimetric assay on maleimide plates

STX was covalently immobilized on maleimide-activated plate. Briefly: (1) 50 uL of 1 mM cysteamine in binding buffer (0.1 M PBS, 10 mM EDTA, pH 7.2) was added and incubated for 2 h at room temperature; (2) after three washing steps with 200 µL of PBST, 50 µL of 2 µg mL^{-1} STX solution in binding buffer containing 10 % v/v formaldehyde was added and incubated overnight at 4°C; (3) three washing steps were performed followed by blocking with 50 uL of 1% w/v BSA in PBST for 30 min.

The competitive assay was performed as follows: (4) once the supernatant was removed, 25 µL, 100 ng/ml of STX solution was added along with 25 µL, 500 nM of STX-aptamer in binding buffer (APT1in PBS buffer with 10 mM phosphate buffer, 2.7 mM KCl, 137 mM NaCl, pH 7.4; APT2, APT3 in 20 mM Tris- HCl, 100 mM NaCl, 2 mM MgCl2, 5 mM KCl, pH 7.5); the resulting mixture was incubated at room temperature for 1 h; (5) after three washing steps, 50 uL of a 1/1000 streptavidin-HRP dilution in 1 % w/v binding buffer-BSA was incubated for 30 min at room

temperature; (6) three washing steps were performed and 100 μL of TMB liquid substrate was added and incubated for 10 min followed by a colorimetric measurement at 620 nm. Measurements were performed in triplicate.

Hybrid Antibody - Aptamer Sandwich Assay

The sandwich assay described by Shkembi et al. was adopted for the detection of saxitoxin. Specifically, 50 μL of 5μg/mL anti-TTX monoclonal antibody in 50 mM carbonate buffer pH 9.4 was used to coat the wells of a MaxiSorp immunoassay plate overnight at 4 °C. The wells were washed three times with 200 μL of PBST, followed by blocking with 200 μL of 1% w/v BSA in PBST for 30 min. The wells were washed again and incubated with 50 μL of 100 ng/ml of STX in PBS for 1 h. After washing, 50 μL of 500 nM biotinylated aptamer in binding buffer was added and left to incubate for 1 h, followed by washing. Fifty microliters of 1/1000 SA-HRP dilution in PBST was then added, followed by a final incubation of 30 min and washing. The TMB substrate (50 μL) was added, and color development proceeded for 10 min followed by a colorimetric measurement at 620 nm. Measurements were performed in triplicate.

In the “reverse” assay format, the plates were functionalized with the avidine 50 μL of 1 μg/mL overnight at 4 °C. The wells were washed three times with 200 μL of PBST and incubated with 50 μL of biotinylated aptamers (500 or 1000 nM) for 1 h. After washing, the plates were incubated with 50 μL of anti-STX antibody (5 μg/mL) in 1% w/v BSA PBST for 1 h, following by washing. Fifty microliters of 1/1000 IgG-HRP dilution in PBST was then added, followed by a final incubation of 30 min and washing. The TMB substrate (50 μL) was added, and color

development proceeded for 10 min followed by a colorimetric measurement at 620 nm. Measurements were performed in triplicate.

CHAPTER VI

INTERLABORATORY VALIDATION OF THE APTAMER–ANTIBODY LATERAL FLOW ASSAY FOR TETRODOTOXIN

6.1 Introduction

Tetrodotoxin (TTX) is one of the most potent natural neurotoxins so far known. It has fascinated chemists, toxicologists, and marine biologists for decades due to its unique chemical structure, remarkable selectivity for voltage-gated sodium channels, and devastating effects on the human nervous system[134]. Initially identified in pufferfish (*Takifugu* spp.), TTX has since been detected in a variety of marine and terrestrial organisms, including blue-ringed octopuses, newts, crabs, gastropods, and bivalve molluscs. For many years, TTX poisoning was considered a regional problem limited to Indo-Pacific waters, where it caused frequent and sometimes fatal poisonings associated with the consumption of pufferfish. Indeed, *fugu* refers to the pufferfish, a delicacy in several Asian cuisines, while tetrodotoxin is the deadly neurotoxin found within it. The toxin is mainly concentrated in the liver, ovaries, and skin, and if the fish is improperly prepared, ingestion can result in severe intoxication characterized by numbness, paralysis, and death by asphyxiation [135]. In Japan, only specially licensed chefs are authorized to prepare *fugu* due to its extreme toxicity. There is currently no known antidote for TTX poisoning, and treatment remains primarily supportive, focusing on maintaining respiratory and cardiovascular function. However, over the past two decades, this paradigm has shifted. Tetrodotoxin and several of its analogues have been reported in temperate and even European marine environments, including the United Kingdom, Greece, and the Netherlands [138] [136]. The pufferfish, originating from the Red Sea, including *Lagocephalus sceleratus*, related to the infamous *fugu* of Japan, is one of the most harmful invasive species now present in the Mediterranean Sea [137]. Indeed, when the Suez Canal was opened 150

years ago, it brought many positive aspects for travel and trade. But it also opened a channel for the mass migration of invasive marine species from the Indo-Pacific region, with significant, and generally negative repercussions for the biodiversity of the sea basins concerned.

This unexpected geographical expansion has significant implications for seafood safety in regions where the toxin had never been considered to be a risk. The European Food Safety Authority [138] has recently recognized TTX as an emerging contaminant of concern, particularly in bivalves and gastropods, which represent an important component of the European diet.

Understanding tetrodotoxin requires an integrated approach that combines chemistry, microbiology, and analytical science. TTX is a small, hydrophilic heterocyclic compound with the molecular formula $C_{11}H_{17}N_3O_8$ and a molecular weight of 319.1 $g \cdot mol^{-1}$ [139]. Its structure is defined by a guanidinium group linked to a highly oxygenated carbon skeleton forming a 2,4-dioxaadamantane cage. This intricate three-dimensional scaffold gives the molecule both rigidity and polarity, allowing it to precisely interact with the narrow pore of voltage-gated sodium channels (Na_v). The TTX chemical behavior is characterized by high water solubility, thermal stability, and sensitivity to pH. Under acidic conditions, TTX exists as a mixture of interconverting species such as 4-epiTTX, 4,9-anhydroTTX, and a lactone form (**figure 64**) [140]. These equilibria complicate its chromatographic separation and quantitative determination. To date, more than twenty-five naturally occurring analogues have been reported, differing in hydroxylation or oxidation patterns [134]. The structural analogues can be grouped into four main categories: isomeric forms (e.g. 4-epiTTX), deoxy derivatives (e.g. 5,6,11-trideoxyTTX), oxidized analogues (e.g. 11-oxoTTX), and C11-nor derivatives (e.g. 11-norTTX-6(S)-ol). Tetrodotoxin itself presents a high

toxic potency (LD50 intraperitoneal in mouse = 10 ug/kg body weight). Each analogue displays different toxic potency (**Table 5**) making necessary to identify individual analogues for a correct risk assessment. The coexistence of closely related molecules in biological matrices represents a major analytical challenge, as many share identical mass spectrometry (MS)-formed fragments and retention times on liquid chromatography (LC) systems. For this reason, analytical techniques must provide both high chromatographic resolution and accurate and selective mass detection to reliably distinguish among TTX analogues.

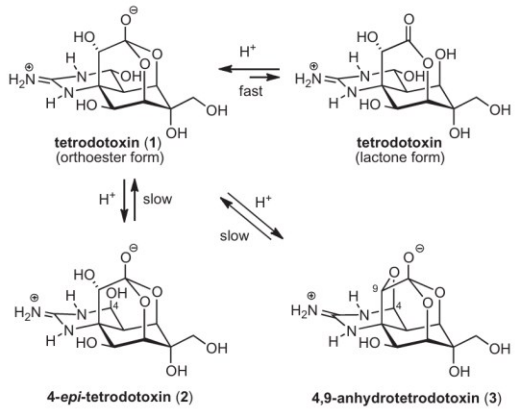

***Figure 64**. TTX (**1**) and its equilibrium with its analogues [140].*

The origin of tetrodotoxin has long been debated. It is now generally accepted that the toxin is synthesized not by the animals in which it accumulates but by symbiotic or free-living marine bacteria. Bacterial genera such as *Vibrio*, *Pseudoalteromonas*, *Pseudomonas*, *Shewanella*, and *Bacillus* have been identified as potential TTX producers, either inhabiting host tissues or existing freely in marine sediments and planktonic communities [141]. These microorganisms are thought to enter marine food webs through microbial association, biofilm formation, or

ingestion, leading to accumulation in organisms that set higher in the trophic chain. Environmental parameters strongly influence TTX production and accumulation. Seasonal variations, particularly rising seawater temperatures, appear to correlate with higher toxin levels, possibly due to enhanced bacterial growth or changes in host metabolism.

Compound	Parameter	RP	Molecular weight	Reference
	i.p. LD_{50} (μg/kg bw)			
TTX	**10**	**1**	319.1	see Table 7, Kao and Fuhrman (1963)
***11-deoxyTTX*[c]**	**70**	**0.14**	303.1	Yasumoto et al. (1988)
6-epiTTX[c]	60	0.17	319.1	Yasumoto et al. (1988)
11-norTTX-6(S)-ol[e]	**54**	**0.19**	289.1	Yotsu et al. (1992)
5-deoxyTTX[c]	970	0.01	303.1	Satake et al. (2014)
	i.p. $LD_{100/99}$[a] (μg/kg bw)			
TTX	**12**	**1**	319.1	Kao and Fuhrman (1963)
***11-oxoTTX*[c]**	**16**	**0.75**	335.1	Yotsu-Yamashita and Mebs (2003)
11-norTTX-6(R)-ol[c]	**70**	**0.17**	289.1	Endo et al. (1988)
	i.p. Lethal potency (MU/mg)			
TTX	**4,500**	**1**	319.1	Nakamura and Yasumoto (1985)
4,9-anhydroTTX[d]	**92**	**0.02**	301.1	Nakamura and Yasumoto (1985)
4-epiTTX[d]	**710**	**0.16**	319.1	Nakamura and Yasumoto (1985)
	i.p. MLD[b] (μg/kg bw)			
TTX	**8**	**1**	319.1	Kao and Fuhrman (1963)
5,6,11-deoxyTTX[f]	**750**	**0.01**	271.1	Yotsu-Yamashita et al. (1995)
	i.v. MLD[b] (μg/kg bw)			
TTX	**8**	**1**	319.1	Tsuda et al. (1964)
Tetrodonic acid[g]	> 300,000	0.00	319.1	Tsuda et al. (1964)
	i.p. IC_{50} (μg/kg bw)			

Table 5. Lethal doses and relative potencies (RPs) for TTX and some of its analogues in mice [138].

Associations between TTX and certain phytoplankton blooms, such as *Prorocentrum minimum*, have also been observed, suggesting a more complex ecological interplay between bacterial symbionts and primary producers [142]. Surveillance studies conducted between 2013 and 2016 revealed the presence of TTX in several European shellfish species, with concentrations ranging in mussels and oysters from 10 to over 200 $\mu g \cdot kg^{-1}$ of tissue [138]. Although these values are generally below the level considered likely to cause acute effects in humans (see below), they demonstrate that TTX contamination is no longer restricted to tropical

regions and may become more prevalent under changing climatic conditions.

TTX acts by binding to the outer pore of voltage-gated sodium channels (Na_v) on excitable membranes. As a result sodium influx is blocked already at nanomolar levels [114]. This blockage prevents depolarization and propagation of action potentials, leading to paralysis of muscles while leaving consciousness intact. Without immediate respiratory support, death may occur due to respiratory and cardiac failure [141]. The minimum lethal dose has been estimated at about 2 mg per person, equivalent to roughly 40 $\mu g \cdot kg^{-1}$ body weight for a 50-kg adult, although serious effects have been reported at much lower doses (EFSA, 2017). As a result, EFSA suggested a thresholds of TTX in seafood corresponding to 44 ug/kg of shellfish.

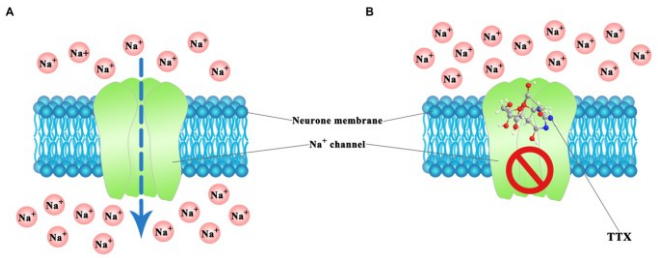

Figure 65. *Schematic figurative representation of the Nav channels in a neuronal cell membrane. (**A**) Normal Na^+ ion flux through the pores; (**B**) Nav channel blocked by TTX molecules [120].*

Analytical chemistry plays a crucial role in understanding and managing the risks associated with tetrodotoxin. Bioassays were the first methods to be developed for the detection of several groups of marine toxins, including TTX-group of toxins, by assessing their toxic effects in biological systems. The mouse bioassay (MBA), which involves intraperitoneal injection followed by mortality recording, has long been used as official method in many countries, and still is in some of them.

However, concerns about ethical implications, low specificity, and variable reproducibility have driven the search for alternative methods [143]. Among cell-based approaches, the Neuro-2a cell-based assay (CBA) utilizes murine neuroblastoma cells to detect TTX by measuring the inhibition of VGSCs [144]. In this assay, Neuro-2a cells are co-exposed to ouabain and veratridine, which synergistically induce cytotoxicity by disrupting sodium homeostasis. The presence of VGSC-blocking toxins inhibits this cytotoxic effect, resulting in a dose-dependent increase in cell viability. Thus, the assay indirectly quantifies toxin activity by measuring the protective effect against OV-induced toxicity [145]. While this assay has shown high sensitivity, it is not devoid of limitations. For instance, the presence of other marine toxins such as palytoxin can modify membrane potential in ways that complicate data interpretation, thereby reducing assay specificity [117]. On the other hand, TTX share with saxitoxins the molecular target, Nav channels, which might result into toxin interference when N2a assay is performed to analyze samples where both STXs and TTXs are contained, as recently reported to occur in the Mediterranean area [148] [146]. In addition, matrix interference represent a significant challenge when cell-based assays are used. Automated Patch Clamp (APC) systems have been developed for TTX [144][147] using Neuro-2a cells. In this automated device, in which a single cell is immobilized on a chip, the membrane potential is precisely controlled, and ionic currents are recorded. APC has been extensively employed in the pharmaceutical industry and is now being adapted as a bioanalytical tool for sample screening and toxin quantification purposes in marine toxin field. The introduction of liquid chromatography coupled with tandem mass spectrometry (LC–MS/MS) has transformed TTX analysis. This technique enables both identification and quantification of individual

analogues with high sensitivity and selectivity. Typical limits of detection range from 0.5 to 5 $\mu g \cdot kg^{-1}$, and limits of quantification from 1 to 25 $\mu g \cdot kg^{-1}$ in shellfish tissue [148][149]. Hydrophilic interaction liquid chromatography (HILIC) is particularly suited to TTX due to its strong polarity, and when combined with multiple reaction monitoring (MRM) experiments in positive electrospray ionization mode, it provides robust and reproducible quantification. High-resolution mass spectrometry (HRMS) further enhances confidence in identification by delivering accurate mass and isotope pattern information [150]. Nevertheless, analytical challenges persist. The scarcity of certified reference materials, instability of certain analogues, and matrix effects in seafood samples limit inter-laboratory comparability. Ongoing research focuses on the harmonization and inter-laboratory validation of LC–MS methods for TTX analysis, with particular attention to the development of isotopically labelled internal standards and the future integration of multi-toxin LC–MS approaches combining TTXs with saxitoxins to enhance analytical efficiency and inter-laboratory comparability[146], [151].

Immunoassays and immunosensors have been extensively explored for the detection of TTX, offering high specificity and low detection limits. These platforms exploit antibodies that may cross-react with multiple congeners within the toxin family, depending on the structural similarity of epitopes. This cross-reactivity can be advantageous when broad-spectrum detection is needed but poses challenges when detecting analogues of differing toxicological relevance [129], [130][152]. Ideally, cross-reactivity should correlate with the toxicological potency of each congener, allowing the immunosensing approach to reflect the true hazard posed by the sample. This approach aligns with the concept of Toxicity Equivalency Factors (TEFs), which are used to express the relative toxicity of congeners with

respect to a reference compound. When antibodies do not reflect these toxic equivalencies either by over or under reacting with certain analogues, quantification becomes less reliable [126].

6.2 Lateral Flow Immuno-Assay

Given the previously discussed advantages and limitations of immunoassays, lateral flow immunoassays (LFIAs) have emerged as one of the most practical ways to translate antigen–antibody recognition into a rapid, field-deployable testing format. In a LFIA, the liquid sample migrates through a laminated strip consisting of a sample pad, a conjugate pad containing the labeled biorecognition element, a nitrocellulose membrane with defined test and control lines, and an absorbent pad. As the sample flows, specific binding events occur along the strip, producing a visually detectable signal within minutes [153], [154]. Depending on the detection setup, the output can be qualitative, semi-quantitative [155], or fully quantitative [156] when a calibrated reader is employed. This approach is often required for complex sample matrices such as shellfish extracts. From an immunochemical perspective, two main assay formats are commonly employed. Sandwich LFIAs rely on two distinct binding events and are therefore suited to multiepitope targets such as proteins, generating a signal that increases with analyte concentration (signal-on). In contrast, competitive LFIAs are used for detection of small molecules that possess only a single epitope. In this format, the native analyte competes with an immobilized hapten–carrier conjugate for a limited number of labeled antibodies, causing the test-line intensity to decrease as analyte concentration rises (signal-off). The selected format determines

not only the direction of the signal but also the calibration strategy and the way matrix effects influence the measurement [157].

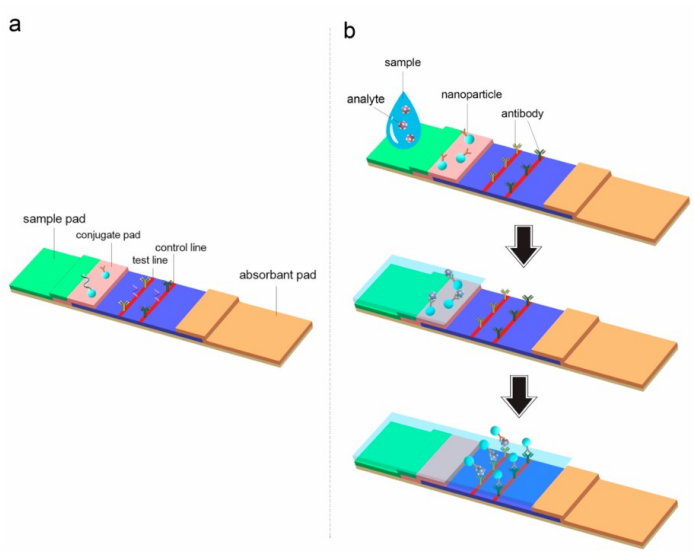

***Figure 66**. (**a**) Schematic illustration of a typical LFA and its main components. (**b**) The assay begins by adding a liquid sample containing target analytes, which bind to nanolabeled detection probes. As the sample flows, these complexes attach to capture probes at the test line (positive result) and the control line (proof of validity) [157].*

The analytical performance of an LFIA results from the interplay between transport and reaction kinetics. Since capillary flow limits the time that the sample spends at the test line, binding is generally less complete than in a benchtop immunoassays. As a result, sensitivity can be lower unless flow dynamics and reaction conditions are optimized. Modern strip designs address this limitation by tailoring the flow profile, using geometric constrictions, delayed-flow layers, or chemical barriers, to slow wicking and extend contact time [158]. Such modifications have been shown to enhance test-line intensity and reduce the limit of detection. In this immunoassay, the choice of label and readout directly determines how

efficiently a molecular binding event is converted into an analytical signal. Colloidal gold remains the standard because it combines straightforward bioconjugation with excellent stability and low production costs, enabling reliable visual detection by the naked eye. Signal generation, however, is only part of the equation. Efficient capture at the test line determines how much of that signal is accumulated where it matters. Passive adsorption of antibodies onto nitrocellulose is simple but leads to random orientations, which reduces effective binding and increases nonspecific background [159]. Performance improves when receptor immobilization is oriented and spaced more precisely, for example, through Protein A/G domains or biotin–streptavidin systems, so that Fc (fragment crystallizable) regions are directed away from the surface and Fab (fragment antigen-binding) domains remain accessible to the target. Likewise, nanostructured capture zones (such as electrospun nanofibers, graphene-oxide coatings, or mesoporous films) increase surface area, slow local flow, and concentrate recognition events, yielding steeper calibration curves and lower detection limits without additional antibody consumption [160]. Transitioning from qualitative to quantitative LFIA depends less on the strip itself than on standardizing readout and calibration. Portable readers, from compact scanners to smartphone-based systems with controlled illumination, stabilize image capture, correct background variation, and linearize the response. This not only reduces false negatives near decision thresholds but also shortens analysis time, as the reader can monitor signal formation in real time instead of waiting for a fixed endpoint.

A recent study employed a lateral flow assay for the rapid and visual detection of TTX using an innovative aptamer–antibody sandwich configuration [152]. This work represents an important advancement in the development of sensitive, low-cost, and easy-to-use analytical tools for

toxin monitoring in seafood and in environmental samples. Specifically, a previously established microplate-based hybrid aptamer–antibody assay was successfully translated into a one-step LFA format. The system relies on an aptamer immobilized on a nitrocellulose membrane combined with an anti-TTX antibody conjugated to gold nanoparticles (AuNPs) serving as a visual reporter. In the presence of TTX, the toxin bridges the antibody and the aptamer, forming a sandwich complex that produces a distinct red band on the test line. Experimental parameters were systematically optimized, including the aptamer concentration, membrane characteristics, conjugate composition, and capillary flow materials, resulting in robust and reproducible performance. The assay achieved a visual limit of detection (LOD) of 0.3 ng/mL in buffer, corresponding to 0.78 mg TTX per kg of tissue, with intra- and inter-assay variation below 13%.

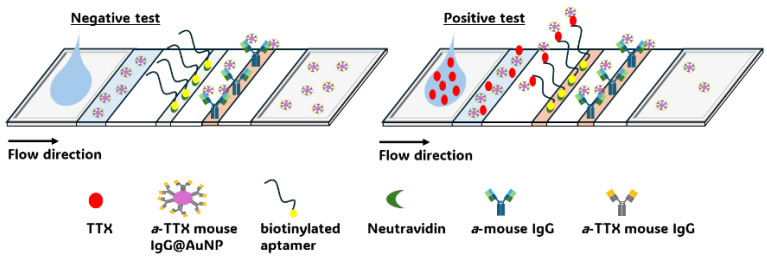

***Figure 67**. Schematic representation of the aptamer–antibody hybrid LFA for TTX.*

Importantly, the LFA exhibited no cross-reactivity with other marine toxins, such as saxitoxin (STX), domoic acid (DA), okadaic acid (OA), brevetoxin (PbTx-2), and ciguatoxin (CTX1B), which are often co-extracted from marine organisms with TTX under the extraction procedures commonly used for lipophilic and hydrophilic toxins. A stability assessment demonstrated that the device retained its functionality for over four years of storage at 4 °C, confirming its suitability for long-

term storage and field use. When applied to naturally contaminated pufferfish tissues, the results showed excellent agreement with those obtained by LC–MS/MS and cell-based assays, validating the accuracy and reliability of the LFIA for real-sample analysis.

This study reports the first colorimetric "signal-on" LFA employing a hybrid aptamer–antibody sandwich format for TTX detection. Compared with conventional competitive LFAs, this signal-on design simplifies result interpretation while enhancing sensitivity and assay robustness. The test can detect toxin concentrations well below current regulatory safety limits, offering an effective and portable platform for seafood safety monitoring and environmental surveillance.

6.3. Interlaboratory Validation of the Aptamer–Antibody Lateral Flow Assay for Tetrodotoxin

6.3.1 Background and Objectives

As described in the previous section, the aptamer–antibody LFA developed by the *Interfibio Research Group* (University Rovira i Virgili, Spain) represents the first colorimetric "signal-on" LFIA for the detection of TTX. The assay integrates a TTX-specific DNA aptamer immobilized on a nitrocellulose membrane with an anti-TTX antibody conjugated to gold nanoparticles, enabling rapid, visual toxin detection through the formation of a sandwich complex. This hybrid format offers enhanced sensitivity and robustness compared to traditional competitive LFAs, allowing visual detection well below current regulatory limits for seafood safety.

To further demonstrate the reproducibility and robustness of this innovative analytical platform, an interlaboratory validation study (Ring

Test) was organized in 2025 by the Interfibio Research Group in collaboration with the Hellenic Centre for Marine Research (HCMR, Greece) and the Institute of Agrifood Research and Technology (IRTA, Spain), where I spent my PhD visiting period abroad. The trial involved 26 participating laboratories from different countries and was designed to evaluate the consistency of the LFA's performance under realistic working conditions, using standardized materials and protocols.

In this context, I participated in the study as an operator within Laboratory ID L09 (University of Naples, Italy), performing a complete series of tests in accordance with the official *TTX LFA Ring TestManual*.

6.3.2 Materials and Kit composition

Each participant received a standardized TTX LFA validation kit, identical across laboratories, containing all reagents and materials required for the test. The package included:

- 61 LFA test cassettes, divided into:

Pack 1: 2 tests for practice;

Pack 2: 12 tests for calibration;

Pack 3: 42 tests for unknown samples;

Pack 4: 5 spare tests for troubleshooting.

- Practice samples (PS1, PS2);
- Six calibrators (CAL1–CAL6) of known TTX concentration;
- Forty-two blinded unknown samples (S01–S42);
- A color intensity reference card;
- Instruction manual.

Upon receipt, the materials were inspected, and temperature-sensitive components were stored according to the protocol: -20 °C for samples and 4 °C for test cassettes. Before testing, all vials were thawed at room

temperature (20-25 °C) for at least 30 minutes and vortexed for 5-10 seconds to ensure homogeneity.

6.3.3 Experimental Setup

All analyses were conducted on July 8th, 2025, at the Department of Pharmacy, University of Naples Federico II, under controlled laboratory conditions (T = 25–27 °C; RH = 53–58%). The workstation was arranged according to the interlaboratory protocol: clean working area, calibrated pipettes, vortex mixer, analytical balance, gloves, timer, and uniform white lighting for image acquisition (**figure 68**).

***Figure 68**. Workstation setup*

Prior to starting the tests, the P200 micropipette was checked gravimetrically using distilled water. The average dispensed mass was 0.151 ± 0.008 g for nominal 150 µL aliquots, confirming accurate volume delivery (relative error ≈ 1%).

6.3.4 Test procedure

Each assay was carried out according to the standardized protocol distributed to all participating laboratories:

- Thaw the sample at room temperature and vortex for 5–10 s;
- Using a calibrated pipette, dispense 150 µL of sample dropwise into the sample window “B” of the LFA cassette, avoiding contact with the strip surface;
- Start the timer immediately and allow the reaction to proceed for 30 min at room temperature;
- After incubation, place the strips on a white A4 background together with the color intensity scale card;
- Capture a top-down photograph (≈20 cm distance) under diffuse white light to document the results.

This uniform workflow ensured that all laboratories operated under comparable conditions, minimizing procedural variability.

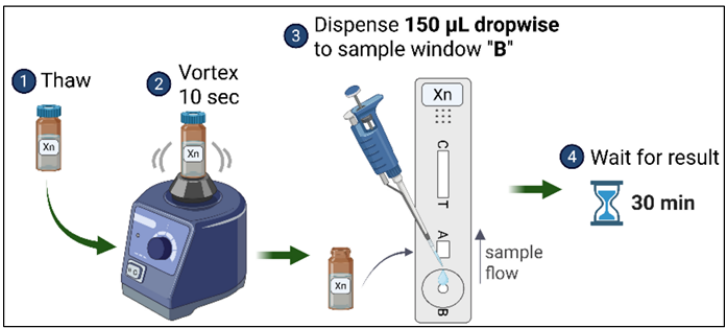

Figure 69. *Schematic representation of the operational steps.*

6.3.5 Practice and Calibration Step

Before testing the unknowns, two practice samples (PS1, PS2) were analyzed to familiarize with the test format and signal interpretation. Both assays produced valid control lines and expected test-line intensities.

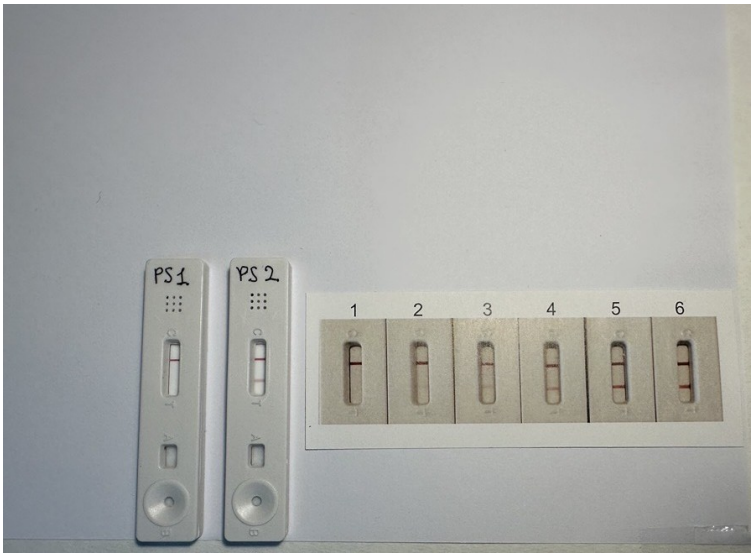

Figure 70. *Results of practice batch*

Subsequently, the six calibrators (CAL1–CAL6) were analyzed to generate a visual intensity scale corresponding to known TTX concentrations.

In my experience, slight deviations were observed between the experimental line intensities and those of the reference color card. Therefore, a semi-quantitative scoring system (from 1 to 4) was introduced for internal consistency:

- Score 1 = no visible test line
- Score 2 = faint but discernible line
- Score 3 = moderate line
- Score 4 = strong line

This approach allowed a reproducible qualitative comparison across all sample sets.

Figure 71. *Results of CAL1a–CAL6a tests.*

6.3.6 Analysis of Unknown Samples

The 42 blinded unknown samples (S01–S42) were analyzed sequentially in four batches, following the same procedure:

- Batch 1: S01–S10
- Batch 2: S11–S20
- Batch 3: S21–S31
- Batch 4: S32–S42

Between batches 2 and 3, the six calibrators were re-tested (CAL1b–CAL6b) to confirm assay stability over time. Again, test lines did not match expected color card intensities and the same semi-quantitative scoring system was adopted.

For each batch, photographs were taken showing unknown samples, and the color reference card on the same sheet, ensuring accurate comparison and traceability.

Throughout the experiment, no irregularities were observed (e.g., smearing, uneven background, timing deviations, or pipetting errors). Control lines appeared consistently, confirming that all assays were valid.

Figure 72. *Results of batch 1*

Figure 73*. Results of batch 2*

Figure 74*. Results of Batch 3*

Figure 75. *Results of Batch 4*

6.3.7 Data Documentation and Submission

Each batch was accompanied by the corresponding evaluation sheet, containing sample IDs, qualitative test interpretation, and comments. The complete dataset was then submitted to the coordinating laboratory (URV) for centralized statistical analysis and interlaboratory comparison.

Sample	**Date** (08072025)	**Environmental conditions** (ºC, % RH)*	**Test result** (positive, negative, invalid)	**Test Line Score 1-4** (1-6 cc)	**Control Line Visible** (Yes/No)	**Comments/ observations**
PS1	08/07/2025	25°C, 57% RH	negative	1 (1 cc)	Yes	
PS2	08/07/2025	25°C, 57% RH	positive	3 (4 cc)	Yes	
CAL1a	08/07/2025	25-26°C, 58% RH	negative	(1 cc)	Yes	Calibrants did not match color card (cc); all samples were evaluated using the alternative scoring scale (1-4), with color card assessments shown in brackets (1-6cc).
CAL2a	08/07/2025	25-26°C, 58% RH	negative	(1 cc)	Yes	
CAL3a	08/07/2025	25-26°C, 58% RH	positive	(1-2 cc)	Yes	
CAL4a	08/07/2025	25-26°C, 58% RH	positive	(4 cc)	Yes	
CAL5a	08/07/2025	25-26°C, 58% RH	positive	(2-3 cc)	Yes	
CAL6a	08/07/2025	25-26°C, 58% RH	positive	(5-6 cc)	Yes	
S01	08/07/2025	25-26°C, 56% RH	positive	3 (4 cc)	Yes	
S02	08/07/2025	25-26°C, 56% RH	positive	3 (4 cc)	Yes	
S03	08/07/2025	25-26°C, 56% RH	negative	1 (1 cc)	Yes	
S04	08/07/2025	25-26°C, 56% RH	negative	1 (1 cc)	Yes	
S05	08/07/2025	25-26°C, 56% RH	positive	4 (4-5 cc)	Yes	
S06	08/07/2025	25-26°C, 56% RH	positive	2 (2-3 cc)	Yes	
S07	08/07/2025	25-26°C, 56% RH	negative	1 (1 cc)	Yes	
S08	08/07/2025	25-26°C, 56% RH	positive	3 (3-4 cc)	Yes	
S09	08/07/2025	25-26°C, 56% RH	positive	2 (2 cc)	Yes	
S10	08/07/2025	25-26°C, 56% RH	positive	2 (1-2 cc)	Yes	
S11	08/07/2025	25-26°C, 56% RH	positive	2 (1-2 cc)	Yes	
S12	08/07/2025	25-26°C, 56% RH	positive	2 (3 cc)	Yes	
S13	08/07/2025	25-26°C, 56% RH	positive	3 (4 cc)	yes	
S14	08/07/2025	25-26°C, 56% RH	negative	1 (1 cc)	Yes	
S15	08/07/2025	25-26°C, 56% RH	positive	2-3 (3 cc)	Yes	
S16	08/07/2025	25-26°C, 56% RH	positive	2 (2 cc)	Yes	
S17	08/07/2025	25-26°C, 56% RH	positive	3 (4 cc)	Yes	
S18	08/07/2025	25-26°C, 56% RH	negative	1 (1 cc)	Yes	
S19	08/07/2025	25-26°C, 56% RH	positive	3-4 (4-5 cc)	Yes	
S20	08/07/2025	25-26°C, 56% RH	positive	2 (2 cc)	yes	
CAL1b	08/07/2025	25°C, 58% RH	negative	(1 cc)	Yes	
CAL2b	08/07/2025	25°C, 58% RH	negative	(1 cc)	Yes	Calibrant did not match color card
CAL3b	08/07/2025	25°C, 58% RH	positive	(2-3 cc)	Yes	Calibrant did not exactly match color card
CAL4b	08/07/2025	25°C, 58% RH	positive	(4 cc)	Yes	

CAL5b	08/07/2025	25°C, 58% RH	positive	(3-4 cc)	Yes	Calibrant did not exactly match color card
CAL6b	08/07/2025	25°C, 58% RH	positive	(5-6 cc)	Yes	Calibrant did not exactly match color card
S21	08/07/2025	25°C, 53% RH	positive	1-2 (1-2 cc)	Yes	
S22	08/07/2025	25°C, 53% RH	positive	2 (2-3 cc)	Yes	
S23	08/07/2025	25°C, 53% RH	negative	1 (1 cc)	Yes	
S24	08/07/2025	25°C, 53% RH	negative	1 (1 cc)	Yes	
S25	08/07/2025	25°C, 53% RH	positive	1-2 (1-2 cc)	Yes	
S26	08/07/2025	25°C, 53% RH	positive	3-4 (4 cc)	Yes	
S27	08/07/2025	25°C, 53% RH	negative	1 (1 cc)	Yes	
S28	08/07/2025	25°C, 53% RH	positive	3 (4 cc)	Yes	
S29	08/07/2025	25°C, 53% RH	negative	1 (1 cc)	Yes	
S30	08/07/2025	25°C, 53% RH	negative	1 (1 cc)	Yes	
S31	08/07/2025	25°C, 53% RH	positive	2 (1-2 cc)	Yes	
S32	08/07/2025	25°C, 53% RH	positive	2 (2 cc)	Yes	
S33	08/07/2025	25°C, 53% RH	positive	1-2 (1-2 cc)	Yes	
S34	08/07/2025	25°C, 53% RH	positive	3 (4 cc)	Yes	
S35	08/07/2025	25°C, 53% RH	positive	4 (4-5 cc)	Yes	
S36	08/07/2025	25°C, 53% RH	positive	2 (2-3 cc)	Yes	
S37	08/07/2025	25°C, 53% RH	positive	4 (4-5 cc)	Yes	
S38	08/07/2025	25°C, 53% RH	negative	1 (1 cc)	Yes	
S39	08/07/2025	25°C, 53% RH	positive	3-4 (4 cc)	Yes	
S40	08/07/2025	25°C, 53% RH	negative	1 (1 cc)	Yes	
S41	08/07/2025	25°C, 53% RH	negative	1 (1 cc)	Yes	
S42	08/07/2025	25°C, 53% RH	negative	1 (1 cc)	Yes	

***** *Approximate conditions for temperature (ºC) and relative humidity (% RH).*

Table 6*. Sample Evaluation*

Overall the above-described analyses of calibrants and unknown samples were performed by one operator (myself) in one working day (July 8th 2025) over 6 hours (12 am to 18 pm).

6.4 Conclusions

This interlaboratory study demonstrated that the aptamer-antibody LFA for TTX, previously reported by Ulises G. Díaz-Avello et al. [152] can be applied by independent laboratories following standardized instructions. Despite the signal could not be fully interpreted following the proposed scale CAL1-6, the test's ease of use underlined its potential for routine monitoring of TTX in seafood and environmental samples. Participation in the Ring Test provided practical validation of the assay's field applicability and confirmed that even without specialized instrumentation, the LFA yields interpretable visual results under the described conditions.

6.5 References

[95] F. Odeh *et al.*, "Aptamers chemistry: Chemical modifications and conjugation strategies," 2020, *MDPI AG*. doi: 10.3390/molecules25010003.

[96] C. Tuerk and L. Gold, "Systematic Evolution of Ligands by Exponential Enrichment: RNA Ligands to Bacteriophage T4 DNA Polymerase." [Online]. Available: https://www.science.org

[97] Y. X. Wu and Y. J. Kwon, "Aptamers: The 'evolution' of SELEX," 2016, *Academic Press Inc.* doi: 10.1016/j.ymeth.2016.04.020.

[98] M. Kohlberger and G. Gadermaier, "SELEX: Critical factors and optimization strategies for successful aptamer selection," Oct. 01, 2022, *John Wiley and Sons Inc*. doi: 10.1002/bab.2244.

[99] S. Y. Lam, H. L. Lau, and C. K. Kwok, "Capture-SELEX: Selection Strategy, Aptamer Identification, and Biosensing Application," Dec. 01, 2022, *MDPI*. doi: 10.3390/bios12121142.

[100] S. Ni *et al.*, “Recent Progress in Aptamer Discoveries and Modifications for Therapeutic Applications,” Mar. 03, 2021, *American Chemical Society*. doi: 10.1021/acsami.0c05750.

[101] G. E. Maio, O. Enweronye, H. E. Zumrut, S. Batool, N. A. Van, and P. R. Mallikaratchy, “Systematic Optimization and Modification of a DNA Aptamer with 2’-O-Methyl RNA Analogues,” *ChemistrySelect*, vol. 2, no. 7, pp. 2335–2340, Mar. 2017, doi: 10.1002/slct.201700359.

[102] A. Fallah, A. A. Imani Fooladi, S. A. Havaei, M. Mahboobi, and H. Sedighian, “Recent advances in aptamer discovery, modification and improving performance,” Dec. 01, 2024, *Elsevier B.V.* doi: 10.1016/j.bbrep.2024.101852.

[103] T. Hianik, “Aptamer-based biosensors,” in *Encyclopedia of Interfacial Chemistry: Surface Science and Electrochemistry*, Elsevier, 2018, pp. 11–19. doi: 10.1016/B978-0-12-409547-2.13492-4.

[104] M. Hocek, “Synthesis of base-modified 2′-deoxyribonucleoside triphosphates and their use in enzymatic synthesis of modified DNA for applications in bioanalysis and chemical biology,” *Journal of Organic Chemistry*, vol. 79, no. 21, pp. 9914–9921, Nov. 2014, doi: 10.1021/jo5020799.

[105] F. Xia *et al.*, “Molecular Engineering of Aptamer Self-Assemblies Increases in Vivo Stability and Targeted Recognition,” *ACS Nano*, vol. 16, no. 1, pp. 169–179, Jan. 2022, doi: 10.1021/acsnano.1c05265.

[106] M. Bauer, M. Strom, D. S. Hammond, and S. Shigdar, “Anything you can do, i can do better: Can aptamers replace antibodies in clinical diagnostic applications?,” Nov. 30, 2019, *MDPI AG*. doi: 10.3390/molecules24234377.

[107] T. Mairal, V. Cengiz Özalp, P. Lozano Sánchez, M. Mir, I. Katakis, and C. K. O'Sullivan, "Aptamers: Molecular tools for analytical applications," *Anal Bioanal Chem*, vol. 390, no. 4, pp. 989–1007, Feb. 2008, doi: 10.1007/s00216-007-1346-4.

[108] Ö. Uğurlu *et al.*, "A review of aptamer-conjugated nanomaterials for analytical sample preparation: Classification according to the utilized nanomaterials," Jan. 25, 2024, *Elsevier B.V.* doi: 10.1016/j.aca.2023.342001.

[109] K. Mpofu, S. Chauke, L. Thwala, and P. Mthunzi-Kufa, "Aptamers and antibodies in optical biosensing," *Discover Chemistry*, vol. 2, no. 1, Feb. 2025, doi: 10.1007/s44371-025-00094-2.

[110] S. Farid, S. Ghosh, M. Dutta, and M. A. Stroscio, "Aptamer-Based Optical and Electrochemical Sensors: A Review," Dec. 01, 2023, *Multidisciplinary Digital Publishing Institute (MDPI)*. doi: 10.3390/chemosensors11120569.

[111] K. D. Cusick and G. S. Sayler, "An overview on the marine neurotoxin, saxitoxin: Genetics, moleculartargets, methods of detection and ecological functions," 2013, *MDPI AG*. doi: 10.3390/md11040991.

[112] "Marine biotoxins in shellfish – Saxitoxin group," *EFSA Journal*, vol. 7, no. 4, Apr. 2009, doi: 10.2903/j.efsa.2009.1019.

[113] L. M. Durán-Riveroll and A. D. Cembella, "Guanidinium toxins and their interactions with voltage-gated sodium ion channels," Oct. 01, 2017, *MDPI AG*. doi: 10.3390/md15100303.

[114] R. González-Cano, M. Carmen Ruiz-Cantero, M. Santos-Caballero, C. Gómez-Navas, M. Á. Tejada, and F. R. Nieto, "toxins Tetrodotoxin, a

Potential Drug for Neuropathic and Cancer Pain Relief?," 2021, doi: 10.3390/toxins.

[115] J. R. McCall, W. Christopher Holland, D. M. Keeler, D. Ransom Hardison, and R. Wayne Litaker, "Improved accuracy of saxitoxin measurement usingan optimized enzyme-linked immunosorbent assay," *Toxins (Basel)*, vol. 11, no. 11, Oct. 2019, doi: 10.3390/toxins11110632.

[116] K. Harju *et al.*, "Optimization of sample preparation for the identification and quantification of saxitoxin in proficiency test mussel sample using liquid chromatography-tandem mass spectrometry," *Toxins (Basel)*, vol. 7, no. 12, pp. 4868–4880, 2015, doi: 10.3390/toxins7124853.

[117] J. Nicolas, T. F. H. Bovee, L. Kamelia, I. M. C. M. Rietjens, and P. J. M. Hendriksen, "Exploration of new functional endpoints in neuro-2a cells for the detection of the marine biotoxins saxitoxin, palytoxin and tetrodotoxin," *Toxicology in Vitro*, vol. 30, no. 1, pp. 341–347, Dec. 2015, doi: 10.1016/j.tiv.2015.10.001.

[118] R. Watanabe, R. Matsushima, T. Harada, H. Oikawa, M. Murata, and T. Suzuki, "Quantitative determination of paralytic shellfish toxins in cultured toxic algae by LC-MS/MS," *Food Additives and Contaminants - Part A*, vol. 30, no. 8, pp. 1351–1357, 2013, doi: 10.1080/19440049.2013.793456.

[119] L. N. Wei *et al.*, "Ultrasensitive 'Hunter of Target': Rabbit Monoclonal Antibody-Based Competitive Lateral Flow Immunoassay for Saxitoxin," *Anal Chem*, vol. 97, no. 2, pp. 1410–1418, Jan. 2025, doi: 10.1021/acs.analchem.4c05998.

[120] J. Sun, M. Zhang, Q. Gao, and B. Shao, “Screening biotoxin aptamer and their application of optical aptasensor in food stuff: a review,” 2024, *Frontiers Media SA*. doi: 10.3389/fchem.2024.1425774.

[121] S. J. Ha, J. H. Park, B. Lee, and M. G. Kim, “Label-free direct detection of saxitoxin based on a localized surface plasmon resonance aptasensor,” *Toxins (Basel)*, vol. 11, no. 5, May 2019, doi: 10.3390/toxins11050274.

[122] S. Cheng *et al.*, “Determination of Saxitoxin by Aptamer-Based Surface-Enhanced Raman Scattering,” *Anal Lett*, vol. 52, no. 6, pp. 902–918, Apr. 2019, doi: 10.1080/00032719.2018.1505900.

[123] L. Qiang *et al.*, “A rapid and ultrasensitive colorimetric biosensor based on aptamer functionalized Au nanoparticles for detection of saxitoxin,” *RSC Adv*, vol. 10, no. 26, pp. 15293–15298, Apr. 2020, doi: 10.1039/d0ra01231a.

[124] L. Hou *et al.*, “Amperometric aptasensor for saxitoxin using a gold electrode modified with carbon nanotubes on a self-assembled monolayer, and methylene blue as an electrochemical indicator probe,” *Microchimica Acta*, vol. 183, no. 6, pp. 1971–1980, Jun. 2016, doi: 10.1007/s00604-016-1836-1.

[125] P. C. Serrano *et al.*, “Electrochemical impedance biosensor for detection of saxitoxin in aqueous solution”, doi: 10.1007/s00216-021-03603-1/Published.

[126] L. Reverté *et al.*, “Detection of Tetrodotoxins in Puffer Fish by a Self-Assembled Monolayer-Based Immunoassay and Comparison with Surface Plasmon Resonance, LC-MS/MS, and Mouse Bioassay,” *Anal Chem*, vol. 87, no. 21, pp. 10839–10847, Nov. 2015, doi: 10.1021/acs.analchem.5b02158.

[127] L. Reverté, K. Campbell, M. Rambla-Alegre, C. T. Elliott, J. Diogène, and M. Campàs, "Immunosensor array platforms based on self-assembled dithiols for the electrochemical detection of tetrodotoxins in puffer fish," *Anal Chim Acta*, vol. 989, pp. 95–103, Oct. 2017, doi: 10.1016/j.aca.2017.07.052.

[128] S. Leonardo *et al.*, "Detection of tetrodotoxins in juvenile pufferfish Lagocephalus sceleratus (Gmelin, 1789) from the North Aegean Sea (Greece) by an electrochemical magnetic bead-based immunosensing tool," *Food Chem*, vol. 290, pp. 255–262, Aug. 2019, doi: 10.1016/j.foodchem.2019.03.148.

[129] M. Campàs, J. Reverté, M. Rambla-Alegre, K. Campbell, A. Gerssen, and J. Diogène, "A fast magnetic bead-based colorimetric immunoassay for the detection of tetrodotoxins in shellfish," *Food and Chemical Toxicology*, vol. 140, Jun. 2020, doi: 10.1016/j.fct.2020.111315.

[130] X. Shkembi *et al.*, "Hybrid Antibody-Aptamer Assay for Detection of Tetrodotoxin in Pufferfish," *Anal Chem*, vol. 93, no. 44, pp. 14810–14819, Nov. 2021, doi: 10.1021/acs.analchem.1c03671.

[131] A. Aballay-González *et al.*, "Detection of paralytic shellfish poisoning (PSP) toxins using a colorimetric immunosensing tool for food safety control," *Talanta Open*, vol. 11, Aug. 2025, doi: 10.1016/j.talo.2025.100463.

[132] S. Cheng *et al.*, "Study of the binding way between saxitoxin and its aptamer and a fluorescent aptasensor for detection of saxitoxin," *Spectrochim Acta A Mol Biomol Spectrosc*, vol. 204, pp. 180–187, Nov. 2018, doi: 10.1016/j.saa.2018.06.036.

[133] R. Zhou *et al.*, "A Novel SELEX Based on Immobilizing Libraries Enables Screening of Saxitoxin Aptamers for BLI Aptasensor Applications," *Toxins (Basel)*, vol. 14, no. 3, Mar. 2022, doi: 10.3390/toxins14030228.

[134] V. Bane, M. Lehane, M. Dikshit, A. O'Riordan, and A. Furey, "Tetrodotoxin: Chemistry, toxicity, source, distribution and detection," 2014, *MDPI AG*. doi: 10.3390/toxins6020693.

[135] S. Itoi *et al.*, "Toxic Takifugu pardalis eggs found in Takifugu niphobles gut: Implications for TTX accumulation in the pufferfish," *Toxicon*, vol. 108, pp. 141–146, Dec. 2015, doi: 10.1016/j.toxicon.2015.10.009.

[136] A. Vlamis *et al.*, "First detection of tetrodotoxin in greek shellfish by UPLC-MS/MS potentially linked to the presence of the dinoflagellate prorocentrum minimum," *Toxins (Basel)*, vol. 7, no. 5, pp. 1779–1807, May 2015, doi: 10.3390/toxins7051779.

[137] C. Malloggi *et al.*, "First Toxicological Analysis of the Pufferfish Sphoeroides pachygaster Collected in Italian Waters (Strait of Sicily): Role of Citizens Science in Monitoring Toxic Marine Species," *Animals*, vol. 13, no. 11, Jun. 2023, doi: 10.3390/ani13111873.

[138] H. K. Knutsen *et al.*, "Risks for public health related to the presence of tetrodotoxin (TTX) and TTX analogues in marine bivalves and gastropods," *EFSA Journal*, vol. 15, no. 4, Apr. 2017, doi: 10.2903/j.efsa.2017.4752.

[139] R. Chau, J. A. Kalaitzis, and B. A. Neilan, "On the origins and biosynthesis of tetrodotoxin," Jul. 2011. doi: 10.1016/j.aquatox.2011.04.001.

[140] T. Nishikawa and M. Isobe, "Synthesis of tetrodotoxin, a classic but still fascinating natural product," *Chemical Record*, vol. 13, no. 3, pp. 286–302, 2013, doi: 10.1002/tcr.201200025.

[141] T. Noguchi and O. Arakawa, “Tetrodotoxin - Distribution and accumulation in aquatic organisms, and cases of human intoxication,” 2008, *MDPI AG*. doi: 10.3390/md20080011.

[142] P. Rodríguez, A. Alfonso, P. Otero, P. Katikou, D. Georgantelis, and L. M. Botana, “Liquid chromatography-mass spectrometry method to detect Tetrodotoxin and Its analogues in the puffer fish Lagocephalus sceleratus (Gmelin, 1789) from European waters,” *Food Chem*, vol. 132, no. 2, pp. 1103–1111, May 2012, doi: 10.1016/j.foodchem.2011.11.081.

[143] “Azman et al International Food Research Journal 20(5) 2963-2966 (2013)”.

[144] M. Campàs, J. Reverté, À. Tudó, M. Alkassar, J. Diogène, and F. X. Sureda, “Automated Patch Clamp for the Detection of Tetrodotoxin in Pufferfish Samples,” *Mar Drugs*, vol. 22, no. 4, Apr. 2024, doi: 10.3390/md22040176.

[145] M. Alkassar *et al.*, “Evaluation of Toxicity Equivalency Factors of Tetrodotoxin Analogues with a Neuro-2a Cell-Based Assay and Application to Puffer Fish from Greece,” *Mar Drugs*, vol. 21, no. 8, Aug. 2023, doi: 10.3390/md21080432.

[146] P. Bordin *et al.*, “First occurrence of tetrodotoxins in bivalve mollusks from Northern Adriatic Sea (Italy),” *Food Control*, vol. 120, Feb. 2021, doi: 10.1016/j.foodcont.2020.107510.

[147] J. Reverté *et al.*, “Toxicity Equivalency Factors for Tetrodotoxin Analogues Determined with Automated Patch Clamp on Voltage-Gated Sodium Channels in Neuro-2a Cells,” *J Agric Food Chem*, vol. 72, no. 32, pp. 18192–18200, Aug. 2024, doi: 10.1021/acs.jafc.4c04321.

[148] A. D. Turner, A. Powell, A. Schofield, D. N. Lees, and C. Baker-Austin, “Detection of the pufferfish toxin tetrodotoxin in European bivalves, England, 2013 to 2014,” *Eurosurveillance*, vol. 20, no. 2, Jan. 2015, doi: 10.2807/1560-7917.ES2015.20.2.21009.

[149] A. D. Turner, M. J. Boundy, and M. D. Rapkova, “Development and single-laboratory validation of a liquid chromatography tandem mass spectrometry method for quantitation of tetrodotoxin in mussels and oysters,” *J AOAC Int*, vol. 100, no. 5, pp. 1469–1482, Sep. 2017, doi: 10.5740/jaoacint.17-0017.

[150] A. Gerssen, T. H. F. Bovee, M. D. Klijnstra, M. Poelman, L. Portier, and R. L. A. P. Hoogenboom, “First report on the occurrence of tetrodotoxins in bivalve mollusks in the Netherlands,” *Toxins (Basel)*, vol. 10, no. 11, Nov. 2018, doi: 10.3390/toxins10110450.

[151] C. Dell’Aversano *et al.*, “First detection of tetrodotoxin and high levels of paralytic shellfish poisoning toxins in shellfish from Sicily (Italy) by three different analytical methods,” *Chemosphere*, vol. 215, pp. 881–892, Jan. 2019, doi: 10.1016/j.chemosphere.2018.10.081.

[152] U. G. Díaz-Avello *et al.*, “Aptamer-antibody sandwich lateral flow test for rapid visual detection of tetrodotoxin in pufferfish,” *Science of the Total Environment*, vol. 978, May 2025, doi: 10.1016/j.scitotenv.2025.179419.

[153] A. H. Iles *et al.*, “Semi-quantitative detection of inflammatory biomarkers using a laser-patterned multiplexed lateral flow device,” *Talanta*, vol. 237, Jan. 2022, doi: 10.1016/j.talanta.2021.122944.

[154] P. Nuntawong, W. Putalun, H. Tanaka, S. Morimoto, and S. Sakamoto, “Lateral flow immunoassay for small-molecules detection in

phytoproducts: a review," Jun. 01, 2022, *Springer Japan*. doi: 10.1007/s11418-022-01605-6.

[155] F. Broccolo, S. Fabris, M. Ciccozzi, and M. Plebani, "A rapid semi-quantitative test for determination of SARS-CoV-2 antibody levels," Apr. 01, 2022, *De Gruyter Open Ltd*. doi: 10.1515/cclm-2022-0035.

[156] Y. Wu, Y. Hu, N. Jiang, R. Anantharanjit, A. K. Yetisen, and M. F. Cordeiro, "Quantitative brain-derived neurotrophic factor lateral flow assay for point-of-care detection of glaucoma," *Lab Chip*, vol. 22, no. 18, pp. 3521–3532, Aug. 2022, doi: 10.1039/d2lc00431c.

[157] K. Omidfar, F. Riahi, and S. Kashanian, "Lateral Flow Assay: A Summary of Recent Progress for Improving Assay Performance," Sep. 01, 2023, *Multidisciplinary Digital Publishing Institute (MDPI)*. doi: 10.3390/bios13090837.

[158] Z. Li *et al.*, "Ball pen writing-without-ink: A truly simple and accessible method for sensitivity enhancement in lateral flow assays," *RSC Adv*, vol. 12, no. 4, pp. 2068–2073, Jan. 2022, doi: 10.1039/d1ra07684a.

[159] S. Y. Gan, G. J. Tye, A. L. Chew, W. K. Ng, and N. S. Lai, "Linker-mediated oriented antibody immobilisation strategies for a more efficient immunosensor and diagnostic applications: A review," Sep. 01, 2023, *Elsevier Ltd*. doi: 10.1016/j.biosx.2023.100379.

[160] Y. Li *et al.*, "Universal probe with oriented antibody to improve the immunochromatographic assay of lead ions in Procambarus clarkii," *Food Quality and Safety*, vol. 7, 2023, doi: 10.1093/fqsafe/fyad015.

PART III

STUDIES ON PHOTORESPONSIVE AZOBENZENE DERIVATIVES AND PROTEIN - PROTEIN INTERACTION MODULATORS WITH POTENTIAL BIOLOGICAL ACTIVITY

CHAPTER VII

INVESTIGATION OF THE PHOTOCHEMICAL AND STRUCTURAL EFFECTS OF ORTHO-SUBSTITUTION IN 7-AZOBENZOTHIAZOLE DERIVATIVES

7.1 Introduction

When light is absorbed by molecules, it can promote electrons to higher energy states and initiate a variety of chemical and physical processes. Depending on the molecular structure and environment, such excitation may lead to bond cleavage or formation, or to reversible structural changes that modify the geometry, polarity, or rigidity of a compound [161]. One of the most important of these light-induced processes is photochromism, which is defined as the reversible transformation of a molecule between two forms that exhibit distinct absorption spectra. This transformation, typically a photoisomerization, alters fundamental molecular properties such as dipole moment, dielectric constant, and refractive index, and can lead to significant changes in optical or mechanical behaviour. Compounds capable of converting light energy into reversible structural changes are collectively referred to as molecular photoswitches [162].

The largest and most widely studied class of molecular photoswitches is that of azobenzenes, composed of two aromatic rings connected by an azo group (–N=N–). These compounds can exist in two isomeric forms, trans and cis. The ability of the N=N double bond to undergo efficient photoinduced isomerization, combined with functionalization of numerous derivatives, makes azobenzenes excellent candidates for applications ranging from materials science to biology. Historically, azo compounds were first discovered in the nineteenth century and initially employed as synthetic dyes due to their intense and tunable colours [163]. Since then, extensive chemical and physical studies have explored how their photoresponsive properties vary across differently substituted and functionalized systems. The trans isomer of azobenzene is the

thermodynamically stable form, lying approximately 10–12 kcal·mol^{-1} lower in energy than the cis isomer [164]. Consequently, under dark conditions and at thermal equilibrium, the molecular population is almost entirely composed of the trans configuration (>99.99%). The trans form adopts an almost planar structure, with both phenyl rings lying in the same plane of the azo linkage, and exhibits a negligible dipole moment, close to zero. In contrast, the cis isomer is bent, with the aromatic rings twisted by about 55° relative to one another, leading to a pronounced dipole moment of roughly 3 Debye [165]. This conformational rearrangement also shortens the distance between the para carbon atoms of the phenyl rings, decreasing from approximately 9.0 Å in the trans isomer to about 5.5 Å in the cis form.

The UV–visible absorption spectrum of azobenzene displays two characteristic bands that reflect its electronic structure (**figure 76**). A weak absorption in the visible region, around 430 nm, corresponds to excitation of the formally dipole-forbidden $S_1(n\pi^*) \leftarrow S_0$ transition, while a strong ultraviolet band near 320 nm arises from the dipole-allowed $S_2(\pi\pi^*) \leftarrow S_0$ transition. These two states govern the reversible trans–cis isomerization of the N=N bond upon photoexcitation [166] .

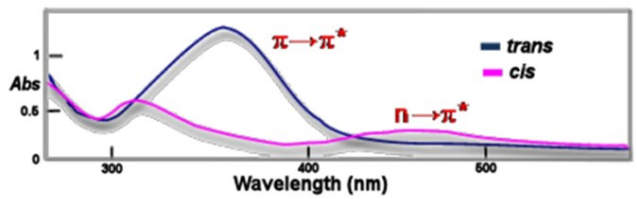

***Figure 76**. Representative UV–Vis absorption spectrum of an azobenzene compound [166].*

High-resolution spectroscopic studies have revealed that excitation to the $S_1(n\pi^*)$ state is mainly accompanied by in-plane changes in the

hybridization of the nitrogen atoms, and that this transition becomes effective through vibronic coupling with the CNNC torsional mode, which is directly involved in the isomerization process. The photoisomerization on the S_1 surface follows an inversion-assisted torsional pathway, separated by a small barrier of about 2 kcal mol^{-1}, leading to a conical intersection with the ground state that enables efficient nonradiative decay and structural rearrangement (**figure 77**) [167]. In contrast, excitation to the $S_2(\pi\pi^*)$ state induces only minor geometrical changes and rapidly relaxes through internal conversion to $S_1(n\pi^*)$, without clear evidence of alternative deactivation channels. The interplay between these two excited states underlies the efficient light-induced switching behaviour of azobenzene. Nevertheless, despite decades of experimental and theoretical work, the precise details of photoisomerization dynamics of functionalized azobenzene derivatives and the relative importance of rotational versus inversion pathways remain an active topic of research [167].

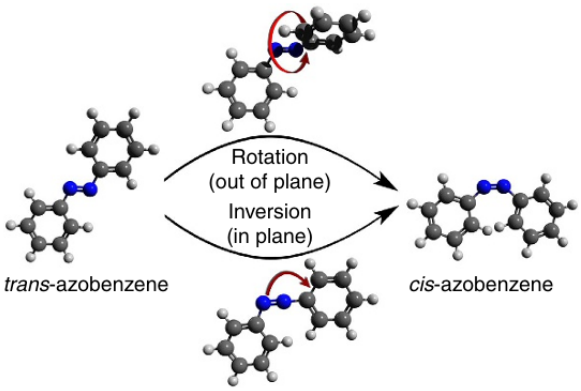

***Figure** 77. Schematic representation of the isomerization pathways of trans-azobenzene. The photoisomerization of trans-azobenzene can proceed through two main routes: a rotational pathway, involving torsion around the central N=N bond, or an inversion pathway, in which the phenyl rings move within the molecular plane toward each other. [167].*

For practical applications, azobenzene derivatives are rarely employed in their unsubstituted form. The introduction of specific functional groups is often required to enable chemical anchoring, solubility tuning, or interaction with a target environment, depending on the intended field of use, whether in materials, molecular devices, or biological systems. Since the nature and the number of substituents on the aromatic rings and their relative positions can strongly affect the photo-isomerization properties, in the rational design of an azocompound, a given functional group may be strategically selected to exert predictable effects on individual photochemical parameter. Substituents capable of donating electron density, such as amino or alkoxy groups, tend to delocalize charge through resonance into the π-system of the azo linkage. When introduced at the para or ortho positions, these groups markedly increase the conjugation between the aromatic rings and the azo bridge, leading to a lowering of the $\pi \rightarrow \pi^*$ excitation energy and thus to a pronounced red shift of the absorption band [169][168]. When a donating group is placed on one phenyl ring and an electron-withdrawing group on the other, the molecule acquires a push–pull character, producing even stronger red shifts and an enhanced dipolar nature of the excited state [171] [169] [170].

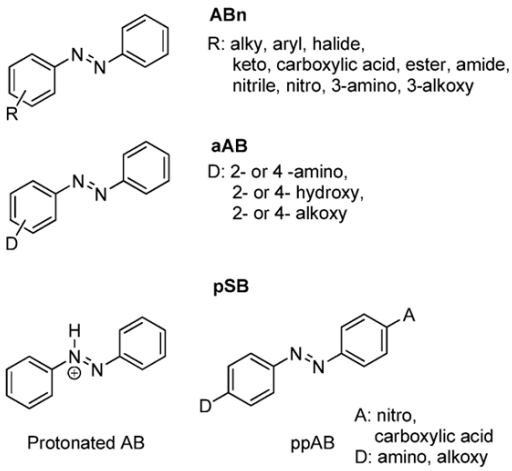

***Figure 78**. Types of substituted azobenzenes [171].*

This behaviour can be rationalized by considering that the excited ππ* state of azobenzene is more polar than its ground state: substituents that stabilize this charge-separated configuration, either through resonance donation or inductive effects, lower the energy of the excited state more than that of the ground state, resulting in absorption at longer wavelengths. In addition to their spectral influence, substituents also affect the thermal cis-to-trans relaxation [175][172]. The rate of this process depends on how the substituents modify the bonding character of the azo linkage. Groups that increase the double-bond polarization or enhance conjugation tend to introduce a greater degree of single-bond character into the N=N unit, thereby reducing the rotational barrier and accelerating thermal reversion. In general, substituents that increase the molecular dipole or strengthen resonance interactions lower the activation energy for the thermal process, leading to faster relaxation of the cis isomer. The relationship between absorption wavelength and thermal kinetics follows a general trend: as the π→π* band shifts toward the visible, the lifetime of the cis isomer typically becomes shorter. Electron-donating substituents, by extending

conjugation and stabilizing the excited state, thus provide visible-light responsiveness but at the cost of rapid thermal decay [168][173]. This trade-off poses an intrinsic challenge for the design of azobenzene photoswitches: achieving red-shifted absorption without compromising the persistence of the metastable cis form. One approach to overcome this limitation is to manipulate substitution pattern and steric environment. While para substitution governs conjugation through resonance, ortho substituents introduce steric interactions that twist the aromatic rings relative to the azo group. Such torsional distortion reduces π-overlap and can slow down the thermal relaxation. Substituents at the ortho position, therefore, can be used to counterbalance the fast thermal back-isomerization induced by strong electronic donors [178][174] [175]. Furthermore, cyclic amino groups or bulky ortho substituents can create a partially shielded microenvironment around the azo bridge, which stabilizes the cis configuration and extends its lifetime. However, due to the intricate interplay among these parameters, the overall impact of such modifications on other key properties often remains difficult to anticipate. Additionally, the surrounding medium play a pivotal role in determining the behavior of azobenzene-based photoswitches, affecting both the efficiency and kinetics of the isomerization process. Environmental factors such as polarity, proticity, pH, and viscosity must therefore be carefully considered as they directly influence the precision, responsiveness, and reliability of spatiotemporal control in both material and biological contexts. Given the inherent challenges in simultaneously optimizing all the properties of azoswitches resulting from specific functionalizations, and considering that the metastable Z isomer can revert to the E isomer either by irradiation or thermal relaxation, research efforts have diverged into two principal directions. The first one focuses on designing

azocompounds with tailored functional groups that enable bidirectional isomerization via irradiation at distinct wavelengths. Azocompounds light-switchable in both directions by light at non-toxic wavelengths, ideally within the visible or near-infrared range are generally preferred for biological and biomedical applications, where precise and fast-reversible photocontrol is essential to minimize off-target effects [181] [176]. The latter aims to modulate the thermal decay kinetics of the metastable Z isomer according to the intended application of the azocompound, thereby employing light exclusively for the E-to-Z conversion. In such cases, the photochemical property essential for achieving precise spatiotemporal bidirectional control, namely, well-separated UV-visible absorption bands for the two isomers, becomes less critical [177]. Instead, a high molar extinction coefficient at the selected wavelength becomes important primarily for the isomer undergoing photoinduced transformation.

In recent years, heteroaryl azo derivatives have emerged as versatile alternatives to classical azobenzenes, offering broader opportunities for electronic and structural modulation [178]. While in azobenzenes the spectral and kinetic properties are mainly tuned through electron-donating or electron-withdrawing substituents on the phenyl rings, the introduction of lone pairs heteroaromatic units inherently modifies the π-conjugation through the participation of heteroatoms such as nitrogen, oxygen, or sulfur. Thus, the electron density distribution within the chromophore is strongly affected by the presence of heteroatoms, thereby reshaping the relative energies of the ππ* and nπ* states [179]. Replacing one or both phenyl rings with heteroarenes preserves the azo photochromism while introducing new functionalities, such as basic or coordinating sites, that allow the molecule to interact with the surrounding medium in very different manner compared to azobenzene. However, the number of

azoswitches incorporating heteroatoms beyond nitrogen reported until today is still limited. Among them, thiazole and benzothiazole derivatives stand out for their strong electron-accepting character and enhanced π-conjugation.

Thiazole-based azoswitches benefit from the presence of a compact five-membered heterocycle containing both nitrogen and sulfur atoms, which imparts moderate electron-accepting ability and enables fine-tuning of absorption energies and isomerization kinetics [180]. In contrast, benzothiazole derivatives possess a fused thiazole-benzene ring that enhances π-conjugation and confers a stronger electron-withdrawing character, particularly at the C2 and C6 positions, which are highly sensitive to substituent effects. Electron-donating groups (e.g., –OH, –OMe) at these positions can increase electron density and shift absorption bands, while electron-withdrawing groups (e.g., $–NO_2$, –CN) stabilize the excited states and influence thermal isomerization rates. This push–pull electronic architecture, where donor and acceptor groups flank the azo linkage and the benzothiazole ring, facilitates intramolecular charge transfer (ICT), leading to enhanced nonlinear optical (NLO) responses. As a result, azobenzothiazole compounds are emerging as promising functional components in NLO materials for advanced applications in photoactive systems and organic photonics [187][181][182][182]. However, photochemical properties of benzothiazole-based azo systems have not been systematically investigated. In particular, the 7-position of the benzothiazole ring represents a unique and underexplored site for azo functionalization, with potential implications for the photochemical behavior of the resulting systems. Unlike the more commonly substituted 2- and 6-positions, the 7-position is electronically distinct, being ortho to the sulfur atom and meta to the nitrogen atom of the heterocycle. This

configuration may significantly influence the π-conjugation and electronic distribution across the molecule, thereby affecting absorption properties and photoisomerization dynamics. Moreover, the increased steric hindrance at this site could impose conformational constraints on the azo group, potentially altering the stability and kinetics of the cis/trans isomers in a manner distinct from other substitution patterns. To expand the knowledge about the potential of sulfur-containing heteroaromatic scaffolds as photo-switchable units with predictable and controllable photochemical properties we synthesized the two azobenzothiazole derivatives **1a** and **1b** (**figure 79**). In the rational design of azo-functionalized heterocycles, the selection of suitable coupling partners is essential not only for achieving regioselective substitution but also for enabling specific intramolecular interactions that can modulate the photochemical behaviour of the resulting compounds. The trimethoxyaniline (TMA) employed in this study was chosen for its two electronically and sterically equivalent positions, which promote predictable electrophilic aromatic substitution with the 7- diazonium benzotiazole salts. This reactivity ensures the consistent formation of azo derivatives bearing an ortho-amino group relative to the azo linkage. Such a substitution pattern is particularly relevant for the potential formation of intramolecular hydrogen bonds between the amino and azo group, an interaction that remains largely underexplored in benzothiazole-based systems. Recent studies have demonstrated that intramolecular hydrogen bonding can significantly influence the stability, isomerization kinetics, and excited-state dynamics of azo compounds, acting as a molecular lock that stabilizes specific isomeric forms and modulates the energy landscape of photoisomerization [191][183]. While such effects have been

investigated in other aromatic scaffolds [184] [185], their role in benzothiazole derivatives remains poorly understood.

Furthermore, the conversion of the amino group into its corresponding amide derivative represents a structurally minimal yet chemically significant modification. Indeed, the presence of a hydrogen atom on the nitrogen allows the amide to maintain its hydrogen-bonding capability, a feature that can play a crucial role in molecular recognition and supramolecular interactions. Conversely, introducing a short alkyl chain terminating in a carboxylic acid group enhances the water compatibility of the resulting molecule.

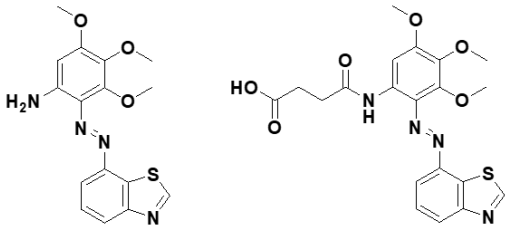

Figure 79. *Chemical structures of the two investigated azobenzothiazole derivatives.*

This structural variation provides a valuable basis for a comparative analysis between the amine and amide species, aimed at elucidating the influence of functionalization on their photochemical and physical properties, including polarity and solubility.

The synthesis of compound **1a** was obtained starting from the diazo coupling reaction using nitrosating reagent, with concerns regarding the neutralization of sulfuric acids used as catalysing reagent. Compound **1b** was directly obtained by reaction of 1a with succinyl anhydride. The obtained molecules where then characterised for their photochemical behaviour using spectroscopic techniques such as UV, fast UV and 1 and

2D NMR. The spectroscopic analyses allowed us to evaluate the effects of polar protic, polar aprotic and non-polar solvents on thermal decay of cis isomers. NMR analyses evidenced the presence of a strongly de-shielded exchangeable proton signal in 1H spectra, showing slow rate in deuterium hydrogen exchange experiments, thus suggesting its involvement in H-bond interaction. Computational studies performed by means of DFT methods on trans/cis isomers of the two compounds evidenced that both species can form in the trans configuration a strong H-bond interaction between the hydrogen bound to the exocyclic nitrogen atom and the azo-group, whereas in the cis configuration a weak H-bond could involve the carboxylic group at the end of the succinyl chain and hydrogen atom bound to exocyclic nitrogen in **1b**.

7.2 Results and Dsicussion

7.2.1 Synthesis of 1a, 1b

Compounds **1a** and **1b** were synthesized following procedures reported in the literature, with appropriate modifications [195] [186] (**figure 80**). 7-aminobenzothiazole was transformed into diazonium salt by reaction with $NaNO_2$ in acidic medium. The diazotization time was optimized by directly monitoring the ratio between 7-aminobenzothiazole and the coupling product by TLC, without isolating the intermediate diazonium salt. A reaction time of 2h was identified as optimal, resulting in enhanced efficiency and a significant reduction in side-product formation. To avoid excessive acidity and minimize dilution during the coupling step, the diazonium salt and 5 M NaOH were added simultaneously and dropwise to a solution of TMA in acetonitrile. Accurate control over reagent addition was essential: delayed introduction of NaOH resulted in the

formation of undesired by-products, including self-coupling of 7-aminobenzothiazole. Notably, the same by-product was also observed when the reaction was performed in reverse, generating the diazonium salt from TMA and employing 7-aminobenzothiazole as the coupling partner. These findings indicate that, with this specific substrate combination, side cross-reactions are highly competitive and could substantially compromise the efficiency of the target compound formation. The functionalized derivative **1b** was subsequently obtained via amidation of **1a**, following the procedure described by Borowiak et al. [186] .Yields were significantly enhanced when the reaction was carried out under strictly anhydrous conditions and a continuous argon atmosphere. The structures of compounds **1a** and **1b** were confirmed by one- and two-dimensional NMR spectroscopy, as well as by mass spectrometric analysis.

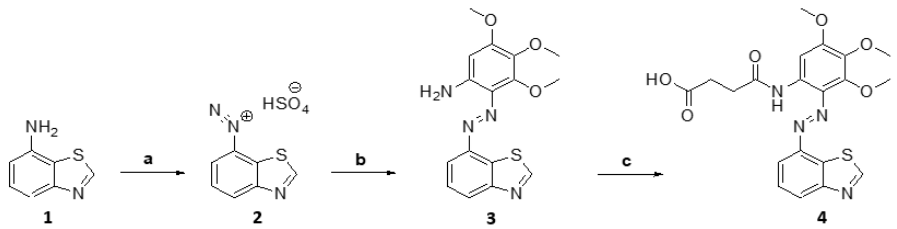

***Figure 80**. **a)** H_2SO_4 96%, $NaNO_2$ at 70°C, and then cooled to 5°C. This solution was added dropwise to the starting amine (**1**) solubilized with CH_3COOH and CH_3CH_2COOH (2:1), 1.5h, 0-5 °C. **b)** Diazonium salt (**2**) added dropwise to coupling agent (3,4,5-trimethoxyaniline) in CH_3CN with few drops of CH_3COOH, pH adjusted simultaneously to 6–7 with NaOH, 2 h, 0–5 °C, stirring. **c)** The resulting compound (**3**) was added to a suspension of K_2CO_3 and succinic anhydride in 1,4-dioxane under anhydrous conditions with an argon atmosphere, 16h at 65 °C to yield the final product (**4**).*

7.2.2 Photochemical properties of 1a and 1b

7.2.2.1 UV-Vis spectroscopy

The UV–vis spectra of the thermodynamically stable *E* isomers of **1a** and **1b** were acquired in dark in different solvents (**Table 7**). In most experimental conditions, a small amount of DMSO (<4%) was added as a co-solvent to improve the solubility of compound **1a** and to minimize potential interferences related to limited solubility in polar media. However, in the specific case of aqueous solutions, a higher concentration of DMSO (50%) was required to achieve complete dissolution of **1a**. **Figure 81A** displays the UV-vis absorption profiles of both molecules in diethyl ether. For compound **1a**, two distinct absorption bands are observed, centered at approximately 350 and 450 nm, corresponding to π→π* and n→π* transitions, respectively, and exhibiting comparable intensities. In compound **1b**, these bands undergo opposite shifts, resulting in near-complete overlap. In this case, the n→π* band appears significantly less intense and emerges as a shoulder on the π→π* band.

Solvent	Polarity index	Dipole moment	Dielectric Constant
DEE	2.8	1.15	4.33
DCM	3.1	1.14	8.93
DMSO	7.2	4.1	46.68
Water	10.2	1.87	80.1

***Table** 7. Polarity index, dipole moment, and dielectric constant of the solvents used for UV–vis measurements.*

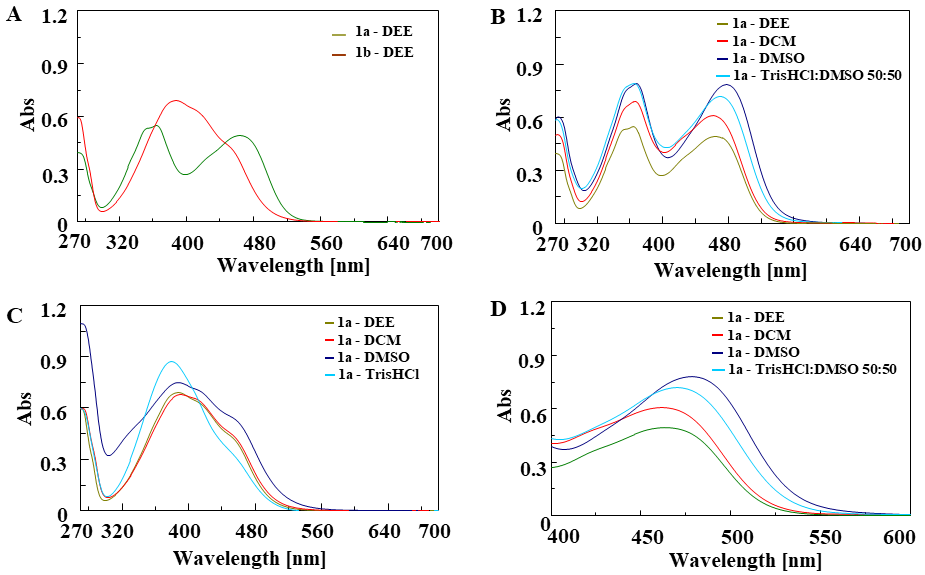

Figure 81. (A) *UV-vis spectra of* ***1a*** *and* ***1b*** *in DEE in the dark. UV-vis spectra of azo compounds acquired in different solvents at room temperature. (**B**)1a (**C**) 1b and (**D**) expanded wavelength scale in **B**.*

Figures 81B and 81C show the UV–vis absorption spectra of compounds **1a** and **1b** acquired in dark and in a range of solvents differing in polarity and hydrogen-bonding capability (**Table 7**). The spectral profiles exhibit negligible variation across the different solvent environments, indicating that solvent effects are not a determining factor under the conditions employed. These results strongly suggest that the observed differences in absorption behavior (**figure 81**) are primarily affected by the distinct molecular structures of compounds **1a** and **1b**. Specifically, the transformation of the amino group in **1a** into an amide in **1b** alters the electronic environment attenuating the contribution of hydrazone-like resonance forms in amide derivative, thereby enhancing the conjugation of the diazo (N=N) moiety and resulting in a red-shift of the π→π* transition band. At once, the reduced involvement in resonance of the lone

pair on the amide nitrogen leads to a blue shift of the n→π* transition, reflecting a diminished delocalization capacity.

Moreover, a slight solvent polarity effect is detectable on n→π* transition of compound **1a** (**figure 81D**), which exhibits a progressive bathochromic shift with increasing solvent polarity. Comparison of the UV–vis spectra of **1a** acquired in diethyl ether with those obtained in aqueous media and DMSO reveals more pronounced shifts in the n→π* band than those observed in dichloromethane. This trend suggests that the magnitude of the bathochromic shift correlates inversely with solvent polarity, indicating that less polar solvents induce smaller shifts in the n→π* transition. These observations are consistent with the hypothesis of a greater contribution of hydrazone-like resonance forms in compound **1a**.

7.2.3 Photoswitching behaviour of 1a and 1b

7.2.3.1 Kinetic measurements

To investigate the isomerization properties of **1a** and **1b** under irradiation with LED at 435 nm by means of UV–vis spectroscopy, three solutions for each compound were prepared using three different solvent systems (DCM, DEE, and 20 mM Tris–HCl buffer, pH 8), with each condition tested in triplicate (**Table 8**).

	$t_{1/2}$ DEE (min)	$t_{1/2}$ DCM (min)	$t_{1/2}$ Buffer Tris–HCl, pH=8 (min)
1a	31	1.7	-
	9.6	1.3	-
	9.7	1.3	-
1b	60	41	300
	61	40	300
	53	41	330

***Table 8**. Experimental conditions for the UV–vis study of **1a** and **1b** photoisomerization under 435 nm LED irradiation in DEE, DCM, and Buffer Tris-HCl pH=8, each in triplicate.*

1a and **1b** were used at 50 and 100 µM, respectively. For each sample, the UV spectrum was acquired before and after light exposure and then in the dark at several time intervals (**figure 82-84**). In all cases, but not for **1a** in water based medium, a substantial decrease in the absorption bands was observed upon irradiation (**figure 84 A-F**). When the samples were kept in the dark (inside the UV cell), the intensity of the UV bands gradually increased, eventually restoring the initial absorption profile. This behaviour indicated a reversible photoisomerization process. Time-dependent UV-vis profiles revealed the presence of isosbestic points in all explored conditions, suggesting a monomolecular photo-induced transformation, most likely corresponding to the Z→E isomerization.

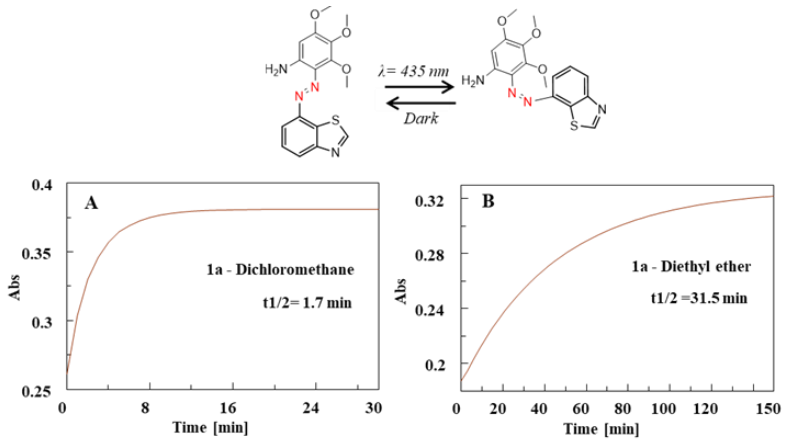

Figure 82. *Kinetic measurements of the photoisomerization of* ***1a*** *in Dichloromethane* ***(A)*** *and Diethyl ether* ***(B)*** *by Uv-vis spectroscopy.*

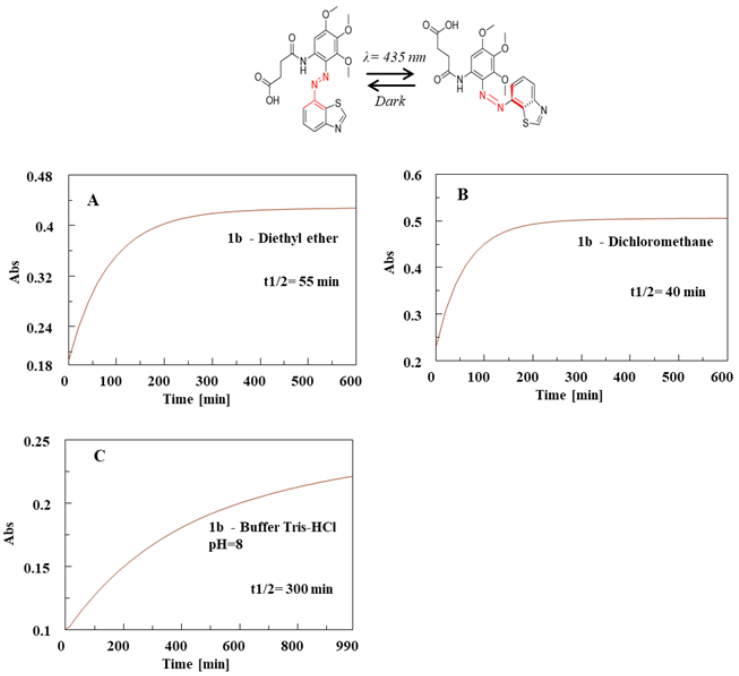

Figure 83. *Kinetic measurements of the photoisomerization of* ***1b*** *in Diethyl ether (A), Dichloromethane (B) and Buffer Tris HCl pH=8 (C) by Uv-vis spectroscopy.*

For both compounds **1a** and **1b**, the Z→E isomerization occurred at different rates depending on the solvent system used. Under the applied experimental conditions (where LED irradiation was performed outside the UV–vis spectrophotometer, allowing spectra to be recorded approximately one minute after exposure) no back-isomerization of **1a** was detected in aqueous media (**figure 84 E**). In contrast, in DCM the Z→E isomerization was faster than in DEE (**figure 82 and figure 84 A,C**).

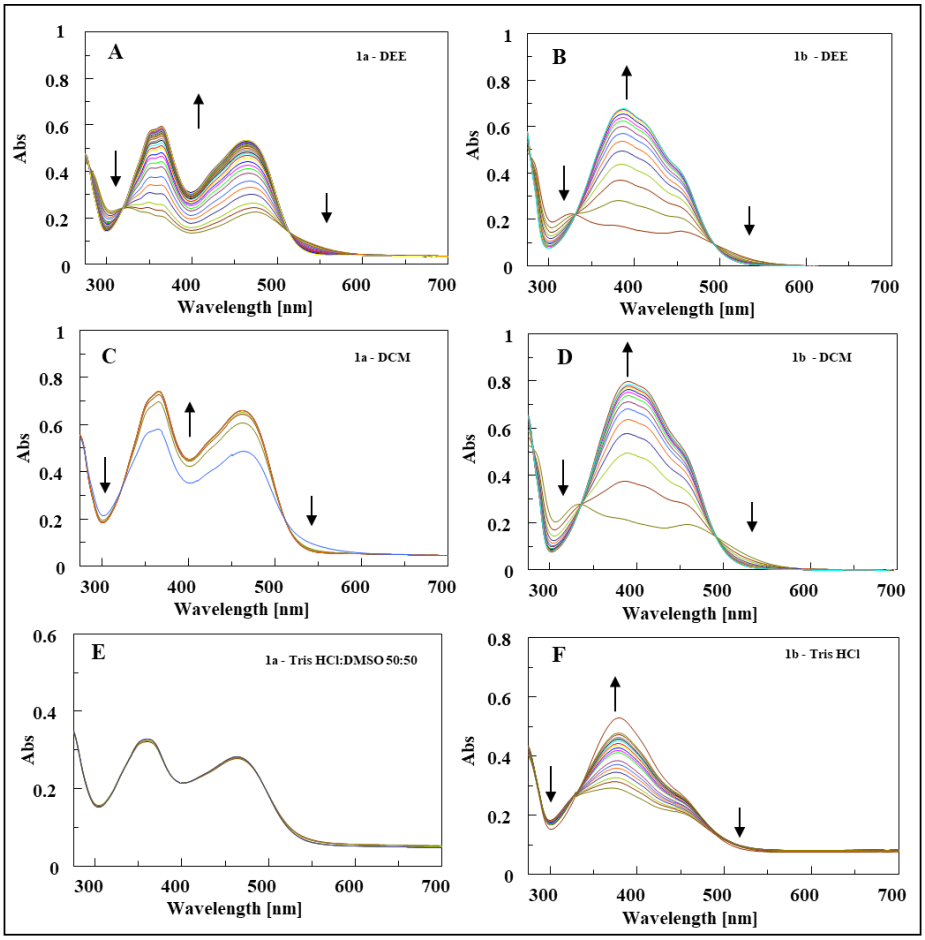

***Figure 84**. Time-dependent UV–vis spectra of **1a** and **1b** acquired in dark and after irradiation with LED at 435 nm in DEE (**A,B**), DCM (**C,D**), and tris HCl buffered solution (**E,F**). The arrows indicate the direction of UV-vis spectra evolution in dark, after light exposure.*

Assuming that the Z isomer of **1a** cannot be detected in water-based solution due to its rapid back-isomerization, the overall data can be summarized as showing a progressive shortening of the Z half-life with increasing solvent polarity and proticity, in agreement with what has been reported for most azobenzene derivatives [187]. Polar and protic solvents can promote hydrazone formation by solvating the azo group and/or

facilitating proton transfer, affecting N=N double-bond character and promoting tautomerism. This thermal relaxation mechanism has been proposed for azobenzenes bearing electron-donating groups on the aromatic ring, to explain the markedly shorter lifetimes of ortho- and para-hydroxy or amino-substituted derivatives in water compared to apolar solvents [188].

A distinct and peculiar behaviour was observed for Z isomer of **1b**, whose back-isomerization was fastest in DCM and progressively slowed down in DEE and in aqueous medium (**figure 83 and figure 84 B,D,F**). In compound **1b**, the introduction of a carboxylic group may significantly alter the dipole moment of the resulting isomers, depending on the relative conformation adopted by the carboxy-alkyl chain. In water-based media, the conformational analysis obtained from DFT calculations using a water-mimicking force field showed that the difference in dipole moment between the E and Z conformations of **1b** at their respective energy minima does not follow the classical behaviour. Indeed, in this case, the E isomer exhibits a higher dipole moment than the Z one. As a result, the transition state in water is expected to be less polar than in most reported azobenzene derivatives. Thus, the ability of water to effectively stabilize the transition state was reduced. This may contribute to the observed increase in the half-life of the Z isomer of **1b**, which rises from approximately 60 minutes in DEE to about 300 minutes in aqueous medium. However, additional factors may also play a role in this behaviour, and further detailed investigations are needed to fully elucidate the underlying mechanisms.

The same samples used for the photoisomerization experiments described above were also subjected to kinetic measurements (**figure 82, 83**). In this case, a single wavelength was selected for each compound (**1a** λ=496 nm;

1b λ=460 nm) and the absorbance variation over time was monitored to evaluate the rate of thermal back-isomerization of the metastable Z forms. The obtained kinetic profiles were fully consistent with the results of time-dependent UV-vis data. Each set of experimental data were fitted using an exponential rise-to-maximum function (three parameters), from which the half-lives ($t_{1/2}$) of the Z metastable species were calculated. In the case of **1a**, the kinetic measurements in aqueous medium (TrisHCl:DMSO 50:50) could not be reliably performed, in agreement with the previous observations showing negligible spectral differences before and after LED irradiation. In contrast, in DCM the calculated half-life was approximately 1.5 minutes, while increasing to about 10 minutes in DEE (**figure 82**). For **1b**, the analyses yielded half-lives of approximately 40 minutes in DCM, 55-60 minutes in DEE, and up to five hours in aqueous medium (**figure 83**).

7.2.3.2 Fast UV spectroscopy

To confirm the "anomalous" behaviour of **1a** additional kinetic measurements were performed by means of fast UV spectroscopy. Unlike the above-described UV–vis spectroscopic experiments, where the samples are first irradiated and subsequently analyzed, the fast UV setup allows simultaneous excitation and detection of the sample. A schematic representation of the optical setup is shown in **figure 85.**

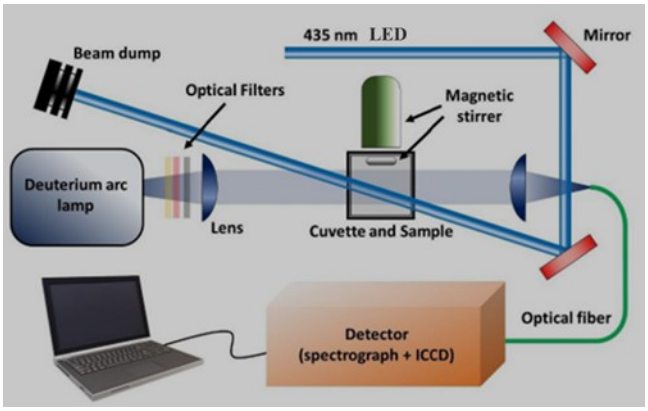

Figure 85. *The optical setup for the UV fast spectroscopy. The excitation light source was the LED at 435 nm while the probe beam was a Mercury–Argon lamp emitting at 404.6 nm. Several optical filters were employed to remove unwanted wavelengths and to reduce the intensity of the LED, thereby avoiding photochemical perturbation of the sample. The light from the lamp was collimated by a pair of UV-grade convex lenses and coupled into an optical fiber connected to the detector, a spectrograph equipped with an intensified CCD (ICCD) operating at a repetition rate of 2 Hz. The LED beam was directed through the sample (2 mL), placed in a quartz cuvette and stirred continuously with a magnetic stirrer, at a small angle relative to the 404 nm probe beam. The transmitted 404 nm signal was recorded during 435 nm irradiation to determine the E→Z half-life time, while the thermal back-isomerization (Z→E) was monitored after switching off the LED in dark conditions. An exponential decay model was used to fit the experimental data, from which the half-life times for both the E→Z and the reverse Z→E isomerization were determined.*

The experiments were designed to investigate the photo-switching kinetics of both compounds in DMSO and aqueous solutions (4% DMSO in water), in order to evaluate their behaviour under biologically relevant and non-toxic conditions. Samples were prepared by dissolving the compounds in the selected solvent systems. Experiments conducted on **1a** in water were hindered by its poor solubility, which caused partial precipitation during the analyses. The isomerization kinetics of compound **1b** were found to be faster in aqueous solution than in DMSO, with complete conversion

occurring in approximately 8 secs versus 7 secs, respectively (**figure 86 C,E**). Despite the rapid photoisomerization, the corresponding Z isomer exhibited relatively long half-lives, approximately 528 mins in DMSO and 390 mins in aqueous medium, in good agreement with the UV–vis spectroscopic data (**figure 86 D,F**). In contrast, compound **1a** showed a faster E→Z isomerization, with a conversion time of approximately 5.5 secs (**figure 86 A**). However, the Z isomer of **1a** displayed a significantly shorter half-life, about 28 mins in DMSO (**figure 86**), when compared to **1b** under the same conditions (**figure 86, Table 9**).

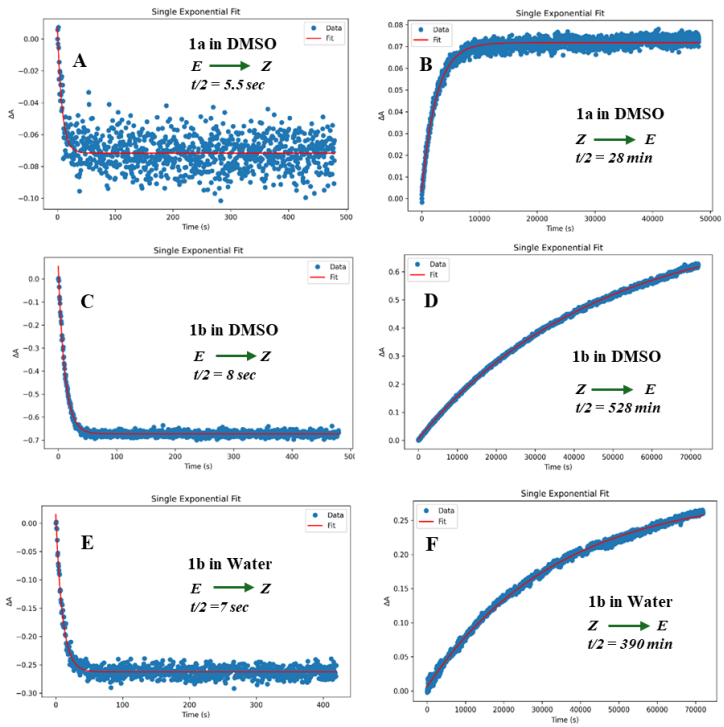

***Figure 86**. (A–F) Kinetic analysis of the photoisomerization of 7-aminobenzothiazole-based azo compounds. Panels (**A,C,E**) show the E → Z conversion under 435 nm LED irradiation (~10 mW); panels (**B,D,F**) show the Z → E thermal relaxation in the dark. Changes in absorbance at selected wavelengths are fitted with single-exponential functions (red lines), from which half-lives and the apparent rate constants were obtained.*

	Solvent	E→Z (λ=435 nm)	Z→E (Dark)
1a	***DMSO***	*~ 5.5 sec*	*29 min*
1b	***DMSO***	*~ 8.0 sec*	*528 min*
	Water	*~ 7.0 sec*	*390 min*

Table 9. *E→Z and Z→E isomerization times of 1a and 1b in DMSO and water.*

7.2.3.3 ^{1}H NMR experiments

To gain further insight into the photo-isomerization properties of **1a** and **1b**, we analyzed the Z→E thermal relaxation by acquiring ^{1}H NMR spectra in the dark and at different times after irradiation at 435 nm (**figures 87**). In dark, the ^{1}H NMR spectra of compounds **1a** and **1b** in DMSO-d_6 revealed distinct proton resonances. For **1a** (chemical shift range: 9.7–5.25 ppm), six proton resonances were observed at 9.50, 8.24, 8.19, 8.15, 7.78, and 6.30 ppm (**figure 87A**). For **1b** (chemical shift range: 12.7–6.0 ppm), six signals were detected at 12.20, 9.61, 8.35, 8.35, 8.20, and 7.92 ppm (**figure 87B**). After LED irradiation, the signals attributed to the E isomers of the compounds strongly decreased and a new set of 6 signals appeared in the same region of the spectra for both compounds. Over time, the intensities of these new resonances gradually decreased, and the ^{1}H NMR spectra reverted to those observed for the compounds in the dark. These transient signals are therefore attributed to the metastable E isomers, generated upon 435 nm LED irradiation. Notably, 35 minutes after LED irradiation, the intensity of the transient resonances associated with the metastable Z isomer of compound **1a** was reduced by approximately 57% compared to the signals observed at 4 minutes post-irradiation. In contrast, the corresponding resonances of the Z isomer of compound **1b** showed only a 16% decrease over the same time interval. Thus, ^{1}H NMR results agreed with those obtained by UV and fast UV

spectroscopy, showing the large differences in half-lives between **1a** and **1b** metastable Z isomers.

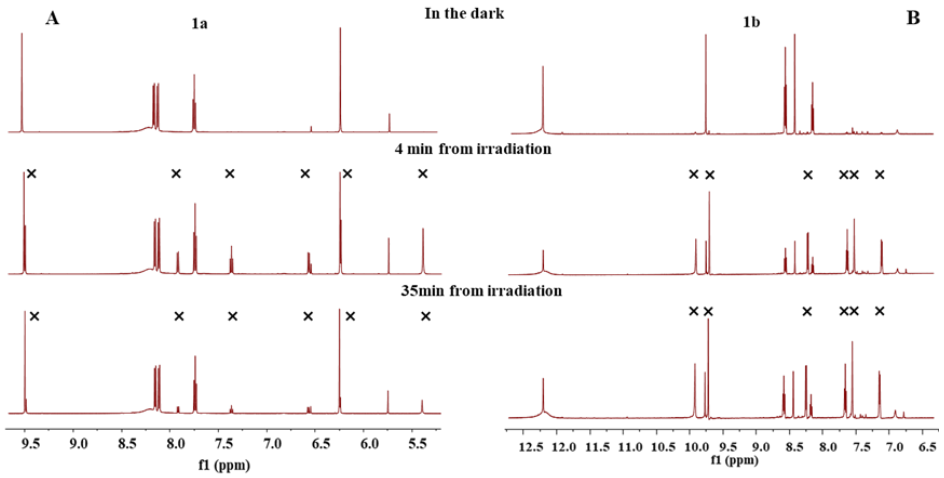

Figure 87*. [1]H NMR spectra of compounds* ***1a (panel A,*** *chemical shift range: 9.75–5.25 ppm) and* ***1b (panel B,*** *chemical shift range 12.75–6.25 ppm), acquired in the dark and at various time points following LED irradiation at 435 nm (4, 35 minutes). Transient resonances, marked with 'x', correspond to the protons of the metastable Z isomers.*

These findings may be rationalized by considering that in azocompounds bearing ortho-substituents capable of forming intramolecular hydrogen bonds with the diazo nitrogen atoms, the E isomer can be preferentially stabilized over the Z isomer, thereby facilitating thermal Z→E isomerization. To investigate the presence of intramolecular hydrogen bonding in compounds **1a** and **1b**, and to determine whether the conversion of the ortho-substituent from an amine (in **1a**) to an amide (in **1b**) affects this interaction, appropriate ^{1}H NMR experiments were performed on both compounds.

7.2.4 Investigation of Intramolecular Hydrogen Bonding in 1a and 1b by ^{1}H NMR Spectroscopy

Considering the presence of two hydrogen atoms on the amino group in compound 1a and one on the amide group in compound 1b, both located in the ortho position relative to the azo (-N=N-) moiety, the formation of an intramolecular hydrogen bond resulting in a six-membered ring is theoretically possible in both cases. Although such interactions are known to be both geometrically and energetically favourable, only a few examples have been reported in the literature. To investigate this possibility, two distinct sets of ^{1}H NMR experiments were performed on both compounds.

7.2.4.1 ^{1}H NMR experiments

The empirical NMR method developed by Abraham et al. [189] enables the quantitative assessment of intramolecular hydrogen bonding involving N-H or O-H protons. The principle of the method relies on measuring the ^{1}H NMR chemical shifts of the hydrogen-bond donor proton in two solvents that differ in both polarity and hydrogen-bond acceptor ability. $CDCl_3$ and DMSO-d_6 are the preferred solvent pair, as they satisfy these criteria: chloroform has a low dielectric constant and cannot act as a hydrogen-bond acceptor, while DMSO is a highly polar solvent capable of accepting hydrogen bonds.

The chemical shift difference between the two solvents, defined as $\delta\Delta = \delta(\text{DMSO}) - \delta(CDCl_3)$, provides a direct measure of the proton's interaction with the solvent and thus its availability to form intermolecular hydrogen bonds. A large positive $\delta\Delta$ indicates that the proton is free to interact with the solvent, whereas a small or negative $\delta\Delta$ suggests that the proton is already engaged in a stable intramolecular hydrogen bond. This

experimental parameter can be converted into the hydrogen-bond acidity descriptor A using the empirical relationship: A=0.0065+0.133δΔ. According to the ranges established by Abraham et al., for N-H groups *A* > 0.16 corresponds to the absence of intramolecular hydrogen bonding, while *A* < 0.05 is indicative of a strong intramolecular hydrogen bond. This approach was applied to evaluate the hydrogen-bonding behaviour of the investigated compounds.

For compound **1b** the ^{1}H NMR spectrum acquired in DMSO, revealed a well-resolved, strongly downfield-shifted resonance at 12.20 ppm, attributed to the amide proton (**figure 88 B**). In $CDCl_3$, the corresponding signal appeared at 12.84 ppm, yielding a δΔ value of –0.64. A derived parameter, known as the hydrogen bond acidity descriptor A, was calculated using δΔ as the experimental input. The resulting A value of –0.079 reflects the low tendency of the N-H proton to engage in intermolecular hydrogen bonding, suggesting instead the presence of a strong intramolecular hydrogen bond. Moreover, the markedly negative δΔ value (–0.644), which has few direct parallels in the literature, may also indicate the influence of additional electronic effects on the observed chemical shift. In contrast, for compound **1a (figure 88A)**, the ^{1}H NMR spectrum acquired in DMSO showed the amide proton resonance at 8.24 ppm, while in $CDCl_3$ the corresponding signal appeared at 7.04 ppm, giving a δΔ value of 1.20. The derived hydrogen bond acidity descriptor A, calculated from δΔ, was 0.166, indicating a strong tendency of the N-H proton to form an intramolecular hydrogen bond.

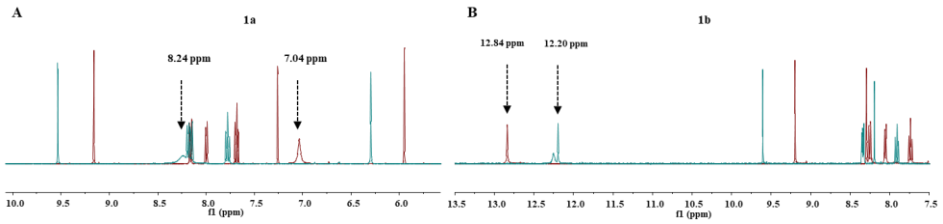

***Figure 88**. Comparison of the ¹H NMR spectra of compounds **1a** (**A**) and **1b** (**B**) recorded in DMSO-d_6 (blue line) and $CDCl_3$ (red line). The amide proton chemical shift in each solvent is reported.*

7.2.4.1 Kinetics of H/D Exchange

To confirm the results obtained from the above-described empirical method, the kinetics of hydrogen–deuterium (H/D) exchange were investigated by performing ¹H NMR experiments and recording spectra before and after the addition of 2% deuterated water (D_2O) to **1a** or **1b** samples in DMSO-d_6 [190]. This approach allows evaluation of the extent of protection conferred by an intramolecular hydrogen bond on the amine or amide proton. In particular, a proton involved in an intramolecular hydrogen bond is expected to undergo H/D exchange more slowly than a free proton in a comparable molecular environment. For this purpose, two reference compounds, TMA and TMA-COOH, were used as controls (**Figure 89A**).

Each of this compound contains the amino or the amide functional group as 1a or 1b, but lack the -N=N-benzothiazole moiety, thus preventing the formation of any intramolecular hydrogen bond. For each molecule, a ¹H NMR spectrum was acquired after keeping the sample in the dark for 24 hours. Subsequently, 2% D_2O was added, and the time evolution of the signal area corresponding to the exchangeable amine or amide proton was monitored. The resulting data are shown in **Figure 89**, revealing the following trend in the H/D exchange rate: TMA > TMA-COOH ≅ **1a** >>

1b. Therefore, the amino proton in compound **1a** and the amide proton in compound **1b** exhibited markedly reduced solvent accessibility compared to the corresponding protons in the reference compounds TMA and TMA-COOH, respectively (**figure 89 C,D**). In addition, a comparison of the H/D exchange rates revealed that TMA exhibited significantly faster exchange than TMA-COOH (**figure 89B**), suggesting that the conversion of the amino group to an amide reduces both the accessibility and the reactivity of the proton toward the surrounding medium. Thus, the decrease in H/D exchange observed in compound **1b c**ompared to **1a** (**figure 89E**) is primarily attributed to the functionalization of the $–NH_2$ group. Taken together, these results suggested that both compounds possess an intramolecular N–H bond of comparable strength.

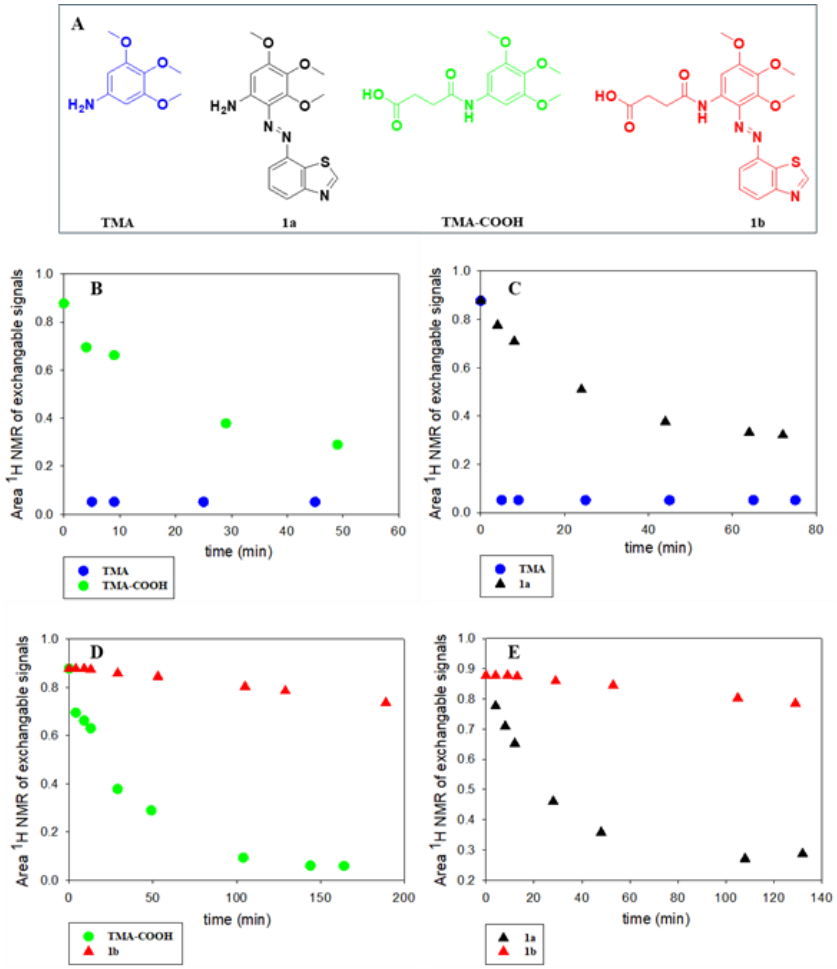

Figure 89. ***A***. *Structure of compounds 1a, 1b and of their corresponding reference compounds. Area of* ^{1}H *NMR exchangeable signals acquired in DMSO-*d_6 *at different time following the addition of 2% of D2O.* ***B.*** *TMA and TMA-COOH;* ***C. 1a*** *and TMA;* ***D. 1b*** *and TMA-COOH;* ***E. 1a*** *and* ***1b***.

7.3 Conclusions

Two 7-substituted azobenzothiazole derivatives, **1a** and **1b**, were synthesized and characterized to investigate how structural variation at the ortho position influences their photochemical and physical behaviour. The introduction of a carboxylic chain through amidation of the amino group

produced significant differences in the photoisomerization kinetics and thermal stability of the resulting compounds. Both molecules showed reversible light-induced interconversion between the trans and cis forms, but the rate of thermal relaxation was strongly affected by the solvent and by the chemical nature of the substituent. In all experiment conditions, the cis isomer of **1b** was more stable than that of **1a**, particularly in aqueous medium, where the lifetime of the metastable form increased from minutes to several hours. This behaviour highlights the influence of both solvent polarity and intramolecular interactions on the energy balance between the two isomers.

NMR analyses provided consistent evidence of specific intramolecular interactions. Both the chemical-shift and the hydrogen–deuterium exchange experiments indicated that, in **1b**, the amide proton is involved in a stable intramolecular hydrogen bond with the azo nitrogen, a result further supported by DFT calculations. Notably, according to literature reports, the presence of an intramolecular hydrogen bond in the trans configuration of azobenzene derivatives is generally associated with a decrease in the half-life of the corresponding cis form.

The combined experimental and computational data demonstrate that a complex interplay of steric effects from the ortho substituents and intramolecular interactions, combined with the polarity and protic nature of the solvent, contributes to the persistence of the cis isomer when the azo group is anchored at position 7 of the benzothiazole ring. The experimental data reported herein provide new insights for the rational design of photoswitchable systems compatible with aqueous environments, thereby facilitating their integration into biomedical applications.

7.4 Materials and Methods

General chemicals, solvents, anhydrous and/or deuterated solvents were purchased from Sigma Aldrich. 7-aminobenzothiazole was purchased from Fluorochem. TLCs were run on Merck silica gel 60 F254 plates and the spots were visualized by means of an UV lamp (Vilber Lourmat VL-4LC, 365 and 254 nm). Silica gel chromatography was performed using Merck silica gel 60 (0.063–0.200 mm). MPLC purifications were carried out using Biotage Sfär Silica HC Duo 20µm. The ^{1}H and 2D NMR experiments (COSY, HSQC, HMBC) were carried out on a Bruker Avance Neo spectrometer 400 MHz (Bruker BioSpin Corporation, Billerica, MA, USA). UV experiments were performed on a JASCO V-750 spectrophotometer, equipped with a PTC-348 temperature controller. Electrospray Mass Spectrometry (ESI-MS) analysis were carried out on a LTQ XL mass spectrometer (Thermo-Fisher Scientific, Waltham, MA, USA).

Synthesis of 1a

Concentrated sulfuric acid (1.8 mL) and sodium nitrite (0.047 g, 0.667 mmol) were mixed at 70 °C and then cooled to 5 °C to form nitrosyl sulfuric acid. This solution was added dropwise to a solution of the starting amine (0.1g, 0.667 mmol) dissolved in a mixture of acetic acid and propionic acid (6.6 mL, 2:1 v/v) in an ice bath. The reaction mixture was stirred for 2 hours at 0–5 °C.

The resulting diazonium salt was added dropwise to a solution of the coupling agent (0.122g, 0.667 mmol) in acetonitrile (4.4 mL) containing a few drops of acetic acid. Simultaneously, the pH was adjusted to 6–7 using a 5 M sodium hydroxide solution. The reaction was stirred continuously for 2 hours at 0–5 °C. Progress of the diazo coupling was monitored by

thin-layer chromatography (TLC, mobile phases: ethyl acetate: hexane 50:50 (v/v)). Upon completion, the reaction mixture was filtered, washed sequentially with Milli-Q water and acetone. The solvent was evaporated under reduced pressure and the residue was dissolved in methanol. The resulting solution was embedded on silica and evaporated to dryness. The powder obtained was loaded onto a Biotage Sfär Silica HC Duo 20 µm column and purified under isocratic conditions using ethyl acetate: hexane (50:50 v/v) as eluent. The fractions containing the desired product were dried under reduced pressure and recrystallized from ethyl acetate to give **1a** as a red crystalline solid (yields: 41%). TLC plate Rf = 0.59 (ethyl acetate: hexane 50:50 (v/v)). ^{1}H NMR: (400 MHz, DMSO-d_6): δ = 9.53 (s, 1H); 8.24 (bs, 2H); 8.19 (d, *J*=7.58,1H); 8.15 (d, J= 8.07 Hz, 1H); 7.78 (t, J=7.78 1H); 6.30 (s, 1H); 4.04 (s, 3H); 3.88 (s, 3H); 3.78 (s, 3H). ^{13}C-NMR: (400MHz, $CDCl_3$): δ = 159.90; 158.40; 155.65; 154.25; 148.20; 139.50;134.70; 126.80; 126.40; 125.30; 124.70; 120.00; 93.91; 62.63; 61.76; 56.14.

Synthesis of 1b

To synthesize the succinate derivative **1b**, the procedure reported by Borowiak *et al.* was adapted with appropriate modifications. Compound **1a** (0.3mmol) was added to a suspension of potassium carbonate (3.36 mmol) and succinic anhydride (2.7 mmol) in 1,4-dioxane (2.0 mL) under anhydrous conditions with an argon atmosphere. The reaction mixture was stirred for 16 h at 65 °C. After completion, Milli-Q water (1.5 mL) and ethyl acetate (1 mL) were added, and the pH was adjusted to 11 using a 1 M aqueous K_2CO_3 solution. The organic phase was removed, and the aqueous phase was acidified to pH ≈ 4 with 1 M HCl, then extracted with ethyl acetate (3 × 15 mL). The combined organic layers were dried over

anhydrous Na_2SO_4 and concentrated under reduced pressure to give **1b** as an orange solid.

^{1}H NMR: (600 MHz, DMSO): δ =12.20 (s, 1H); 9.61 (s, 1H); 8.35 (d, 1H); 8.35 (d, 1H); 8.20 (s, 1H); 7.92 (t, 1H); 4.08 (s, 3H);3.95 (s, 3H); 3.88 (s, 3H); 2.81 (t, 2H); 2.63 (t, 2H); ^{13}C-NMR: (400MHz, $CDCl_3$): δ = 176.43; 171.66; 160.14; 158.31; 155.59; 154.25; 147.20; 138.85; 130.01; 127.79; 127.22; 127.02; 126.33; 120.21; 98.86; 62.98; 61.69; 56.66; 33.24; 29.22.

UV Spectroscopy

UV experiments were performed by means of Jasco 750 in Diethyl ether (DEE), Dichloromethane (DCM), Acetonitrile, Dimethyl sulfoxide (DMSO) and 20 mM of Tris HCl-Buffer pH = 8 using a quartz cuvette o.l. 0.5 cm. **1a** and **1b** were used at the final concentration of 50 μM 100 μM, respectively. To acquire the UV spectra before the LED irradiation, the samples were kept in the dark for 24 h. UV spectra of the Z isomers were acquired after irradiation of the samples at 435 nm (1 min, 1 LED 435 nm Roithner Lasertechnik). The thermal decay of Z isomers was monitored by the further sequential acquisition of spectra until the UV profile became that of the initial E isomers. Kinetics curves were obtained by measuring the change in absorption at λ= 400 nm after LED irradiation. All parameters of kinetic measurements were reported in S2-S3.

Mono- , bi-dimensional NMR and Mass Spectrometry analyses:

^{1}H NMR spectrum of 1a (DMSO-d_6, 400 MHz)

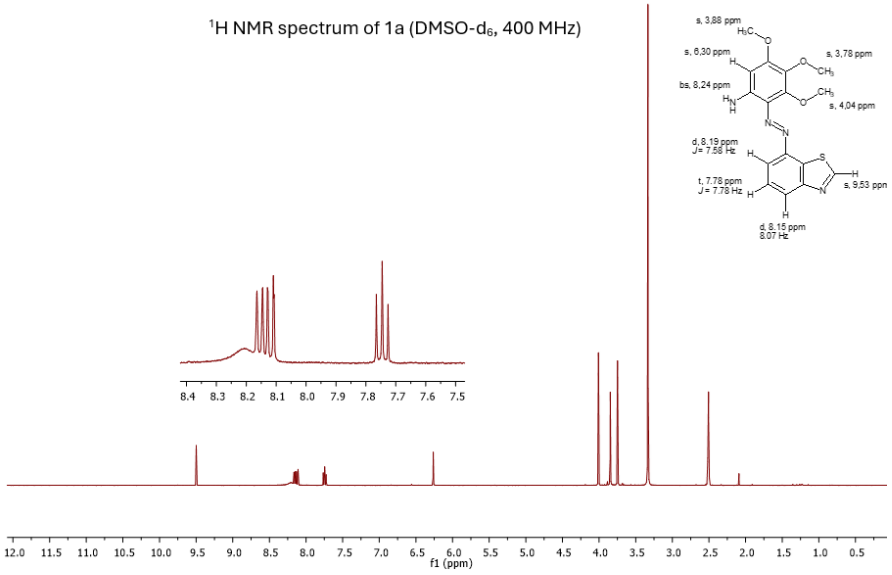

^{13}C NMR spectrum of 1a (DMSO-d_6, 400 MHz)

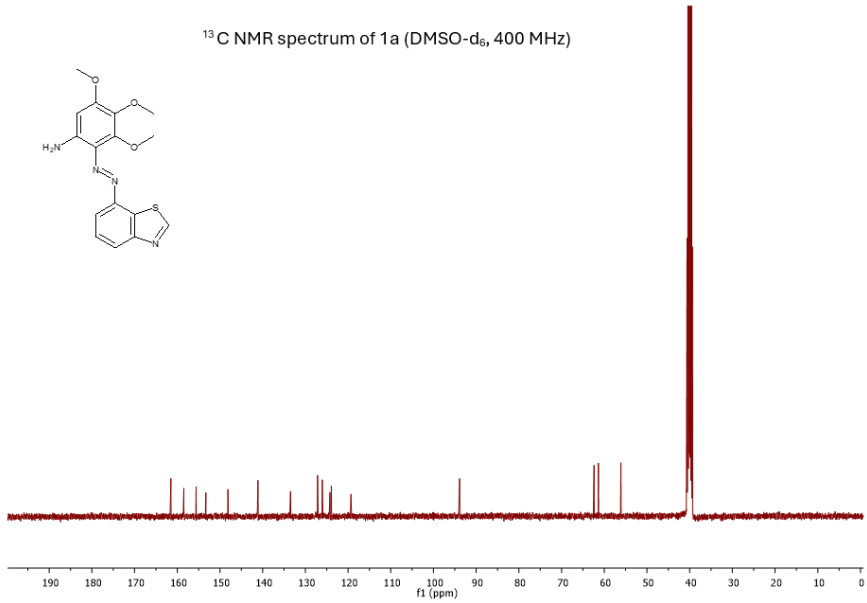

^{1}H NMR spectrum of 1b (DMSO-d_6, 600 MHz)

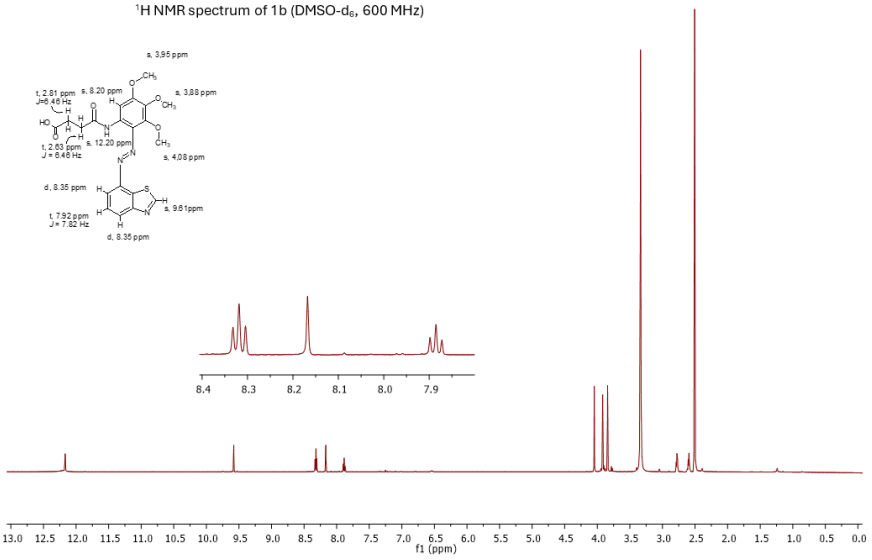

^{13}C NMR spectrum of 1b ($CDCl_3$, 400 MHz)

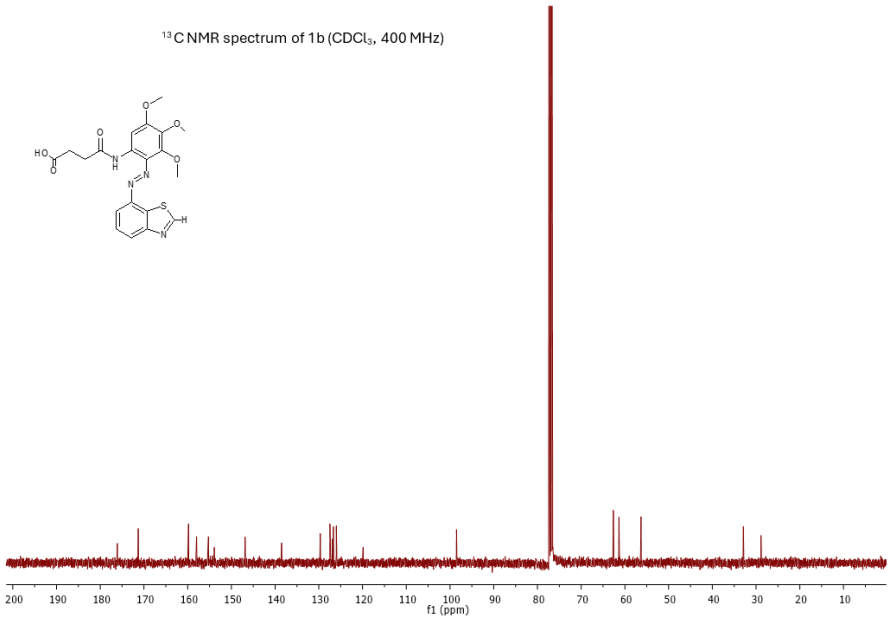

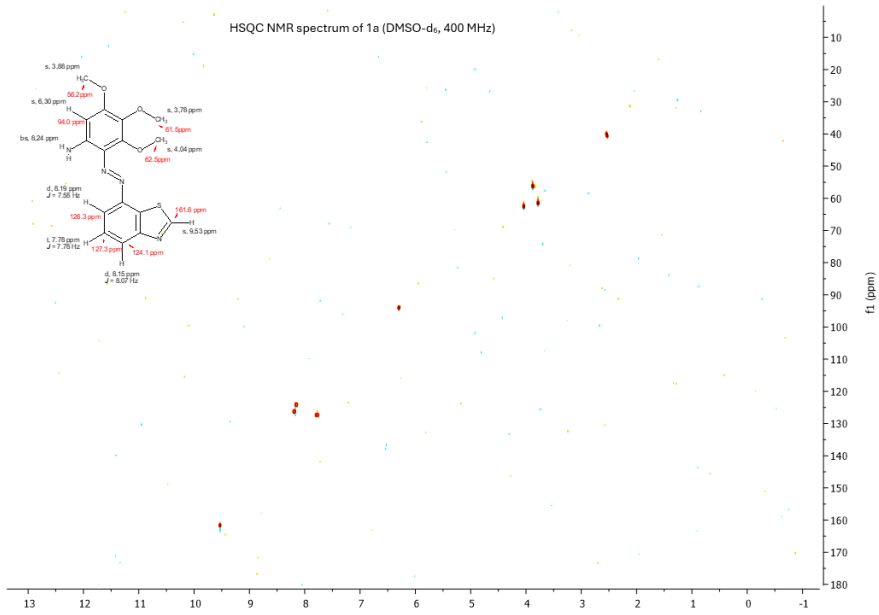
HSQC NMR spectrum of 1a (DMSO-d6, 400 MHz)
f1 (ppm)

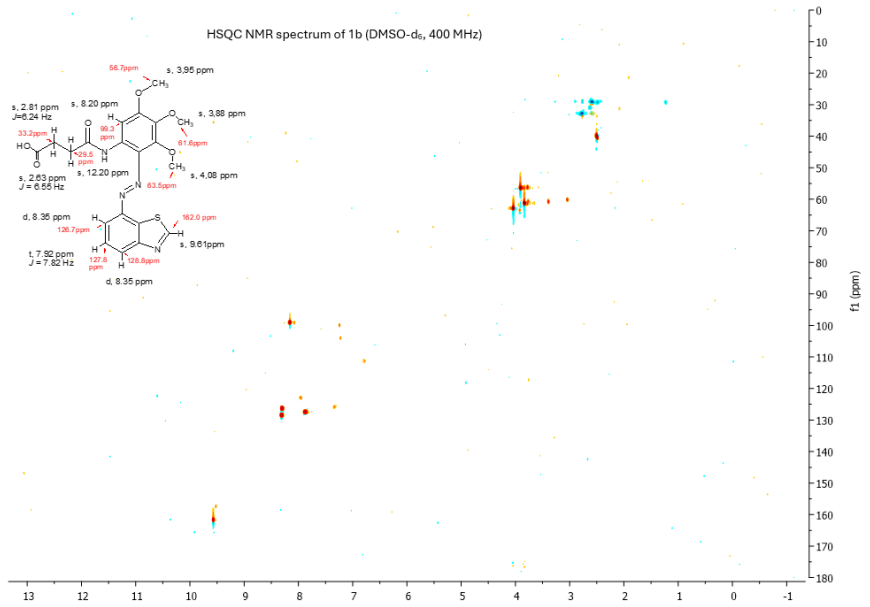
HSQC NMR spectrum of 1b (DMSO-d6, 400 MHz)
f1 (ppm)

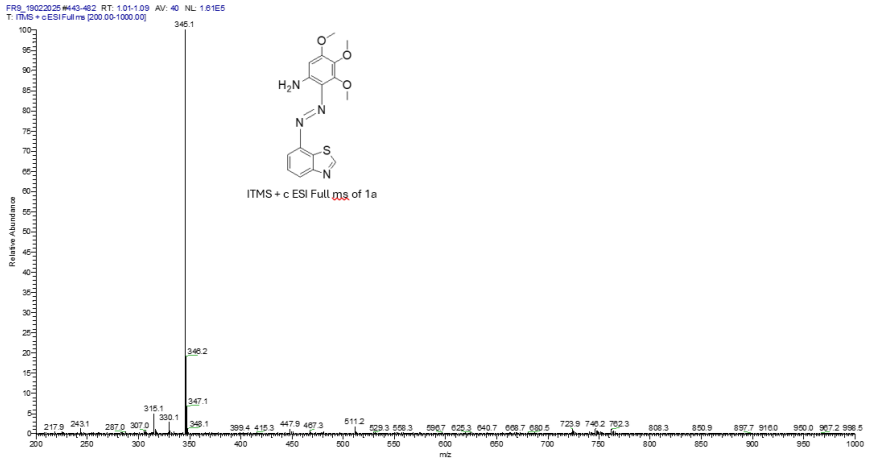

ITMS + c ESI Full ms of 1a

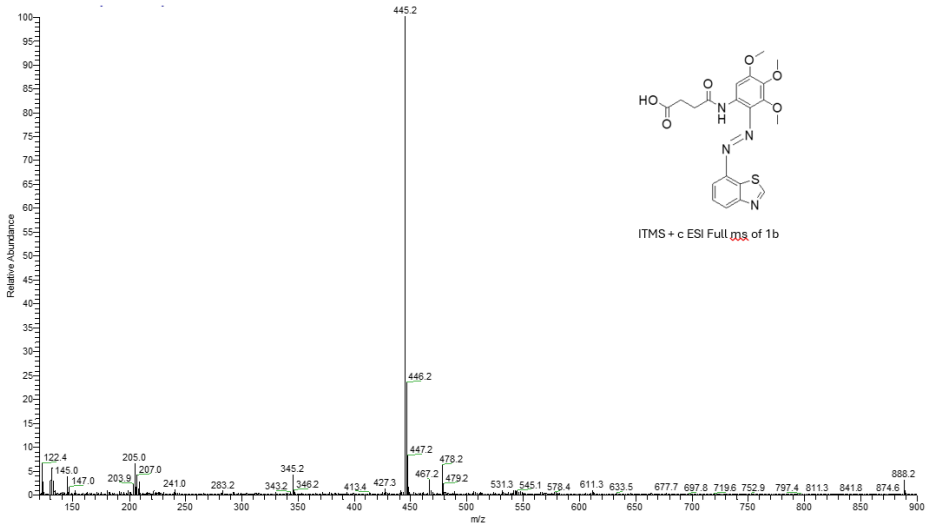

ITMS + c ESI Full ms of 1b

CHAPTER VIII

Tetrasubstituted Pyrrole Derivative Mimetics of Protein–Protein Interaction Hot-Spot Residues: A Promising Class of Anticancer Agents Targeting Melanoma Cells

This chapter is published in:

Persico, M., Galatello, P., Ferraro, M. G., Irace, C., Piccolo, M., **Abduvakhidov, A**., Tkachuk, O., d'Aulisio Garigliota, M. L., Campiglia, P., Iannece, P., Varra, M., Ramunno, A., & Fattorusso, C. (2023). Tetrasubstituted Pyrrole Derivative Mimetics of Protein–Protein Interaction Hot-Spot Residues: A Promising Class of Anticancer Agents Targeting Melanoma Cells. *Molecules*, *28*(10), 4161. https://doi.org/10.3390/molecules28104161

8.1 Introduction

The development of anticancer therapeutics has progressively evolved from the discovery of broadly cytotoxic agents to the design of molecules capable of selectively modulating the molecular interactions that regulate cell proliferation, survival, and differentiation. Among these processes, *protein–protein interactions* (PPIs) play a central role, acting as key nodes and hubs within the signaling networks that control essential cellular functions [191]. The deregulation of specific PPIs contributes to tumor initiation and progression by enabling cells to acquire several cancer-related traits, such as sustained proliferative signaling, evasion of growth suppressors, and resistance to apoptosis. Consequently, PPIs have emerged as promising therapeutic targets in oncology [192].

For a long time, PPIs were considered "undruggable" targets because their interfaces are usually large, relatively flat, and lack the well-defined cavities typical of enzyme active sites or receptor–ligand interactions. However, structural and biophysical studies have revealed that many protein interfaces contain discrete regions known as *binding hot spots*, which contribute disproportionately to the overall binding energy of the complex and can be selectively targeted by small molecules [193]. These discoveries have overturned the traditional view of PPIs as inaccessible to chemical modulation and opened the way for the rational design of molecules that mimic key structural and functional features of natural protein interfaces.

A paradigmatic example is the *MDM2–p53* interaction, which plays a fundamental role in the regulation of the p53 tumor suppressor. Under normal physiological conditions, MDM2 binds to p53, promoting its

ubiquitination and subsequent proteasomal degradation. In many tumors, overexpression of MDM2 leads to functional inactivation of p53, thereby allowing uncontrolled proliferation. The discovery of small-molecule antagonists such as *nutlin-3a* demonstrated that it is possible to disrupt this interaction, stabilize p53, and reactivate its transcriptional program of cell-cycle arrest and apoptosis [204] [194].
Following this success, other oncogenic PPIs have been targeted with similar approaches. For example, inhibition of the Bcl-xL/Bak complex has been achieved through the design of α-helix mimetics capable of reproducing the key hydrophobic residues involved in the interaction [195]. Comparable strategies have been applied to block the estrogen receptor/coactivator interface, which is essential for hormone-dependent tumor growth [196] and to interfere with the β-catenin/BCL9 complex within the Wnt signaling pathway (The name Wnt is resultant from a fusion of the name of the Drosophila segment polarity gene *wingless* and the name of the vertebrate homolog, *integrated or int-1)*, a crucial regulator of cell proliferation and differentiation [197].
The recognition that small molecules can successfully target oncogenic PPIs prompted deeper investigation into the structural features that govern these macromolecular interactions. Among secondary-structure elements, the α-helix is the most recurrent motif mediating PPIs. In many complexes, α-helical segments bind by presenting non-polar side chains toward complementary hydrophobic pockets on the partner protein. Structural analyses showed that only a limited number of residues, typically three positioned at i, i + 3/4, and i + 7 along the helical axis, account for most of the binding free energy and are defined

as hot-spot residues [198]. Reproducing this spatial arrangement within a compact, synthetically accessible scaffold became a central goal in α-helix mimicry. Early approaches relied on conformationally constrained peptides designed to stabilize helical conformations. Although valuable as structural models, these peptide-based systems often faced pharmacokinetic challenges, such as limited cell permeability and susceptibility to enzymatic degradation, which restricted their therapeutic application. These limitations motivated the exploration of non-peptidic scaffolds capable of reproducing α-helical side-chain orientations while offering improved drug-like properties. The work of Kutzki et al. [195] demonstrated that terphenyl derivatives could successfully replicate the hydrophobic pattern of the Bcl-xL/Bak interface, yielding potent inhibitors of anti-apoptotic Bcl-2 family proteins. Subsequently, Becerril et al. [196] designed small-molecule helix mimetics that blocked the estrogen receptor/coactivator interaction by arranging aromatic substituents to emulate the *i, i + 3, i + 4* topology of key leucine residues. Together, these studies established the conceptual foundation for designing rigid molecular frameworks able to project functional groups in spatial orientations analogous to those of helical hot-spot residues. Comparable strategies were later extended to other oncogenic PPIs, such as the β-catenin/BCL9 complex of the Wnt signaling pathway, where synthetic scaffolds reproducing the hydrophobic surface of the BCL9 α-helix effectively disrupted binding [197]. Structural and computational analyses of these systems revealed that successful helix mimetics share three key traits: a rigid core ensuring the correct geometric arrangement of substituents, a hydrophobic face complementing the target groove,

and peripheral groups capable of establishing favorable polar interactions [199].

Despite these advances, challenges remain. Many aromatic scaffolds such as terphenyls display poor aqueous solubility, whereas certain peptide-derived mimetics may lack the conformational rigidity required for optimal binding. To address these issues, research has increasingly focused on heterocyclic frameworks that combine structural preorganization, synthetic versatility, and tunable physicochemical properties. In particular, pyrrole-based molecules have attracted attention because their five-membered aromatic core allows the orientation of multiple substituents along distinct spatial vectors, enabling the emulation of α-helical hydrophobic triads while maintaining molecular compactness and potentially drug-like profiles [200]. These features make heteroaromatic systems promising candidates for the next generation of helix-mimetic anticancer agents.

Building on these structural and conceptual advances, our work was conceived to further explore pyrrole-based frameworks as tunable scaffolds for α-helix mimicry and PPI modulation. In particular, the study aimed to design, synthesize and biologically evaluate a new family of tetrasubstituted pyrrole derivatives capable of reproducing the hydrophobic residue arrangement typical of α-helical hot spots, while improving physicochemical properties such as solubility and conformational stability. The choice of the pyrrole nucleus was guided by its planar aromatic nature, which enables the precise spatial positioning of substituents, and by its electronic characteristics, which can favor stabilizing π–π and CH–π contacts with hydrophobic protein pockets [201].

To achieve these objectives, a rational design strategy was adopted, supported by computational modeling to evaluate the ability of the proposed scaffolds to reproduce α-helical topologies and to identify plausible interaction modes with protein targets. Synthetic methodologies were developed and optimized to access diverse substitution patterns on the pyrrole core, enabling a systematic investigation of structure–activity relationships. The resulting compounds were then subjected to biological assays to assess their capacity to modulate protein–protein interactions relevant to cancer cell survival and proliferation. Through this integrated approach, the study aimed to validate the pyrrole nucleus as a versatile template for the development of small-molecule α-helix mimetics with potential anticancer activity.

8.2 Results and Discussion

8.2.1 Design and Synthesis of the New TSP Derivatives

The information obtained from our first series of tetrasubstituted pyrroles (TSPs)[200] indicated that the three aromatic rings, designated as X, Y, and Z, act as key pharmacophoric elements capable of mimicking the side chains of three hydrophobic residues typically involved in α-helix-mediated PPIs. Replacement of the Z ring with a methyl group resulted in a complete loss of biological activity, as did modifications of the methylene linker length connecting the amide bond to the Y ring, or substitution of the latter with a cyclohexyl moiety. These findings emphasized the structural relevance of the three aromatic rings for maintaining the correct spatial arrangement required

for target recognition. Furthermore, some preliminary guidelines for substitution on the aromatic rings X and Y were identified. The introduction of bulky electron-withdrawing substituents (R_1), such as $–NO_2$ and $–CF_3$, led to inactive compounds, suggesting that excessive steric and electronic perturbation on the X ring is detrimental to binding. In contrast, the introduction of halogen atoms at the *meta* position of the Y ring maintained or enhanced activity, highlighting the favorable contribution of moderate electron-withdrawing groups to molecular recognition.

Based on these observations, further exploration of the TSP scaffold was performed by systematically modifying the reference compound 1 (**Table 10**).

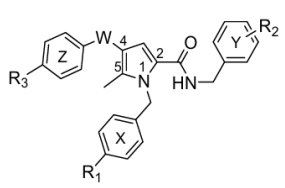

1, 9a-f, 9h-i, 10a-b

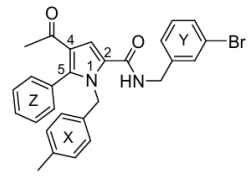

9g

Cpd	W	R_1	R_2	R_3
1	C=O	CH_3	3-Cl	H
9a	C=O	Cl	3-Cl	H
9b	C=O	OCH_3	3-Cl	H
9c	C=O	F	3-Cl	H
9d	C=O	CH_3	4-Cl	H
9e	C=O	Cl	4-Cl	H
9f	C=O	H	3-CF_3	H
9h	C=O	CH_3	3-Cl	CH_3
9i	C=O	CH_3	3-Cl	OCH_3
10a	C=O	NH_2	3-Cl	H
(±)10b	CHOH	CH_3	3-Cl	H

Table 10. *Representation of 2D structures of compounds1, 9a-i and 10a,b.*

The *para* position of the X ring was investigated by introducing substituents with different electronic and steric features (i.e., Cl, OCH_3, F and NH_2 ; **9a-c**, and **10a**, **Table 10**). Additional derivatives were

designed by introducing simultaneous modifications on both aromatic rings, combining *para*-substituted X rings with *meta*-substituted Y rings (i.e., R1:*p*-Cl and R2: *p*-Cl (**9e**); R1: H and R2: *m*-CF_3 (**9f**)). To assess the influence of substitution on the Y ring, the chlorine atom of **compound 1** was shifted from the *meta* to the *para* position, yielding derivative **9d**. The Z ring was also modified by introducing electron-donating groups at the *para* position (–CH_3 and –OCH_3), generating compounds **9h** and **9i**, respectively. Additional structural modifications included the exchange of the Z phenyl ring with the methyl group at position 5 (**9g**) and the reduction of the carbonyl group at position 4 to a hydroxyl group, yielding compound **10b**, thus providing a hydrogen bond interaction with the target and, at same time, modifying the geometry of the carbon atom from planar to tetrahedral.

The synthetic route for the preparation of compounds **9a–i** and **10a,b** is outlined in **figure 90**. Briefly, (±)-serine methyl ester hydrochloride (2) was reacted with p-toluenesulfonyl chloride to yield the corresponding intermediate 3, which was then treated with di-tert-butyl dicarbonate ($(Boc)_2O$) in the presence of a catalytic amount of 4-dimethylaminopyridine (DMAP) to afford the dehydroalanine derivative 4. This intermediate was subsequently condensed with the appropriate β-diketone (**5a–c**) in the presence of cesium carbonate (Cs_2CO_3) as a base, and the crude product was treated with 10% trifluoroacetic acid (TFA) in dichloromethane at room temperature to yield pyrrole derivatives 6a–d. Both regioisomers **6a** and **6b** were isolated from the reaction with **5a.** N-benzylation of intermediates **6a–d** with commercially available benzyl bromides provided esters **7a–i**, which were subsequently hydrolyzed under reflux with 2 M NaOH to

yield the corresponding carboxylic acids **8a–i**. Acidification with 2 M HCl followed by coupling with the appropriate amine, using 1-hydroxybenzotriazole (HOBt) and O-benzotriazol-1-yl-N,N,N′,N′-tetramethyluronium hexafluorophosphate (HBTU) in the presence of N-methylmorpholine (NMM) and DMF, afforded the final compounds 1 [200] and **9a–i** (**Table 10**) in good yields. Compounds **10a** and **±10b** were obtained by reduction of **9j** and **1**, respectively, using Fe/NH4Cl or NaBH4. Compounds 1-(4-methylphenyl) butane-1,3-dione **5b** and 1-(4-methoxyphenyl)butane-1,3-dione **5c** (**figure S1**) were synthesized by Claisen condensation of 4-methylacetophenone 11a or 4-methoxyacetophenone **11b** with ethyl acetate in the presence of NaH (60% w/w, dispersion in mineral oil).

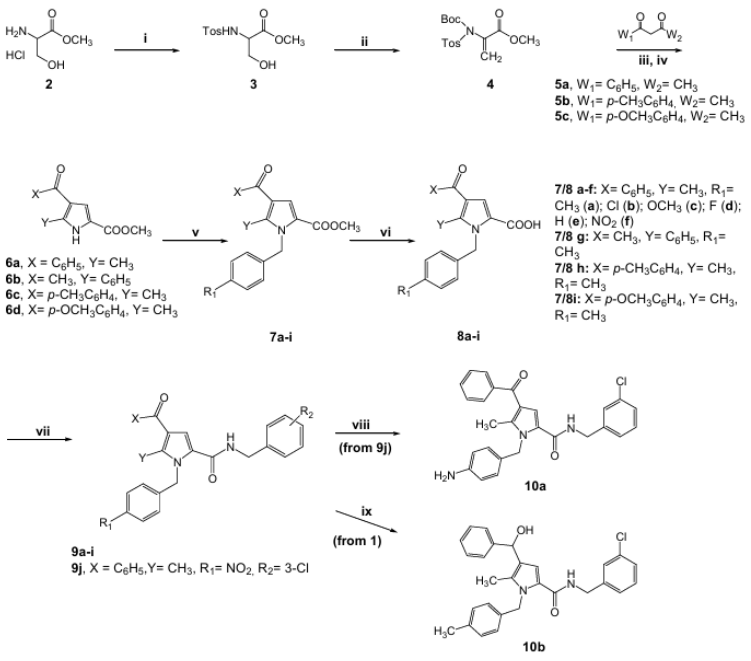

Figure 90. Reagents and conditions: (i) TsCl, TEA, DCM, rt, 12 h; (ii) (Boc)2O, DMAP; CH3CN, rt, 3h; (iii) Cs2CO3, dry CH3CN, 12 h, rt; (iv) TFA, DCM, rt, 12

h; (v) appropriate benzyl bromide, NaOH (50% w/v), TBAH, DCM, from 0 °C to rt, 18 h; (vi) 2 M NaOH, MeOH, reflux; (vii) HOBT, HBTU, NMM, DMF, rt, 12 h; (viii) Fe/NH4Cl/THF, 100 °C, 2 h; (ix) NaBH4, EtOH, 50 °C, 18 h.

8.2.2 Solubility assay

The solubility of all synthesized compounds was evaluated in a phosphate-buffered saline (PBS) solution (Sigma-Aldrich, Merck KGaA, Darmstadt, Germany; pH 7.4) using UV–visible spectroscopy [202]. For each compound, the precipitation point was determined by monitoring the increase in UV absorption of PBS in the wavelength range of 600–800 nm upon successive additions of small aliquots of a DMSO stock solution at a known concentration. Since no absorption bands are present in this spectral region, the observed increase in optical density was attributed to light scattering arising from the formation of insoluble particulate matter in PBS. The UV absorption data were plotted as a function of the added volume of the DMSO solution (x-axis), and the precipitation point was identified as the intersection of the two linear regions obtained from bilinear curve fitting. The x-coordinate of this intersection corresponded to the specific microlitre volume of DMSO added to 1.4 mL of PBS at which precipitation occurred. From this value, the concentration of each compound in PBS at the precipitation point was calculated, providing an estimate of its apparent solubility. The graphical representation of these measurements is reported in **Figure 91** (for **compound 1**, **10a**, and nutlin-**3a**) and **Figure S2** (for compounds **9a–i** and **±10b**), while the calculated solubility values are summarized in **Table 11**. Interestingly, the solubility data indicated that the behavior of the TSP derivatives is strongly influenced by the ionic composition of the

buffered medium. In particular, the previously reported solubility value of **compound 1** measured in 20 mM PBS (pH 7.4) containing 150 mM KCl [200] was significantly higher (≈6.8 µM) than that determined in the present conditions. This difference may be partially attributed to the variation in ionic charge density between the two buffers, which can affect hydrophobic interactions among nonpolar solutes and consequently modify apparent solubility [203][204].

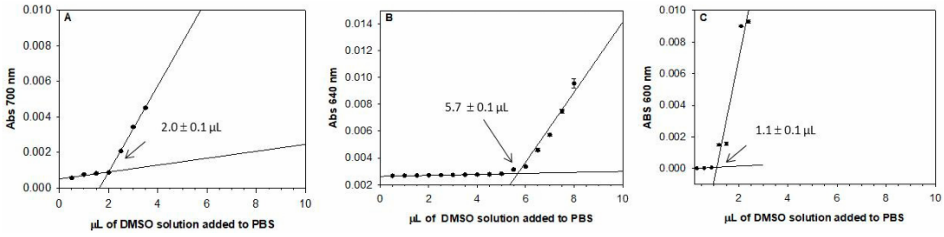

Figure 91. *Graphical representation of the UV absorption of PBS measured at 700, 640, or 600 nm as a function of the volume (µL) of DMSO solutions containing compounds 1 (**A**), 10a (**B**), or nutlin-3a (**C**), respectively. DMSO stock solutions (2.6 mM) of compounds 1 and 10a were added to 1.4 mL of PBS in 0.5 µL increments. To obtain at least three data points before reaching the precipitation point, the DMSO solution of nutlin-3a (2.6 mM) was added in smaller increments of 0.3 µL. The volumes corresponding to the precipitation points and the associated standard errors were calculated from the equations of the fitted lines. In all cases, the final DMSO concentration in PBS did not exceed 0.6% (v/v) [200].*

For compounds dissolved in DMSO at the same final concentration, the ratio between the calculated volumes of the DMSO solutions at the precipitation points can be directly related to the ratio of the compound solubilities. The newly synthesized derivatives **9a–i** exhibited solubility values similar to those of the reference **compound 1** (3.5 μM) and the control compound **nutlin-3a** (2.4 μM; **Table 11**). In contrast, compound **10a** showed markedly higher solubility, being 5.2- and 2.8-fold more soluble than **nutlin-3a** and **compound 1**, respectively. Among all tested derivatives, **10a** was the most soluble compound, followed by the racemic mixture **(±)10b**. The remaining compounds, including **nutlin-3a**, displayed substantially lower solubility under the same experimental conditions, with values ranging between 1.5 and 3.9 μM.

Cpd	Solubility [a] (μM)
1	3.5 ± 0.1
9a	3.9 ± 0.1
9b	3.1 ± 0.2
9c	3.9 ± 0.2
9d	3.1 ± 0.2
9e	3.5 ± 0.3
9f	2.6 ± 0.1
9g	1.5 ± 0.2
9h	<1.0
9i	<1.0
10a	10.5 ± 0.1
(±)10b	6.7 ± 0.6
nutlin-3a	2.4 ± 0.2

[a] data are reported as the mean ± SEM.

Table 11. *Solubility (M) in a PBS solution (pH = 7.4) of compounds* ***1, 9a–i, 10a,b****, and* ***nutlin-3a****.*

8.2.3 Biological Evaluation

To assess the biological effects of compounds **1, 9a–i,** and **10a,b,** specific human tumor models were employed within a preclinical framework. In line with previous pharmacological investigations [200][205], human malignant cell lines of different histological origins and characterized by high proliferative capacity in vitro were selected, namely, the p53 wild-type human melanoma cell line A375 and the colorectal carcinoma cell line HCT-116. Moreover, selective toxicity against the healthy cell line L6 was also investigated. Cell growth inhibition was measured after 48 hours of exposure to increasing concentrations of the compounds (1.5–25 μM) in both tumor and healthy cell lines. The reference compound nutlin-3a was included as a positive control. Following 48-hour treatments at the indicated concentrations, IC_{50} values were calculated from concentration–effect curves based on the estimation of a cell survival index, a parameter derived concurrently from the evaluation of cellular metabolic activity and the live/dead cell ratio, as reported in **Table 12**. The evaluation of the cell survival index showed a typical concentration-dependent sigmoidal trend, yielding IC_{50} values in the low micromolar range.

Cpd	A375 [a] IC_{50} (μM) [b]	L6 [c] IC_{50} (μM) [b]	SI [d]	HCT-116 [e] IC_{50} (μM) [b]
1	20 ± 4	42 ± 3	2.1	41.4 ± 6
9a	18 ± 4	48 ± 5	2.7	36.4 ± 8
9b	24 ± 14	40 ± 5	1.7	46 ± 18
9c	13 ± 4	35 ± 4	2.7	55.9 ± 7
9d	15 ± 5	25 ± 6	1.7	35.4 ± 6
9e	23 ± 6	38 ± 2	1.6	34.6 ± 6
9f	27 ± 8	35 ± 7	1.3	28.4 ± 7
9g	18 ± 5	71 ± 5	3.9	34 ± 6
9h	24 ± 6	42 ± 7	1.7	56.3 ± 15
9i	16 ± 6	66 ± 5	4.2	167.6 ± 9
10a	10 ± 4	55 ± 7	5.6	41.3 ± 6
(±)10b	15 ± 5	54 ± 6	3.6	25 ± 5
nutlin-3a	15 ± 3	18 ± 4	1.2	12.5 ± 5

[a] Human melanoma cell line. [b] IC_{50} values are expressed as mean values ± SEM (n = 30). [c] Rat myoblast cell line. [d] SI = IC_{50} L6/IC_{50} A375. [e] Human colon cancer cell line.

Table 12. *IC_{50} values (μM) and selectivity index (SI) of compounds **1, 9a–i, 10a,b**, and the positive control **nutlin-3a** against human cancer cell lines (A375 and HCT-116) and the healthy cell line (L6) after 48 hours of incubation.*

Overall, as reported in **Table 12**, all tested compounds were more active against the melanoma A375 cell line compared with the colon cancer HCT-116 cells. In particular, all derivatives displayed IC_{50} values between 10 and 27 μM in A375 cells, comparable to that of nutlin-3a (15 ± 3 μM). Conversely, in HCT-116 cells, compound **9i** was inactive (IC_{50} > 100 μM), while the remaining compounds showed IC_{50} values ranging from 25 to 56 μM, generally higher than that of **nutlin-3a** (12.5 ± 5 μM). Importantly, regarding cytotoxicity against the healthy L6 cells, all compounds displayed IC_{50} values ranging from 35 to 72 μM, with the exception of 9d (IC_{50} = 25 ± 6 μM). Accordingly, the selectivity index (SI) toward A375 cells was between 1.3 and 5.6, higher than that observed for **nutlin-3a** (SI = 1.2; **Table 12**). In detail, no significant differences in IC_{50} values in the A375 cell line were observed among the newly synthesized pyrrole derivatives compared with lead **compound 1**, except for: (i) **9c** (IC_{50} = 13 ± 4 μM), bearing

at R_1 a strong electron-withdrawing and potential hydrogen-bond-acceptor substituent such as fluorine, and (ii) **10a** (IC_{50} = 10 ± 4 μM), bearing at the same position an electron-donating and hydrogen-bond-donor/acceptor substituent (i.e., an amino group; **Tables 10**). In particular, compound **10a** was the most active pyrrole derivative among those tested, being slightly more potent than nutlin-3a (**Table 12**). Taken together, these findings suggest that the new TSP derivatives exert their antiproliferative effects through a mechanism of action analogous to that of the reference **compound 1**, likely involving interference with specific molecular pathways leading to apoptosis, rather than nonspecific cytotoxicity.

8.2.3 Apoptosis Studies

To verify our hypothesis that the mechanism of action of these TSP derivatives is related to their ability to interfere with PPIs involved in cell-cycle regulation in cancer cells, the most active compounds were selected for further investigation. Specifically, compounds **10a** and **9c**, which showed the highest cytotoxicity against the melanoma A375 cell line, and compounds **9f** and **10b**, active against the colon cancer HCT-116 line, were chosen to further investigate their mechanism of action. Since cell death in tumor cells typically occurs through apoptosis, necrosis, or autophagy, we first evaluated the ability of the selected compounds to induce cellular morphological changes in A375 melanoma cells after 48 hours of exposure at their respective IC_{50} concentrations (13 ± 4 μM for **9c** and 10 ± 4 μM for **10a**). The obtained results were compared with those of nutlin-3a, used as a positive control (**Figure 92**).

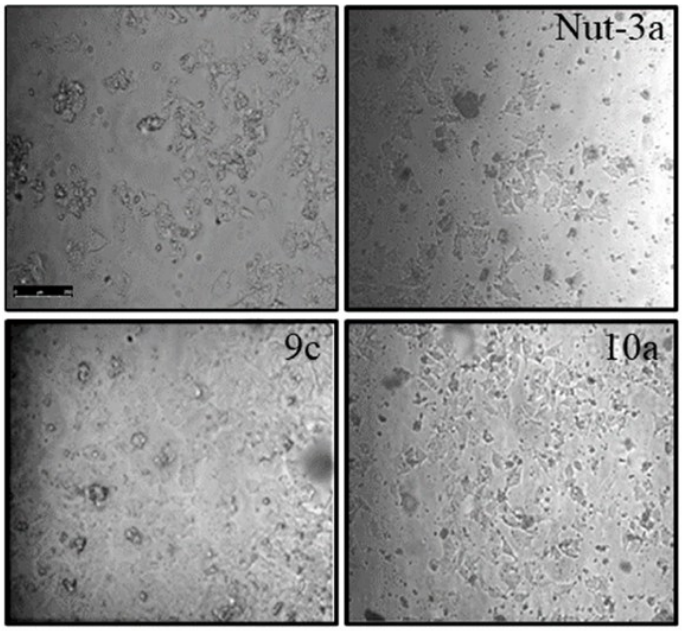

***Figure 92**. Cytomorphological alterations in vitro. Representative microphotographs at a 200× magnification (20× objective and a 10× eyepiece) by phase-contrast light microscopy of human melanoma A375 cells, treated or not (Ctrl) for 48 h with IC_{50} micromolar concentrations of **nutlin-3a** (Nut-3a) as a positive control for cytotoxic and antiproliferative effects and with IC_{50} concentrations of compounds **9c** and **10a**, respectively, showing the cellular morphological changes and the cytotoxic effects throughout bioscreens in vitro. Microphotographs are representative of three independent experiments. Scale bar: 250 µm.*

Cytomorphological analysis by phase-contrast light microscopy, performed to dynamically monitor the treated cell populations, revealed marked alterations consistent with the activation of programmed cell-death pathways (**Figure 92**). In particular, microscopic analyses showed that the reduction in the cell survival index was associated with evident cytotoxic effects and with the appearance of characteristic morphological hallmarks of apoptosis.

Specifically, the onset of apoptosis was indicated by membrane blebbing and cell shrinkage, eventually leading to the formation of balloon-like structures suggestive of plasma membrane disintegration. In addition to losing their normal morphology, cells displayed a pronounced rounding-up phenotype after 48 hours of incubation, together with enhanced surface blebbing and progressive shrinkage.

To confirm the possible activation of apoptosis, fluorescence microscopy experiments were then performed to simultaneously detect apoptotic and/or necrotic cells and to further investigate the biological effects induced in A375 cells by exposure to the most active derivatives under investigation (**Figure 93**).

Using the phosphatidylserine (PS) sensor (FITC), a consistent activation of apoptosis was observed in A375 cells following 48 h exposure to IC_{50} concentrations of **9c** and **10a**. During apoptosis, PS is translocated from the inner to the outer leaflet of the plasma membrane, where it serves as an early/intermediate hallmark of programmed cell death. The appearance of PS on the cell surface, detected as green fluorescence, therefore confirmed the onset of apoptotic processes. Notably, the fluorescence patterns observed for both derivatives closely resembled those produced by **nutlin-3a**, used as a positive control. Furthermore, no evidence of concurrent necrotic phenomena was detected under the same experimental conditions (absence of red fluorescence, TRITC filter; **Figure 93**). Taken together, these findings indicate that the anticancer activity of the new TSP derivatives, similarly to that observed for the reference compound 1 [205], is primarily associated with their ability to activate apoptotic cell-death pathways.

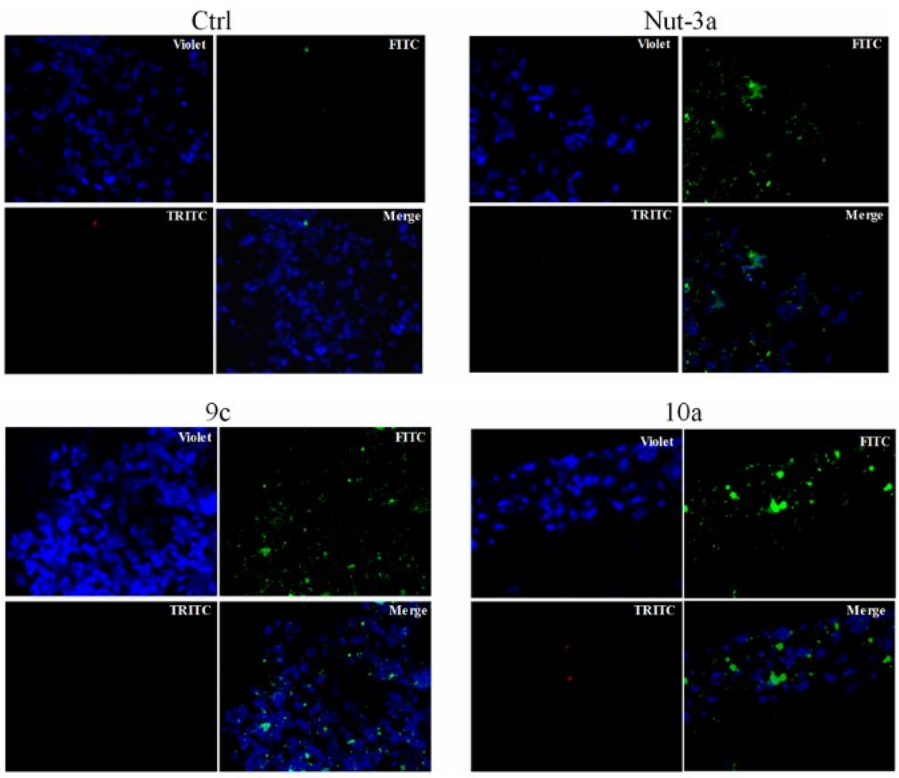

Figure 93. *Apoptosis and necrosis detection in human A375 melanoma cells. Apoptosis/necrosis detection by fluorescent microscopy analysis showing the whole cells (CytoCalcein Violet 450 cell cytoplasm labeling dye, violet channel), the phosphatidylserine (PS) early apoptotic sensor (green fluorescence, FITC filter), and the red membrane-impermeable 7-AAD dye to label the nucleus of necrotic cells (red fluorescence, TRITC filter) in control A375 cultures (Ctrl) or A375 treated with* IC_{50} *of* ***nutlin-3a*** *for 48 h or with* IC_{50} *of compounds* ***9c*** *and* ***10a*** *for 48 h, respectively. In merged images (Merge), individual fluorescent patterns from each channel from the same cell population were overlapped as shown. The displayed fluorescence images are representative of three independent experiments.*

8.2.4 Computational Studies

8.2.4.1 Conformational Analysis

The conformational properties of compounds **9a–i, 10a,** and **(±)-10b** were investigated through an in-depth conformational analysis combining force-field-based and quantum mechanical computational methods. In previous studies, the conformational behavior of related TSP derivatives had been examined using semi-empirical PM6[206] calculations performed in vacuum [200]. In the present work, a more accurate description of molecular geometry and energetics was achieved by applying density functional theory (DFT) methods [207] in combination with the conductor-like polarizable continuum model (C-PCM) [208] to simulate an aqueous environment.

The calculations revealed two parallel sets of specular conformers for each compound, characterized by identical conformational energies and absolute torsion angle values but opposite signs. These mirror-image conformers represent conformational enantiomers, here designated as E1 and E2 (**Table 13**). For the chiral compound **10b**, tested as a racemic mixture, the specular conformers correspond to those of the enantiomer with opposite configuration.

The low-energy conformers of **compounds 1, 9a–i,** and **10a** ($\Delta E < 2$ kcal/mol) could be clustered into two major conformational families, TCC and TCT, according to the antiperiplanar (T) or synperiplanar (C) orientations of torsion angles τ_1, τ_2, and τ_3 (**Figure S4; Table 13**). The TCC family was slightly favored over the TCT family, both in terms of conformer population (~28% vs. ~25%) and conformational energy. In compound **(±)-10b**, the carbonyl group at C4 is reduced to a hydroxyl group, which changes the hybridization of torsion angle τ_3

from sp^2 to sp^3. Compound **(±)-10b** exhibited the same conformational preference as **compounds 1, 9a–i,** and **10a** with respect to torsion angles τ_1 and τ_2 (family TC), while showing three different orientations of the Z ring (Figure 5D). For compound **9g**, the low-energy conformers displayed τ_1 and τ_2 values consistent with the TC family (the most favored also in this case) and the TT family. In **9g**, the Z ring is shifted from the carbonyl group at C4 (whose orientation is defined by τ_3) to the C5 position. In this case, the τ_3 torsion angle consistently adopted a synperiplanar (C) conformation with respect to C5 (**Figure 94 C**).

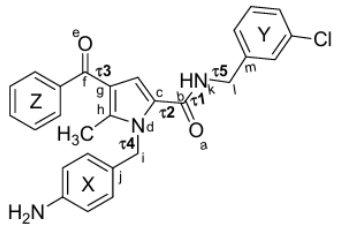

Family [a]	Sub-Family	ΔE_{GM} (kcal/mol)	Distances (Å)			Torsional Angles (°) [b–f]				
			d1 (X-Y)	d2 (X-Z)	d3 (Y-Z)	τ1	τ2	τ3	τ4	τ5
TCC	I	0.00	6.4	8.7	9.3	−174	26	−21	77	−112
TCC	II	0.49	5.6	9.3	10.2	−174	28	22	75	−82
TCT	I	1.57	7.4	7.2	11.0	−174	27	−148	102	−111
TCT	III	1.65	9.7	7.2	10.7	−173	27	−148	101	123

Table 13*. Conformational energy, structural classification, and pharmacophore distances (Å) of calculated DFT conformers of* ***10a****.*

Notably, all compounds exhibited the same conformational preference for torsion angles τ_1 and τ_2 (TC family) and similar τ_4 values (~90°). This feature is likely due to the formation of an intramolecular hydrogen bond between the carbonyl group of the amide function and the X aromatic ring (**Figure 94**). In summary, the low-energy conformers of the new TSP derivatives, as well as those of the reference **compound 1**, can be classified into two main conformational

families characterized by similar τ_1, τ_2, and τ_4 values, while differing primarily in τ_3 and τ_5. Comparison between the present results and those previously obtained [200] highlights some important differences. Specifically: (i) in the former PM6-based study, low-energy conformers included the cis conformation of the amide bond (τ_1), and (ii) the TCC and TCT families showed a shorter distance between the X and Y aromatic rings than that predicted by the present DFT calculations, likely due to overestimation of intramolecular interactions in the absence of solvent effects.

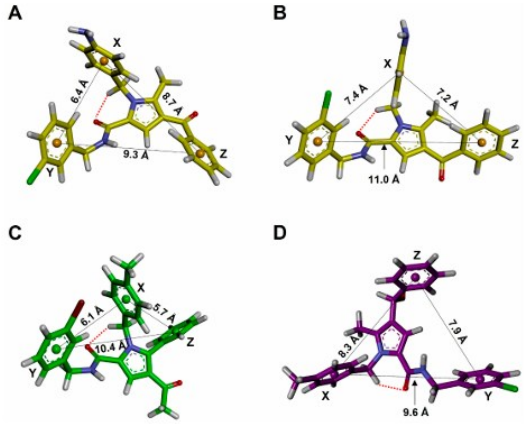

***Figure 94**. DFT lowest-energy conformers of TSP conformational families: TCC I (**10a**; (**A**)), TCT I (**10a**; (**B**)), TCC I (**9g**; (**C**)), and TCG⁻ III (R-**10b**; (**D**)). The intramolecular distances between the X, Y, and Z rings are reported.*

8.2.4.2 Investigation of the Peptidomimetic Ability of the New TSPs

To identify the helix-based hydrophobic motif(s) whose consensus structures (i.e., the spatial orientation of hot-spot residues) can be mimicked by TSPs, the peptidomimetic ability of **compounds 1, 9a–i, 10a**, and **(±)-10b** was investigated through a comparative analysis

between their low-energy DFT conformers and the experimentally determined structures of hydrophobic PPI motifs (coiled coil and LxxLL). In particular, the TSP conformers were grouped according to their intramolecular distances. The hot-spot residues of the selected PPI motifs were identified, and the distances between the centroids of their interacting side chains were compared with the distances between the centroids of the X, Y, and Z aromatic rings in the TSP conformers.

Pharmacophore	TSP Ring	PPI Motif			
		^{23}VxxLxxxV^{30}		^{14}LxxxLxxL^{21}	
		Hot-Spot Residues [a]			
1	X	i + 3	**i + 3**	**i + 4**	i + 4
	Y	i	**i + 7**	**i**	i + 7
	Z	i + 7	**i**	**i + 7**	i
2	X	i + 3	**i + 3**	**i + 4**	i + 4
	Y	i	**i + 7**	**i**	i + 7
	Z	i + 7	**i**	**i + 7**	i
3	X	i + 3	**i + 3**	**i + 4**	i + 4
	Y	i	**i + 7**	**i**	i + 7
	Z	i + 7	**i**	**i + 7**	i
4	X	i	**i + 7**	**i**	i + 7
	Y	i + 7	**i**	**i + 7**	i
	Z	i + 3	**i + 3**	**i + 4**	i + 4

[a] The PPI residues mimicked by the conformational enantiomer E2 or by the configurational enantiomer S of **10b** are evidenced in bold.

Table 14. *Correspondence between the aromatic rings of TSP derivatives and the interacting residues of the considered PPI motifs obtained by the structural superimposition.*

Conformers that met the predefined distance similarity criteria were superimposed on the PPI motifs by fitting the centroids of the aromatic rings X, Y, and Z onto the centroids of the hot-spot side chains. Conformers with a calculated root-mean-square deviation (RMSD) value below 2.5 Å were considered mimetic of the corresponding PPI motif. Four distinct pharmacophoric models were identified (corresponding to the conformers shown in **Figure 94**), each capable

of reproducing the intramolecular distances between the hot-spot residues of hydrophobic PPI motifs involved in the formation of parallel and antiparallel coiled-coil structures (**Table 13**).

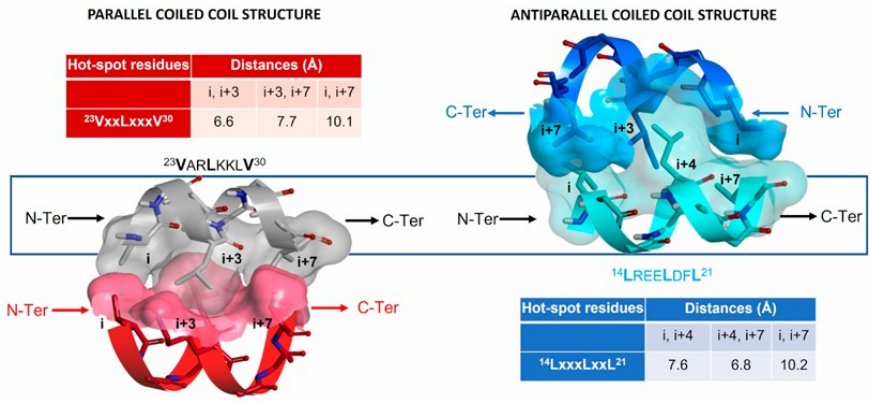

***Figure 95**. Parallel (left) and antiparallel (right) coiled coil structures (PDB: 2ZTA and 1GRJ, respectively). The two interacting coiled coil motifs are represented as ribbons, the heavy atoms and the polar hydrogens of the hot-spot residues are displayed as sticks and colored by atom type, the residue position is labeled, and the solvent accessible surface is shown. A dark blue frame evidences the coiled coil motifs mimicked by the TSPs; the sequence of the motif is reported together with the distances between the hot-spot residues (red and blue tables).*

Notably, the orientation of the TSP pharmacophoric moieties (i.e., X, Y, and Z rings) and the presence of conformational enantiomers reflect structural features typical of PPI motifs forming parallel and antiparallel coiled coils. The i + 3 and i + 4 hot-spot residues of the parallel and antiparallel coiled coil structures are symmetrically positioned with respect to the helix axis and to the other hot-spot residues i and i + 7, thus allowing the recognition of two different faces of the α-helix in the two types of PPI (parallel and antiparallel coiled coil structures; **Figure 95**).

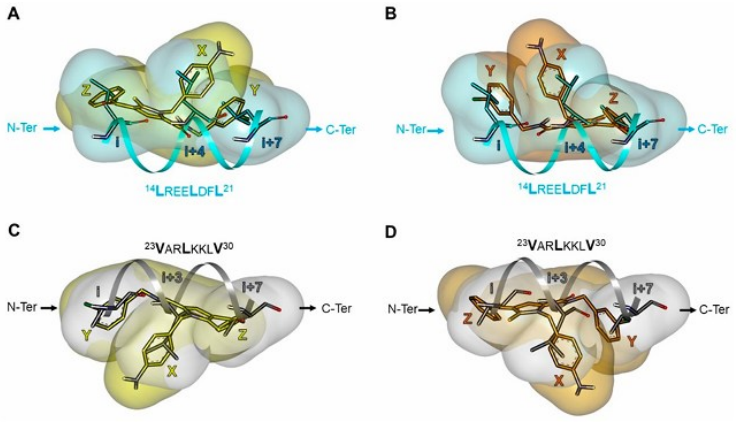

Figure 96. *TCC I conformer of* ***10a*** *(i.e., pharmacophore 1) superimposed on the hot-spot residues of coiled coil motifs involved in the formation of parallel and antiparallel PPI. E1 conformational enantiomer (yellow) superimposed on the "antiparallel" (cyan; (**A**)) and parallel (white; (**C**)) coiled coil motif; E2 conformational enantiomer (orange) superimposed on the "antiparallel" (cyan; (**B**)) and parallel (white; (**D**)) coiled coil motif. The centroids of the X, Y, and Z rings are superimposed on the centroids of the side chains of the hot-spot residues. The heavy atoms and the polar hydrogens of* ***10a*** *and the hot-spot residues are displayed as sticks and colored by atom type. Molecular volumes are showed as soft surface.*

A comparable structural relationship was observed between the conformational/configurational enantiomers of the TSP derivatives (**figure 95**), and this feature may contribute to their peptidomimetic properties. The distance between the Y and Z rings represents the longest intra-molecular distance (~10 Å; **figure 94A–C**) and the X ring mimics the "central" hot-spot residue of the motif (i.e., i + 3 or the i + 4 in parallel or antiparallel coiled coil structure, respectively). The Y and Z rings can alternately mimic the hot-spot residue i or i + 7 depending (a) on the enantiomer when comparing the two enantiomers to the same PPI motif (**figure 96** vs. **figure 96B** and **figure 96C** vs. **figure 96D**) or (b) on the PPI motif when comparing the same

enantiomer to the two motifs (**figure 96A** vs. **figure 96C** and **figure 96B** vs. **figure 96D**). Only in one pharmacophoric model of **(±)-10b** (no. 4 in **Table 13**) was the distance between the X and Y rings the longest (~10 Å; **Figure 94D**). In this case, the Z ring mimics the "central" hot-spot residue of the motif, whereas the X and Y rings alternately reproduce the i or i + 7 residues. Pharmacological studies have shown that the anticancer activity of TSPs is associated with the activation of apoptotic cell-death pathways, confirming the mechanism of action previously proposed for **compound 1** [205] and consistent with the present computational results. This suggests that the newly synthesized TSPs share the same biological mechanism. Previous pharmacological investigations on the effects of **compound 1** in melanoma cells (M14 [200] and A375 [205]) demonstrated its ability to impair melanoma viability by reducing the p53–MDM2 interaction and restoring p53 functionality and transcriptional activity. Melanoma is one of the few cancers in which p53 is rarely mutated; however, its inactivation may occur indirectly through sustained activation of MDM2 due to deletions in the CDKN2A (Cyclin-Dependent Kinase Inhibitor 2A) locus, which encodes for p14ARF [209]. P14ARF is a tumor suppressor protein that regulates p53 function by inhibiting the formation of the p53–MDM2 complex, which otherwise leads to p53 degradation. Specifically, the N-terminal 37 amino acids of p14ARF bind to a region of MDM2 distinct from the p53-binding site, sequestering MDM2 within nucleoli and promoting cell cycle arrest [210]. Based on the hypothesis that TSP derivatives could mimic p14ARF in its interaction with MDM2, a bioinformatic and structural analysis was carried out on the first two N-terminal helices of p14ARF

(αH1: residues 4–14; αH2: residues 20–29) using the X-ray structure of the mouse p19ARF tumor suppressor protein (PDB ID: 1HN3; **Figure S6**). Interestingly, the αH2 helix of p14ARF displayed a coiled-coil-like motif characterized by hydrophobic residues at positions i, i + 3, i + 4, and i + 7 (i.e., ^{220}VRVFVVHI^{27}). Remarkably, this motif lies within a region of p14ARF known to interact with MDM2, acting as a negative allosteric modulator of p53–MDM2 binding [210].

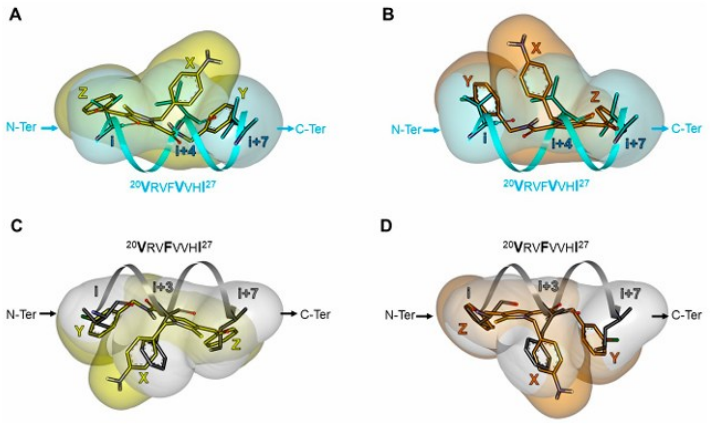

Figure 97*. TCC I conformer of* ***10a*** *(i.e., pharmacophore 1) superimposed on the coiled coil motif present on αH2 of p14ARF. E1 conformational enantiomer (yellow) superimposed on the i, i + 4, and i + 7 residues (cyan; (****A****)) and the i, i + 3, and i + 7 residues (white; (****C****)); E2 conformational enantiomer (orange) superimposed on the i, i + 4, and i + 7 residues (cyan; (****B****)) and the i, i + 3, and i + 7 residues (white; (****D****)). The centroids of the X, Y, and Z rings are superimposed on the centroids of the side chains of the hot-spot residues. The heavy atoms and the polar hydrogens of* ***10a*** *and of the hot-spot residues are displayed as sticks and colored by atom type. Molecular volumes are showed as soft surface.*

Therefore, it can be hypothesized that TSP derivatives capable of reproducing key hot-spot residues involved in the p14ARF–MDM2 interaction might also bind to MDM2, leading to a decreased formation

of the p53–MDM2 complex (**Figure 97**). However, no experimental structural data are currently available for the p14ARF–MDM2 complex; thus, detailed modeling of the interaction between TSPs and MDM2 is not yet feasible and will require future dedicated studies.

8.2.4.3 SAR Analysis

Once it was established that all the compounds share the ability to reproduce, through their X, Y, and Z aromatic rings, the spatial orientation of the side chains corresponding to the i, i + 3/4, and i + 7 residues of a coiled-coil PPI motif, we attempted to rationalize the observed structure–activity relationships (SARs) by distinguishing the contributions of pharmacokinetic and pharmacodynamic properties to the overall biological activity.

The calculated cLogD values for **nutlin-3a, 1**, and the new TSP derivatives **9a–i** and **10a,b** were approximately 5 or higher, indicating a high degree of lipophilicity, consistent with the findings from the solubility assays.

In light of the obtained results, some considerations can be made: (i) a large number of compounds show the same solubility but different activity, and (ii) although no relationships were found between compound activity and solubility (R2 = 0.2963), the two compounds nevertheless show significantly higher solubility; **(±)-10b** and **10a** are the most active ones. In detail, the introduction of an NH_2 group as the R_1 substituent (**10a**) and the reduction of the carbonyl group **((±)-10b)** both resulted in increased solubility and enhanced antiproliferative activity. These findings suggest that pharmacokinetic factors may have contributed to the improved biological profiles of these derivatives.

Conversely, substitution of the CH_3 group with a fluorine atom in the para position of the X ring (**9c**), shifting the chlorine atom from the meta to the para position on the Y ring (**9d**), or introducing a methoxy group in the para position of the Z ring (**9i**) led to increased activity that was not associated with improved solubility. Similarly, replacement of the Z phenyl ring with a methyl group at C5 (9g) maintained biological activity despite reduced solubility (**Figure 98**).

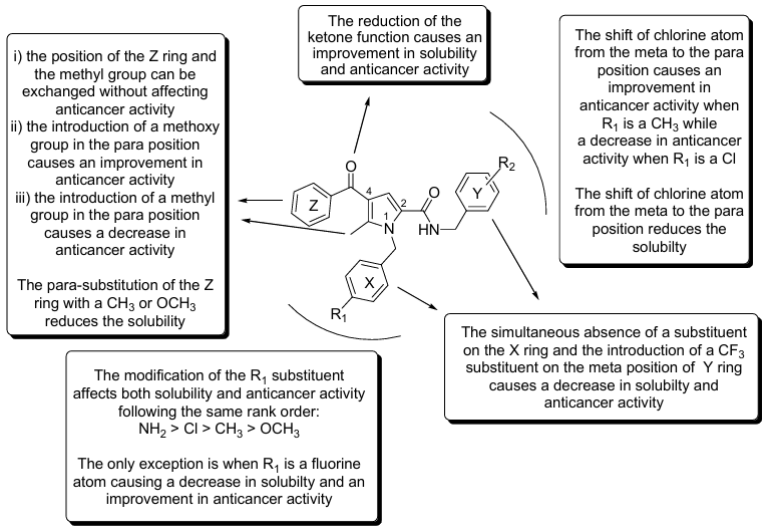

***Figure 98**. Schematic representation of the SARs of new TSP derivatives.*

8.3 Conclusions

Starting from the previously identified hit **compound 1**, a small and rationally designed series of new anticancer TSP derivatives was developed, leading to the identification of a new hit, **10a**, characterized by improved solubility and the highest antiproliferative activity among both the newly synthesized and previously reported TSPs. The combination of computational and experimental investigations enabled

the refinement of the 3D pharmacophore model and clarified the influence of specific substituents on the pharmacokinetic and pharmacodynamic properties of these compounds. Altogether, the results support the hypothesis that the anticancer activity of TSP derivatives is related to their ability to reproduce structural motifs involved in PPIs that activate apoptotic cell-death pathways.

In particular, the new TSPs share distinctive structural features with the hot-spot residues of protein motifs forming parallel and antiparallel coiled-coil structures, such as those present in the N-terminal domain of the tumor suppressor $p14^{ARF}$.

However, although this study confirmed that tetrasubstituted pyrrole derivatives represent a promising scaffold for mimicking protein–protein interaction hot-spot residues, several limitations remain unresolved and require further investigations. The antiproliferative activities of the tested compounds are moderate, with the IC_{50} values in the micromolar range and selectivity toward melanoma cells remains limited. A critical issue is their low and ion-sensitive solubility, which not only complicates formulation but may also mask the true biological potential of these compounds. Only compound **10a** showed an improvement of solubility in water respect to the previous reported compound 1. Poor solubility can lead to reduced effective concentrations at the cellular level, underestimating intrinsic potency. To address this, future work should explore strategies such as the use of specific delivery systems or solubilizing excipients in cell-based assays that could help verify whether limited activity is due to poor solubility rather than weak target recognition.

Furthermore, to support the molecular modeling hypotheses, direct experimental validation is essential. Specific biophysical binding or cell-based functional assays could confirm interaction with the intended PPI interface. Combining these approaches with computational refinement will provide a robust framework for correlating predicted pharmacophore features with observed biological activity.

8.4 Materials and Methods

Chemistry

Melting points were measured on a Gallenkamp melting point apparatus. NMR spectra were acquired on a Bruker Avance 300 MHz or a Bruker Ascend 400 MHz spectrometer. Splitting patterns are described as singlet (s), doublet (d), triplet (t), quartet (q), quintuplet (qt), and broad (br). Mass spectra were obtained by electrospray ionization (ESI-HRMS, positive mode) using an LTQ Orbitrap XL mass spectrometer (Thermo Fisher Scientific, San Jose, CA, USA) equipped with Xcalibur software. The Orbitrap mass analyzer was calibrated according to the manufacturer's directions using a mixture of caffeine, methionine, arginine, phenylalanine, and alanine acetate (MRFA) and Ultramark 1621 in a solution of acetonitrile, methanol, and acetic acid. Chromatographic separations were performed on silica gel (Kieselgel 40, 0.040–0.063 mm, Merck KGaA, Darmstadt, Germany). Reactions and product mixtures were routinely monitored by thin-layer chromatography (TLC) on Merck 0.2 mm precoated silica (60 F254) aluminium sheets with visualization by irradiation with a UV lamp. All starting materials, reagents, and solvents (reagent-

grade) were purchased from Sigma-Aldrich and used without further purification. Compounds 1, 3, 4, 6a,b, 7a, 7e, 7f, 8a, 8e, 8f and 9j were obtained as previously reported [200].

Methyl 5-methyl-4-(4-methylbenzoyl)-1H-pyrrole-2-carboxylate (6c)

To a suspension of methyl 2-(N-(tert-butoxycarbonyl)-4-methylphenyl-sulfonamido)acrylate 4 (0.925 g, 2.60 mmol) in dry ACN (20 mL), 1-(p-tolyl)butane-1,3-dione **5b** (0.504 g, 2.86 mmol) and Cs_2CO_3 (1.27 g, 3.90 mmol) were added, and the resulting mixture was stirred at room temperature for 12 h. Then, the solvent was removed under reduced pressure, and the resulting residue was dissolved in EtOAc and washed with H_2O. The organic phase was dried (Na_2SO_4) and filtered, and the solvent was removed under vacuum. The resulting residue was dissolved in DCM (18 mL), and trifluoroacetic acid (TFA) (2.0 mL) was added. After 12 h, the organic phase was washed with brine (2 × 25 mL) and 1 M NaOH (2 × 20 mL), dried (Na_2SO_4), and filtered, and the solvent was removed under vacuum. The resulting residue was purified by silica gel flash column chromatography (mobile phase: EtOAc/petroleum ether, 40–60 °C, 1:1 v/v) to provide the title compound as a white powder. Yield: 65%. ^{1}H NMR (300 MHz, $CDCl_3$) δ: 2.45 (s, 3H), 2.65 (s, 3H), 3.87 (s, 3H), 7.11 (s, 1H), 7.28 (d, 2H, J = 7.6 Hz), 7.73 (d, 2H, J = 7.9 Hz), 9.56 (brs, 1H).

Methyl 4-(4-methoxybenzoyl)-5-methyl-1H-pyrrole-2-carboxylate (6d)

Starting from 1-(4-methoxyphenyl)butane-1,3-dione **5c** and following the same procedure described for 6c, the title compound was obtained

as a white powder. Yield: 58%. ^{1}H NMR (300 MHz, $CDCl_3$) δ: 2.64 (s, 3H), 3.88 (s, 3H), 3.90 (s, 3H), 6.98 (d, 2H, J = 8.7 Hz), 7.12 (s, 1H), 7.85 (d, 2H, J = 8.7 Hz), 9.52 (brs, 1H).

General Procedure for the Synthesis of Esters (7a–i)

Sodium hydroxide (8 mL, 50% w/v) and tetra-n-butylammonium hydroxide (TBAH) (0.5 mL, 40% w/v) were added to a stirred mixture of esters **6a–d** (1 mmol) in dichloromethane (12 mL) at 0 °C. After 15 min, a solution of the appropriate aryl bromide (1.5 mmol) in dichloromethane (5 mL) was added dropwise. The resulting mixture was allowed to warm to room temperature, stirred in these conditions for 18h, and then washed with H_2O, 2M HCl, and brine. The organic phase was dried (Na_2SO_4) and filtered, and the solvent was removed under vacuum. The resulting residue was purified by silica gel flash chromatography (mobile phase: EtOAc/n-hexane, 1:4 v/v).

Methyl 4-benzoyl-1-(4-chlorobenzyl)-5-methyl-1H-pyrrole-2-carboxylate (7b)

White powder. Yield: 67%. ^{1}H NMR (300 MHz, $CDCl_3$) δ: 2.58 (s, 3H), 3.77 (s, 3H), 5.69 (s, 2H), 6.96 (d, 2H, J = 8.2 Hz), 7.26–7.32 (m, 3H), 7.48–7.61 (m, 3H), 7.83 (d, 2H, J = 7.1 Hz).

Methyl 4-benzoyl-1-(4-methoxybenzyl)-5-methyl-1H-pyrrole-2 carboxylate (7c)

White powder. Yield: 74%. ^{1}H NMR (300 MHz, $CDCl_3$) δ: 2.62 (s, 3H), 3.80 (s, 3H), 3.82 (s, 3H), 5.68 (s, 2H), 6.88 (d, 2H, J = 8.7 Hz),

7.00 (d, 2H, J = 8.7 Hz), 7.26 (s, 1H), 7.49–7.61 (m, 3H), 7.84 (d, 2H, J = 8.4 Hz).

Methyl 4-benzoyl-1-(4-fluorobenzyl)-5-methyl-1H-pyrrole-2-carboxylate (7d)

White solid. Yield: 66%, mp: 87–89 °C. ^{1}H NMR (300 MHz, $CDCl_3$) δ: 2.58 (s, 3H), 3.77 (s, 3H), 5.68 (s, 2H), 7.01 (m, 4H), 7.26 (s, 1H), 7.46–7.57 (m, 3H), 7.82 (d, 2H, J = 6.8 Hz).

Methyl-4-acetyl-1-(4-methylbenzyl)-5-phenyl-1H-pyrrole-2-carboxylate (7g)

White solid. Yield: 77%, mp: 116–118 °C. ^{1}H NMR (300 MHz, $CDCl_3$) δ: 2.13 (s, 3H), 2.30 (s, 3H), 3.81 (s, 3H), 5.39 (s, 2H), 6.68 (d, 2H, J = 8.0 Hz), 7.03 (d, 2H, J = 8.0 Hz), 7.23 (d, 2H, J = 8.0 Hz), 7.37–7.47 (m, 3H), 7.58 (s, 1H).

Methyl 5-methyl-4-(4-methylbenzoyl)-1-(4-methylbenzyl)-1H-pyrrole-2-carboxylate (7h)

White solid. Yield: 73%, mp: 110–112 °C. ^{1}H NMR (300 MHz, $CDCl_3$) δ: 2.33 (s, 3H), 2.45 (s, 3H), 2.57 (s, 3H), 3.77 (s, 3H), 5.68 (s, 2H), 6.91 (d, 2H, J = 7.5 Hz), 7.13 (d, 2H, J = 7.5 Hz), 7.26–7.31 (m, 3H), 7.75 (d, 2H, J = 7.8 Hz).

Methyl 4-(4-methoxybenzoyl)-5-methyl-1-(4-methylbenzyl)-1H-pyrrole-2-carboxylate (7i)

White solid. Yield: 79%, mp: 129–132 °C. ^{1}H NMR (300 MHz, $CDCl_3$) δ: 2.33 (s, 3H), 2.54 (s, 3H), 3.77 (s, 3H), 3.90 (s, 3H), 5.67 (s,

2H), 6.91 (d, 2H, J = 7.5 Hz), 6.98 (d, 2H, J = 7.9 Hz), 7.13 (d, 2H, J = 7.8 Hz), 7.27 (s, 1H), 7.86 (d, 2H, J = 7.2 Hz).

General Procedure for the Synthesis of Acids (8a–i)

To a solution of esters **7a–i** (1 mmol) in methanol (10 mL), 2M NaOH (5 mmol) was added, and the resulting mixture was refluxed until no starting material was detected by TLC (DCM as eluent). The solvent was removed under reduced pressure; then, the residue was acidified with 2M HCl (pH ~ 3) and extracted with EtOAc. The organic phase was dried (Na_2SO_4) and filtered, and the solvent was removed under vacuum. The resulting residue was purified by silica gel flash chromatography (mobile phase EtOAc/EtOH, 9:1 v/v, as eluent) and recrystallized from ethyl ether/petroleum ether (40–60 °C).

4-Benzoyl-1-(4-chlorobenzyl)-5-methyl-1H-pyrrole-2-carboxylic acid (8b)

White solid. Yield: 95%, mp: 163–165 °C. ^{1}H NMR (300 MHz, DMSO-d6) δ: 2.45 (s, 3H), 5.73 (s, 2H), 7.02 (s, 1H), 7.05 (s, 2H), 7.40 (d, 2H, J = 8.4 Hz), 7.52–7.65 (m, 3H), 7.72 (d, 2H, J = 6.8 Hz).

4-Benzoyl-1-(4-methoxybenzyl)-5-methyl-1H-pyrrole-2-carboxylic acid (8c)

White solid. Yield: 97%. ^{1}H NMR (300 MHz, $CDCl_3$) δ: 2.61 (s, 3H), 3.81 (s, 3H), 5.64 (s, 2H), 6.87 (d, 2H, J = 8.6 Hz), 6.99 (d, 2H, J = 8.5 Hz), 7.40 (s, 1H), 7.48–7.61 (m, 3H), 7.84 (d, 2H, J = 7.2 Hz).

4-Benzoyl-1-(4-fluorobenzyl)-5-methyl-1H-pyrrole-2-carboxylic acid (8d)

White solid. Yield: 96%, mp: 187–188 °C. ^{1}H NMR (300 MHz, DMSO-d6) δ: 2.50 (s, 3H), 5.73 (s, 2H), 7.07 (m, 3H), 7.18 (m, 2H), 7.51–7.64 (m, 3H), 7.72 (d, 2H, J = 7.2 Hz).

4-Acetyl-1-(4-methylbenzyl)-5-phenyl-1H-pyrrole-2-carboxylic acid (8g)

White solid. Yield: 78%, mp: 173–175 °C. ^{1}H NMR (300 MHz, $CDCl_3$) δ: 2.14 (s, 3H), 2.30 (s, 3H), 5.37 (s, 2H), 6.68 (d, 2H, J = 7.7 Hz), 7.03 (d, 2H, J = 7.7 Hz), 7.23 (d, 2H, J = 7.1 Hz), 7.38–7.49 (m, 3H), 7.69 (s, 1H).

5-Methyl-4-(4-methylbenzoyl)-1-(4-methylbenzyl)-1H-pyrrole-2-carboxylic acid (8h)

White solid. Yield: 93%, mp: 193–195 °C. ^{1}H NMR (300 MHz, $CDCl_3$) δ: 2.33 (s, 3H), 2.45 (s, 3H), 2.56 (s, 3H), 5.65 (s, 2H), 6.91 (d, 2H, J = 7.2 Hz), 7.13 (d, 2H, J = 7.2 Hz), 7.28 (d, 2H, J = 7.5 Hz), 7.38 (s, 1H), 7.74 (d, 2H, J = 7.8 Hz).

4-(4-Methoxybenzoyl)-5-methyl-1-(4-methylbenzyl)-1H-pyrrole-2-carboxylic acid (8i)

White solid. Yield: 93%, mp: 202–204 °C. ^{1}H NMR (300 MHz, $CDCl_3$) δ: 2.33 (s, 3H), 2.54 (s, 3H), 3.90 (s, 3H), 5.65 (s, 2H), 6.91 (d, 2H, J = 7.6 Hz), 6.98 (d, 2H, J = 8.4 Hz), 7.12 (d, 2H, J = 7.7 Hz), 7.39 (s, 1H), 7.85 (d, 2H, J = 8.4 Hz).

General Procedure for the Synthesis of Compounds (9a–i)

To a solution of the acids 8a–i (1 mmol) in DMF (5 mL), HOBT (2.5 mmol) and HBTU (2.5 mmol) were added, and the resulting mixture was stirred for 20 min at room temperature. Then, N-methylmorpholine (NMM) (5 mmol) and the appropriate amine (2.5 mmol) were added, and the resulting mixture was stirred at room temperature for 12 h. The solvent was removed under reduced pressure, and the resulting residue was taken up in EtOAc and washed successively with 2M $KHSO_4$, saturated solution of $NaHCO_3$, and brine. The organic phase was dried (Na_2SO_4), filtered, and concentrated under reduced pressure. The residue was purified by silica gel flash chromatography (mobile phase: EtOAc/petroleum ether (40–60 °C) 1:1 v/v as eluent) and recrystallized from EtOAc/n-hexane to provide the title compounds 9a–i in good yields.

4-Benzoyl-N-(3-chlorobenzyl)-1-(4-chlorobenzyl)-5-methyl-1H-pyrrole-2-carboxamide (9a)

White solid. Yield: 89%, mp: 117–119 °C. ^{1}H NMR (400 MHz, $CDCl_3$) δ: 2.57 (s, 3H), 4.51(d, 2H, J = 6.0 Hz), 5.75 (s, 2H), 6.27 (brt, 1H, J = 3.4 Hz), 6.88 (s, 1H), 7.02 (d, 2H, J = 8.4 Hz), 7.10 (d, 1H, J = 6.0 Hz), 7.25–7.34 (m, 5H), 7.49–7.53 (m, 2H), 7.57–7.61 (m, 1H), 7.82 (d, 2H, J = 8.4 Hz); ^{13}C NMR (101 MHz, $CDCl_3$) δ: 12.2, 43.1, 47.9, 115.6, 120.5, 124.8, 126.0, 128.0 (2C), 128.1, 128.6, 129.3, 129.4, 130.3, 132.0, 133.6, 134.9, 136.1, 140.2, 140.6, 142.0, 161.6, 192.3. HRMS (ESI, m/z) $[M + H]^+$ calcd. for $[C_{27}H_{23}Cl_2N_2O_2]^+$ 477.1131; found 477.1126.

4-Benzoyl-N-(3-chlorobenzyl)-1-(4-methoxybenzyl)-5-methyl-1H-pyrrole-2-carboxamide (9b)

White solid. Yield: 81%, mp: 137–138 °C. ^{1}H NMR (300 MHz, $CDCl_3$) δ: 2.56 (s, 3H), 3.79 (s, 3H), 4.48 (d, 2H, J = 5.9 Hz), 5.66 (s, 2H), 6.15 (brt, 1H, J = 5.4 Hz), 6.80 (s, 1H), 6.84 (d, 2H, J = 7.6 Hz), 7.00 (d, 2H, J = 8.3 Hz), 7.07 (d, 1H, J = 4.8 Hz), 7.19–7.27 (m, 3H), 7.44–7.57 (m, 3H), 7.77 (d, 2H, J = 7.9 Hz); ^{13}C NMR (75 MHz, $CDCl_3$) δ: 12.3, 43.1, 47.9, 55.6, 114.5, 115.6, 120.3, 124.9, 126.1, 128.0, 128.1 (2C), 128.6, 129.4, 129.6, 130.3, 131.9, 134.9, 140.4, 140.7, 142.2, 159.2, 161.8, 192.3. HRMS (ESI, m/z) $[M + H]^+$ calcd. for $[C_{28}H_{26}ClN_2O_3]^+$ 473.1626; found 473.1623.

4-Benzoyl-N-(3-chlorobenzyl)-1-(4-fluorobenzyl)-5-methyl-1H-pyrrole-2-carboxamide (9c)

White solid. Yield: 69%, mp: 130–132 °C. ^{1}H NMR (300 MHz, $CDCl_3$) δ: 2.55 (s, 3H), 4.49 (d, 2H, J = 6.0 Hz), 5.71 (s, 2H), 6.25 (brt, 1H, J = 5.4 Hz), 6.85 (s, 1H), 6.99–7.10 (m, 5H), 7.21–7.29 (m, 3H), 7.45–7.59 (m, 3H), 7.77–7.81 (m, 2H); ^{13}C NMR (75 MHz, $CDCl_3$) δ: 12.2, 43.0, 47.9, 115.6, 116.0 (d, JCF = 21.6 Hz), 120.4, 124.7, 126.0, 128.0, 128.1, 128.3 (d, JCF = 8.1 Hz), 128.6, 129.4, 130.3, 132.0, 133.3 (d, JCF = 3.2 Hz), 134.9, 140.2, 140.6, 142.1, 161.6, 162.4 (d, JCF = 244.5 Hz), 192.3. HRMS (ESI, m/z)) $[M + H]^+$ calcd. for $[C_{27}H_{23}ClFN_2O_2]^+$ 461.1427; found 461.1422.

4-Benzoyl-N-(4-chlorobenzyl)-5-methyl-1-(4-methylbenzyl)-1H-pyrrole-2-carboxamide (9d)

White solid. Yield: 90%, mp: 154–156 °C. ^{1}H NMR (300 MHz, $CDCl_3$) δ: 2.37 (s, 3H), 2.58 (s, 3H), 4.49 (d, 2H, J = 5.9 Hz), 5.72 (s, 2H), 6.15 (brt, 1H, J = 5.6 Hz), 6.82 (s, 1H), 6.95 (d, 2H, J = 7.9 Hz), 7.15 (m, 4H), 7.28–7.30 (m, 2H), 7.47–7.60 (m, 3H), 7.81 (d, 2H, J = 6.9 Hz); ^{13}C NMR (75 MHz, $CDCl_3$) δ: 12.2, 21.4, 42.9, 48.2, 115.4, 120.3, 125.0, 126.5, 128.6, 129.1, 129.3, 129.4, 129.8, 131.9, 133.6, 134.6, 137.1, 137.3, 140.4, 142.2, 161.8, 192.4. HRMS (ESI, m/z) $[M + H]^+$ calcd. for $[C_{28}H_{26}ClN_2O_2]^+$ 457.1677; found 457.1669.

4-Benzoyl-N,1-bis(4-chlorobenzyl)-5-methyl-1H-pyrrole-2-carboxamide (9e)

White solid. Yield: 68%, mp: 147–149 °C. ^{1}H NMR (300 MHz, $CDCl_3$) δ: 2.52 (s, 3H), 4.44 (d, 2H, J = 5.9 Hz), 5.68 (s, 2H), 6.14 (brt, 1H, J = 5.4 Hz), 6.80 (s, 1H), 6.96 (d, 2H, J = 8.4 Hz), 7.10 (d, 2H, J = 8.4 Hz), 7.24–7.29 (m, 4H), 7.43–7.57 (m, 3H), 7.78 (m, 2H); ^{13}C NMR (75 MHz, $CDCl_3$) δ: 12.1, 42.9, 47.9, 115.5, 120.5, 124.8, 128.0, 128.6, 129.2, 129.3 (2C), 129.4, 132.0, 133.6, 133.7, 136.1, 137.0, 140.2, 142.0, 161.6, 192.3. HRMS (ESI, m/z) $[M + H]^+$ calcd. for $[C_{27}H_{23}Cl_2N_2O_2]^+$ 477.1131; found 477.1122.

4-Benzoyl-1-benzyl-5-methyl-N-(3-(trifluoromethyl)-benzyl)-1H-pyrrole-2-carboxamide (9f)

White solid. Yield: 87%, mp: 139–141 °C. ^{1}H NMR (400 MHz, $CDCl_3$) δ: 2.53 (s, 3H), 4.55 (d, 2H, J = 6.1 Hz), 5.74 (s, 2H), 6.21 (brt, 1H, J = 5.5 Hz), 6.83 (s, 1H), 7.02 (d, 2H, J = 6.5 Hz), 7.23–7.57 (m, 10H), 7.77 (m, 2H); ^{13}C NMR DEPT-q (101 MHz, $CDCl_3$) δ: 12.2, 43.1, 48.5, 115.7, 120.3, 124.3 (q, JCF = 273.7 Hz), 124.6 (m, 2C),

124.9, 126.5, 127.7, 128.6, 129.1, 129.4, 129.5, 131.2 (q, JCF = 32.3 Hz), 131.9, 137.5, 139.7, 140.3, 142.3, 161.8, 192.3. HRMS (ESI, m/z) $[M + H]^+$ calcd. for $[C_{28}H_{24}F_3N_2O_2]^+$ 477.1784; found 477.1767.

4-acetyl-N-(3-bromobenzyl)-1-(4-methylbenzyl)-5-phenyl-1H-pyrrole-2-carboxamide (9g)

White solid. Yield: 74%, mp: 157–159 °C. ^{1}H NMR (300 MHz, $CDCl_3$) δ: 2.13 (s, 3H), 2.48 (s, 3H), 4.67 (d, 2H, J = 5.8 Hz), 5.59 (s, 2H), 6.76 (brt, 1H, J = 5.8 Hz), 6.87 (d, 2H, J = 7.6 Hz), 7.21 (m, 3H), 7.33 (t, 1H, J = 7.5 Hz), 7.45 (m, 3H), 7.57–7.69 (m, 5H); ^{13}C NMR (75 MHz, $CDCl_3$) δ: 21.5, 29.4, 43.0, 49.1, 113.4, 123.0, 123.9, 126.4, 126.5, 129.0, 129.4, 129.9, 130.5, 130.8 (2C), 131.0, 131.4, 135.4, 137.1, 140.9, 143.0, 161.8, 194.3. HRMS (ESI, m/z) $[M + H]^+$ calcd. for $[C_{28}H_{26}BrN_2O_2]^+$ 501.1172; found 501.1159.

N-(3-chlorobenzyl)-5-methyl-4-(4-methylbenzoyl)-1-(4-methylbenzyl)-1H-pyrrole-2-carboxamide (9h)

White solid. Yield: 78%, mp: 134–136 °C. ^{1}H NMR (300 MHz, $CDCl_3$) δ: 2.36 (s, 3H), 2.46 (s, 3H), 2.55 (s, 3H), 4.50 (d, 2H, J = 5.8 Hz), 5.72 (s, 2H), 6.26 (brt, 1H, J = 6.2 Hz), 6.87 (s, 1H), 6.96 (d, 2H, J = 7.5 Hz), 7.09–7.16 (m, 3H), 7.22–7.31 (m, 5H), 7.72 (d, 2H, J = 8.0 Hz); ^{13}C NMR (75 MHz, $CDCl_3$) δ: 12.2, 21.4, 21.9, 43.0, 48.2, 115.5, 120.4, 124.7, 126.1, 126.5, 127.9, 128.0, 129.2, 129.6, 129.7, 130.2, 134.5, 134.8, 137.3, 137.6, 140.7, 142.0, 142.6, 161.7, 192.1. HRMS (ESI, m/z) $[M + H]^+$ calcd. for $[C_{29}H_{28}ClN_2O_2]^+$ 471.1834; found 471.1821.

N-(3-chlorobenzyl)-4-(4-methoxybenzoyl)-5-methyl-1-(4-methylbenzyl)-1H-pyrrole-2-carboxamide (9i)

White solid. Yield: 69%, mp: 136–138 °C. ^{1}H NMR (300 MHz, $CDCl_3$) δ: 2.32 (s, 3H), 2.50 (s, 3H), 3.87 (s, 3H), 4.48 (d, 2H, J = 5.9 Hz), 5.68 (s, 2H), 6.21 (brt, 1H, J = 5.7 Hz), 6.83 (s, 1H), 6.93 (m, 4H), 7.07 (m, 3H), 7.22 (m, 3H), 7.80 (d, 2H, J = 8.7 Hz); ^{13}C NMR (75 MHz, $CDCl_3$) δ: 12.1, 21.4, 43.0, 48.2, 55.8, 113.8, 115.3, 120.5, 124.7, 126.1, 126.5, 128.0 (2C), 129.8, 130.3, 131.8, 132.8, 134.6, 134.8, 137.3, 140.7, 141.6, 161.8, 162.9, 191.2. HRMS (ESI, m/z) $[M + H]^+$ calcd. for $[C_{29}H_{28}ClN_2O_3]^+$ 487.1783; found 487.1770.

1-(4-aminobenzyl)-4-benzoyl-N-(3-chlorobenzyl)-5-methyl-1H-pyrrole-2-carboxamide (10a)

To a solution of EtOH (30 mL), THF (7 mL), and saturated solution of NH_4Cl (7 mL), 9j (0.305 g, 0.625 mmol) and iron powder (0.523 g, 9.37 mmol) were added, and the resulting mixture was stirred for 2 h at 100 °C. After cooling to room temperature, the reaction mixture was diluted with EtOH and filtered on a celite pad. The organic solvents were removed under vacuum and the residue was taken up in EtOAc, washed with brine, dried (Na_2SO_4), and filtered. The organic solvent was removed under reduced pressure, and the residue was purified by silica gel flash chromatography using EtOAc/petroleum ether (40–60 °C)/DCM (7: 1.5: 1.5) as mobile phase to provide the title compound as a white solid. Yield: 81%, mp: 129–131 °C. ^{1}H NMR (400 MHz, $CDCl_3$) δ: 2.54 (s, 3H), 3.57 (brs, 2H), 4.46 (d, 2H, J = 6.0 Hz), 5.57 (s, 2H), 6.24 (brt, 1H, J = 6.0 Hz), 6.60 (d, 2H, J = 8.2 Hz), 6.78 (s, 1H), 6.86 (d, 2H, J = 8.2 Hz), 7.06 (m, 1H), 7.21 (m, 2H), 7.41–7.53

(m, 4H), 7.75 (d, 2H, J = 7.7 Hz); ^{13}C NMR (101 MHz, $CDCl_3$) δ: 12.3, 43.0, 48.0, 115.6 (2C), 120.2, 125.0, 126.1, 127.4, 127.9, 128.0, 128.1, 128.5, 129.4, 130.3, 131.8, 134.8, 140.5, 140.8, 142.1, 146.0, 161.9, 192.3. HRMS (ESI, m/z) $[M + H]^+$ calcd. for $[C_{27}H_{25}ClN_3O_2]^+$ 458.1630; found 458.1624.

(±)N-(3-chlorobenzyl)-4-(hydroxy(phenyl)methyl)-5-methyl-1-(4-methylbenzyl)-1H-pyrrole-2-carboxamide (10b)

To a solution of 1 (0.300 g, 0.656 mmol) in EtOH/H_2O (10:1.5), $NaBH_4$ (0.027 g, 0.723 mmol) was added over 20 min. The reaction mixture was stirred at 50 °C for 18 h. After cooling to room temperature, the reaction mixture was taken up in EtOAc and washed with 1N HCl (2 × 20 mL). The organic phase was dried (Na_2SO_4) and filtered, and solvent was removed under vacuum. The resulting residue was purified by flash chromatography on silica gel using petroleum ether (40–60 °C)/EtOAc (7:3) as eluent to provide the title compound as a white solid. Yield: 78%, mp: 107–109 °C. ^{1}H NMR (400 MHz, $CDCl_3$) δ: 2.00 (d, 1H, J = 3.7 Hz), 2.19 (s, 3H), 2.31 (s, 3H), 4.38–4.50 (m, 2H), 5.62 (q, 2H, J = 16.0 Hz), 5.84 (d, 1H, J = 3.6 Hz), 6.08 (brt, 1H, J = 6.1 Hz), 6.42 (s, 1H), 6.88 (d, 2H, J = 7.8 Hz), 7.09 (d, 3H, J = 7.5 Hz), 7.18–7.30 (m, 4H), 7.34–7.42 (m, 4H); ^{13}C NMR (101 MHz, $CDCl_3$) δ: 10.7, 21.4, 42.9, 48.2, 70.0, 110.8, 123.9, 124.6, 126.0, 126.4, 126.5, 127.6, 127.8, 128.0, 128.7, 129.6, 130.2, 133.2, 134.8, 135.7, 136.9, 141.1, 142.2, 162.0. HRMS (ESI, m/z) $[M + H]^+$ calcd. for $[C_{28}H_{27}ClN_2O_2Na]^+$ 481.1653; found 481.1635.

Cell Cultures

Human epithelial melanoma A375 cells, human colorectal carcinoma HCT-116 cells, and normal rat L6 myoblast were grown in DMEM (Invitrogen, Paisley, UK) supplemented with 10% fetal bovine serum (FBS, Cambrex, Verviers, Belgium), L-glutamine (2 mM, Sigma, Milan, Italy), penicillin (100 units/mL, Sigma), and streptomycin (100 μg/mL, Sigma) and cultured in a humidified 5% carbon dioxide atmosphere at 37 °C, according to ATCC recommendations. A375 and HCT-116 were used as preclinical human cancer models in vitro, while rat L6 were used as control healthy cells.

Bioscreens In Vitro for Anticancer Activity

The antiproliferative activity of 1, 9a–i, and 10a,b was investigated through the estimation of a "cell survival index", arising from the combination of cell viability evaluation with cell counting, as previously reported [211]. The cell survival index is calculated as the arithmetic mean between the percentage values derived from the MTT assay and the automated cell count. Cells were inoculated in 96-microwell culture plates at a density of 104 cells/well and allowed to grow for 24 h. The medium was then replaced with fresh medium and cells were treated for an additional 48 h with a range of concentrations (from 1.5 to 25 μM) of 1, 9a–i, and 10a,b. Using the same experimental procedure, cell cultures were also incubated with DMSO as negative controls (vehicle), as well as with cisplatin (cDDP) and nutlin-3a as positive controls for cytotoxic and antiproliferative effects, respectively. Cell viability was evaluated using the MTT assay procedure. Cell number was determined by TC20 automated cell

counter (Bio-Rad, Milan, Italy), providing an accurate and reproducible total count of cells and a live/dead ratio in one step by a specific dye (trypan blue) exclusion assay. The calculation of the concentration required to inhibit the net increase in the cell number and viability by 50% (IC_{50}) is based on plots of data (n = 6 for each experiment) and repeated five times (total n = 30). IC_{50} values were calculated from a dose–response curve by nonlinear regression using a curve-fitting program, GraphPad Prism 5.0, and are expressed as mean values ± SEM (n = 30) of five independent experiments.

Apoptosis/Necrosis Detection

The evaluation of apoptosis and/or necrosis induction after treatments in vitro was investigated by using the Apoptosis/Necrosis Detection kit (ab176749, Abcam, Discovery Drive, Cambridge Biomedical Campus, Cambridge, UK), which is optimized to simultaneously detect cell apoptosis (green), necrosis (red), and healthy cells (blue) by fluorescence microscopy analysis. During apoptosis, phosphatidylserine (PS) is transferred to the outer leaflet of the plasma membrane. As a universal indicator of the initial/intermediates stages of cell apoptosis, the appearance of PS on the cell surface can be detected before cytomorphological changes are observed. Thus, the phosphatidylserine (PS) early apoptotic sensor has green fluorescence (Ex/Em = 490/525 nm) upon binding to membrane PS. Conversely, loss of plasma membrane integrity, as demonstrated by the ability of a membrane-impermeable 7-AAD (Ex/Em = 546/647 nm) to label the nucleus, represents a straightforward approach to demonstrate late-stage apoptosis as well as necrosis. In addition, this kit also provides a

live-cell cytoplasm-labeling dye, CytoCalcein Violet 450 (Ex/Em = 405/450 nm), for labeling living-cell cytoplasm. A375 and HCT-116 cells were inoculated in 96-microplates (black wells/clear flat bottom) at a density of 5×10^3 cells × well and allowed to grow for 24 h. Then, cells were treated for 24 h with IC_{50} values of 9c and 10a for A375 and of compound 9f and (±)10b for HCT-116 cells, respectively. Cells were also incubated with nutlin-3a, here used as positive controls. After removing the medium, the cells were washed three times with 100 µL assay buffer, stained with 200 µL assay buffer, 2 µL Apopxin Green Solution, 1 µL 7-ADD, and 1 µL CytoCalcein Violet 450, and incubated at RT for 30 min protected from light. Finally, 200 µL assay buffer was replaced and cells were analyzed under a fluorescence microscope at Ex/Em = 490/525 nm for apoptosis detection, at Ex/Em = 550/650 nm for necrosis detection, and at Ex/Em = 405/450 nm for healthy cell recognition.

Statistical Analysis

All data were presented as mean values ± SEM. The statistical analysis was performed using Graph-Pad Prism (Graph-Pad software Inc., San Diego, CA, USA), and an ANOVA test for multiple comparisons was performed followed by Bonferroni's test.

Solubility Assay

The solubility of each molecule in PBS was quantified measuring the UV scattering in the range of 600–800 nm (JASCO UV-530 spectrophotometer, equipped with ETC-505 T temperature controller). DMSO solutions of 1, 9a, 9b, 9c, 9d, 9e, 9f, ±10b, and nutlin-3a were used at a final concentration of 2.6 mM, whereas those of 9g, 9h, and

9i were used at 1.0 mM. A total of 1400 µL of degassed PBS was placed in a quartz cuvette (o.l. 0.5 cm), equilibrated 5 min at 37 °C, and then titrated by 7–10 successive additions of 0.5 µL or 0.3 µL from the DMSO solution. Each titration was performed without removing the cuvette from the UV cell and, after each addition, the solution was equilibrated 1 min a 37 °C under gently stirring before the acquisition of the UV data. For each molecule, the solubility was expressed as the mean ± SEM (n = 3).

Molecular Modeling Studies

Molecular modeling calculations were performed on SGI Origin 200 8XR12000 and E4 Server Twin 2 × Dual Xeon 5520 equipped with two nodes. Each node: 2 × Intel Xeon QuadCore E5520, 2.26 Ghz, 36 GB RAM. The molecular modeling graphics were carried out on a personal computer equipped with an Intel(R) Core (TM) i7-4790 processor and SGI Octane 2 workstations.

Conformational Analysis

The apparent pKa and clogD (pH 7.4) values of 9a–i and 10a,b were calculated by using ACD/Percepta software (ACD/Percepta software, version 2017.1.3, Advanced Chemistry Development, Inc., Toronto, ON, Canada, 2017, http://www.acdlabs.com, accessed on 5 September 2022). All new compounds and the reference compound 1 were considered neutral in all calculations performed as a consequence of the estimation of percentage of neutral/ionized forms computed at the pH 7.2 (cytoplasmic value) using the Handerson–Hasselbalch equation. The newly designed pyrrole derivatives were built using the

Small Molecule tool of Discovery Studio 2017 (Dassault Systèmes BIOVIA, San Diego, CA, USA). Atomic potentials and charges were assigned using the CHARMm. Then, all compounds were subjected to molecular mechanic (MM) energy minimization (ε = 80 * r) until the maximum RMS derivative was less than 0.01 kcal/Å using Conjugate Gradient as minimization algorithm.

All the rotatable bonds included in the conformational search are sigma bonds not included in rings and, by consequence, are free to rotate. Nevertheless, the torsion angles τ1, τ2, and τ3 are affected by π electron conjugation and can be found in a synperiplanar or antiperiplanar conformation.

The conformational space of the compounds was sampled using the random search algorithm Boltzmann Jump for the random generation of a maximum of 400 conformations. Applying this method, each random perturbation is either accepted or rejected according to the Metropolis selection criterion with a ratio according to the Boltzmann distribution (T = 300 K). Finally, an energy threshold value of 20 kcal/mol was used as selection criteria. The generated structures were then subjected to MM energy minimization until the maximum RMS derivative was less than 0.01 kcal/Å using Conjugate Gradient as minimization algorithm and the Generalized Born implicit solvent model with a solvent dielectric constant value of 80. The resulting conformers were ranked by their potential energy values (i.e., energy difference from the global minimum (ΔEGM)) and those showing a ΔEGM ≤ 5 kcal/mol were selected for further analysis.

The selected structures were classified into conformational families named TTT, TTC, TCC, TCT, TCG−, TCA−, and TCG+ according to

the values of the torsion angles τ1, τ2, and τ3 (i.e., synperiplanar, = C; antiperiplanar = T; synclinal = G−; anticlinal = A−; synclinal = G+). The obtained families were divided into subfamilies according to the values of the torsion angle τ5 (using the roman numbers). The ranges of torsion angle values used for the classification were the following: 0° to ±30° (synperiplanar, C); 30° to 90° (synclinal, G+); −30° to −90° (synclinal, G−); 90° to 150° (anticlinal, A+); −90° to −150° (anticlinal, A−) and ±150° to 180° (antiperiplanar, T).

The lowest-energy conformers of each conformational family were then subjected to DFT calculations (Gaussian 16 package). Since the compounds 1, 9a–f, 9h–i, and 10a presented—in the case of the conformational families TCC and TCT—a MM lowest-energy conformer belonging to two different subfamilies, we included in the DFT calculations of these compounds the minimum conformers of the subfamilies I and II for the TCC family and the minimum conformers of the subfamilies I and III for the TCT family. All structures were fully optimized at the B3LYP/6–31+G(d,p) level [212] using the conductor-like polarizable continuum model (C-PCM) [208]. The C-PCM method allows the calculation of the energy in the presence of a solvent. In this case, all structures were optimized as a solute in an aqueous solution. In order to characterize every structure as minimum, a vibrational analysis was carried out (keyword = freq). The RMS force criterion was set to 3×10^{-4} a.u. The electronic distribution has been calculated using the natural bond orbital (NBO) method.

The resulting DFT conformers were ranked by their potential energy values (i.e., ΔE from the global energy minimum) and those showing a ΔEGM < 2 kcal/mol were selected and classified into conformational

families/subfamilies by applying the same criteria used for the MM conformers. The distances between the pharmacophore moieties were calculated for each conformer using the centroids of the aromatic rings X, Y, and Z.

Structural and Bioinformatics Studies

The experimentally determined structures of (i) the two-stranded parallel coiled coil of the GCN4 leucine zipper, (PDB ID: 2ZTA); (ii) the antiparallel coiled coil of GreA transcript cleavage factor from E. coli (PDB ID: 1GRJ); and (iii) the LxxLL motif of the nuclear receptor coactivator 5 in complex with the estrogen receptor β (PDB ID: 2J7X) were downloaded from the Protein Data Bank (PDB; http://www.rcsb.org/pdb/, accessed on 12 December 2022). All structures were analyzed using the Simulation and Macromolecule tools of Discovery Studio 2017 (Dassault Systèmes BIOVIA, San Diego, CA, USA).

The centroids of the hot-spot residues responsible for PPI (i.e., coiled coil: i, i + 3, i + 4, i + 7; LxxLL: i, i + 3, i + 4) were built considering the ring carbon atoms of aromatic side chains and all the heavy atoms of aliphatic amino acids side chains. Then, the distances between the centroids of the interacting residues were calculated. The resulting distance maps were crossed with the pharmacophore distances of the TSPs, considering the lowest-energy DFT conformers ($\Delta EGM \leq 2$ kcal/mol). According to the pharmacophoric distances (using the same specified distance similarity criteria), the selected subfamilies were grouped, and, for each group, a pharmacophore was built calculating the average values of the pharmacophore distances. The TSP

conformational subfamilies showing the best match with the experimentally determined distances of the interacting residues of the PPI motifs were selected (two distances differing less than 1.0 Å and one less than 1.5 Å).

A representative conformer of each pharmacophore (considering both conformational/configurational enantiomers) was superimposed on the PPI motifs by fitting the centroids of the TSP pharmacophore groups (i.e., the aromatic rings X, Y, and Z) on the centroids of the side chains of the interacting residues of the PPI motifs, and the root-mean-square distance (RMSD) values of the fitted conformers were calculated. The TSP conformers with a calculated root-mean-square distance (RMSD) value < 2.5 Å were considered mimetic of that motif.

A structural and bioinformatics analysis was then performed on the experimentally determined structures of p19ARF, a putative molecular target of our TSPs. The structure of mouse p19ARF tumor suppressor protein (PDB ID: 1HN3) was downloaded from the Protein Data Bank (PDB; http://www.rcsb.org/pdb/, accessed on 12 December 2022). Moreover, the full-length sequence of the human homologue of mouse p19ARF (p14ARF) was downloaded from the UniProtKB/Swiss-Prot Data Bank (http://www.uniprot.org, accessed on 12 December 2022). A pairwise alignment was performed using the sequences of p19ARF and its human homologue p14ARF (PROMALS 3D server; http://prodata.swmed.edu/promals3d/promals3d.php, accessed on 12 December 2022)[213].

The presence of protein-recognition motifs was checked on the first two N-terminal helices of p14ARF (αH1, residues 4–14; αH2, residues 20–29) (consensus sequence

[VLIFYWM]xx[VLIFYWM][VLIFYWM]xx[VLIFYWM]; Predict Sequence Properties protocol, Discovery Studio 2017). A homology model of human p14ARF was built (Macromolecule, Discovery Studio 2017) on the bases of the sequence alignment with mouse p19ARF, and the hot-spot residues of the identified PPI motifs on the αH2 of p14ARF were introduced in the structure of p19ARF (PDB ID: 1HN3). Finally, the selected DFT conformers of our TSPs matching the above-specified similarity criteria with the considered PPI motifs were superimposed on the newly identified PPI motif on human p14ARF (H_2) by fitting the centroids of the pharmacophore groups (i.e., the aromatic rings X, Y, and Z) on the centroids of the side chains of the hot-spot residues of the PPI motif. The RMSD values of the fitted conformers were calculated.

Additional Data and Supporting Figures from "Tetrasubstituted Pyrrole Derivative Mimetics of Protein–Protein Interaction Hot-Spot Residues: A Promising Class of Anticancer Agents Targeting Melanoma Cells", Cells. *Molecules*, *28*(10), 4161. https://doi.org/10.3390/molecules28104161

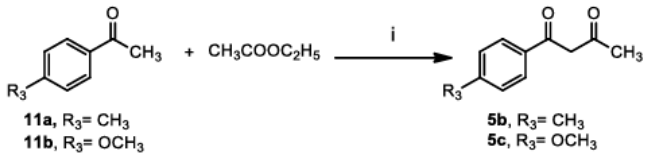

Figure S1. Reagents and conditions: i) NaH (60 % dispersion in mineral oil), dry DMF, rt, 3h, then 60°C, 1h

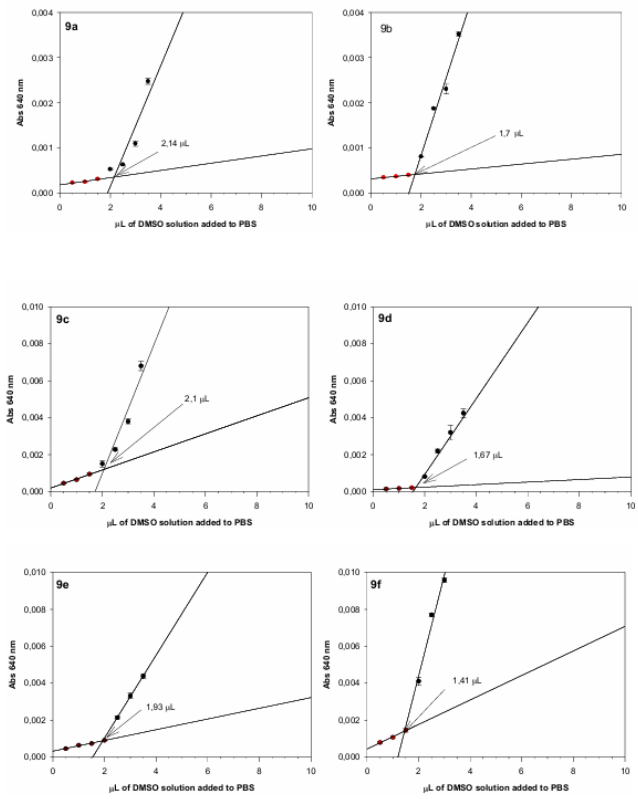

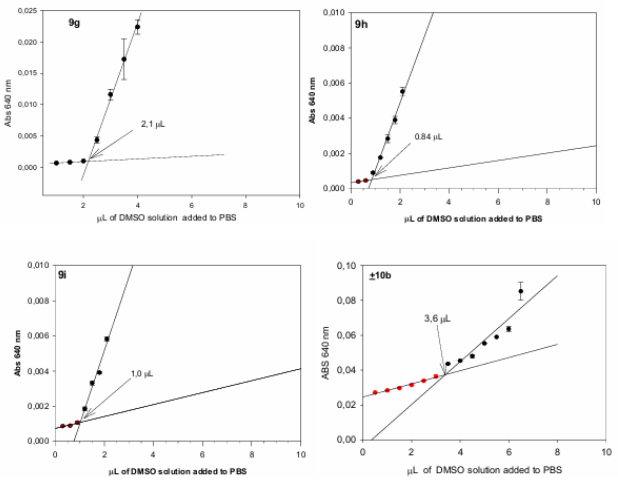

Figure S2. Graphical representation of the absorption of PBS measured at 640 vs µL of added DMSO solutions containing the species indicated in each panel. DMSO solutions (2,6 mM, for 9a, 9b, 9c, 9d, 9e, 9f, ±10b or 1,0 mM for 9g, 9h, 9i) were added to 1400 µL of PBS 0.5 at time. In all cases the final % (Vol/Vol) of DMSO in PBS was ≤0.6%

8.5 References

[161] Z. L. Pianowski, "Recent Implementations of Molecular Photoswitches into Smart Materials and Biological Systems," Apr. 05, 2019, *Wiley-VCH Verlag*. doi: 10.1002/chem.201805814.

[162] M. Irie, "Photochromism: Memories and SwitchesIntroduction," *Chem Rev*, vol. 100, no. 5, pp. 1683–1684, May 2000, doi: 10.1021/cr9800681.

[163] J. Griffiths, "1. Photochemistry of Azobenzene and its Derivatives."

[164] A. Georgiev *et al.*, "Synthesis, structure, spectral properties and DFT quantum chemical calculations of 4-aminoazobenzene dyes. Effect of

intramolecular hydrogen bonding on photoisomerization," *Spectrochim Acta A Mol Biomol Spectrosc*, vol. 175, pp. 76–91, Mar. 2017, doi: 10.1016/j.saa.2016.12.005.

[165] A. Georgiev, A. Stoilova, D. Dimov, D. Yordanov, I. Zhivkov, and M. Weiter, "Synthesis and photochromic properties of some N-phthalimide azo-azomethine dyes. A DFT quantum mechanical calculations on imine-enamine tautomerism and trans-cis photoisomerization," *Spectrochim Acta A Mol Biomol Spectrosc*, vol. 210, pp. 230–244, Mar. 2019, doi: 10.1016/j.saa.2018.11.033.

[166] E. Merino and M. Ribagorda, "Control over molecular motion using the cis-trans photoisomerization of the azo group," Jul. 12, 2012. doi: 10.3762/bjoc.8.119.

[167] E. M. M. Tan, S. Amirjalayer, S. Smolarek, A. Vdovin, F. Zerbetto, and W. J. Buma, "Fast photodynamics of azobenzene probed by scanning excited-state potential energy surfaces using slow spectroscopy," *Nat Commun*, vol. 6, Jan. 2015, doi: 10.1038/ncomms6860.

[168] M. Dong, A. Babalhavaeji, S. Samanta, A. A. Beharry, and G. A. Woolley, "Red-Shifting Azobenzene Photoswitches for in Vivo Use," *Acc Chem Res*, vol. 48, no. 10, pp. 2662–2670, Oct. 2015, doi: 10.1021/acs.accounts.5b00270.

[169] I. S. Anggia, D. Hayati, and J. Hong, "Synthesis and photophysical characterization of push-pull azobenzene derivatives featuring different π-bridges for photoresponsive applications," *Dyes and Pigments*, vol. 234, Mar. 2025, doi: 10.1016/j.dyepig.2024.112550.

[170] J. C. Corchado *et al.*, “Theoretical study of solvent effects on the ground and low-lying excited free energy surfaces of a push-pull substituted azobenzene,” *Journal of Physical Chemistry B*, vol. 118, no. 43, pp. 12518–12530, Oct. 2014, doi: 10.1021/jp506876v.

[171] H. M. D. Bandara and S. C. Burdette, “Photoisomerization in different classes of azobenzene,” *Chem Soc Rev*, vol. 41, no. 5, pp. 1809–1825, Feb. 2012, doi: 10.1039/c1cs15179g.

[172] “G. S. Hartley, J. Chem. Soc., 1938, 633–642.”.

[173] A. H. Heindl and H. A. Wegner, “Rational Design of Azothiophenes—Substitution Effects on the Switching Properties,” *Chemistry - A European Journal*, vol. 26, no. 60, pp. 13730–13737, Oct. 2020, doi: 10.1002/chem.202001148.

[174] D. Bléger, J. Schwarz, A. M. Brouwer, and S. Hecht, “O - fluoroazobenzenes as readily synthesized photoswitches offering nearly quantitative two-way isomerization with visible light,” *J Am Chem Soc*, vol. 134, no. 51, pp. 20597–20600, Dec. 2012, doi: 10.1021/ja310323y.

[175] C. L. Forber, E. C. Kelusky, N. J. Bunce, and M. C. Zerner, “Electronic Spectra of cis-and frans-Azobenzenes: Consequences of Ortho Substitution,” 1985. [Online]. Available: https://pubs.acs.org/sharingguidelines

[176] K. Aggarwal *et al.*, “Visible Light Mediated Bidirectional Control over Carbonic Anhydrase Activity in Cells and in Vivo Using Azobenzenesulfonamides,” *J Am Chem Soc*, vol. 142, no. 34, pp. 14522–14531, Aug. 2020, doi: 10.1021/jacs.0c05383.

[177] A. Kerckhoffs, M. Ahmad, and M. J. Langton, “Transient Photoactivation of Anionophores by Using Redshifted Fast-Relaxing Azobenzenes,” *Chemistry - A European Journal*, vol. 30, no. 64, Nov. 2024, doi: 10.1002/chem.202402382.

[178] J. García-Amorós and D. Velasco, “Recent advances towards azobenzene-based lightdriven real-time information-transmitting materials,” Jul. 04, 2012. doi: 10.3762/bjoc.8.113.

[179] S. Crespi, N. A. Simeth, and B. König, “Heteroaryl azo dyes as molecular photoswitches,” Mar. 01, 2019, *Nature Publishing Group*. doi: 10.1038/s41570-019-0074-6.

[180] R. Lin *et al.*, “Phenylazothiazoles as Visible-Light Photoswitches,” *J Am Chem Soc*, vol. 145, no. 16, pp. 9072–9080, Apr. 2023, doi: 10.1021/jacs.3c00609.

[181] M. M. M. Raposo, M. C. R. Castro, A. M. C. Fonseca, P. Schellenberg, and M. Belsley, “Design, synthesis, and characterization of the electrochemical, nonlinear optical properties, and theoretical studies of novel thienylpyrrole azo dyes bearing benzothiazole acceptor groups,” *Tetrahedron*, vol. 67, no. 29, pp. 5189–5198, Jul. 2011, doi: 10.1016/j.tet.2011.05.053.

[182] M. R. S. A. Janjua, “Computational Study on Non-linear Optical and Absorption Properties of Benzothiazole based Dyes: Tunable Electron-Withdrawing Strength and Reverse Polarity,” *Open Chem*, vol. 15, no. 1, pp. 139–146, 2017, doi: 10.1515/chem-2017-0017.

[183] A. H. Chen, Z. J. Knepp, C. A. Guzman, E. R. Young, and L. A. Fredin, “Intramolecular subtleties in indole azo dyes revealed by

multidimensional potential energy surfaces," *Physical Chemistry Chemical Physics*, vol. 27, no. 13, pp. 6430–6437, Mar. 2025, doi: 10.1039/d5cp00110b.

[184] H. S. Samuel, U. Nweke-Maraizu, and E. E. Etim, "Review Article: Understanding Intermolecular and Intramolecular Hydrogen Bonds: Spectroscopic and Computational Approaches," Oct. 01, 2023, *Sami Publishing Company*. doi: 10.48309/jcr.2023.407989.1235.

[185] A. Jezierska, P. M. Tolstoy, J. J. Panek, and A. Filarowski, "Intramolecular hydrogen bonds in selected aromatic compounds: Recent developments," Nov. 01, 2019, *MDPI*. doi: 10.3390/catal9110909.

[186] M. Borowiak *et al.*, "Optical Manipulation of F-Actin with Photoswitchable Small Molecules," *J Am Chem Soc*, vol. 142, no. 20, pp. 9240–9249, May 2020, doi: 10.1021/jacs.9b12898.

[187] H. M. D. Bandara and S. C. Burdette, "Photoisomerization in different classes of azobenzene," *Chem Soc Rev*, vol. 41, no. 5, pp. 1809–1825, Feb. 2012, doi: 10.1039/c1cs15179g.

[188] J. Volarić, W. Szymanski, N. A. Simeth, and B. L. Feringa, "Molecular photoswitches in aqueous environments," Nov. 21, 2021, *Royal Society of Chemistry*. doi: 10.1039/d0cs00547a.

[189] M. H. Abraham, R. J. Abraham, W. E. Acree, A. E. Aliev, A. J. Leo, and W. L. Whaley, "An NMR method for the quantitative assessment of intramolecular hydrogen bonding; Application to physicochemical, environmental, and biochemical properties," *Journal of Organic*

Chemistry, vol. 79, no. 22, pp. 11075–11083, Nov. 2014, doi: 10.1021/jo502080p.

[190] R. W. Newberry and R. T. Raines, "A prevalent intraresidue hydrogen bond stabilizes proteins," *Nat Chem Biol*, vol. 12, no. 12, pp. 1084–1088, Dec. 2016, doi: 10.1038/nchembio.2206.

[191] A. A. Ivanov, F. R. Khuri, and H. Fu, "Targeting protein-protein interactions as an anticancer strategy," Jul. 2013. doi: 10.1016/j.tips.2013.04.007.

[192] E. Stefan, J. Troppmair, and K. Bister, "Targeting the Architecture of Deregulated Protein Complexes in Cancer," in *Advances in Protein Chemistry and Structural Biology*, vol. 111, Academic Press Inc., 2018, pp. 101–132. doi: 10.1016/bs.apcsb.2017.07.001.

[193] X. Xie *et al.*, "Recent advances in targeting the 'undruggable' proteins: from drug discovery to clinical trials," Dec. 01, 2023, *Springer Nature*. doi: 10.1038/s41392-023-01589-z.

[194] B. L. Grasberger *et al.*, "Discovery and cocrystal structure of benzodiazepinedione HDM2 antagonists that activate p53 in cells," *J Med Chem*, vol. 48, no. 4, pp. 909–912, Feb. 2005, doi: 10.1021/jm049137g.

[195] O. Kutzki, H. S. Park, J. T. Ernst, B. P. Orner, H. Yin, and A. D. Hamilton, "Development of a potent Bcl-xL antagonist based on α-helix mimicry," *J Am Chem Soc*, vol. 124, no. 40, pp. 11838–11839, Oct. 2002, doi: 10.1021/ja026861k.

[196] J. Becerril and A. D. Hamilton, "Helix mimetics as inhibitors of the interaction of the estrogen receptor with coactivator peptides,"

Angewandte Chemie - International Edition, vol. 46, no. 24, pp. 4471–4473, 2007, doi: 10.1002/anie.200700657.

[197] L. R. Hoggard, Y. Zhang, M. Zhang, V. Panic, J. A. Wisniewski, and H. Ji, "Rational Design of Selective Small-Molecule Inhibitors for β-Catenin/B-Cell Lymphoma 9 Protein-Protein Interactions," *J Am Chem Soc*, vol. 137, no. 38, pp. 12249–12260, Sep. 2015, doi: 10.1021/jacs.5b04988.

[198] Z. Wang and H. Ji, "Targeting the Side-Chain Convergence of Hydrophobic α-Helical Hot Spots to Design Small-Molecule Mimetics: Key Binding Features for i, i + 3, and i + 7," *J Med Chem*, vol. 62, no. 21, pp. 9906–9917, Nov. 2019, doi: 10.1021/acs.jmedchem.9b01324.

[199] B. N. Bullock, A. L. Jochim, and P. S. Arora, "Assessing helical protein interfaces for inhibitor design," *J Am Chem Soc*, vol. 133, no. 36, pp. 14220–14223, Sep. 2011, doi: 10.1021/ja206074j.

[200] M. Persico *et al.*, "New anticancer agents mimicking protein recognition motifs," *J Med Chem*, vol. 56, no. 17, pp. 6666–6680, Sep. 2013, doi: 10.1021/jm400947b.

[201] J. Ribas, E. Cubero, F. J. Luque, and M. Orozco, "Theoretical study of alkyl-π and aryl-π interactions. Reconciling theory and experiment," *Journal of Organic Chemistry*, vol. 67, no. 20, pp. 7057–7065, Oct. 2002, doi: 10.1021/jo0201225.

[202] C. A. Lipinski, F. Lombardo, B. W. Dominy, and P. J. Feeney, "Experimental and computational approaches to estimate solubility

and permeability in drug discovery and development q settings," 2001. [Online]. Available: www.elsevier.com/locate/drugdeliv

[203] W.-H. Xie, W.-Y. Shiub, and D. Mackayb, "A Review of the Effect of Salts on the Solubility of Organic Compounds in Seawater," 1997.

[204] R. Zangi, M. Hagen, and B. J. Berne, "Effect of ions on the hydrophobic interaction between two plates," *J Am Chem Soc*, vol. 129, no. 15, pp. 4678–4686, Apr. 2007, doi: 10.1021/ja068305m.

[205] M. C. Proto *et al.*, "Tetra-substituted pyrrole derivatives act as potent activators of p53 in melanoma cells," *Invest New Drugs*, vol. 38, no. 3, pp. 634–649, Jun. 2020, doi: 10.1007/s10637-019-00813-4.

[206] J. J. P. Stewart, "Optimization of parameters for semiempirical methods V: Modification of NDDO approximations and application to 70 elements," *J Mol Model*, vol. 13, no. 12, pp. 1173–1213, Dec. 2007, doi: 10.1007/s00894-007-0233-4.

[207] M. F. Budyka and I. V. Oshkin, "Comparative semiempirical and DFT study of styrylnaphthalenes and styrylquinolines and their photocyclization products," *Int J Quantum Chem*, vol. 111, no. 14, pp. 3673–3680, Nov. 2011, doi: 10.1002/qua.22797.

[208] M. Cossi, N. Rega, G. Scalmani, and V. Barone, "Energies, structures, and electronic properties of molecules in solution with the C-PCM solvation model," *J Comput Chem*, vol. 24, no. 6, pp. 669–681, Apr. 2003, doi: 10.1002/jcc.10189.

[209] E. Hodis *et al.*, "A landscape of driver mutations in melanoma," *Cell*, vol. 150, no. 2, pp. 251–263, Jul. 2012, doi: 10.1016/j.cell.2012.06.024.

[210] E. L. DiGiammarino, I. Filippov, J. D. Weber, B. Bothner, and R. W. Kriwacki, “Solution structure of the p53 regulatory domain of the p19Arf tumor suppressor protein,” *Biochemistry*, vol. 40, no. 8, pp. 2379–2386, Feb. 2001, doi: 10.1021/bi0024005.

[211] C. Irace *et al.*, “Antiproliferative effects of ruthenium-based nucleolipidic nanoaggregates in human models of breast cancer in vitro: Insights into their mode of action,” *Sci Rep*, vol. 7, 2017, doi: 10.1038/srep45236.

[212] C. Lee, eitao Yang, and R. G. Parr, “Development of the Colic-Salvetti correlation-energy formula into a functional of the electron density.”

[213] J. Pei, B. H. Kim, and N. V. Grishin, “PROMALS3D: A tool for multiple protein sequence and structure alignments,” *Nucleic Acids Res*, vol. 36, no. 7, pp. 2295–2300, Apr. 2008, doi: 10.1093/nar/gkn072.